Universität Hamburg
DER FORSCHUNG | DER LEHRE | DER BILDUNG

Applications of Functional One-Dimensional Nanostructures Studied by Light Scattering

Dissertation

zur Erlangung des Doktorgrades
an der Fakultät für Mathematik, Informatik und Naturwissenschaften
im Fachbereich Physik
der Universität Hamburg

vorgelegt von
Tomke Eva Glier

Hamburg
2021

Gutachter der Dissertation:	Prof. Dr. Michael Rübhausen
	Prof. Dr. Stephan V. Roth
Zusammensetzung der Prüfungskommission:	Prof. Dr. Daniela Pfannkuche
	Prof. Dr. Michael Rübhausen
	Prof. Dr. Stephan V. Roth
	Prof. Dr. Nils Huse
	Dr. Sylvio Haas
Vorsitzende der Prüfungskommission:	Prof. Dr. Daniela Pfannkuche
Vorsitzender des Fach-Promotionsausschusses Physik:	Prof. Dr. Wolfgang Hansen
Leiter des Fachbereichs Physik:	Prof. Dr. Günter H. W. Sigl
Dekan der Fakultät MIN:	Prof. Dr. Heinrich Graener
Tag der Disputation:	15.11.2021

The senses deceive from time to time,
and it is prudent never to trust wholly
those who have deceived us even once.
René Descartes

Persistent Identifier: urn:nbn:de:gbv:18-ediss-96917

Abstract

One-dimensional (1D) nanocrystals represent a versatile and functional class of materials characterized through a high transport efficiency along the long axis, and a confined cylindrical surface. Silver nanowires (Ag-NWs) are excellent building blocks for 2D conductive networks, which are used as functional fillers in 3D printing polymer composites. The morphology of randomly oriented Ag-NWs is studied as a function of concentration, as well as during external modifications and within a polymer matrix by, *inter alia*, grazing incidence X-ray scattering. Flexible and conductive Ag-NW composites are fabricated and investigated under mechanical stress. Key network properties are revealed by a Monte Carlo based model. The electrical nanowire network, dominated by the tunneling resistances between the nanowires, strongly interacts with the supporting polymer matrix. A 3D-printed flexible capacitor is demonstrated as a prototype for 3D printed flexible electronic devices. Furthermore, in order to investigate the low-energy excitation spectrum as well as the interaction between the electronic system with lattice degrees of freedom within 1D nanostructures, Raman spectroscopy is utilized. We developed a Raman microscope with ultra-small spot sizes down to 200 nm – 300 nm to study local phenomena on the nanoscale. Surface enhanced Raman spectroscopy (SERS) is used to study a chemical selective system based on the electronic transitions between semiconducting zinc oxide nanowires and 4-mercaptopyridine. Plasmonic enhancements of the Raman response are observed in nanowires of the topological insulator Bi_2Se_3 as a function of wire diameter. The modification of the quasi-relativistic surface states by geometrical confinement from 2D to 1D results in a gap opening of the spin-polarized Dirac-states as a consequence of the formation of a Spin-Berry phase.

Zusammenfassung

Eindimensionale (1D) Nanokristalle repräsentieren eine vielseitige, funktionale Klasse nanoskaliger Systeme. Sie zeichnen sich durch ihre Fähigkeit des effizienten Transports entlang der axialen Richtung, sowie durch eine, durch den Durchmesser in der Ausdehnung beschränkte, zylindrische Oberfläche aus. Silber Nanodrähte (Ag-NWs) sind hervorragend als Bestandteile von 2D leitfähigen Netzwerken geeignet. Nanodraht-Netzwerke werden zur Funktionalisierung von Polymerkompositen für den 3D Druck verwendet. Die Morphologie der zufällig angeordneten Ag-NWs wird als Funktion der Konzentration, sowie unter externen Einflüssen und eingebettet in eine Polymer-Matrix untersucht. Dies geschieht unter anderem mit Röntgenstreuung unter streifendem Einfall. Flexible und leitfähige Ag-NW-Komposite werden hergestellt und in mechanischen Stress-Tests untersucht. Die Netzwerkeigenschaften werden mit einem Modell, das auf einer Monte-Carlo-Methode beruht, erfolgreich beschrieben. Das elektrisch leitfähige Nanodrahtnetzwerk, das durch die Tunnelwiderstände zwischen den Nanodrähten dominiert wird, interagiert maßgeblich mit der Polymer-Matrix. Als Prototyp für ein 3D gedrucktes, flexibles, elektronisches Bauteil, wird ein flexibler Ag-NW-Kondensator präsentiert. Des Weiteren wird Raman-Spektroskopie verwendet, um das nieder-energetische Anregungsspektrum sowie die Interaktion zwischen dem elektronischen System und den Gitterschwingungen im nanoskaligen Festkörper zu untersuchen. Ein Raman-Mikroskop wird vorgestellt, das einen ultra-kleinen Spotdurchmesser von 200 nm – 300 nm erreicht. Oberflächenverstärkte Raman-Spektroskopie (SERS) wird angewendet, um die elektronischen Übergänge zwischen halbleitenden Zinkoxid Nanodrähten und 4-Mercaptopyridin zu untersuchen. Plasmonische Verstärkungseffekte der Raman-Antwort werden in Nanodrähten bestehend aus dem Topologischen Isolator Bi_2Se_3 als Funktion des Drahtdurchmessers beobachtet. Die Modifikation der quasi-relativistischen Oberflächenzustände durch ein geometrisches *confinement* des Festkörpers von 2D nach 1D resultiert in einem Öffnen der spin-polarisierten Dirac-Zustände als Folge der Bildung einer Spin-Berry Phase.

Contents

1 Chapter 1 Introduction

1.1 Preface

"I would like to describe a field, in which little has been done, but in which an enormous amount can be done in principle. This field is not quite the same as the others in that it will not tell us much of fundamental physics (in the sense of, "What are the strange particles?") but it is more like solid-state physics in the sense that it might tell us much of great interest about the strange phenomena that occur in complex situations. Furthermore, a point that is most important is that it would have an enormous number of technical applications."

Richard Feynman in *There's Plenty of Room at the Bottom*, 1960.[1]

For a long time people have been dealing with extreme dimensions that cannot be experienced through our senses. In astronomy, one of the oldest sciences, celestial bodies and phenomena were observed and interpreted from many different perspectives. Democritus of Abdera (460 - 370 BC) identified the milky way as an assembly of millions of stars.[2] The development of telescopes, photography, high-performance computers, and space travel accompanied and enabled the enormous advances in the acquisition and interpretation of data and knowledge.[3] In the fourth century BC, Democritus began another journey into unexplored areas and thought about breaking matter into its smallest parts. He coined the term 'atom', the smallest and indivisible particle.[4] With these metaphysical thoughts, Democritus entered a state of mind that could not be experienced and, from his point of view, was completely undefined. He represented the idea of matter made up of particles, in contrast to the idea that matter is a continuum.[5] Today, the nature of particles that form matter is investigated in particle physics with enormous technical efforts in e.g. particle accelerators.[6] A huge development of experimental techniques enables us today to be close to an extremely small world and to recognize phenomena that are different in nature from our macroscopic world.

On a scale 10-1000 times larger than a single atom, a finite number of atoms form clusters and structures with a size of up to $100 \cdot 10^{-9}$ m. They are studied by nanoscience. In general,

nanoscience deals with structures having at least one dimension with a size of between 1 to 100 nm.[7] This field is crossing the borders between physics, chemistry, life science, biology, and materials science, and offers a great amount of technical applications.[7, 8, 9] The term nanotechnology is used to refer to any type of technology on the nanoscale with applications in the everyday world.[10] Nanoscience, therefore, merges with nanotechology in many cases. There is a large number of nanostructures, many of which are highly specialized for certain applications, for example solid-state nanoparticles in various forms, nanoporous surfaces, biomolecules, organic vesicles, and micelles.[11, 12] Today's fields in nanotechnology are e.g. paints and coatings, energy storage systems and solar cells, cosmetics, health care, medicine, functional textiles, and electronic devices like processors, transparent electrodes, and memory storage.[7, 10] This huge diversity in materials, scientific fields, and applications makes nanoscience a significant part of modern science.

In this thesis, functional one-dimensional (1D) solid-state nanostructures and their applicability are investigated. The work includes different kinds of materials, which are zinc oxide nanowire arrays, single bismuth selenide nanowires, and networks from silver nanowires. This combination makes is possible to observe different applications of 1D nanoscience phenomena.

1.2 One-Dimensional Nanostructures

One-dimensional (1D) nanostructures have two dimensions in the range between 1 nm and 100 nm and one dimension that is substantially larger, resulting in elongated anisotropic shapes with high aspect ratios. Analogous to the macroscopic world, 1D structures enable efficient transport as used in e.g. wiring and pipes in networks or as bridges.[13] 1D nanostructures are, therefore, excellent building-blocks for functional devices allowing transport of electrons, excitons, and phonons. The connection of sticks, rods, or wires to electrical networks represent a very efficient way to build 2D layers with a high sheet conductivity but low amount of material.[14, 15]

When the dimension of a crystal is large compared to the electron wavelength, electrons behave like free particles within the crystal. But if the crystal dimensions reach a small critical size, confinement occurs and electronic, vibronic, and optical properties change compared to the bulk crystal.[16] Since 1D nanostructures exhibit two confined dimensions, confinement effects are observed as a function of their diameter.[17] In addition,

nanoparticles exhibit extremely high surface-to-volume ratios compared to macroscopic objects leading to enhanced surface properties.

Many different 1D materials have been subject of research over the past few decades. Carbon nanotubes, fibers consisting of graphene with diameters between 1 nm and 50 nm, have been discovered in 1991 by Iijima and co-workers.[18] Another class of functional 1D nanostructures is represented by metal nanowires. Many different fabrication processes have been reported, including wet chemical synthesis (bottom up) with capping agents as well as lithography (top down).[19, 20] Typical utilized metals are silver, gold, and copper. Semiconducting materials like zinc oxide, silicon, or gallium arsenide are also often used in the shape of 1D nanostructures. Other advanced functional properties are magnetizability, thermoelectricity, and the existence of quasi-relativistic surface states.[21, 22]

In addition to the material, shape and arrangement of nanowires also determine their functionality. Single nanowires represent a fully ordered system. Modifying the nanowire surface to e.g. nanobrushes or core-shell structures enables the surface roughness to be maximized or the surface to be passivated.[23] Nanowire networks combine 2D and 1D properties in a very efficient way.[14] The nanowires can be orientated randomly or regularly to form 2D networks. Alignment of nanowires leads to a controlled anisotropy. Arrays of vertically orientated nanowires represent substrates with giant surface to volume ratios.[24]

1.3 Outline of the Thesis

The thesis is organized as follows. Chapter 2 deals with theoretical concepts for condensed matter and the interaction of electromagnetic fields with matter. We focus on the material systems used in this work as well as on the scattering techniques employed. The latter are primarily Raman spectroscopy and grazing incidence X-ray scattering. In chapter 3, key experimental techniques are presented including a custom-made micro-Raman setup with ultra-small spot sizes as well as the development of a stretching setup for flexible composites. Chapter 4 reports on the conducted experiments. The experiments and results are described in detail together with respective models and simulations. Section 4.1 is about the development and application of printable, conductive, transparent, and flexible silver nanowire composites. Section 4.2 focuses on the application of nanowires for surface enhanced Raman scattering including quasi-relativistic surface states in bismuth selenide. The work is complemented by publication reprints, which were created during this thesis.

Chapter 2

2 Theoretical Background

2.1 Condensed Matter

Condensed matter exists in different forms, which are divided into crystalline solids like insulators, metals, and semiconductors, and soft matter such as polymers, liquids, colloids, foams, and liquid crystals. Crystalline solids have an atomic periodic order that is described by the Bravais lattices and a basis. Due to the periodicity of the crystal structures, they can be viewed both in position space and in momentum space, as unit cells that repeat themselves periodically.[25] Crystal lattices are dynamic. Lattice vibrations are signified by phonons being the quanta of the oscillation field. Since, viewed from the electronic system, the atomic core movements are slow, the properties of crystals can be roughly divided into the properties that are determined by the phonons and the properties of the electronic system. The occurrence of electron-lattice interactions is considered in terms of perturbation theory.[26, 27]

In quantum mechanics, the total energy of an electron is given by the Hamiltonian

$$\hat{H} = \hat{T} + \hat{V}, \tag{2.1}$$

with the kinetic energy term T and the potential energy V. For a free or quasi-free particle with $V \approx 0$, the stationary Schrödinger equation (SGE)

$$\hat{H}\Psi(\vec{r}) = E\Psi(\vec{r}) \tag{2.2}$$

is solved with $\hat{H} = \hat{T} = -\frac{\hbar^2\nabla^2}{2m}$ and eigenfunctions $\Psi(\vec{r}) = \exp(i\vec{k}\cdot\vec{r})$ resulting in the parabolic energy dispersion relation

$$E(k) = \frac{\hbar^2 k^2}{2m}. \tag{2.3}$$

The general relativistic dispersion relation, formulated by Paul A. M. Dirac in 1928, is given as[28, 29]

$$E^2 = (pc)^2 + (mc^2)^2 \tag{2.4}$$

where p denotes the momentum, c is the velocity of light and m is the particle's rest mass. From equation 2.4 we get two solutions

$$E = \pm\sqrt{(pc)^2 + (mc^2)^2} = \pm mc^2\sqrt{\left(\frac{p}{mc}\right)^2 + 1}, \tag{2.5}$$

which can be attributed to the particle and its corresponding antiparticle. For particles without rest mass like photons, a linear dispersion relation directly results with $E = \pm pc$. By substitution of $x = \frac{p}{mc}$ and using the Taylor series for small x, we can derive for the non-relativistic limit ($p << m$)

$$E = \pm mc^2\sqrt{1+x^2} \;\approx\; \pm mc^2\Big(1 + \frac{x^2}{2}\Big) = \pm\Big(mc^2 + \frac{p^2}{2m}\Big). \tag{2.6}$$

This corresponds to the typical parabolic dispersion relation for the free particle as shown in Eq. 2.3. At $p = 0$ an energy gap $\Delta E = 2mc^2$ occurs between particle and antiparticle, which is proportional to the particle's rest mass m.

Based on the energy gap and the typical electronic properties, three different classes of crystalline solids are commonly distinguished: metals, semiconductors, and insulators. Their typical band structures are shown schematically in Fig. 2.1. The Fermi energy E_F denotes the highest electron energy in the ground state. In insulators, the Fermi energy lies between the valence (black) and conduction bands (blue) within the band gap. The valence band is, therefore, completely filled and the band gap has to be overcome in order to generate free charge carriers in the conduction band.[30] Insulators typically exhibit band gaps larger than 4 eV. Materials with smaller band gaps (1 eV – 4 eV) are semiconductors (see Fig. 2.1 (b)).[31, 32] At $T = 0$, semiconductors behave like insulators. At a finite temperature, however, charge carriers are excited from the valence band into the conduction band and enable electrical charge transfer. Narrow-gap semiconductors with band gaps smaller than 1 eV are sensitive towards lattice defects and doping, can exhibit 'non-trivial' band topology and are prone to develop relativistic states.[33, 34] In comparison, metals have a half-filled conduction band as illustrated in Fig. 2.1 (c).[30] This enables the electrons to contribute freely to charge transport.

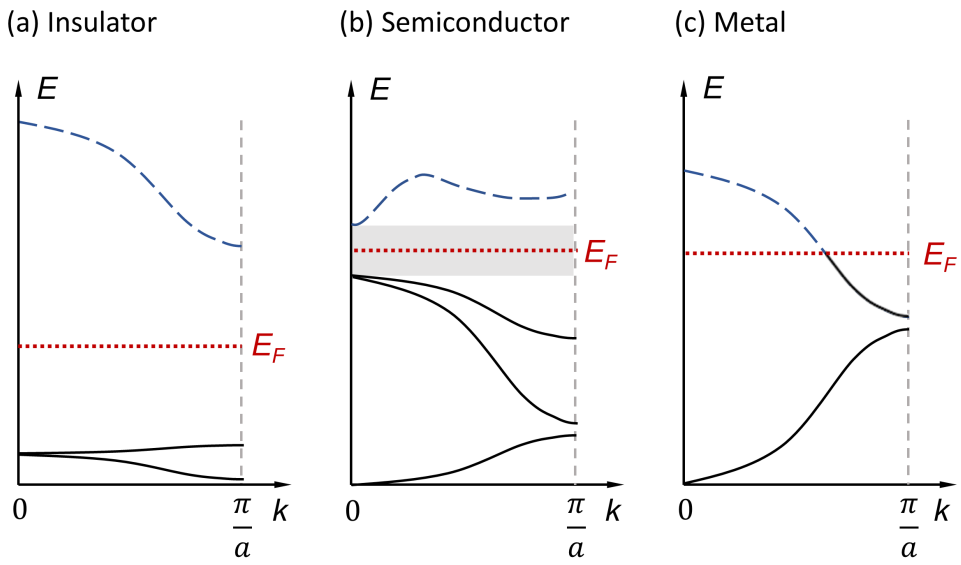

Figure 2.1: Typical schematic electronic band structures of (a) an insulator with large band gap, (b) a semiconductor with small band gap (gray), and (c) a metal with half-filled conduction band. The Fermi energy is denoted as E_F (red). The dashed line at $k = \pi/a$ represents the border of the 1st Brillouin zone.

In the following subsections, basic theoretical concepts for the description and understanding of the relevant materials are presented. Silver nanowires are used as building blocks for electrical charge transfer in the bulk metallic limit (section 4.1). Semiconducting zinc oxide nanowires are utilized as substrate for surface enhanced Raman scattering based on resonant electronic excitation between the semiconductor electronic bands and molecular orbitals (section 4.2.2). We introduce the tight binding model to understand the formation of electronic band structures for simple scenarios. The discovery of the quantum Hall effect and the fractional Hall effect in the 1980s have shown that the classification into electronic conductors and band insulators is not the entire story.[35] In this work, topological insulators represent quasi relativistic states that can exhibit a linear dispersion relation (section 4.2.3). This leads us to cover basic concepts of topology and the occurrence of quasi-relativistic quantum states.

2.1.1 Electronic Properties of Metals

In order to describe the basic electronic properties of metals, the valence electrons can be viewed as a sea of quasi-free electrons, in which the positively charged atomic nuclei are embedded. Since the electronic wave functions of the valence electrons are expanded, their behavior is delocalized within the metal crystal leading to a high electrical conductivity and a high electronic contribution to the thermal conductivity. A simple model derived

from this picture is called the jellium model.[36] This model is particularly suitable for alkali metals and copper, silver, and gold, since here, besides the quasi-free s-electrons, only electrons are present in completely filled atomic shells. It is assumed that the electrons are not interacting with the atomic cores or each other. The electrons, therefore, are considered as free particles trapped in a 3D potential well with infinite walls and a volume of V. We solve the stationary SGE

$$\hat{H}\Psi(\vec{r}) = -\frac{\hbar^2}{2m}\nabla^2\Psi(\vec{r}) = E\Psi(\vec{r}), \tag{2.7}$$

where $\hat{H}$ is the Hamiltonian for a free particle and $\vec{r}$ is the electron position. As eigenfunctions we obtain plane waves

$$\Psi(\vec{k}) = \frac{1}{\sqrt{V}}\exp(i\vec{k}\cdot\vec{r}), \tag{2.8}$$

where $\vec{k}$ is the wave vector and the wavelength is given as $\lambda = 2\pi/|\vec{k}|$. The result is the dispersion relation of free particles (see Eq. 2.3 and Fig. 2.2 (a)). With periodic boundary conditions within the given volume $V = L_x \cdot L_y \cdot L_z$ the allowed wave numbers are

$$k_x = \frac{2\pi}{L_x}n_x, \quad k_y = \frac{2\pi}{L_y}n_y, \quad k_z = \frac{2\pi}{L_z}n_z, \tag{2.9}$$

with the integer quantum numbers n_x, n_y, n_z. With this, the density of states (DOS) $D(E)$ in the energy space can be calculated as[36]

$$D(E) = \frac{L_x L_y L_z}{2\pi^2}\left(\frac{2m}{\hbar^2}\right)^{3/2}E^{1/2}. \tag{2.10}$$

Fig. 2.2 (a) shows the DOS $D(E) \propto \sqrt{E}$ and the parabolic dispersion relation. The Fermi energy is denoted as E_F.

In a thin metal film with a thickness d in the nanometer range, the electrons are confined in z-direction. We, therefore, assume a boundary condition, where only standing waves with a wavelength of $\lambda_z = 2d/j$ can exist in z-direction with j being an integer. This leads to energy eigenvalues of $E(k) = E_j + (\hbar^2(k_x + k_y)^2)/2m$ and a splitting of the dispersion $E(k)$ in sub-bands as illustrated in Fig. 2.2 (b). A constant DOS $D(E) \propto E^0$ results as given in Eq. 2.11.[36] The total DOS is the sum of the DOS of the single sub-bands as shown in Fig. 2.2 (b). Analogously, a 1D nanostructure with a small rectangular

cross-section and a length L_x can be modeled in the same way, resulting in a dispersion $E(k) = E_{i,j} + (\hbar^2 k_x^2)/2m$ (Fig. 2.2 (c)) and a density of states proportional to $E^{-1/2}$ occurs (Eq. 2.12 and Fig. 2.2 (c)).[36] These confinement effects are expected to be relevant when the crystal size reaches the average wavelength of the particle.[37] In section 4.1, silver nanowires are utilized for conductive networks. We use nanowires with an average diameter of 150 nm to 200 nm to obtain maximum undisturbed electrical conductivity, but minimum amount of material and high aspect ratios.

$$\text{2D jellium} \quad D(E) = \frac{L_x L_y}{2\pi} \left(\frac{2m}{\hbar^2}\right) E^0 = \text{const}, \tag{2.11}$$

$$\text{1D jellium} \quad D(E) = \frac{L_x}{\pi} \left(\frac{2m}{\hbar^2}\right)^{1/2} E^{-1/2}. \tag{2.12}$$

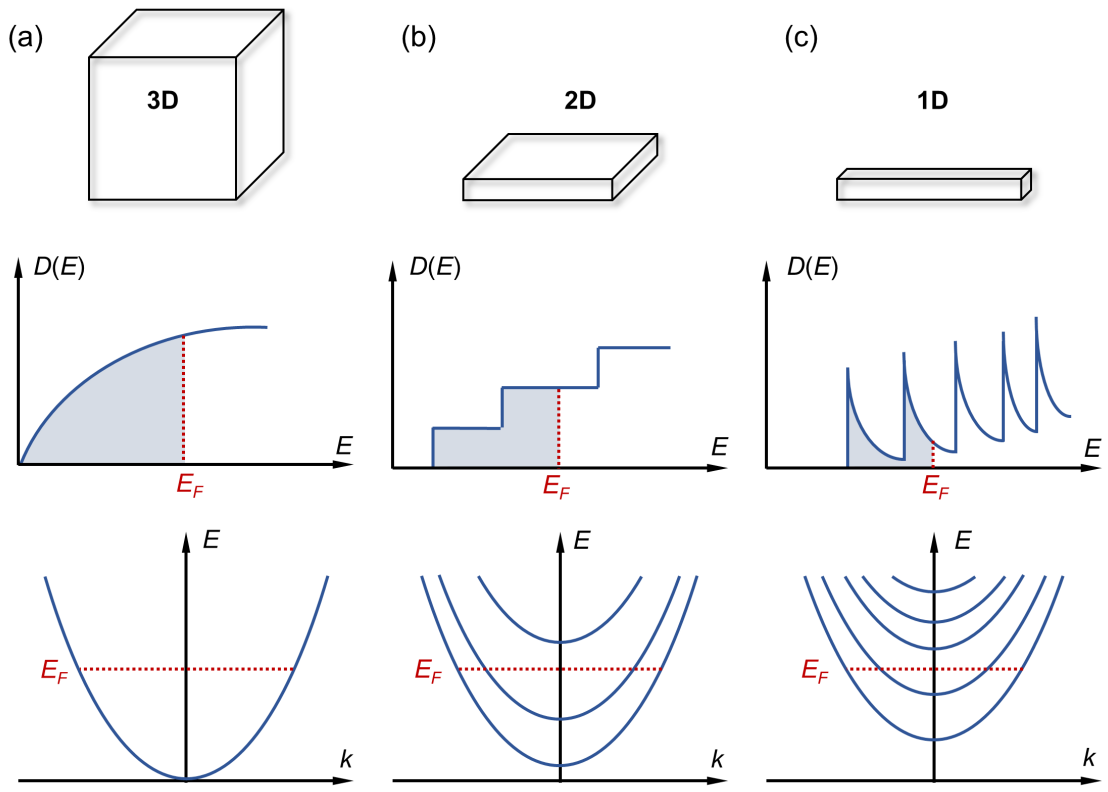

Figure 2.2: (a) Density of states $D(E)$ and dispersion $E(k)$ for free electrons in a 3D jellium (see Eq. 2.10). E_F denotes the Fermi energy. (b) Electronic density of states $D(E)$ (see Eq. 2.11) and dispersion $E(k)$ for a jellium confined in one dimension. (c) Density of states $D(E)$ and dispersion $E(k)$ in a 1D jellium (see Eq. 2.12).

2.1.2 Semiconductors

A semiconductor is characterized by an energy band gap of up to 4 eV.[32] The electrical properties can be strongly influenced by the size of the band gap, especially in the case of narrow-gap semiconductors.[33] The resistivity of semiconductors varies from $10^{-2}\,\Omega\,\mathrm{cm}$ to $10^{9}\,\Omega\,\mathrm{cm}$.[32] There are several types of semiconductors, the most common of which are classified by the following terms.

Pure element or compound. Pure element semiconductors are e.g. silicon, germanium, and selenium. Semiconducting binary compounds are also widely used. The most important compounds are III-V-semiconductors like gallium arsenide (GaAs), gallium nitride (GaN), indium antimonide (InSb), gallium antimonide (GaSb), and aluminum antimonide (AlSb) as well as the II-VI-semiconductors like zinc sulfide (ZnS), zinc oxide (ZnO), cadmium sulfide (CdS), cadmium selenide (CdSe), and cadmium telluride (CdTe).[31]

Direct or indirect. In direct semiconductors, the lower edge of the conduction band and the upper edge of the valence band are at the same wave vector k. The transition between valence and conduction band can take place directly at the same point in the Brillouin zone. Correspondingly, this does not apply to indirect semiconductors.[31]

Intrinsic or doped. In intrinsic semiconductors, free charge carriers are generated by transport of electrons out of the valence band to the conduction band. The doping of semiconductors creates electronic states in the band gap and, therefore, enables the facilitated excitation of electrons from these levels.[31]

To describe the electronic properties of semiconductors it becomes necessary to take the periodic potential of the atomic cores into account ($V(\vec{r}) = V(\vec{r}+\vec{T})$). Bloch's theorem states that the solutions of the SGE in a periodic potential are plane waves $\exp(i\vec{k}\cdot\vec{r})$, which correspond to the solutions for a free particle, modulated by $u_{\vec{k}}(\vec{r})$, which has the same periodicity as the lattice ($u_{\vec{k}}(\vec{r}) = u_{\vec{k}}(\vec{r}+\vec{T})$).[38] Thus, the Bloch-wave function is

$$\Phi_k(\vec{r}) = u_{\vec{k}}(\vec{r})\exp(i\vec{k}\cdot\vec{r}). \tag{2.13}$$

The tight binding model[39] is a model for calculating band structures based on superposition of atomic wave functions $\Phi_A(\vec{r})$, which solve the SGE for the single atom

$$\hat{H}_A(\vec{r}-\vec{R})\Phi_A^i(\vec{r}-\vec{R}) = E_A^i\Phi_A^i(\vec{r}-\vec{R}). \tag{2.14}$$

$\vec{R}$ denotes the translation vector to the lattice point at which the atom i is located.[30] The linear superposition of the atomic wave functions leads to

$$\Psi_k^i(\vec{r}) = \frac{1}{\sqrt{N}} \sum_{\vec{R}} \exp(i\vec{k} \cdot \vec{R}) \Phi_A^i(\vec{r} - \vec{R}), \tag{2.15}$$

with $\Psi_k(\vec{r})$ complying with Bloch's theorem. The Hamiltonian can be separated into the atomic problem and a correction for the periodic lattice potential

$$\hat{H} = \hat{H}_A + \tilde{V}(\vec{r} - \vec{R}), \tag{2.16}$$

or reformulated for the total potential:

$$V(\vec{r}) = \sum_{\vec{R}} V_A(\vec{r} - \vec{R}) = V_A(\vec{r} - \vec{R}) + \tilde{V}(\vec{r} - \vec{R}). \tag{2.17}$$

The following assumptions are made. Firstly, strong localization of the wave functions and small overlap $\int d^3r \ \Phi_m^*(\vec{r}) \Phi_n(\vec{r} - \vec{R})$ of the wave functions with its nearest neighbors are assumed. It is, therefore, reasonable to reduce the sum to the z nearest neighbors. Secondly, we imagine $E(\vec{k})$ being near the atomic energy E_A. Finally, we assume radial symmetric s-type atomic wave functions. With this, the energy $E(\vec{k})$ can be simplified to

$$E(\vec{k}) = E_A^i - |A| \cdot \sum_{i=1}^{z} \exp(-i\vec{k}_i \cdot \vec{R}_i), \tag{2.18}$$

with $|A|$ being the exchange integral.[30]

Considering a typical 3D cubic lattice with opposite neighbors as it is the case for the fcc lattice, Eq. 2.18 can be expressed as

$$E(\vec{k}) = E_A^i - |A| \cdot \sum_{i=1}^{z/2} \exp(-i\vec{k}_i \cdot \vec{R}_i) + \exp(i\vec{k}_i \cdot \vec{R}_i) = E_A^i - |A| \cdot \sum_{i=1}^{z/2} 2\cos(\vec{k} \cdot \vec{R}_i). \tag{2.19}$$

For small wave vectors, a parabolic dispersion is obtained with $\cos(x) \approx 1 - \frac{x^2}{2}$. This resembles the result from Eq. 2.6. Furthermore, it becomes clear that the nature of the dispersion relation depends on the symmetry of the respective lattice type. For cubic lattices, linear terms contributing to the dispersion relation disappear due to symmetry.

For e.g. the honeycomb lattice in graphene, this is not the case and linear terms remain.[40] The comparison of the parabolic dispersion relation for cubic lattices at small wave vectors derived from the tight binding model (Eq. 2.19) with the classical parabolic dispersion of a free particle (Eq. 2.3) results in an effective mass m^* being proportional to $|A|^{-1}$.

In this work, zinc oxide (ZnO) nanostructures are used as substrate for surface enhanced Raman scattering (SERS). ZnO crystallizes in the wurtzite structure as demonstrated in Fig. 2.3 (a).[41] It has a direct and wide band gap of around 3.44 eV at the Γ-point, which corresponds to the near UV-spectral range. A band structure calculation taken from Janotti and Van de Walle[41] is shown in Fig. 2.3 (b) as a reference. ZnO exhibits a large free-exciton binding energy increasing with quantum confinement on the nanometer scale. The free excitons are significantly confined for films thinner than 20 nm.[42] For nanosized ZnO crystals with a size of 10 nm - 20 nm, excitonic states at 100 meV - 400 meV below the conduction band have been found.[24, 42]

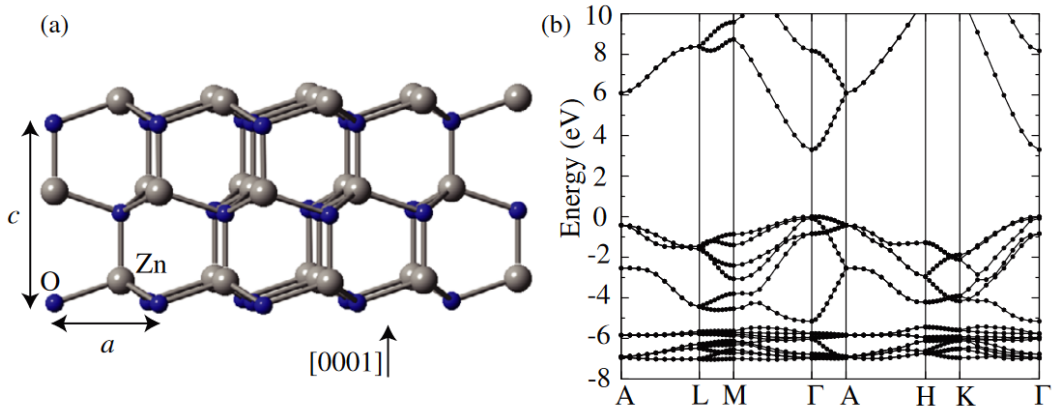

Figure 2.3: (a) Wurtzite structure of the ZnO crystal. Zinc atoms are depicted in gray, oxygen atoms are illustrated in blue. The lattice parameters a and c are indicated by arrows. (b) Calculated electronic band structure of ZnO. The maximum of the valence band has been set to zero. Figure taken from [41]. Copyright 2009 IOP Publishing.

2.1.3 3D Topological Insulators

Topological insulators (TIs) represent a class of Dirac materials that enables fascinating possibilities for the construction and realization of exotic quantum states and quasi-relativistic particles. TIs exhibit insulating or semiconducting bulk electronic states and metallic surface states. The special nature of the TI surface states lies in segments of linear electronic dispersion and the insensitivity of their electrical conductivity to non-magnetic defects.[34, 43] The latter can be attributed to a linking of direction of movement and spin

of the charge carriers in the TI surface states, suppressing back scattering of electrons. The presence of the surface states has been demonstrated by angle-resolved photoemission spectroscopy.[44, 45, 46]

In general, phases are defined by symmetry breaking, which occurs at a phase transition and which changes the characteristic order of a phase. In contrast, topological phases are defined by a stable topological order. Topology is a concept from mathematics, where geometrical objects are classified by their topological invariants. In the case of TIs, topology is used to classify the electronic band structure in terms of the Berry phase. We consider the adiabatic theorem of quantum mechanics. The Hamiltonian $\hat{H}(t)$ undergoes a slow and cyclic evolution resulting in $\hat{H}(t) = \hat{H}(0)$. The corresponding evolution of its eigenstate is $|\Psi(t)\rangle = e^{i\alpha}|\Psi(0)\rangle$. M. Berry[47] has shown that there is, in addition to a dynamic phase γ_d, a geometric phase space factor $\gamma(C)$ (see Eq. 2.20), which is independent of time and depends only on the closed path C taken in phase space. This phase describes the evolution of the eigenfunctions. A non-zero difference in this phase, thus, expresses that the solutions of the Hamilton operator have changed after a closed path in phase space for non-trivial systems. This geometric phase is called Berry phase.[47]

$$\alpha = \gamma_d + \gamma(C) \tag{2.20}$$

The Berry phase for a Bloch state $|m(\vec{r})\rangle = \exp(i\vec{k}\cdot\vec{r})u_{m,k}(\vec{r})$ is defined as[47, 34]

$$\gamma_m(C) = \oint_C \langle u_{m,k}|i\nabla_{\vec{k}}|u_{m,k}\rangle \; d\vec{k} = \oint_C \vec{A}_m(\vec{k}) \, d\vec{k}, \tag{2.21}$$

where C denotes the cyclic path in momentum space and m is the band index. With Stokes' theorem, Eq. 2.21 can be transferred to a surface integral

$$\gamma_m = \int_S \vec{F}_m(\vec{k}) \; \hat{n} \; d^2k, \tag{2.22}$$

where $\hat{n}$ is the normal on the surface. For closed surfaces, as it is the case for the 1st Brillouin zone, γ_m corresponds to the Chern theorem leading to $\gamma_m = 2\pi \, C_m$, where C_m is the integer Chern invariant for the electronic sub band m.[48, 49] $\vec{F}_m(\vec{k})$ is the Berry curvature given by the curl of $\vec{A}$ as $\vec{F}_m = \nabla \times \vec{A}_m$. The constant C_m is invariant under smooth adiabatic transformations, and, therefore, classifies the topological order. A 'trivial' topology yields $\nabla \times \vec{A}_m = 0$ and, therefore, $C_m = 0$. Chern invariants of $C_m \neq 0$ are

obtained for $\nabla \times \vec{A}_m \neq 0$ representing 'non-trivial' topological phases in correspondence with the existence of a vortex field.[48]

An exemplary 3D TI is Bi_2Se_3, which exhibits a bulk band gap of 0.3 eV and a single Dirac cone at the Γ-point. The typical band structure of an 'ordinary' insulator is schematically shown in Fig. 2.4 (a), were E_F denotes the Fermi energy, and VB and CV are the valence band and conduction band, respectively. In Bi_2Se_3, however, band inversion is observed, which results from strong spin-orbit coupling (SOC) and a small band gap as illustrated in Fig. 2.4 (a) causing a 'non-trivial' topology with a Chern invariant of $C = \pm 1$. For conventional semiconductors, SOC usually causes spin splitting and spin relaxation.[50] Only in few narrow-gap materials with heavy atoms like Bi_2Se_3 or HgTe SOC results in band inversion.[51, 52] Calculations of the band structure for Bi_2Se_3 with and without SOC have shown that mostly Bi p_z states from the conduction band and Se p_z states from the valence band are inverted.[53]

The TI surface is a boundary between the TI and an 'ordinary' insulator like vacuum or air. Since the topological invariants of the TI and the surrounding medium are different, no continuous transformation can occur.[34] An intermediary is required whose role is taken over by the TI surface states. In terms of the relativistic dispersion relation (see Eq. 2.4), parabolic bands occur with an energy gap of $2mc^2$ for $p << m$ as shown in Eq. 2.6. The energy gap can only be closed when the mass approaches zero yielding a linear dispersion relation. The relativistic natures of narrow-gap semiconductors has been discussed by Fradkin and co-workers.[33] The conductive surface states of TIs are usually described by an adapted Dirac equation[54] and exhibit a linear and spin polarized dispersion at the Γ-point, which is illustrated by dotted lines in Fig. 2.4. At the TI-vacuum interface, the local inversion symmetry is broken, but time inversion symmetry ($t \rightarrow -t$) is retained, which can be stated as $E(\vec{k},\uparrow) = E(-\vec{k},\downarrow)$.[49] Dirac cones are known from graphene. However, the origin is completely different. As outlined in section 2.1.2 geometrical lattice symmetries lead to parabolic dispersion relations for cubic lattices and, in contrast, linear terms remain in $E(\vec{k})$ for honeycomb lattices. Furthermore, Dirac cones in 3D TIs exhibit spin polarization caused by SOC, which is not the case for graphene. In Fig. 2.4 (b) the TI Dirac cone is schematically represented. The arrows circling around the cone at the Fermi energy E_F illustrate the spins coupled to the direction of momentum of the electrons moving around the Fermi surface.

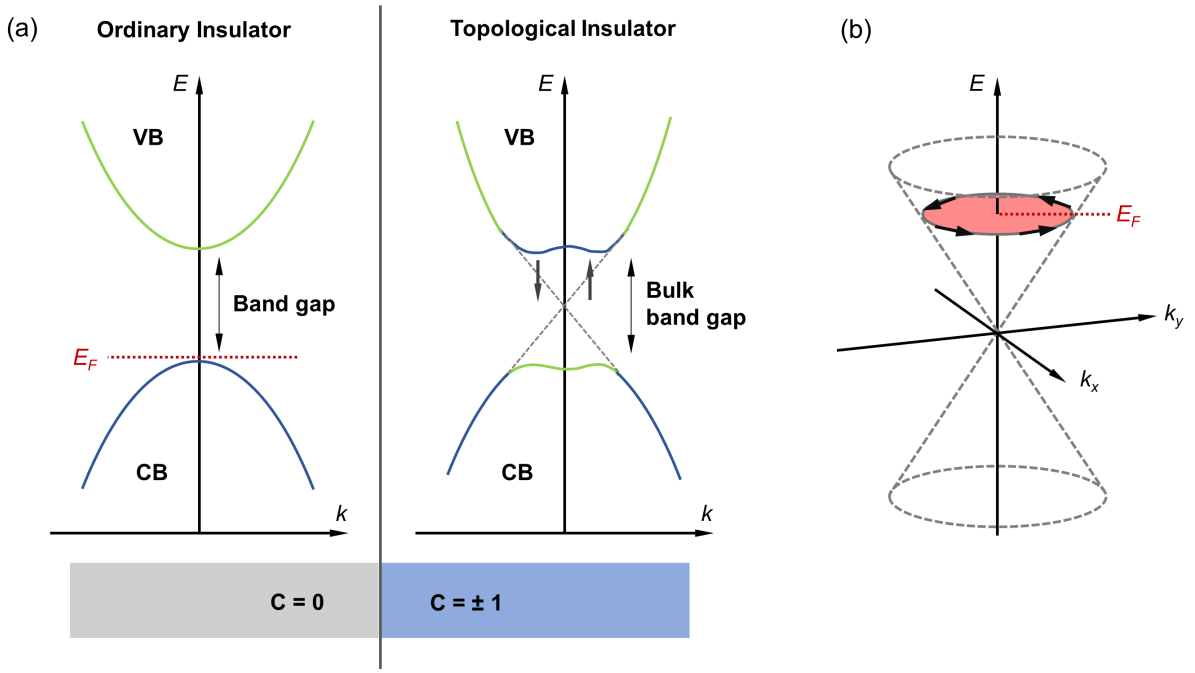

Figure 2.4: (a) Basic electronic band structure (Energy (E) against wave vector (k)) of a trivial insulator with a topolgical invariant $C = 0$ (left) and a TI with $C = \pm 1$ (right). E_F is the Fermi energy. For the TI, band inversion within the bulk electronic band structure is pictorially shown. Surface states with nearly linear dispersion, where each dispersion branch exhibit opposite spin orientation (arrows up and down), are depicted by gray dotted lines. (b) Dirac cone in two dimensions k_x and k_y for a 3D TI. The spin direction is always coupled to the direction of movement of the electrons. The red disc represents an exemplary cut of the Dirac cone at the Fermi energy and the black arrows depict the spin directions.

The above considerations primarily correspond to a 3D TI in a bulk or 2D geometry like a film or nanoflake with thicknesses above a critical confinement. For ultra-thin films of thicknesses $d < 6\,\mathrm{nm}$ splitting of the insulating bulk band due to confinement in one dimension as well as a gap opening of the surface states is observed due to hybridization between the top and bottom surface.[55, 56] In the case of circular nanowires, on the other hand, hollow metallic cylinders are realized, leading to splitting into 1D sub bands.[57] The main reason for this lies in the curvature of the surface, the available circular path and the corresponding boundary conditions that occur. The surface electron spin is constrained to lie in the tangent plane of the nanowire surface, leading to a 2π rotation along the wire perimeter. This results in an additional π-Berry phase of the Dirac particle. As shown by theoretical studies[58, 59, 51, 44, 60] the energy dispersion relation for surface states in 1D circular TI nanowires can be expressed as

$$E^2(k) \propto k^2 + \frac{n^2}{R_0^2}, \tag{2.23}$$

where R_0 is the radius of the nanowires. A simple comparison with Eq. 2.4 shows a correspondence to the Dirac dispersion with a mass increasing with $R_0 \to 0$.[44] A dispersion relation considering the band index m, the wire radius R_0, as well as an applied magnetic flux with the ratio $r = \Phi/\Phi_0$, and the flux quantum $\Phi_0 = \hbar/2e$ has been derived by P. Iorio and co-workers:[58, 59]

$$E(k) = sC_2\sqrt{k^2 + (1 + 2m - 2r)^2\tilde{\Delta}^2(R_0)}, \tag{2.24}$$

with the band gap $\Delta(R_0) = 2C_2\tilde{\Delta}(R_0) = C_1R_0^{-1}$. C_1 and C_2 represent the interorbital and interspin couplings.

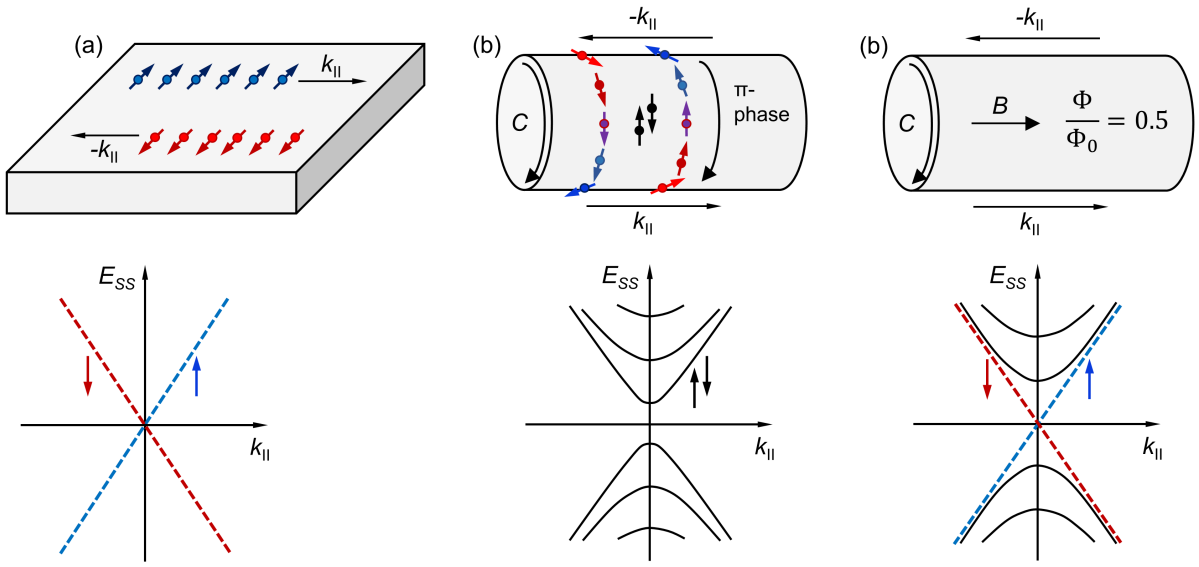

Figure 2.5: (a) Spin-polarized surface states in a bulk TI. Spin-momentum locking is indicated by the blue and red particles moving on the flat TI surface. (b) The morphing of the TI into a cylinder leads to a curved surface in which the particle spin is tangential and circles around the perimeter C. The electron wave function picks up a π-Berry phase yielding a gap opening at the Dirac point and doubly degenerated sub bands. (c) The application of a magnetic field $\vec{B}$ along the wire axis with odd multiples of $\Phi/\Phi_0 = r = 0.5$ compensates the Berry phase for the sub-band of $m = 0$ leading to a spin-polarized Dirac state.

The application of a magnetic flux through the nanowire results in two main scenarios. For even multiples of $r = 0.5$ (incl. 0) doubly degenerated sub bands occur as illustrated in Fig. 2.5 (b). For odd multiples of $r = 0.5$ and a sub band index $m = 0$ Eq. 2.24 develops to $E(k) \propto k$ and the part corresponding to the mass term becomes zero allowing a state at the Dirac point. The effect of a magnetic flux on the transport properties of a metallic surface in the non-relativistic case is described by the Aharonov-Bohm effect.[47] The electron wave function gets a phase of $2\pi\Phi/\Phi_0$.[61] Thus, a 1D Dirac state is realized at a magnetic flux of $\Phi_0/2$ because this value compensates the curvature induced π-Berry

phase.[62, 63, 64] Fig. 2.5 shows the helical (spin-polarized) surface states for a bulk TI (a), the band structure splitting into spin-degenerated sub bands for the TI nanowire with zero flux (b), and a half flux quantum (c).

In this work Bi_2Se_3 nanowires are investigated by means of Raman scattering (see section 4.2.3). Bi_2Se_3 crystallizes in a rhombohedral crystal structure that grows along the c-axis in multiples of so-called quintuple layers of alternating Bi and Se layers.[65] The structure is pictorially shown in Fig. 2.6. Four vibrational modes are usually detected by Raman spectroscopy as indicated in Fig. 2.6.[66] In section 4.2.3 the two high energy modes (E_g^2 and A_{1g}^2) are observed.

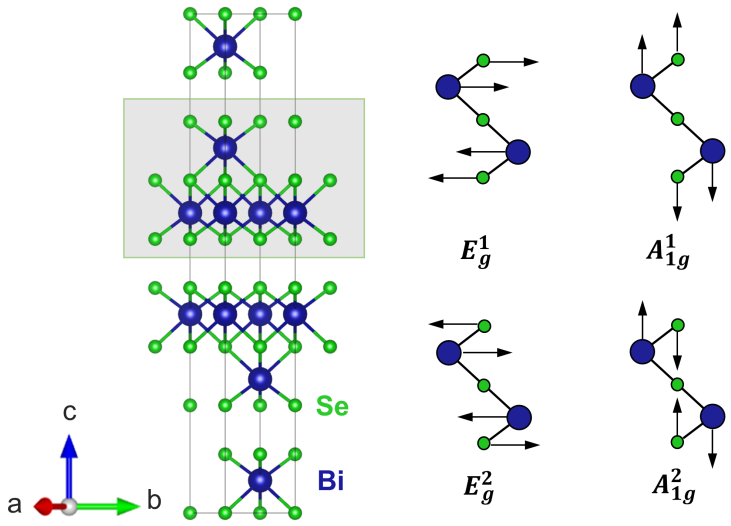

Figure 2.6: Crystal structure and Raman active vibrational modes of the 3D topological insulator Bi_2Se_3. Bismuth atoms are depicted in blue, selenium atoms are shown in green. Quintuple layers (gray) are stacked along the c-axis. The Raman modes are illustrated on the right, which have the following order as a function of energy: E_g^1, A_{1g}^1, E_g^2, and A_{1g}^2.

2.2 Interaction of Electromagnetic Fields with Matter

Light scattering is a two photon process, where an incidence photon is annihilated and a scattered photon is created. Scattering can occur without any energy transfer between the incoming photon and the scattering medium, resulting in an elastic process. Elastic scattering, therefore, probes the motionless atomic lattice. One differentiates between coherent and non-coherent scattering. During coherent scattering the incoming and outgoing wave have a constant phase relationship. If coherent radiation undergoes coherent

and elastic scattering, the scattered rays can interfere.[25] This phenomenon is usually called diffraction, and used in e.g. crystal lattice structure elucidation.[67] Crystalline solids are characterized through their periodicity in lattice distance d. The Laue condition indicates maximum interference at[25]

$$\vec{k}_{\mathrm{sc}} - \vec{k}_{\mathrm{inc}} = \Delta\vec{k} = \vec{G}_{hkl}, \tag{2.25}$$

where $\vec{k}_{\mathrm{sc}}$ is the wave vector of the scattered photon, $\vec{k}_{\mathrm{inc}}$ is the wave vector of the incident photon, and $\vec{G}_{hkl}$ is the reciprocal lattice vector with $\left|\vec{G}_{hkl}\right| = 2\pi/d$. A measure for the scattering potential of a crystal basis is the structure factor considering the arrangement of atoms within the basis and the electron density of each atom. In order to probe atomic distances in the range of Ångströms, the wavelength of the used radiation has to be in the size range of the investigated atomic structure. Synchrotrons are excellent X-ray sources with a wide range of possible wavelength between 0.02 nm ($6{\cdot}10^4$ eV) to 6 nm ($2{\cdot}10^2$ eV).[68] Synchrotron radiation exhibit high flux, small beam divergence, and a high level of polarization. A typical X-ray diffraction (XRD) experiment can be carried out by using a Θ-2Θ stage, where the sample is illuminated with a monochromatic X-ray beam in reflection mode. The angle of incidence Θ equals the angle of reflection, leading to an angle of 2Θ between light source and detector. Instead of moving the light source and detector in equidistant steps, it is common practice to use a static monochromatic X-ray source and a 2D detector to map the scattering pattern in the reciprocal space of crystalline powders, nano colloids, or suspensions. Fully ordered systems are investigated in crystallography, whereas systems with random orientation are studied by e.g. solution scattering. Small angle X-ray scattering (SAXS) denotes a widely used technique giving information about the average size, shape and dispersity of nanosized structures.[69] For measuring SAXS signals, large sample to detector distances (SDD) in the range of up to 1 m – 10 m are necessary in order to resolve small angles of less than 0.1°.[70]

If we take into account that the atomic lattice at temperatures $T > 0$ changes over time, we also observe inelastic scattering processes on the dynamic lattice. Inelastic scattering leads to a redistribution of the elastic scattering intensity from the Bragg reflex (at $T = 0$) to an inelastic background. The Laue condition can be modified to $\Delta\vec{k} = \vec{G}_{hkl} \pm \vec{q}$, where $\hbar\vec{q}$ is the crystal momentum of a vibronic lattice excitation. The scattered photon is then shifted in energy compared to the incident photon by $\omega = \omega_0 \pm \omega_q$, where ω_q corresponds

to the energy of the phonon lattice excitation. This results in energy and momentum conservation for the inelastic scattering process.[25]

The spectral analysis of scattered X-rays by spectroscopy reveals information about the electronic structure of molecules and solids (RIXS and XAS).[71] However, the relative change in energy of an X-ray photon scattered at a phonon is very small. We, therefore, use inelastic light scattering spectroscopy in the visible spectral range to obtain energy shifts of inelastic scattered photons of 1 to 10 %. Inelastic scattering at optical phonons, which have high frequencies also at the center of the Brillouin zone, is called Raman scattering.[72] The following sections provide a basic insight into Raman scattering and X-ray scattering as used in this work.

2.2.1 Raman Scattering

Inelastic light scattering processes as Raman scattering are two photon processes, where an incident photon is annihilated and a scattered photon is created. This goes hand in hand with the generation (Stokes) or annihilation (anti-Stokes) of an excitation within the investigated medium.[72] The intensities of the anti-Stokes lines are normally significantly weaker than those of the Stokes lines.

The Raman cross-section, which represents the probability of an interaction between an incident particle and the scattering medium, is determined by the polarizability of the medium, its susceptibility.[73] A vibrational state is Raman-active if the medium experiences a change in polarizability during the vibration.[74, 72] Usually monochromatic light from lasers in the visible, near-infrared, or near-ultraviolet spectral range are utilized. Since $\lambda_{\mathrm{inc}} >> a$, where a is the lattice parameter or atomic distance and λ_{inc} is the incidence wavelength, $k_{\mathrm{inc}}, k_{\mathrm{sc}} << \pi/a$. From $\vec{k}_{\mathrm{inc}} = \vec{k}_{\mathrm{sc}} \pm \vec{q}$ follows, that Raman spectroscopy probes optical phonons in the center of the Brillouin zone at $\Delta\vec{k} = \vec{q} \simeq 0$.[74] One differentiates between resonant Raman scattering and non-resonant Raman scattering. In the resonant case, the incident photon energy equals the transition energy from an initial electronic state i to a final electronic state f. The scattering intensity in resonant Raman scattering is enhanced compared to the non-resonant case, and depends strongly on the laser excitation energy.[75]

This chapter is aimed to give an overview on appropriate quantum-mechanical tools for describing the Raman scattering process. Initially, the first order perturbation theory is introduced resulting in Fermi's Golden Rule for the scattering cross-section. We will

focus on phononic Raman scattering, which originates from the coupling of radiation to the electronic system, which is coupled to the phonons by electron-phonon interaction. An overview on radiation-electron interaction and electron-phonon interaction is presented. The Raman scattering intensity can also be calculated from a Four-Photon Greens Function.[76] From this, one can often derive semi-phenomenological models for the Raman response.[27]

First Order Perturbation Theory and Fermi's Golden Rule.
We consider a quantum mechanical system *via*

$$\hat{H}(t)\,|\Psi,t\rangle = i\hbar\frac{\delta}{\delta t}\,|\Psi,t\rangle\,. \tag{2.26}$$

with a Hamiltonian $\hat{H}(t)$ separated into a time-independent (also called unperturbed) Hamiltonian $\hat{H}_0$ and the so-called interaction Hamiltonian $\hat{H}_{int}(t)$, which is a time-dependent perturbation and small compared to $\hat{H}_0$. The unperturbed state has a set of energy eigenvalues E_n^0 and time-independent eigenvectors Ψ_n^0

$$\hat{H}_0\,\Psi_n^0 = E_n^0\,\Psi_n^0. \tag{2.27}$$

In the following, we will use the interaction picture[77], in which Ψ_I is defined as

$$|\Psi,t\rangle_I = \exp\left(i\frac{\hat{H}_0(t-t_0)}{\hbar}\right)|\Psi,t\rangle\,, \tag{2.28}$$

where $\exp(-i\frac{\hat{H}_0(t-t_0)}{\hbar})\,|\Psi,t_0\rangle$ is the time evolution of the unperturbed system, and t_0 is the point in time at which the perturbation starts. The combination of equation 2.28 and 2.26 leads to[78]

$$\begin{aligned} i\hbar\frac{\delta}{\delta t}\,|\Psi,t\rangle_I &= \exp\left(i\frac{\hat{H}_0(t-t_0)}{\hbar}\right)\hat{H}_{int}(t)\exp\left(-i\frac{\hat{H}_0(t-t_0)}{\hbar}\right)|\Psi,t\rangle_I \\ &= \hat{H}_{int}(t)_I\;|\Psi,t\rangle_I\,, \end{aligned} \tag{2.29}$$

which results in the Neumann series[79, 78] after integration

$$
\begin{aligned}
|\Psi,t\rangle_I &= |\Psi,t_0\rangle_I + \frac{1}{i\hbar}\int_{t_0}^{t} dt' \hat{H}_{int}(t')_I \, |\Psi,t'\rangle_I \\
&= |\Psi,t_0\rangle_I + \frac{1}{i\hbar}\int_{t_0}^{t} dt' \hat{H}_{int}(t')_I \, |\Psi,t_0\rangle_I + \\
&\left(\frac{1}{i\hbar}\right)^2 \int_{t_0}^{t} dt' \int_{t_0}^{t'} dt'' \hat{H}_{int}(t')_I \, \hat{H}_{int}(t'')_I \, |\Psi,t_0\rangle_I + \dots .
\end{aligned}
\tag{2.30}
$$

We are now interested in the probability of a transition from the unperturbed groundstate $|\Psi,t<t_0\rangle = |n,t\rangle$ to an excited state $|\Psi,t>t_0\rangle = |m,t\rangle$, which is the perturbed system. The probability amplitude for the transition is given as $\langle m,t|\Psi,t\rangle$. With the first order Neumann series (Eq. 2.30) it becomes

$$
\begin{aligned}
\langle m,t|\Psi,t\rangle &= \langle m| \left[|\Psi,t_0\rangle_I + \frac{1}{i\hbar}\int_{t_0}^{t} dt' \hat{H}_{int}(t')_I \, |\Psi,t_0\rangle_I \right] \\
&= \langle m|n\rangle + \frac{1}{i\hbar}\int_{t_0}^{t} dt' \, \langle m|\hat{H}_{int}(t')_I|n\rangle \\
&= \delta_{nm} + \frac{1}{i\hbar}\int_{0}^{t} dt' \exp(-i\omega_{mn}t') \, \langle m|\hat{H}_{int}|n\rangle \, .
\end{aligned}
\tag{2.31}
$$

where δ_{nm} is the Kronecker delta, and $\omega_{mn} = \frac{E_m - E_n}{\hbar}$.[78] t_0 is set to 0 in the third line. This yields for the transition probability[78]

$$
P_{nm} \propto |\langle m,t|\Psi,t\rangle|^2 = \left| \frac{1}{i\hbar}\int_{0}^{t} dt' \exp(-i\omega_{mn}t') \right|^2 |\langle m|H_{int}|n\rangle|^2. \tag{2.32}
$$

The evaluation of the integral results in an oscillating time dependency of the shape $\sin^2(\omega_{mn}\cdot t/2)\,\omega_{mn}^{-2}$, which has its main contribution at $\omega_{mn}=0$.[80] We consider the system to be exposed to the perturbation for a long time t, and, therefore, substitute a Dirac delta-function $\delta(E_m - E_n)$ and obtain the following expression

$$
P_{nm} = \frac{2\pi t}{\hbar}\delta(E_m - E_n)|\langle m|H_{int}|n\rangle|^2. \tag{2.33}
$$

The transition probability per unit time corresponds to Fermi's 'Second Golden Rule' and is given by Eq. 2.34.[78] ω_q is introduced to take energy transfer into account in inelastic processes.

$$\rho_{nm} = \frac{2\pi}{\hbar}\delta(E_m - E_n \pm \hbar\omega_q)|\langle m|H_{int}|n\rangle|^2. \tag{2.34}$$

The Process of Phononic Raman Scattering.

In order to understand the nature of the interaction Hamiltonian $\hat{H}_{int}$ within a phononic Raman scattering process, we consider the coupling of light to phonons *via* the coupling of light to electrons and the electron-phonon interaction. This results for the entire Hamiltonian in

$$\hat{H} = \hat{H}^0_{\text{elec}} + \hat{H}^0_{\text{pho}} + \hat{H}_{\text{elec+pho}}. \tag{2.35}$$

In a first step, we will pay attention to the interaction between a radiation field and the electrons of the scattering medium. The free electron propagator is given by[26]

$$G_0(\vec{k},\omega_{\text{elec}}) = \frac{1}{\omega_{\text{elec}} - \epsilon_k + i\delta_k} = \frac{\omega_{\text{elec}} - \epsilon_k}{(\omega_{\text{elec}} - \epsilon_k)^2 + \delta_k^2} + i\frac{-\delta_k}{(\omega_{\text{elec}} - \epsilon_k)^2 + \delta_k^2} \tag{2.36}$$

where $\hbar\omega_{\text{elec}}$ is the electronic energy, ϵ_k is the respective dispersion relation of electrons and holes, and δ_k is the electronic damping. The interaction of a radiation field, expressed by a vector potential $\vec{A}$, with an electron with momentum operator $\hat{p}_j$ and the position vector $\vec{r}_j$, can be described by the substitution of $\hat{p}_j \rightarrow \hat{p}_j + e\vec{A}(\vec{r}_j)$. The kinetic energy term of an electron is given by $\hat{p}^2/2m_e$. The Hamiltonian, which describes the coupling of electrons to a radiation field can be written as[72]

$$\hat{H}_{eA} = \hat{H}_{A^2} + \hat{H}_{pA} = \frac{e^2}{2m_e}\sum_j \vec{A}(\vec{r}_j)\cdot\vec{A}(\vec{r}_j) + \frac{e}{m_e}\sum_j \vec{A}(\vec{r}_j)\hat{p}_j. \tag{2.37}$$

As result two terms for the perturbation Hamiltonian ($\hat{H}_{pA}$ and $\hat{H}_{A^2}$) are obtained describing, firstly, the linear interaction between the vector potential of light and electrons, and, secondly, the quadratic coupling of the vector potential of light to electrons as shown in Eq. 2.37. The linear term in the vector potential contributes to Raman scattering

only in second order perturbation theory leading to a resonance denominator resulting in a scattering intensity, which depends strongly on the laser-excitation energy. In the non-resonant limit, the linear term can be neglected.[72, 27]

The polarizability of the electronic system, also called polarization bubble π_0, consists of a real part R and an imaginary part ρ.

$$\pi_0^2 = (R + i\rho) \cdot (R - i\rho) = R^2 + \rho^2. \tag{2.38}$$

Electron-phonon interaction leads to additional contributions to the electronic propagators, which are expressed as electron-phonon self-energy contributions. We assume the bare phonon propagator, which is given as[26]

$$D^0(\omega, \vec{k}) = \frac{\Omega_{\vec{k}}}{\omega^2 - \Omega_{\vec{k}}^2 + i\Gamma\Omega_{\vec{k}}} \tag{2.39}$$

with $\Omega_{\vec{k}}$ being the phonon dispersion relation and Γ being the phonon damping. For vanishing electron-phonon interaction, this would lead to a Lorentzian line-shape of the Raman response function. By considering the electron-phonon self-energy corrections in the metallic limit following the Hartee and Fock corrections[26] it has been shown that the response function can be derived as[27]

$$\tilde{R}(\omega) = T_e^2 \pi_0 - T_e^2 g^2 \pi_0^2 D^{\text{full}}(\omega). \tag{2.40}$$

T_e denotes the photon-electron interaction and g is the electron-phonon coupling constant. Importantly, it is assumed, that all coupling constants are constant, real, and independent of the momentum.[27] The intensity $I(\omega)$ can be expressed after correction to the scattering volume and for constant temperatures as $I(\omega) = -\text{Im}(\tilde{R}(\omega))$. With equation 2.38 and

$$D^{\text{full}}(\omega) = \frac{D^0(\omega)}{1 + g^2 \pi_0 D^0(\omega)} = \frac{\Omega\left[\omega^2 - \Omega^2\left(1 - g^2 \frac{R}{\Omega}\right) - i(g^2\rho + \Gamma)\Omega\right]}{\left[\omega^2 - \Omega^2\left(1 - g^2 \frac{R}{\Omega}\right)\right]^2 + \Omega^2(g^2\rho + \Gamma)^2} \tag{2.41}$$

follows for the intensity $I(\omega)$

$$I(\omega) = T_e^2 \left(\rho + g^2 \frac{(g^2\rho + \Gamma)\,\Omega^2}{\left[\omega^2 - \Omega^2\left(1 - g^2\frac{R}{\Omega}\right)\right]^2 + \Omega^2(g^2\rho+\Gamma)^2} \left[(R)^2 - (\rho)^2 - 2R\rho\, \frac{\omega^2 - \Omega^2\left(1 - g^2\frac{R}{\Omega}\right)}{(g^2\rho+\Gamma)\Omega} \right] \right). \tag{2.42}$$

This corresponds to a Fano line-shape as is becomes clear when introducing the Fano parameter $q = \frac{R}{\rho}$:

$$I(\omega) = T_e^2 \left(\rho + g^2 \frac{2\Omega}{(\omega^2 - \Omega^2)^2 - 4\Gamma^2\Omega^2} \left[q^2 - 1 + \frac{2q(\omega^2 - \Omega^2)}{\Omega\Gamma} \right] \right) \tag{2.43}$$

However, in this expression the electron-phonon coupling constant g can not be determined anymore as it is a pre-factor, which is not influencing the line shape.[27].

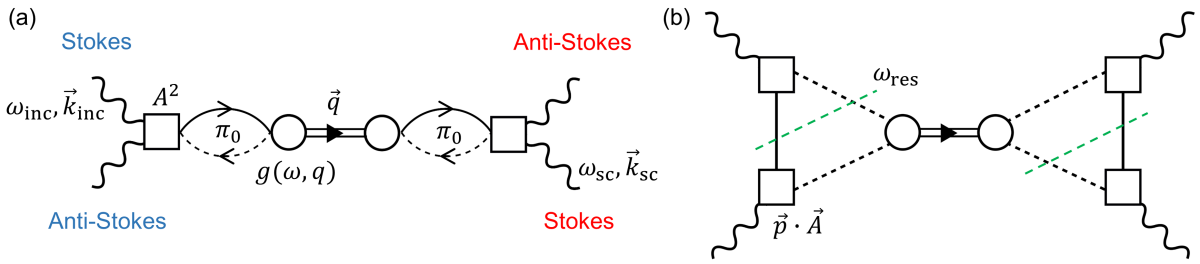

Figure 2.7: (a) Feynman diagram showing the Raman process in the non-resonant limit. The Stokes process yields for a red shift (left to right), whereas the corresponding Anti-Stokes process results in a blue shift. The incoming photon is coupled to the electronic system by the quadratic term (see Eq. 2.37). The electronic excitation is coupled to a phonon $\vec{q}$ by the coupling constant $g(\omega, q)$. (b) Feynman diagram illustrating the resonant Raman process. The green dashed lines depict the resonance frequency ω_{res}.

A Feynman diagram representing the Four-Photon Greens function of the electron-phonon Raman process in the non-resonant limit is illustrated in Fig. 2.7 (a).[76] The incoming light couples to the electronic system *via* the A^2 matrix element (square), inducing the polarization of the scattering medium. The electron-phonon coupling is depicted as circle, followed by the phonon propagator as doubled line arrow. The Stokes process, resulting in a red-shift of the scattered light (left to right in the diagram) as well as the Anti-Stokes process characterized by a blue shift of the scattered light (right to left) are highlighted in the figure. The calculation of this Feynman diagram requires some strong simplifications. The assume all coupling constants to be constant, real, and independent. The Raman scattering intensity can be approximated by

$$I^{\text{non-res}}(\omega) = -\text{Im}[\tilde{R}(\omega)] = -\text{Im}\Big[\Big(T_e^{A\cdot A}\Big)^2 g^2 \pi_0^2 D^0\Big], \tag{2.44}$$

with $T_e^{A\cdot A}$ being the non-resonant A^2 photon-electron matrix element.

Analogously, we can describe the resonant Raman process as illustrated in Fig. 2.7 (b). The notation equals the notation in (a). In the resonant case, the coupling of the radiation field to the electrons by the $\vec{p}\cdot\vec{A}$ term is considered yielding a Raman response that depends on the incidence photon energy $\hbar\omega_{\text{inc}}$. If we assume that the phononic excitation is independent from the electronic susceptibility, and all coupling constants are constant, real, and independent from the momentum, the response function and can be approximated by

$$I^{\text{res}}(\omega, \omega_{\text{inc}}) = -\text{Im}[\tilde{R}(\omega, \omega_{\text{inc}})] = -\text{Im}\Big[\Big(T_e^{p\cdot A}\Big)^4 g^2 \pi_0(\omega_{\text{inc}})^2 D^0\Big] \tag{2.45}$$

with $T_e^{p\cdot A}$ being the resonant $\vec{p}\cdot\vec{A}$ photon coupling. This model is used extensively in chapter 4.2.2 and Refs. [24] and [22].

2.2.2 X-Ray Scattering of Nanostructures

The characterization and imaging of nanoscale systems is a large field, since characterization of size, dispersity, composition, and shape is a fundamental prerequisite for the successful use of nano materials as e.g. porous materials, phase separated block copolymers, nano colloids, and nanoparticle composites. Monochromatic X-ray scattering results in averaged structure information in the reciprocal space over a macroscopic sample volume in contrast to microscopy, which obtains direct but local imaging. Large structures with sizes up to the nanometer range are examined using small-angle X-ray scattering (SAXS).[69] The information about the large structures lies in the small scattering angles. Correspondingly, inter-atomic distances are investigated by wide angle X-ray scattering (WAXS). X-ray scattering is usually non-destructive and enables the investigation of particles in their natural solution or matrix environment.[69] This is highly advantageous for the *in situ* investigation of reaction and growth kinetics.[81, 82]

In the case of X-ray scattering, the elastic scattering of photons on electrons in the atomic shell is generally observed. Elastic scattering, also called Thomson scattering, occurs when electrons are accelerated by the photon field.[83] The emitted radiation has the

same frequency as the incoming photon. Emitted waves from two neighboring atoms are coherent, leading to diffraction patterns, which carry structural information about the investigated particles. Inelastic scattering leads to a background signal without spacial information. The elastic scattering intensity $I(Q)$ can be defined as the product of the form factor $F(Q)$ and structure factor $S(Q)$.[69] As form factor we define the Fourier transform of the electron density distribution within the material or atom. In WAXS, the structure factor contains information about the arrangement of individual atoms within the basis of the crystal lattice. In SAXS, the observed size scale is two order of magnitude larger than for WAXS. We, therefore, can analogously describe the arrangement of neighboring nanoparticles by the structure factor.[84]

The SAXS experiment in transmission mode is illustrated in Fig. 2.8 (a). The monochromatic X-ray beam hits the sample perpendicular. The transmitted direct beam is located in the center of the resulting scattering pattern, usually blocked by a beam block. The 2D detector then collects scattered photons, which form Bragg diffraction rings at scattering angles 2Θ. In the limit of small angles, the scattered angle 2Θ is given as $2\Theta = \lambda/a$, where λ is the wavelength of the probing X-ray beam and a is the dimension of the investigated objects. In comparison, grazing incidence SAXS (GISAXS) is carried out in reflection mode under a small incidence angle smaller than 1° as illustrated in Fig. 2.8 (b). A macroscopic footprint of the incident X-ray beam at the sample surface is obtained, leading to large statistics and surface sensitivity. In this work, GISAXS is utilized to investigate 2D surfaces of silver-nanowire networks. The following paragraph gives an overview of the related theory.

GISAXS. In GISAXS the X-ray beam with a wave vector $\vec{k}_i$ impinges under a small angle $\alpha_i < 1°$ on the sample surface, which defines the (x,y)-plane with the x-axis in beam direction (see Fig. 2.8 (b)). The penetration depth can be modified from a few nm to up to 100 nm by changing the angle of incidence, resulting in low background signal from the substrate.[85] At the scattering plane ((x,z)-plane), the photons are scattered in the in plane exit angle α_f and an out-of plane angle 2Θ. The scattering vector $\vec{Q}$ is given in Eq. 2.46, where λ is the wavelength of the monochromatic X-rays. The specular reflected signal appears at $Q_x = Q_y = 0, Q_z \neq 0$ with a specular peak at $\alpha_i = \alpha_f$, which is usually blocked by a beam block. The depth sensitive information is contained along Q_z, whereas Q_x and Q_y contain in-plain information of the sample. In GISAXS typically $Q_x << Q_y, Q_z$.[70, 85]

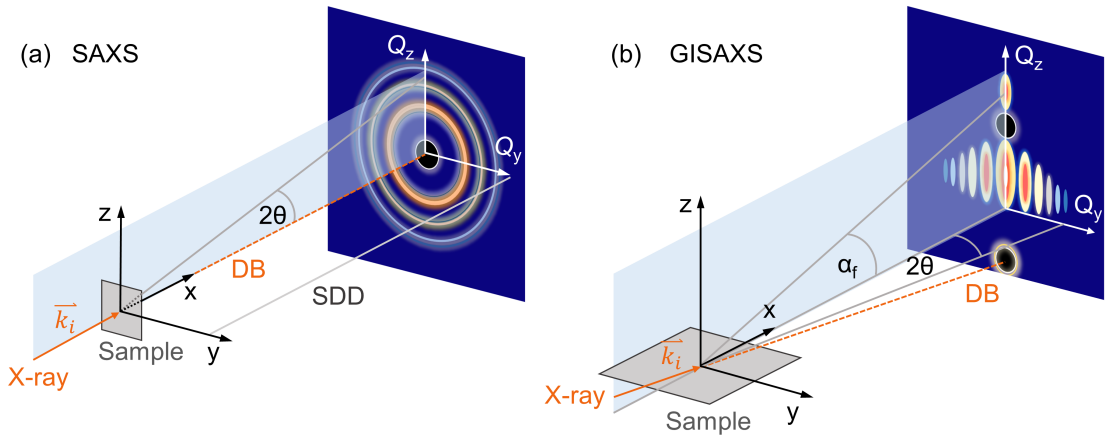

Figure 2.8: (a) Schematic view on the SAXS setup. The X-rays penetrate the sample. Around the direct beam (DB), which is blocked by a beam block (black), diffraction rings at scattering angles 2Θ are formed on the 2D detector. The scattering plane is spanned by Q_z and Q_y.The distance between sample and detector is denoted as SDD. (b) Grazing incidence SAXS configuration, where the X-ray beam hits the sample in an angle of incidence $\alpha_i < 1°$. The sample is oriented in the (x,y)-plane and scattered light is emitted with the angle α_f in vertical and 2Θ in horizontal direction. The specular peak at $\alpha_i = \alpha_f$ and the direct beam (DB) are blocked by beam blocks (black).

$$\vec{Q} = \begin{pmatrix} Q_x \\ Q_y \\ Q_z \end{pmatrix} = \frac{2\pi}{\lambda} \cdot \begin{pmatrix} \cos(2\Theta)\cos(\alpha_\mathrm{f}) - \cos(\alpha_\mathrm{i}) \\ \sin(2\Theta)\cos(\alpha_\mathrm{f}) \\ \sin(\alpha_\mathrm{i}) + \sin(\alpha_\mathrm{f}) \end{pmatrix} \tag{2.46}$$

For X-rays any material is optically thinner than air or vacuum. It is, therefore, possible to observe total external reflection of the X-rays impinging the sample. The critical angle α_c for total external reflection is specific for the material and given by

$$\alpha_c = \sqrt{2\mathrm{Re}(1-n)} \propto \sqrt{\rho} \tag{2.47}$$

with n being the refractive index of the material and ρ representing the material electron density.[70] At $\alpha_f = \alpha_c$ interference of diffuse scattering leads to an enhanced signal, called Yoneda peak.[86]

A mathematical description of diffraction in first order can be obtained from the first Born approximation. In this approximation, we only consider single scattering and neglect all types of multiple scattering. A fixed phase relationship between incoming and scattered photons is assumed, leading to coherent scattering. For this scenario, the scattering amplitude A_{Sc} can be expressed as[25]

$$A_{Sc}(t) \propto \exp(-i\omega_0 t) \int \rho(\vec{r}) \exp(i(\vec{k}_i - \vec{k}_f) \cdot \vec{r})\, d\vec{r}. \tag{2.48}$$

Here, $\rho(\vec{r})$ is the density of scattering centers (electrons), and $(\vec{k}_f - \vec{k}_i)$ corresponds to the scattering vector q. The integration takes place over the whole region involved in the scattering process. The form factor F in the first order Born approximation is determined by the shape of the scattering particle and given as[87]

$$F = \int_S \exp(-i\vec{q} \cdot \vec{r})\, d^3r. \tag{2.49}$$

During scattering at interfaces and surfaces, multiple scattering processes and reflection-refraction effects significantly take place. For this reason, in GISAXS theory the scattering cross-section is usually calculated within the distorted wave Born approximation (DWBA), a perturbation formalism that also considers reflection-refraction effects at interfaces.[88] Fig. 2.9 illustrates four terms of the scattering process included in the DWBA cross section for clusters on top of a reflecting substrate.[89, 87]

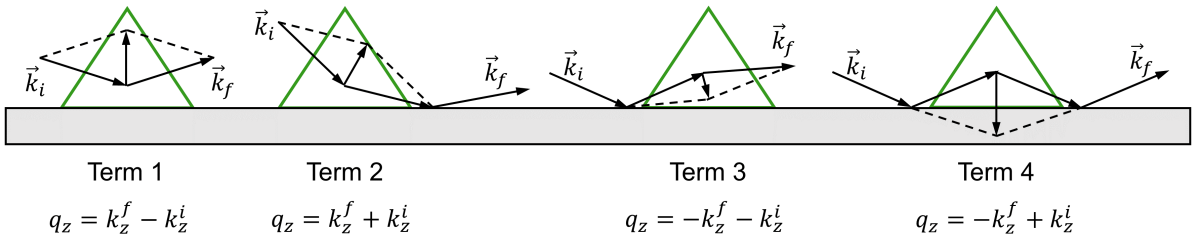

Figure 2.9: Four terms for scattering at clusters (green) on top of a substrate (gray). The first term corresponds to the first Born approximation.

With this, we can define the form factor corresponding of the displayed sample geometry consisting of insulated clusters by[87]

$$\begin{aligned} F(\vec{q}_{||}, k_z^i, k_z^f) = F(\vec{q}_{||}, k_z^f - k_z^i) &+ R_F(\alpha_i) F(\vec{q}_{||}, k_z^f + k_z^i) \\ &+ R_F(\alpha_f) F(\vec{q}_{||}, -k_z^f - k_z^i) \\ &+ R_F(\alpha_i) R_F(\alpha_f) F(\vec{q}_{||}, -k_z^f + k_z^i), \end{aligned} \tag{2.50}$$

where $R_F(\alpha_i)$ and $R_F(\alpha_f)$ are the Fresnel reflection coefficients, which weight the terms 2, 3, and 4, respectively.

Chapter 3

3 Experimental Techniques

3.1 Raman Spectroscopy

In this work, Raman spectroscopy (see section 2.2.1) was carried out at the UT-3 Raman spectrometer[90], which is located at the Center for Free-Electron Laser Science (CFEL) in Hamburg. The UT-3 spectrometer is equipped with a fully reflective entrance optics with a numerical aperture of 0.5, which collects the Raman signal with high efficiency.[90] The spectrometer itself is an achromatic system based on on- and off- axis parabolic mirrors and two sets of three holographic gratings each for the visible and the UV. Strong stray light rejection and high resolution are obtained for wavelength from the deep ultraviolet (UV) from 165 nm to near infrared (NIR) up to 1000 nm.[90] In order to cover the wide range of incident energies, two Tsunami Ti:Sapphire laser systems 3950-X1BB (Spectra Physics Lasers Inc., California) are used. They are pumped with a green Millennia Pro Xs 10sJS and Millennia eV diode laser (Spectra Physics Lasers Inc., California), respectively. The fundamental laser line of the Tsunami systems can be tuned between 700 nm and 1000 nm. We then frequency double, triple, or quadruple this fundamental line with second harmonic generation (SHG), third harmonic generation (THG), or fourth harmonic generation (FHG) (Spectra Physics Lasers Inc., California), respectively. The pulse width is determined by an auto correlator (APE GmbH, Berlin) and typically around 1 ps. For measurements in the green, the Millennia laser is directly used for continuous wave (CW) at 532 nm.

Raman measurements were performed in two principle configurations: macro-Raman[24] and micro-Raman spectroscopy[22]. In macro-Raman configuration, the incoming laser beam is widend with a spatial filter and focused at the sample by the parabolic entrance optics.[90] The back-scattered Raman signal is collected by the entrance optics and coupled into the spectrometer. In macro-Raman configuration, the spot diameter at the sample is around 20 µm. We further developed a custom-made micro-Raman setup for Raman measurements with high local resolution as described in the following subsection. Typically, micro-Raman spectroscopy is carried out with spot diameters of 1 µm to 1.5 µm.[91, 92] The

setup described in the following exhibits spot sizes down to 200 nm – 300 nm depending on the laser energy.

3.1.1 Micro-Raman Setup

Micro-Raman spectroscopy with ultra-small spot sizes of 200 nm – 500 nm enable controlled measurements of single nanostructures as well as the optimization of sample to substrate ratio in the scattering volume. For the investigation of single solid-state nanostructures, we require the following properties and skills. (I) Integrated light microscope with high resolution for locating sample structures and positioning of the laser spot. (II) Degrees of freedom for all optical components and the whole setup in order to align the setup to the spectrometer. (III) Precise movement of the sample position in x, y, and z for scanning and mapping in the sample plane, and adjustment of the optimum focus position. (IV) Achromatic optics in a wide spectral range for resonance studies. (V) Microscope objective with large numerical aperture to collect as much as possible of the weak Raman signal. (VI) High stability and precision of the overall setup to conduct measurements with local accuracy of only tens of nanometers.

Fig. 3.1 shows a Computer Aided Design (CAD) drawing of the custom-made micro-Raman setup. The construction is mounted on a backbone out of aluminum, which ensures the stability of the setup. The incoming monochromatic laser light enters the setup from the left, is guided trough a spacial filter, and is focused at the sample by an infinity corrected microscope objective 50X Mitutoyo Plan Apo HR (NA = 0.75) or 50X Mitutoyo Plan Apo (NA = 0.5), respectively. The scattered light is focused by the focusing objective IC50 (Olympus, Japan) to the entrance optics of the UT-3 spectrometer (NA = 0.5). A white light source QTH10/M (Thorlabs, USA) is mounted at the back of the construction, and incoupled into the beam path by a beam splitter BS064 (Thorlabs, USA) with 70 % reflection and 30 % transmission. The white light is focused at the sample together with the probe laser light for Raman. A motorized mirror is used to switch between light microscopy and the Raman mode. With the mirror out, the reflected light is focused at the CCD camera by an appropriate tube lens. We use a 5 M pixel CCD chip DFK37BUX264 (The Imaging Source, USA) with a pixel size of 3.45 µm × 3.45 µm. With a magnification of 50 X, the imaged size per pixel equals around 70 nm. With the inserted mirror, the reflected light is redirected to the spectrometer axis. Fig. 3.2 represents a schematic illustration of the micro-Raman setup. The beam path of the incoming laser light is

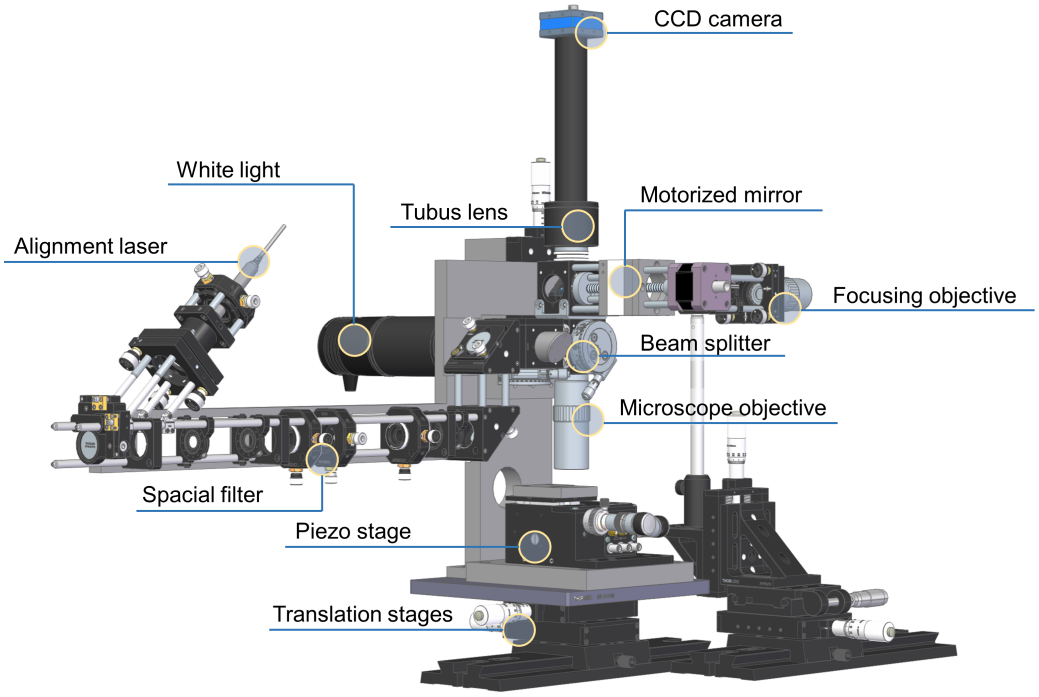

Figure 3.1: CAD drawing of the micro-Raman setup. The incoming laser light enters from the left, passing a spacial filter, is focused at the sample by the infinity corrected microscopy objective (50 X, NA = 0.75/0.5), and exits the setup at the right. The construction is extended by a 50 X light microscope pathway, starting with a whitelight source, which is incoupled in the beam path by a beam-splitter cube. The reflected light from the sample is focused on a CCD camera by a tube lens. A motorized 45° mirror, which can be moved in and out the beam path by a stepper motor, is used to switch between light microscope and Raman mode. The sample is located on top of a piezo stage for precise positioning and movement. CAD file provided by L. Westphal.[93]

depicted in orange. The scattered and reflected light is shown in rainbow colors, indicating the inelastic scattering process. The setup is mounted on linear micrometer translation stages for x, y, and z translation degrees of freedom as shown in Fig. 3.1. The optical elements are mounted with a cage system (Thorlabs, USA). Lense holders contain x, y, and z translations. Mirror holders contain tip and tilt screws. The black arrows in Fig. 3.2 depict the adjustment degrees of freedom available for each component. The sample is placed on top of a multi-axis piezo scanner P-517 (PI, Germany), which is controlled by an E-710.3CD controller (PI, Germany) for precise positioning of the sample with respect to the laser spot and scanning during the measurements. All used parts, item numbers, and manufacturers are listed in the appendix (Tab. B.2, B.1, and B.3).

The measurements presented in this work were carried out with an incidence laser energy of 2.33 eV (532 nm). The maximum power in front of the microscope was 280 mW, which corresponds to a maximum laser power at the sample of around 1.3 mW. The loss of laser power is due to the optical elements in front the sample (spatial filter: 80 % transmission,

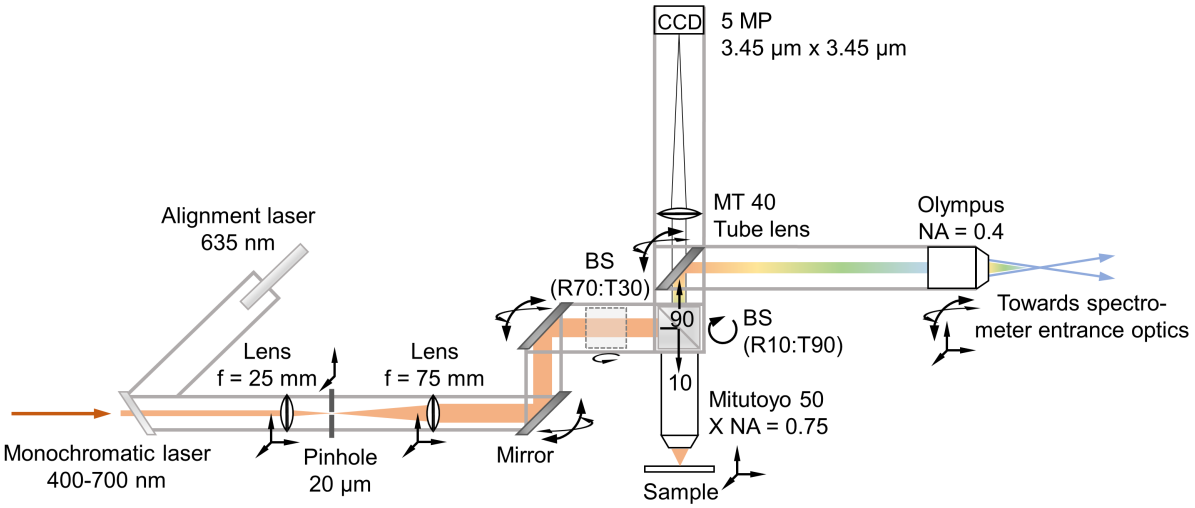

Figure 3.2: Schematic representation of the micro-Raman setup. The incoming laser light (orange arrow left) enters the spatial filter of the setup, consisting of the first lens (25 mm), a 20 µm pinhole and the second lens (75 mm). Two 45° mirrors are used to adapt the beam height and to introduce additional degrees of freedom for alignment. The beam is reflected at a beam splitter (BS) with 10 % reflection and 90 % transmission, and focused at the sample by the Mitutoyo 50 X objective (NA = 0.75/0.5). The reflected light is transmitted through the BS and reflected by 90° by the motorized mirror. The signal is, finally, focused on the entrance optics of the spectrometer by an Olympus objective. The black arrows at the individual optical elements indicate the available degrees of freedom. See Tab. B.2, B.1, and B.3 for details.

beam splitter 1: 30 % transmission, beam splitter 2: 10 % transmission). The power at the sample was measured with a power meter with Si photodiode sensor PM160 (Thorlabs, USA). Measurement on bismuth selenide nanowires were conducted with a laser power at the sample of 140 µW. The Raman data were normalized to the respective laser power and integration time. In order to correct the obtained Raman intensities for the scattering volume, the spot diameter is crucial. For the measurements at 532 nm and the microscope objective 50X Mitutoyo Plan Apo (NA = 0.5), the spot full width at half maximum (FWHM) was determined to be (544 ± 13) nm as illustrated in Fig. 3.3.[93, 22] With the 50X Mitutoyo Plan Apo HR (NA = 0.75), spot sizes of down to 200 nm – 300 nm were found for laser wavelength of 400 nm – 633 nm. Compared to typical micro-Raman instruments with spot sizes of around 1.5 µm, the spot diameter is by a factor of 5 smaller, leading to an area reduced by more than one order of magnitude. With this, the contrast between sample and substrate for nanosized samples smaller than the spot diameter increases drastically. With a laser power of 140 µW, power densities between $58 \times 10^3\,\mathrm{W\,cm^{-2}}$ and $101 \times 10^3\,\mathrm{W\,cm^{-2}}$ were reached for the presented experiments. The results obtained by micro-Raman spectroscopy are discussed in section 4.2.

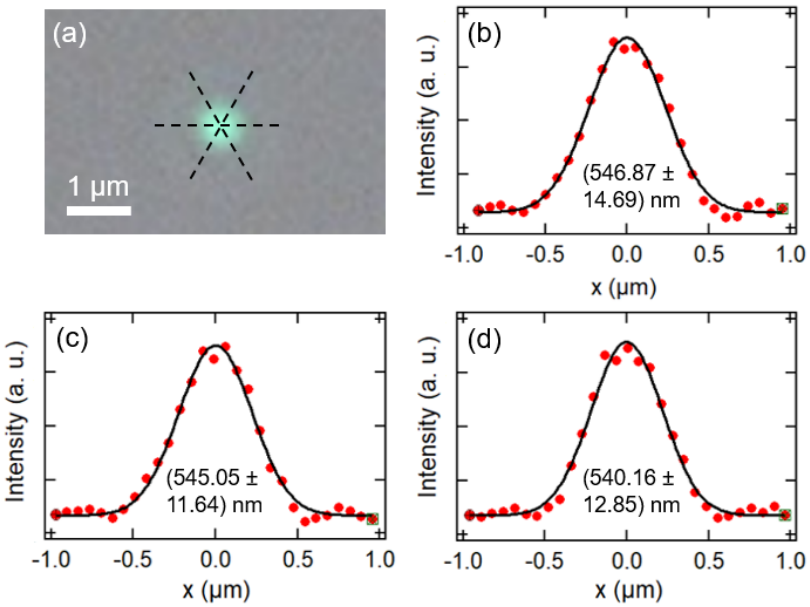

Figure 3.3: (a) Light microscopy image of the 532 nm laser spot on a <111> silicon substrate. The black dashed lines depict the cuts taken for (b)-(d). (b)-(d) Pixel intensity as a function of distance for the three directions indicated in (a). The FWHM resulting from a Gaussian fit (black line) is given in the figures. Figure taken from [22] (Supporting Information).

3.2 X-Ray Scattering

Grazing incidence X-ray scattering (GIXS) was carried out at the X-ray scattering beamline MiNaXS/P03 at PETRA III (DESY, Hamburg).[94] The beamline P03 provides endstations for microfocus (Mi) and nanofocus (Na) and is designed for small, ultra-small, and wide angle scattering experiments in transmission and grazing incidence reflection, allowing a variety of experimental applications for materials science and time-resolved studies.[81, 82, 95, 96, 97, 98] In this work, microfocus X-ray scattering is used to obtain large footprints in grazing incidence for optimum sample statistics from surfaces and interfaces. *Via* grazing incidence small angle X-ray scattering (GISAXS) (see section 4.3) the morphology of nanowire networks at the interface within 3D printed conductive composites was investigated.[14, 97] For this, sample to detector distances (SDD) in the range of 3600 mm – 4990 mm and wavelength of around 0.97 Å(12.8 keV) were used. The spot size was around $(20 \times 30)\,\mu m^2$. Samples were adjusted in height, tilt, and angle, and were scanned through the beam in 50 µm steps to avoid radiation damage. For detection, a 2D Pilatus 1M detector (Dectris Ltd., Switzerland) with a pixel size of $(172 \times 172)\,\mu m^2$ and an image size of (981×1043) pixels, or a Pilatus 300k detector (Dectris Ltd., Switzerland) with a pixel size of $(172 \times 172)\,\mu m^2$ and an image size of (487×619) pixels was employed. The GISAXS data were analyzed using the software package DPDAK.[99]

3.3 Stretching of Silver-Nanowires Composites

The current section is aimed to give an overview on the experimental setup developed for mechanical stress tests of silver-nanowire (Ag-NW) composites. Flexible Ag-NW composites were fabricated as described in section 4.1. Experimental details about the synthesis and sample preparation are given in text boxes related to the experimental results in section 4.1. The characterization of the flexible and conductive nanowire composites was carried out, among other things, by observing the electrical and network properties during mechanical stress. The setup described below has been developed to measure the electrical conductivity of flexible and conductive samples during stretching.[100] Furthermore, the setup is suitable for *operando* grazing incidence small angle X-ray scattering (GISAXS) measurements, which provides nano-scale surface sensitive morphological information (see section 2.2.2), as well as optical microscopy. The stretching setup should meet the following requirements: (I) Flat design that is compatible with microscopy and X-ray scattering methods. (II) Ensuring a straight and untwisted sample surface for microscopy and X-ray scattering in reflection mode. (III) Integrated electrical contacts for four-point sheet resistance measurements.

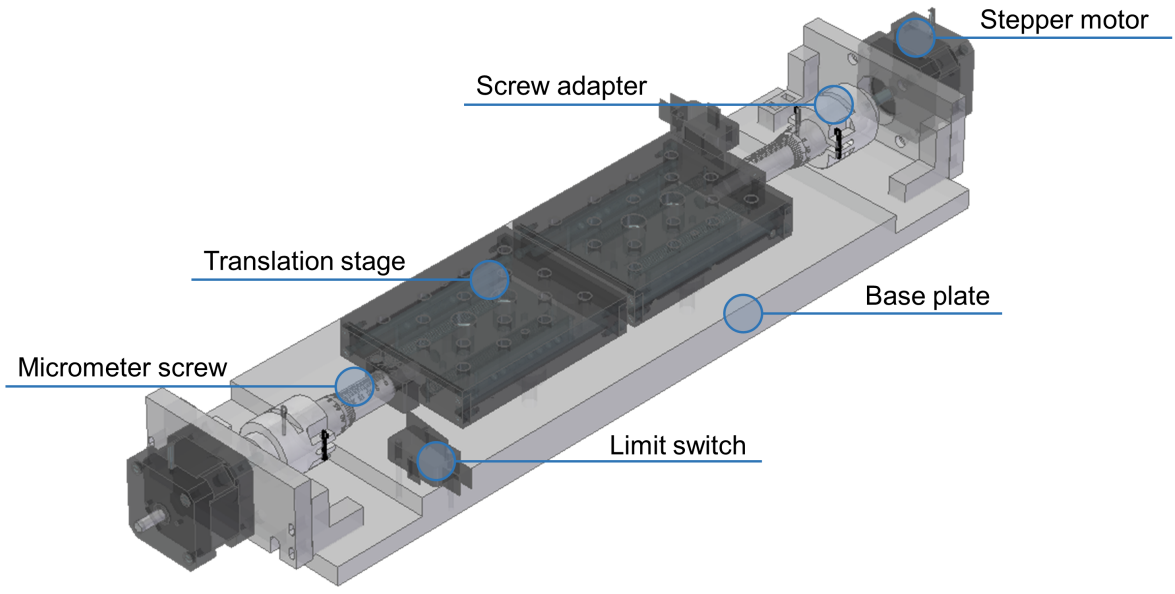

Figure 3.4: CAD drawing of the basic stretching setup construction. The baseplate (gray) is made from aluminum. Two 25 mm translation stages with micrometer drive PT1 (Thorlabs, USA) are mounted on the base. An adapter is connecting the shaft of the stepper motors with the micrometer screws. Two limit switches enable an absolute positioning of the stages.

Fig. 3.4 shows a CAD drawing of the custom-made stretching setup, which consists of an aluminum base plate on which two single-axis translation stages PT1/M (Thorlabs,

USA) are mounted. Both have a travel range of 25 mm with a translation of 0.5 mm per revolution. Each stage is driven by a stepping motor 0.9-NEMA 17 (Nanotec, Germany). The stepping motors are controlled by a closed-loop-stepping motor-controller SMCI33-2 (Nanotec, Germany) with an encoder controlled guaranteed resolution of 2 µm. The sample is mounted on two PEEK plates on top of the translation stages (see Fig. 3.5 (c)). The construction allows the free-standing sample to be investigated by e.g. an X-ray beam without the influence of a substrate. The used components and devices are listed in Tab. B.4 in the appendix.

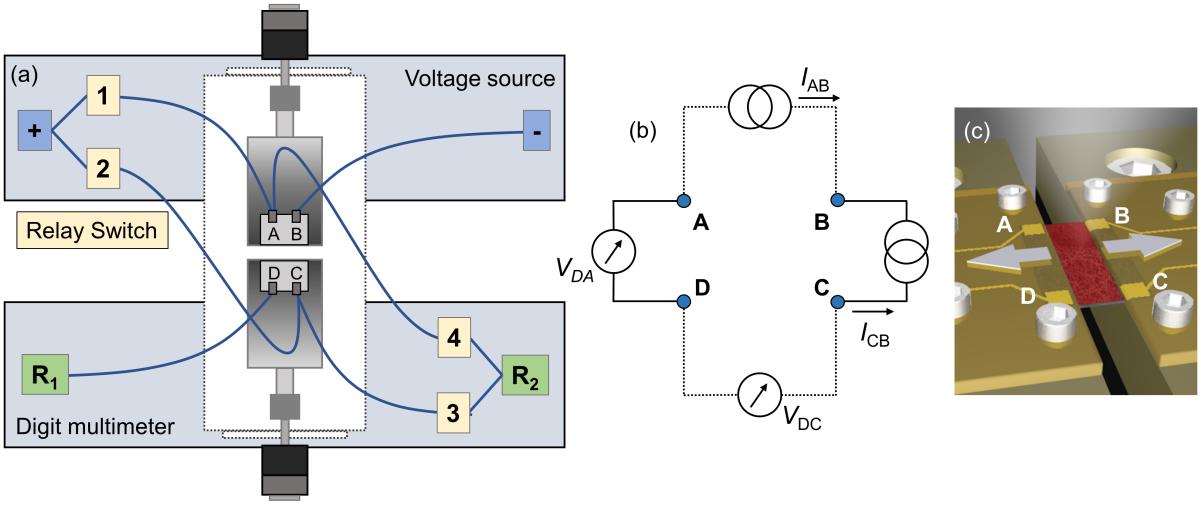

Figure 3.5: (a) Sketch of the stretching setup together with four-point conductivity measurement configuration. A DC voltage/current source GS200 (Yokogawa, Japan) and a 34401A 6 1/2 Digit Multimeter (Keysight, USA) are controlled *via* a GPIB connection. A relay card K8090 (Velleman, Belgium) is integrated in order to switch automatically between the two measurement directions. The numbers in yellow boxes depict the respective relay inputs/outputs. (b) Four-point conductivity measurement to determine the sheet resistance as shown by Van der Pauw. The electrical contacts are labeled with the letters A, B, C, and D, corresponding to the labeling in (a). The two measurement directions (see main text) are denoted by solid and dashed lines. (c) Sample (red) clamped by polyimide plates containing the gold contacts. PEEK plates are mounted underneath the sample for an insulating environment. The white arrows depict the stretching direction.

As shown by Van der Pauw, the sheet resistance ρ of a sample of arbitrary shape can be determined from two currents and two voltages.[101] The measurement setup is based on four electrical contacts, which are located at the edge of the sample as shown in Figure 3.5. A current I_{AB} is driven from contact A to contact B, and the voltage drop V_{DC} between contact D and contact C is measured (see Fig. 3.5 (b)). We calculate the resistance $R_{AB,DC}$ as

$$R_{AB,DC} = \frac{V_{CD}}{I_{AB}}. \tag{3.1}$$

Subsequently, a current I_{CB} is driven from contact C to contact B, and the voltage V_{DA} between contact D and contact A is measured resulting in the resistance $R_{BC,DA}$. The sheet resistance ρ_{sq} in Van der Pauw approximation is given by

$$\rho_{sq} = \frac{\pi}{\ln(2)} \cdot \frac{R_{AB,DC} + R_{BC,DA}}{2} \cdot f, \tag{3.2}$$

with f being a correction factor for the sample shape, which depends on the ratio $R_{AB,DC}/R_{BC,DA}$ as given in equation 3.3.[101] The sheet resistance in units Ω/sq does not depend on the size of the sample area.

$$\cos\left(\frac{R_{AB,DC}/R_{BC,DA} - 1}{R_{AB,DC}/R_{BC,DA} + 1} \cdot \frac{\ln(2)}{f}\right) = \frac{1}{2} \cdot \exp\left(\frac{\ln(2)}{f}\right). \tag{3.3}$$

Fig. 3.5 (a) illustrates the conductivity measurement setup adapted to our stretching device. The four contacts A, B, C, and D are made from gold and integrated in a polyimide plate (MPI for the structure and dynamics of matter, Hamburg), which is used to clamp the composite samples. A relay card K8090 (Velleman, Belgium) automatically switches between the two measuring directions. A DC voltage/current source GS200 (Yokogawa, Japan) and a 34401A 6 1/2 Digit Multimeter (Keysight, USA) are used, which can be controlled *via* a GPIB connection. For this, a KUSB-488B USB to GPIB converter (Keithley, USA) is applied. The devices and stepper motors are controlled by a python 3.8 script.[100] In Fig. 3.5 (c) a sketch of the stretching setup with the four electrical contacts (gold) and the sample (red) is shown.

Chapter 4

4 Experiments and Results

4.1 Functional Silver-Nanowire Composites

4.1.1 Introduction

Functional polymer nanocomposites show enormous versatility for a wide variety of applications.[102] In the case of anisotropic conductive nanofillers like inorganic nanowires[103, 104] or carbon nanotubes[105], films of two-dimensional (2D) conductive networks are of great interest because of various electronic and optical applications in for example solar cells, OLEDs, and sensors.[106, 107, 108, 109] Various routes have been developed for fabricating 1D nanostructures like template-directed syntheses or the assembly of nanoparticles.[110] Silver-nanowire (Ag-NW) composites offer a process for large scale, flexible, transparent, and conductive materials, as used in photovoltaics, touch screens, and flexible electronics.[111, 112, 113, 114, 115] They are a promising alternative to indium tin oxide.[116] The composites can easily be tailored to their particular application as the matrix material is interchangeable and tunable, for example in terms of color, optical, and mechanical properties. By using highly flexible polymers, flexible Ag-NW electrodes can be produced, which can be used for strain sensors and flexible electronics.[117, 118, 119] Flexible electrodes for foldable touch displays are some of the most demanding applications of these materials.

In addition to the network and material properties, the manufacturing processes for industrial applications also play a decisive role. The embedding of nanowires in a printable polymer matrix allows rapid prototyping and high design flexibility. Additive manufacturing and functional printing of components have developed to be important and innovative industrial processes.[120, 121] Photopolymers have tunable viscosities, are curable by illumination with UV-light, and are well suited to create three dimensional structures and functional devices *via* layer by layer additive manufacturing.[122] Thus, in this work, silver-nanowire-photopolymer composites are used to manufacture highly conductive, transparent, and flexible electrodes by printing methods.

In order to achieve a conductive 2D nanowire network, a percolation of the metal nanostructures within the polymer is necessary. If fillers with high aspect ratio are used, the percolation threshold is reached even at low nanomaterial concentrations. A conductive network of anisotropic nanowires is characterized by a high surface coverage, which leads to high optical transparency. Hence, we focus on the optimization of nanowires with ultra-high aspect ratio.

In the following sections, the investigation of Ag-NW networks and composites for functional printing and flexible electronics is reported from different points of view. First, the synthesis of Ag-NWs as well as the fabrication of Ag-NW networks are explained. Experimental details of the synthesis and the fabrication steps are given in separate text boxes. The Ag-NWs are synthesized by a polyol route (section 4.1.2) and characterized by scanning electron microscopy (SEM), grazing incidence small angle X-ray scattering (GISAXS), and conductivity measurements as a function of the Ag-NW concentration (section 4.1.3). The sections 4.1.4 and 4.1.5 present a Monte Carlo simulation together with a percolation model for Ag-NW networks.[15] The experimentally observed concentration dependence of the electrical properties is successfully reproduced by this model. Section 4.1.6 then reports on the controlled modification of Ag-NW networks by atmospheric plasma treatment combining *in situ* grazing incidence X-ray scattering studies with a Monte Carlo simulation of nanowire networks upon plasma treatment.[97] In section 4.1.7, the fabrication of Ag-NW polymer composites is reported and in section 4.1.8 flexible Ag-NW composites are investigated in detail under mechanical stress. During stretching, conductivity measurements and light microscopy are utilized to monitor changes in the network functionality and morphology.[15] The applicability of the Ag-NW composites as strain sensors is demonstrated over several stretching cycles.[123] A Monte Carlo simulation dominated by the quantum mechanical tunneling of the electrons at the nanowire junction is used to understand the network behavior upon mechanical strain. The Ag-NW composite material is applied as a transparent top contact on top of a solar cell and a flexible capacitor (section 4.1.9).[14]

4.1.2 Synthesis of Silver Nanowires

In 2002, Y. Sun *et al.* demonstrated a simple but effective wet chemical method for the synthesis of silver nanowires.[19] The polyol method is based on the reduction of the precursor silver nitrate ($AgNO_3$) by glycol aldehyde in the presence of polyvinylpyrrolidone

(PVP) as a capping agent. Ethylene glycol is typically used as solvent, which is oxidized to glycol aldehyde by the oxygen in air at temperatures between 140°C and 160°C.[124] In the early stage of the reaction, nuclei consisting of a few silver atoms are formed, which develop to seeds with a five-fold twinned structure. The seeds are assemblies of five tetrahedral single crystals with a surface consisting of {111}-facets. In {111}-facets the surface coverage is maximal and the total free energy is low, which makes them kinetically favored.[125] However, five tetrahedrons, each with an angle of 70.53° between two sides, only fill $5 \cdot 70.53° = 352.65°$, and a gap of 7.35° occurs. This gap is compensated by internal lattice strain.[126] From a critical seed size, the internal strain can no longer be compensated by the low free energy of the {111}-facets. For this reason, structural control can be achieved during the synthesis by controlling the size of the seeds and, accordingly, the number of free zero-valent silver atoms. The addition of chloride ions (Cl^-) leads to a lower reduction rate caused by the reaction with silver ions to silver chloride (AgCl). This results in small seeds with a stable five-fold twinned shape.[125, 127] Oxygen from air is also oxydizing zero-valent silver atoms back to silver ions. In oder to avoid this uncontrollable oxidative etching process, redox active metals salts like CuI/CuII are typically added to the synthesis.[125, 127] Experimental details of the Ag-NW synthesis are given in the text box below (Experimental Details 4.1). The used chemicals are listed in the appendix (Tab. B.5). The synthesis results in nanowires with a pentagonal shape as shown in Fig. 4.1 (a).[14] Fig. 4.1 (b) and (c) show the length and diameter distribution of an exemplary batch.[97] Most of the wires exhibit lengths between 5 µm and 20 µm. Much longer wires with length up to 160 µm are also present. The diameters are normal distributed and a mean diameter of around 212 nm is observed for this exemplary synthesis.[97] Average aspect ratios for polyol syntheses performed with same experimental parameters between 86 and 197 have been found.[128] During the growth process, the capping agent PVP passivates the {100}-facets and enables one-dimensional growth at the {111}-facets.[129, 125] The final silver nanowires, therefore, exhibit a stabilizing but insolating PVP shell. A washing procedure with acetone and isopropanol is used to remove remaining and redundant PVP from the nanowire suspension as outlined below (Experimental Details 4.2). The washing procedure leads to a decrease in sheet resistance of drop-casted nanowire networks by a factor of about 10.

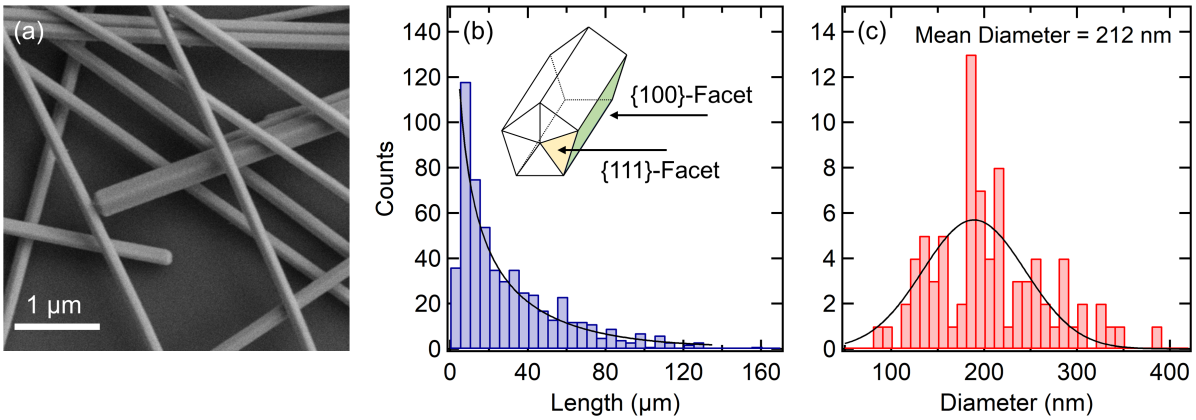

Figure 4.1: (a) SEM image of silver nanowires. Adapted from [14]. Licensed under CC BY, https://creativecommons.org/licenses/by/4.0/. (b) Exemplary length histogram of Ag-NWs measured by SEM. The inset shows schematically the pentagonal shape of the nanowires. (c) Diameters of Ag-NWs for an exemplary batch. The mean diameter is 212 nm. Adapted with permission from [97]. Copyright 2021 Elsevier.

Experimental Details 4.1.

Synthesis. An oil bath was heated up to 155°C. 6 mL ethylene glycol were filled into an unsealed vial and heated for 50 min in the preheated oil bath. A copper chloride ($CuCl_2$) solution was prepared by adding 0.018 g $CuCl_2 \cdot 2H_2O$ to 2 mL ethylene glycol ($c = 0.0519\,\text{mol L}^{-1}$). A solution consisting of 3 mL ethylene glycol, 0.03 g PVP 55000 ($n = 0.00055$ mmol), 0.06 g PVP 360000 ($n = 0.00017$ mmol) and 3 µL of the $CuCl_2$ solution ($n = 0.000156$ mmol) was prepared and added to the preheated solvent after 50 min. The resulting solution was heated for further 15 min and stirred at 600 rpm. A silver nitrate ($AgNO_3$) solution consisting of 0.03 g $AgNO_3$ ($n = 0.18$ mmol) and 2 mL ethylene glycol was filled into a syringe, which was controlled by a neMESYS syringe pump (Cetoni, Germany). The magnetic stir bar was removed and the injection of the $AgNO_3$ solution was started after 65 min with a flow rate of 1.88 mL/h. The synthesis was quenched after 235 min by immersing the vial in 16°C water.[128] See also Tab. B.5.

Experimental Details 4.2.

Washing. After the synthesis, the Ag-NW suspension was washed successively twice with isopropanol, twice with acetone, and twice with isopropanol. After each washing step, the suspension was centrifuged at 2000 rpm for 10 min. The supernatant was removed and replaced with fresh solvent.

4.1.3 Silver-Nanowire Networks

Ag-NW networks are easy to fabricate by drop-casting of a Ag-NW suspension on a flat and clean surface from silicon or glass (Experimental Details 4.3).[14, 130] The Ag-NWs are stored in isopropanol, which evaporates at room temperature in a few minutes, resulting in a dried Ag-NW network. Drop-casting leads to networks of randomly distributed and orientated nanowires as shown in Fig. 4.2 (a) and (b).[128] Above a critical concentration, these networks have an electrical sheet conductivity due to percolation even with small amounts of silver, which makes them promising candidates for transparent electronics.[14] This is a consequence of the high aspect ratio of the used nanowires. Compared to composites of spherical fillers, anisotropic sticklike fillers reach the percolation threshold at a lower amount of the filler material, since the percolation threshold is decreasing with increasing aspect ratio (length/diameter).[131, 132, 133, 134, 135, 136] In the case of anisotropic nanowires, the network resistance decreases exponentially with nanowire concentration.[14, 15, 137, 138] Sheet resistances for several samples with nanowire concentrations between 25 µg cm^{-2} and 80 µg cm^{-2} are shown in Fig. 4.2 (c).[14] An exponential curve is used as guide to the eye.

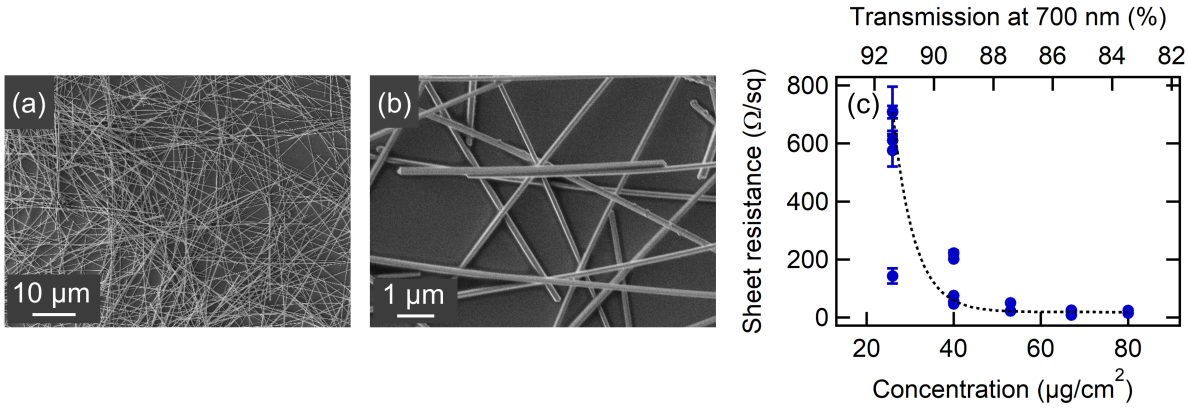

Figure 4.2: (a) SEM image at low magnification showing a Ag-NW network with a concentration of around 100 µg cm^{-2}. (b) SEM image of the same network at higher magnification. (c) Sheet resistance for several samples as a function of Ag-NW concentration. Please note the critical behavior at around 25 µg cm^{-2}. The top axis denotes the experimentally determined optical transmission at 700 nm corresponding to the network concentration.[14, 128]

On the top axis in Fig. 4.2 (c), the optical transmission of the Ag-NW networks at 700 nm is shown. The transmission was measured in the optical spectral range (400 nm to 900 nm) through silver nanowire networks deposited on glass substrates (see also Fig. 4.20 (b) and appendix A for more details). The substrate transmission is subtracted from the sample transmission. A linear behavior of the transmission as a function of nanowire concentration

has been observed.[14, 128] Reproducible sheet resistances of (17.5 ± 8.1) Ω/sq are obtained at 86 % transmission at 700 nm with a Ag-NW density of 65 µg cm^{-2}, which is comparable to those of ITO.[128, 116]

Grazing incidence small angle X-ray scattering (GISAXS) is a surface sensitive method which enables the investigation of the nanowire morphology within the network with high statistics (see section 2.2.2). Fig. 4.3 summarizes the GISAXS results obtained from a Ag-NW network deposited on a silicon wafer as reference substrate.[14] Details on the measurement procedure and parameters are given in section 3.2 and Tab. B.7 in the appendix. Two intensity flares with an angle of 36° to the vertical can be clearly seen in the 2D GISAXS pattern presented in Fig. 4.3 (a). This key feature is simulated in Fig. 4.3 (b) by using the software IsGISAXS (V 1.6).[87] An anisotropic pyramid with an aspect ratio of 10:1 and a radius of 60 nm is assumed as the scattering object in order to model the surface of the nanowires facing the beam. The facet angle with respect to the sample surface is 36° in agreement with the pentagonal structure of the nanowires with a facet angle of 36° as shown in Fig. 4.3 (c).[14] The object is aligned with its long axis along the beam. By using the distorted-wave Born approximation (DWBA) reflection and refraction effects were also included (see also section 2.2.2).[14, 96]

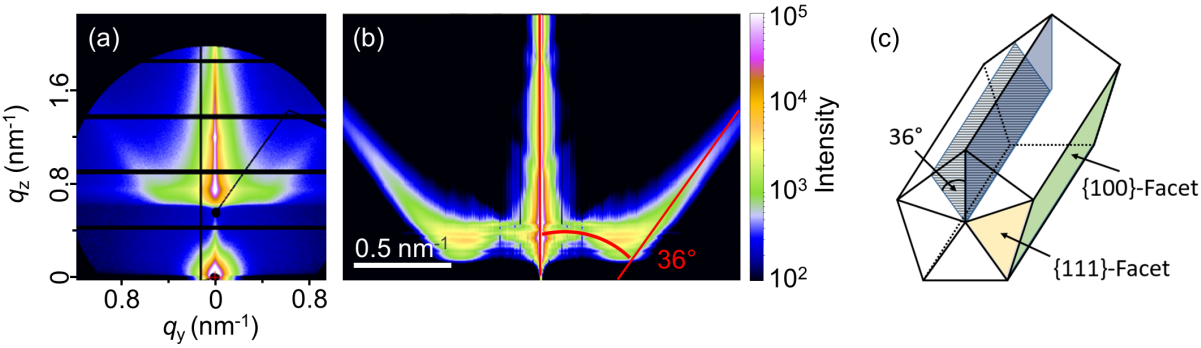

Figure 4.3: (a) 2D GISAXS pattern of a Ag-NW network with a concentration of 58 µg cm^{-2} deposited on a silicon wafer. (b) Simulation of the key features observed in (a) *via* IsGISAXS. (c) Pentagonal shape of the investigated nanowires, which causes the intensity flares at 36° to the vertical. Adapted from [14]. Licensed under CC BY, https://creativecommons.org/licenses/by/4.0/.

Experimental Details 4.3.

Drop-Casting. The Ag-NW suspension (Ag-NWs in isopropanol, $c = 2\,\mathrm{g\ L^{-1}}$) was dropped on a cleaned substrate (silicon or glass). The substrates were cleaned by solvents (acetone, isopropanol, destilled water). In order to define the drop-casted area, a template with a size of (1.5 x 2) cm^2 was used. The suspension spread homogeneously over the substrate and the solvent evaporated.

4.1.4 Percolation Theory

Networks of randomly oriented 1D particles like carbon nanotubes and metal nanowires are of great interest in various fields such as electronics and sensors. The most important property of these networks is their electrical or thermal conductivity, as it determines the network functionality for many applications. The dependence of the conductivity on the network density is, therefore, a central question for material development. The conductivity of a 2D or 3D nanowire network correlates strongly with the interconnectivity of the network.[15] A percolation model is needed to model and understand the functional properties of these networks. Percolation denotes the formation of connected clusters in a random network of particles.[139] When two points, areas, or boundaries A and B of a network sample are connected through paths and clusters formed by the particles, a percolation is obtained. The so-called percolation threshold determines the critical density at which percolation is statistically reached.[140] There are a lot of scenarios that can be well described by percolation theory like epidemics and forest fires. In each case, a percolation model has to be created, which represents the physical properties of the scenario. An exact solution has only been found for a few special cases.[141, 142] Mostly Monte Carlo methods are used as approximation methods for calculating the percolation behavior.[131, 132, 143, 144, 145]

Most percolation problems are based on randomly or regularly distributed sites in 2D or 3D space that are connected to one another in a certain way. A binding criterion is needed that determines which sites are connected.[139] Fig. 4.4 illustrates three steps of a percolation model. In Fig. 4.4 (a) 7 sites are randomly positioned in a 2D area with the coordinates x_i and y_i. In Fig. 4.4 (b) each site is assigned a radius R_i that defines a circle around the site. We can now define the following bonding criterion: If the distance d_{ij} (see Eq. 4.1) between sites i and j is smaller than the sum of the radii R_i and R_j, the particles are bonded. This is a suitable model for spherical or disc like particles.[146]

$$d_{ij} = \sqrt{(x_i - x_j)^2 + (y_i - y_j)^2} \tag{4.1}$$

In order to define anisotropic particles like sticks and wires, a further parameter for its orientation has to be introduced. The angle Θ_i describes the angle of the stick to the vertical. We can now use the criterion above to test whether an intersection comes into question: If the distance d_{ij} (Eq. 4.1) between sites i and j is larger than the sum of the

radii R_i and R_j, a bonding can be excluded. Furthermore, a second criterion is needed. The distances A_i and A_j are calculated (see Eq. 4.2 and Fig. 4.5 (d)).[143, 147, 132] If $A_i \leq L_i/2$ and $A_j \leq L_j/2$, an intersection between the wires i and j is found.

$$A_i = d_{ij}\left|\frac{\cos(\theta_i+\gamma)}{\sin(\theta_j-\theta_i)}\right| ; \quad A_j = d_{ij}\left|\frac{\cos(\theta_j+\gamma)}{\sin(\theta_j-\theta_i)}\right| ; \quad \gamma = \arctan\left[\frac{y_i-y_j}{x_i-x_j}\right] \tag{4.2}$$

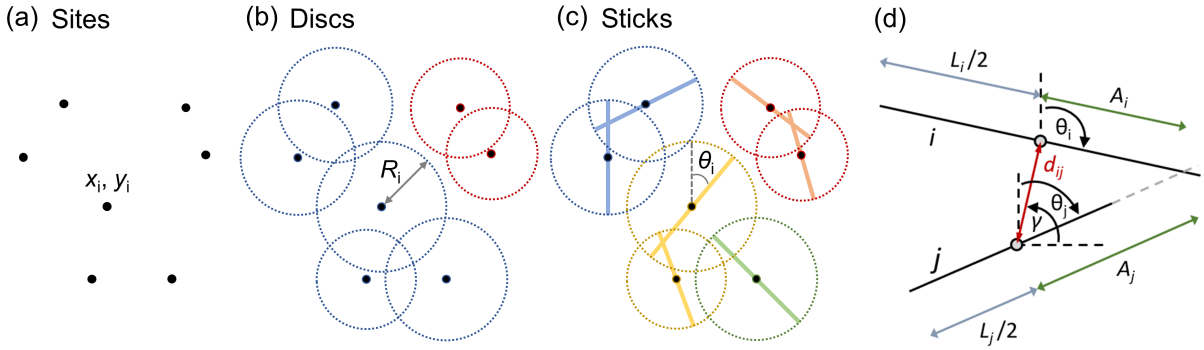

Figure 4.4: (a) Sites with random position x_i and y_i. (b) Each site is assigned a radius R_i that defines a circle around the site. Two clusters (blue and red) are formed by intersecting discs. (c) For sticks and wires, the angle Θ_i denotes the angle of the stick i to the vertical. Four groups (blue, red, yellow, green) of intersecting wires are present. (d) Pictorial description of geometrical quantities, which were used in Eq. 4.2 to check whether two wires i and j are intersecting.[131, 132] Image (d) adapted from [15]. Licensed under CC BY-NC https://creativecommons.org/licenses/by-nc/3.0/.

4.1.5 Monte Carlo Simulation

The pioneers of Monte Carlo methods are Enrico Fermi, Nicholas Metropolis, Arianna W. Rosenbluth, Marshall N. Rosenbluth, and Augusta H. Teller.[148, 149, 150, 151] Shortly before the start of World War II, Enrico Fermi researched the diffusion of neutrons. He used Monte Carlo methods that enabled him to perform statistical sampling even before the term 'Monte Carlo' was coined. The name 'Monte Carlo' later served as a code name to keep this valuable calculation method, which finally led to Hiroshima, a secret.[151, 152] The development of Monte Carlo simulation went hand in hand with the development of the first electronic and programmable digital computers. In 1953, Metropolis *et al.* published a fundamental work on the calculation of the state equation of a 2D system of rigid spheres by means of Monte Carlo integration, which was carried out at the Los Alamos MANIAC.[148]

Monte Carlo methods are based on a large number of random experiments. They are used to numerically solve problems that cannot be solved analytically.[153] When considering nanowire networks, a single nanowire cannot represent the properties of a complete network.

Even a collection of several wires can only reflect the network properties to a limited extent. It is necessary to consider a large number of nanowires that form a network in order to compensate for statistical fluctuations and to map the properties of the network and not the individual wires. According to the law of large numbers, a large number of random experiments enables isotropic samples to be generated from random anisotropic wires.

The following describes a model using a Monte Carlo method for Ag-NW networks and their electrical properties. Basic parts of the used python code are shown in the gray parts of the text. The presented simulation method is finally used to model the sample properties with regard to the concentration dependence of the network resistance (Fig. 4.7), plasma treatment of Ag-NW networks (section 4.1.6), and stretching of flexible Ag-NW composites (section 4.1.8 and section 4.1.9).

Simulation of Ag-NW networks. Considering a network made from randomly orientated nanowires, each single nanowire i that is located on a sample with the size $x \times y$ is determined by the following parameters: Its length L_i, the positions of its center (x_i, y_i), and the orientation of the wire, which is determined by the angle θ_i, the angle between the wire and the vertical (see Fig. 4.4). These parameters are illustrated in Fig. 4.5 (a). For the Monte Carlo simulation, the position x_i, y_i, and the orientation angle θ_i are determined by using a random generator. The allowable interval for the wire position is the sample size. In order to create an isotropic network, a value between $-90°$ and $90°$ is chosen randomly for the orientation angle.[131] The experimentally used nanowires exhibit a specific length distribution, which was determined by SEM evaluation (see Fig. 4.1). Thus, a histogram of the nanowire lengths is given and each individual length is drawn randomly from this histogram. By this, an array is generated containing a list of parameters for each nanowire, namely the positions x_i and y_i, the length L_i, the orientation angle θ_i, and a wire number for future identification. This array can be graphically represented by plotting all wires as a vector in a two-dimensional field as shown in Fig. 4.5 (b). A sample of $350\,\mu m \times 350\,\mu m$ with a nanowire concentration of $10\,\mu g\,cm^{-2}$ consisting of 1000 wires is shown. For later network simulations samples with 4000 to 10000 wires were used.[15] Fig. 4.5 (c) shows a sample in which the individual clusters formed by intersecting wires are shown in different colors. The centers of the wires are marked with dots. One can see a dominant cluster that is highlighted in light blue. This cluster is in contact with all four sides of the sample and, thus, achieves percolation as shown in Fig. 4.5 (d). Below is a Python code using the

Monte Carlo method to create a nanowire sample as described above. The result is an array that lists all of the parameters required for all wires.

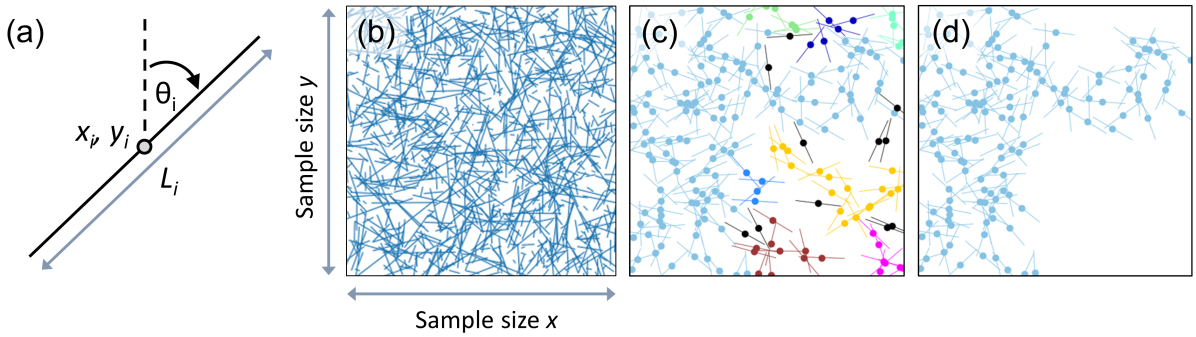

Figure 4.5: (a) A single nanowire is represented by the following parameters: The position of its center (x_i, y_i), its length L_i, and its orientation, which is determined by the angle θ_i. (b) An exemplary simulated nanowire network. The sample size determines the interval, in which the nanowire positions are determined randomly. Adapted from [15]. Licensed under CC BY-NC https://creativecommons.org/licenses/by-nc/3.0/. (c) A simulated network where the individual clusters were identified using the bonding criterion described above and marked in different colors. (d) The light blue cluster reaches percolation from the left to the right and from the bottom to the top of the sample.

```
import random

# Initialization #
N = 10000 # Number of wires
size_x = 500 # Sample size x = 500 µm
size_y = 500 # Sample size y = 500 µm

# Create Array for wire parameters #
dtype = [('x', float), ('y', float), ('L', float), ('Theta', float), ('WireNo',
int)]
Sample = np.array([ ], dtype = dtype)

# Length distribution in 10 µm intervals, first class starts at 5 µm #
His = np.array([0.35, 0.18, 0.12, 0.09, 0.07, 0.06, 0.05, 0.03, 0.03, 0.02])
Histogram = His*N

for i in range(N):
     # Define wire number, wire position, and orientation angle #
     Wire = i
     x = random.random()*size_x
     y = random.random()*size_y
     Theta = random.random()*180-90

     # Choose length out of length distribution #
     Counter = 0
```

```
     Found = 0
     while Found == 0 and Counter < 1000:
          Class = random.randrange(0, (len(Histogram)-1), 1)
          if int(Histogram[Class]) > 0:
               Histogram[Class] = Histogram[Class]-1
               Length_Class = Class*10+5
               L = random.random()*10+Length_Class
               Found = 1
          Counter += 1
     if Found == 0:
          print('No length was found for wire', Wire)
          L = 27 # The mean length is 27 µm #
     values = [(x, y, L, Theta, Wire)]
     Parameters = np.array(values, dtype = dtype)
     Sample = np.append(Sample, Parameters, axis=0)

# => return array 'Sample' #
```

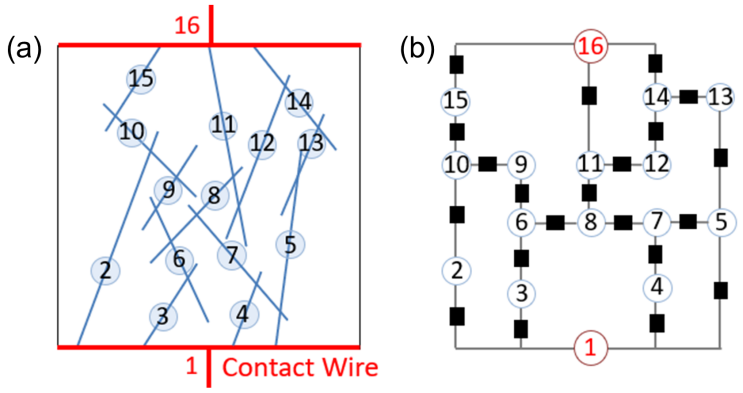

Figure 4.6: (a) Network of 14 wires and 2 contact wires (red). The resistance will be calculated between the contact wires 1 and 16. (b) Resistor network corresponding to the network shown in (a). Every node (numbered) represent a wire and every resistor (black squares) depict a tunneling junction. Adapted from [15]. Licensed under CC BY-NC https://creativecommons.org/licenses/by-nc/3.0/.

In order to calculate the electrical resistance of the simulated networks, they are translated into resistor networks consisting of nodes and resistors. Since silver is an excellent conductor, the resistance of a Ag-NW network is mostly dominated by the tunneling junctions between the nanowires. Therefore, each node represents a nanowire and each resistor represents a nanowire-nanowire junction.[140, 147, 143] Fig. 4.6 (a) and (b) show a nanowire network and the corresponding resistor network, respectively. Two permanent contact wires (1 and 16 in Fig. 4.6) are used to contact the two dimensional sample.[15] In order to translate a simulated Monte Carlo network into the corresponding resistor network, the wire-to-wire junctions within the network must be found. For this purpose, the two binding criteria

introduced in section 4.1.4 (see Fig. 4.4) are used. The corresponding Python code is shown below. It is used to find all tunneling junctions within a network. If an intersection is found, the wire numbers for the two wires i and j are listed in a new array. By this, the procedure results in an array containing all combinations of intersecting wires. The functions 'Calc_dij' and 'Calc_Aij' represent Eq. 4.1 and 4.2, respectively.

```
import numpy as np

def Calc_dij(x_i, x_j, y_i, y_j):
     dij = np.sqrt(((x_i-x_j)**2+(y_i-y_j)**2))
     return dij

def Calc_Aij(dij, Theta_i, Theta_j, x_i, x_j, y_i, y_j):
     alpha = np.arctan((y_i - y_j)/(x_i - x_j))*(180/np.pi)
     denominator = np.sin((Theta_j-Theta_i)*(np.pi/180))
     Ai = dij*np.sqrt((np.cos((Theta_j+alpha)*(np.pi/180))/denominator)**2)
     Aj = dij*np.sqrt((np.cos((Theta_i+alpha)*(np.pi/180))/denominator)**2)
     return Ai, Aj

# Find all junctions #
N = len(Sample) # Sample = array with wire parameters
dtype = [('Wire1', int), ('Wire2', int)]
Intersections = np.array([ ], dtype = dtype)

for i in range(N):
     x_i = sample[i]['x']
     y_i = sample[i]['y']
     L_i = sample[i]['L']
     for j in range(i+1, N):
          x_j = sample[j]['x']
          y_j = sample[j]['y']
          L_j = sample[j]['L']
          dij = Calc_dij(x_i, x_j, y_i, y_j)
          if i != j and dij < (L_i/2 + L_j/2):
               Theta_j = sample[j]['Theta']
               Theta_i = sample[i]['Theta']
               Ai, Aj = Calc_Aij(dij, Theta_i, Theta_j, x_i, x_j, y_i, y_j)
               if Ai <= L_i/2 and Aj <= L_j/2:
                    # An intersection is found!  Save the combination i,j #
                    Junction = [(i,j)]
                    values = np.array(Junction, dtype = type)
                    Intersections = np.append(Intersections, values, axis = 0)

# => return array 'Intersections' #
```

In a next step, the network resistance has to be calculated. A normalized quantum-mechanical tunneling resistance $r_{ij} = 1$ of the junction between the wires i and j is assumed, resulting in a conductance of $c_{ij} = r_{ij}^{-1} = 1$. The resistance between wires that are not intersecting is infinity resulting in a conductance of 0. With V_i being the electric potential at the i-th wire and I_i being the current flowing in the system at the i-th wire, Kirchhoff's Law can be written as[154]

$$L\vec{V} = \vec{I} \tag{4.3}$$

where L is the Laplace matrix as given in Eq. 4.4. The matrix elements c_{ij} are 0 when the wires i and j do not intersect and 1 when the wires intersect. The diagonal elements $(i = j)$ are given as $c_{ii} = \sum_{j=1}^{N} c_{ij}$.[154]

$$L = \begin{pmatrix} c_{11} & -c_{12} & \cdots & -c_{1N} \\ -c_{21} & c_{22} & \cdots & -c_{2N} \\ \vdots & \vdots & \ddots & \vdots \\ -c_{N1} & -c_{N2} & \cdots & c_{NN} \end{pmatrix} \tag{4.4}$$

The network resistance can now be calculated by a Greens function method reported by F. Y. Wu.[154] The resistance between two nodes i and j is given by Eq. 4.5, where ψ_i are the eigenvectors and λ_i are the eigenvalues of L. By using contact wires as shown in Fig. 4.6, the resistance between two sides of the network is calculated.

$$R_{\alpha\beta} = \sum_{i=1}^{N} \frac{1}{\lambda_i} \left| \psi_{i\alpha} - \psi_{i\beta} \right|^2 \tag{4.5}$$

A Python routine that creates the Laplace matrix L is shown below. We use a $N \times N$ matrix where N is the number of wires in the network. The matrix is filled with the help of the previously created list of all wire-to-wire junctions.

```
# Sample = sample parameter array #
# Intersections = list of junctions #

N = len(Sample)

# Create N x N Matrix #
Zeile = [ ]
for j in range(0, N):
     Zeile.append(0)
Matrix = np.array([Zeile])

for i in range(1, N):
     Zeile = [ ]
     for j in range(0, N):
          Zeile.append(0)
     Zeile = np.array(Zeile)
     Matrix = np.append(Matrix, [Zeile], axis = 0)

for n in range(len(Intersections)):
     i = Intersections[n]['Wire1']
     j = Intersections[n]['Wire2']
     Matrix[i][j] = -1
     Matrix[j][i] = -1
     Matrix[i][i] = Intersections(Matrix[i][i]+1)
     Matrix[j][j] = Intersections(Matrix[j][j]+1)
```

We determine the eigenvectors and eigenvalues of the Laplace matrix by using the numpy function numpy.linalg.eigh.[155] The resistance is calculated according to Eq. 4.5.

```
# Calculate resistance #

StartPoint = 0
EndPoint = len(Sample)-1
N = len(Matrix)
ew,ev = linalg.eigh(Matrix)
ew_abs = np.abs(ew)
ew_sort = sorted(ew_abs)

R = 0
for i in range(0, N):
     if ew_abs[i] != ew_sort[0]:
          Phi = np.abs(ev[StartPoint][i]-ev[EndPoint][i])
          R += 1/ew_abs[i]*(Phi)**2

# => return R #
```

We are now able to simulate the electrical resistance of networks with different nanowire concentrations. Fig. 4.7 (a) shows in green the experimental data, which was already discussed in Fig. 4.2 (c). The simulated resistances are presented in blue.[14, 15] The nanowire concentration used for the experiment is shown on the upper axis and the concentration used for the simulation, called the effective concentration, is shown on the lower axis. The experimental concentrations are by a factor of four higher than the corresponding effective concentrations used for the simulation.[15] The latter corresponds to the concentration of Ag-NWs that effectively contribute to the conductive network and is lower due to the effective distribution of nanowires within the sample. A small amount of side products (particles and rods) in the Ag-NW suspension further reduces the effective concentration. In addition, the drop casting of nanowires results in a coffee ring with more concentrated areas at the edges of the samples, which were removed before the samples were measured. These effects lower the effective concentration of the remaining network.

Fig. 4.7 (b) shows the network interconnectivity as a function of nanowire concentration. We define interconnectivity C_{Inter} as the number of junctions within the network divided by the total number of wires making up the network. A linear function $C_{Inter} = f \cdot c_{eff}$ was fitted to the data, where c_{eff} denotes the effective concentration, resulting in a proportionality factor of $f = (0.24242 \pm 0.000232)\,\mathrm{cm^2 \mu g^{-1}}$.

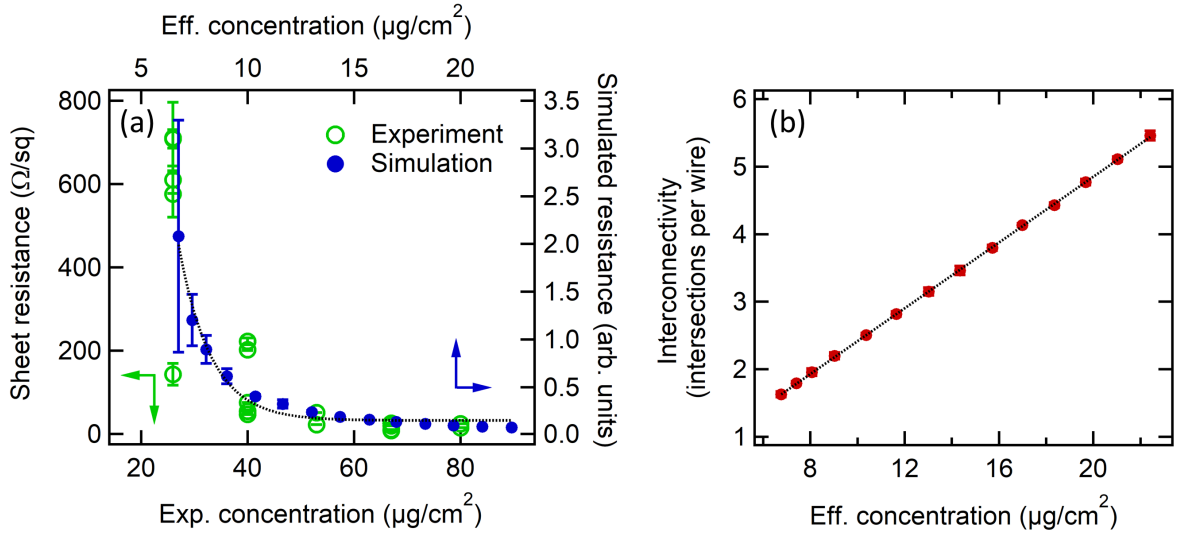

Figure 4.7: (a) Electrical resistance of Ag-NW networks as a function of nanowire concentration. The experimental data are shown in green and are plotted against the left and the bottom axis. The simulated data are shown in blue and plotted against the right and the top axis. The black dotted line denotes an exponential guide to the eye. (b) Interconnectivity as a function of nanowire concentration. The interconnectivity denotes the average number of intersections per wire. A proportionality factor of $f = (0.24242 \pm 0.000232)\,\mathrm{cm^2 \mu g^{-1}}$ was found.

4.1.6 Atmospheric Plasma Treatment of Ag-NW Networks

Plasma denotes a mixture of ions and free electrons, which is also described as ionized gas. Plasma cleaning procedures are used to clean surfaces from organic residues, waste, and contamination.[156] C. C. Wu and co-workers demonstrated the chemical modification of indium tin oxide surface layers by oxygen plasma treatment leading to drastic improvements for organic light emitting diodes.[157] Furthermore, plasma treatment is often used as pre-treatment to activate polymer, ceramic, or glass surfaces for bonding and coating.[158, 159] This versatility leads to a variety of industrial applications.[160]

Plasma treatment often takes place in chambers, which are evacuated and filled with the appropriate gas at a specific pressure for the treatment. In comparison, atmospheric plasma denotes plasma that is created in air without any vacuum and pressure control. Therefore, atmospheric plasma can be easily integrated into existing manufacturing processes. For example, the usefulness of plasma treatments for the pre-treatment of polymers in 3D printing processes have been demonstrated.[161, 162] In the past two decades, many handheld pencil-like plasma torches have been commercialized.[163, 164] They convince with their simple and flexible handling and the possibility of treating surfaces locally.

By using local atmospheric plasma treatment, the Ag-NW network morphology, chemical composition, and electrical resistance can locally be modified. In combination with the integrability of atmospheric plasma devices in printing and additive manufacturing processes, this paves the way for a printing technology with which complex electronic structures and devices can be produced in multiple dimensions. We experimentally investigated the impact of atmospheric plasma treatment on Ag-NW networks by conductivity measurements, scanning electron microscopy (SEM), *operando* granzing incidence small angle X-ray scattering (GISAXS), grazing incidence wide angle X-ray scattering (GIWAXS), and X-ray photoelectron spectroscopy (XPS).[97] In the following, the experimental results of L. O. Akinsinde *et al.* are briefly summarized. In this thesis, the electrical properties of Ag-NW networks during atmospheric plasma treatment are modeled using the Monte Carlo method presented above considering a constant plasma etching rate.

Experimental observations. Fig. 4.8 (a)-(f) show SEM images of Ag-NW networks for different atmospheric plasma treatment times.[97] The samples have been fabricated as described in section 4.1.3 with a nanowire concentration of 26 µg cm^{-2}. After the first 4 s of plasma treatment, only small changes in the nanowire shape can be observed like

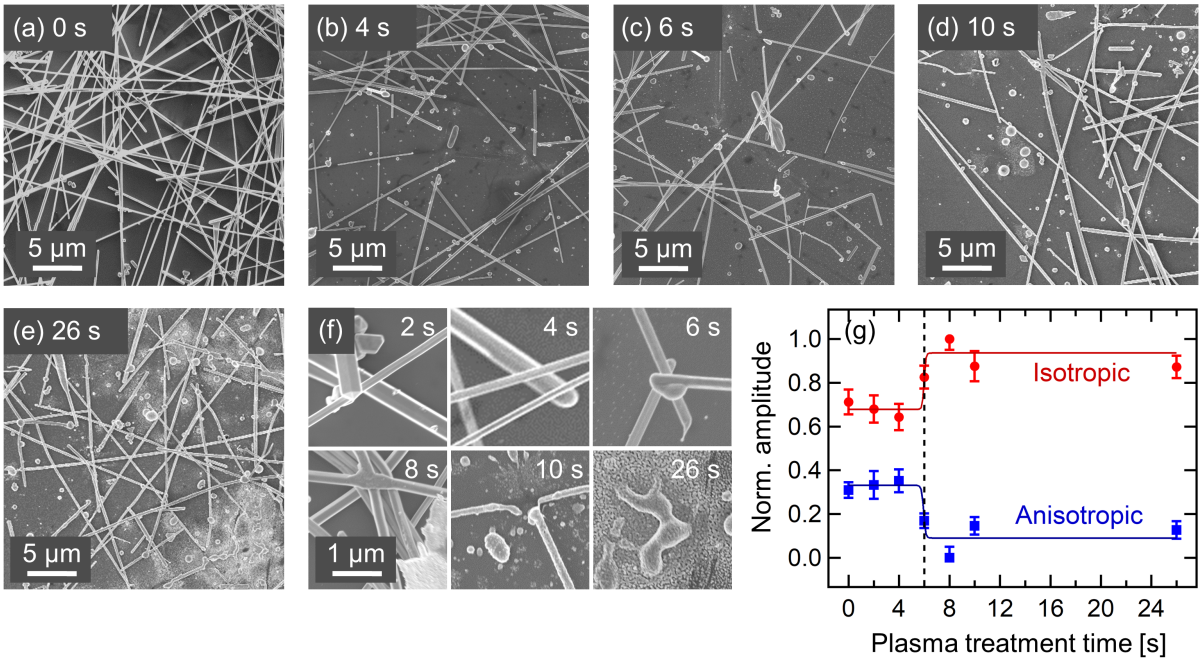

Figure 4.8: (a)-(e) Exemplary SEM images for Ag-NW networks with a concentration of 26 µg cm^{-2} after different plasma treatment times (0 s, 4 s, 6 s, 10 s, 26 s). Please not that different areas of the same sample are shown. (f) SEM images at high magnification for different plasma treatment times. (g) Normalized amplitude obtained by evaluation of the SEM images with the FINE algorithm for the isotropic fiber family (red) and the anisotropic fiber family (blue) as a function of plasma treatment time. Reprinted with permission from [97]. Copyright 2021 Elsevier.

rounding of the pentagonal tips as shown in Fig. 4.8 (f) (4 s). Longer treatment times (> 6 s) lead to fragmentation of nanowires and the formation of particle-like structures (see panel for 10 s in Fig. 4.8 (f)). After 26 s plasma treatment, large bright shaded areas are observable (see 4.8 (e)), which are characterized by fragmented and melted nanowires and debris (see panel 26 s in (f)). In order to obtain a quantitative measure for the changes in network morphology upon plasma treatment, the Fiber Image Network Evaluation (FINE) algorithm was employed.[165, 166] Based on SEM images the FINE algorithm determines the number of fiber families, their amplitudes, mean orientation, and dispersion, based on the cumulative angular orientation distribution. Nanowires contribute to an anisotropic class of fiber families. Spherical and particle-like structures are detected as an isotropic fiber family. The obtained amplitudes for isotropic and anisotropic fiber families are shown in Fig. 4.8 (g). Sigmoidal curves are used as guides to the eye. An increase in the isotropic family and a corresponding decrease in the anisotropic fiber family can be observed after 6 s plasma treatment indicating a sharp transition from small changes on the nanowire surface to drastic morphological changes due to destruction, fragmentation, and melting of nanowires.

The observed morphological changes have a strong influence on the interconnectivity of the network and, thus, on the electrical network resistance (see Fig. 4.7). The network resistance was measured in an *operando* experiment in combination with GISAXS and GIWAXS.[97] *Via* GISAXS, the Ag-NW shape can be monitored. As discussed in Fig. 4.3, the pentagonal Ag-NWs show strong intensity flares at 36° to the vertical, which stem from the reflection at the <100> facets of the nanowires.[14] *In situ* GISAXS measurements show the decrease of the flare signal with increasing plasma treatment time (see Tab. B.7 for details).[97] This can be attributed to a rounding of the nanowires in the first seconds of plasma treatment. Together with the results from SEM, an initial treatment phase (phase I) between 0 s and 6 s plasma treatment can be tracked down. In addition, the oxidation of silver (Ag) to silver oxide (Ag_2O) is observed by GIWAXS. The Bragg signal intensity for Ag_2O is increasing as a function of plasma treatment time following a sigmoidal shape. In phase I, oxidation is weak. Between 6 s and 16 s plasma treatment, a strong increase in the intensity of Ag_2O is observed. Between 16 s and 26 s, the Ag_2O intensity is saturated. This observation indicates a third phase starting at 16 s plasma treatment. XPS measurements confirm the oxidation of Ag to Ag_2O in phase II.[97] Furthermore, the transformation to AgO is detected in phase III.[97] In summary, three characteristic phases have been found for Ag-NW networks upon plasma treatment. In phase I, small morphological changes, rounding of Ag-NWs, and weak oxidation occurs. In phase II, silver is oxidized to silver oxide and fragmented and disconnected nanowires were found. phase III is characterized by the destruction of the nanowire networks and final oxidation to AgO. The resistance is depending exponentially on the plasma treatment time in the first two phases, but with different rates of resistance change upon treatment (see Fig. 4.11 (f)).[97] This makes it possible to engineer the resistance by means of atmospheric plasma treatment.

Monte Carlo simulation. During atmospheric plasma treatment, an interplay between morphological changes and oxidation processes takes place, which leads to three characteristic phases. The observed network changes result in a reduction in network interconnectivity, which is modeled in the following. Considering a constant etching rate, each nanowire exhibit an individual life time according to its thickness. The thickness distribution of the used nanowires was measured by SEM and is presented in Fig. 4.11 (a). The black solid line represents the sum of two Gaussian functions fitted to the data. A critical nanowire thickness of $r_{\mathrm{crit},i} = 0.5\, r_{0,i}$ is assumed at which the nanowire i is not conductive anymore, corresponding to a critical mass of $m_{\mathrm{crit},i} = 0.25\, m_{0,i} = 0.25\, \rho\pi r_{0,i}^2 \cdot L_i$,

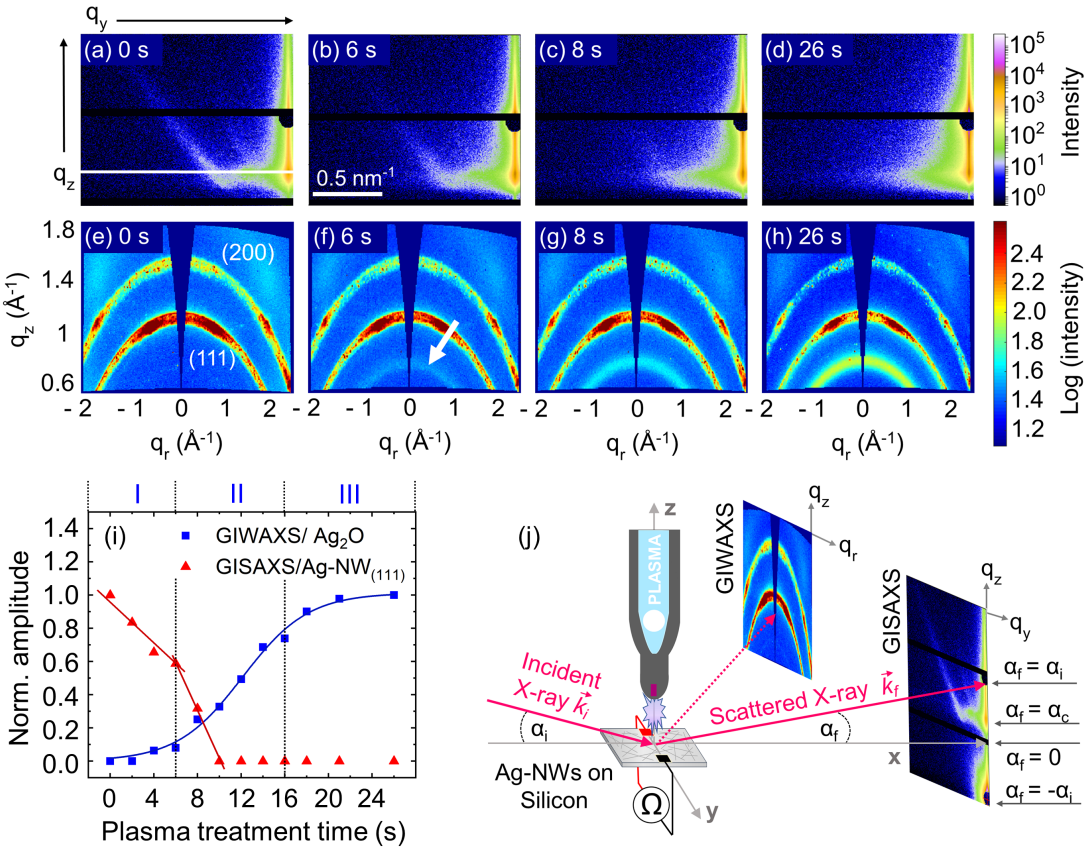

Figure 4.9: (a)-(d) GISAXS images of Ag-NW network with a concentration of 26 µg cm^{-2} for different atmospheric plasma treatment times (0 s, 6 s, 8 s, 26 s). (e)-(h) GISWAXS pattern of the same Ag-NW sample for the same plasma treatment times. (i) GISAXS flare intensity representing the pentagonal shape of the nanowires (red), and GIWAXS Ag_2O Bragg intensity (blue) as a function of plasma treatment time. Three characteristic phases are indicated by dashed lines. Phase I: 0 s - 6 s, Phase II: 6 s - 16 s, Phase III: > 16 s. (j) Schematic view on the experimental *operando* GISAXS, GIWAXS, and conductivity setup. For more experimental details see Ref. [97]. Reprinted with permission from [97]. Copyright 2021 Elsevier.

where $r_{\mathrm{crit},i}$ and $r_{0,i}$ are the critical and the initial radii of the nanowire i, respectively, and L_i is the length of the wire i. Fig. 4.10 shows an exemplary nanowire network created by the Monte Carlo method described in section 4.1.5 for different plasma etching times. Conductive wires are depicted in blue and destructed wires are shown in orange. More and more wires are switched off on a time axis from 0 s to 20 s plasma treatment.

The simulation was carried out with an effective concentration of 11 µg cm^{-2}. By calculating the network resistance and fitting the simulation results to the experimental resistance data, a constant etching rate of 570 ng s^{-1} cm^{-2} was found. For an exemplary nanowire with a length of 25 µm and a radius of 100 nm, this etching rate corresponds to $2.4 \cdot 10^9$ atoms per second. Fig. 4.11 (e) shows the normalized number of conductive wires (blue) and the normalized number of intact nanowire junctions (red) as a function of plasma treatment time. The corresponding mean network resistances during plasma

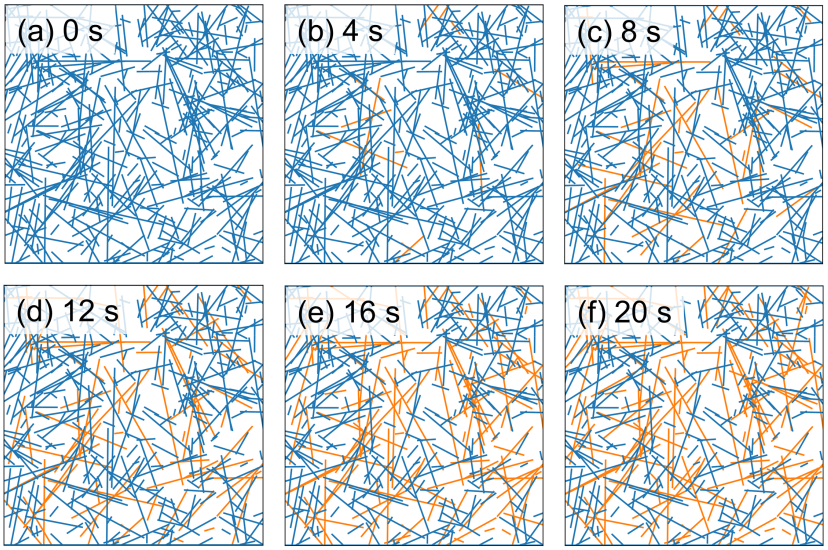

Figure 4.10: Monte Carlo simulated nanowire network for different plasma treatment times. With increasing plasma treatment time, more and more nanowires are disconnected from the network. Disconnected wires are depicted in orange.

treatment together with the experimental data are presented in Fig. 4.11 (f). The error bars denote the standard deviation obtained from five Monte Carlo simulations. The results agree in all three plasma treatment phases with the experimental data.[97] This experiment and simulation provide a basic understanding of nanowire network tuning in terms of electrical resistance as a function of network connectivity.

4.1.7 Silver-Nanowire Composites

Nancomposites are multiphase solid materials, which have one constituent that has at least one dimension in the nanometer range.[167] Nanocomposites, in general, offer a great potential as functional and advanced materials for miscellaneous applications.[168] One class of nanocomposites are polymer nanocomposites, in which a filler material with a size in the nanometer range is embedded in a polymer matrix.[169] Polymer nanocomposites are characterized by their adjustable properties, which can be attributed to the adaptability of the polymer matrix. The use of filler nanoparticles leads to a high matrix-filler interface, and enables the improvement of e.g. mechanical and optical properties, flamability resistance, thermal performance, electronic as well as membrane characteristics, and polymer blend compatibility.[170, 102] Metal nanofillers are very suitable to tune the electrical and thermal conductivity as well as optical properties.[171, 172, 173]

Printing of polymer nanocomposites in three dimensions enables the combination of the multitude of functions that composites offer with a manufacturing process that is

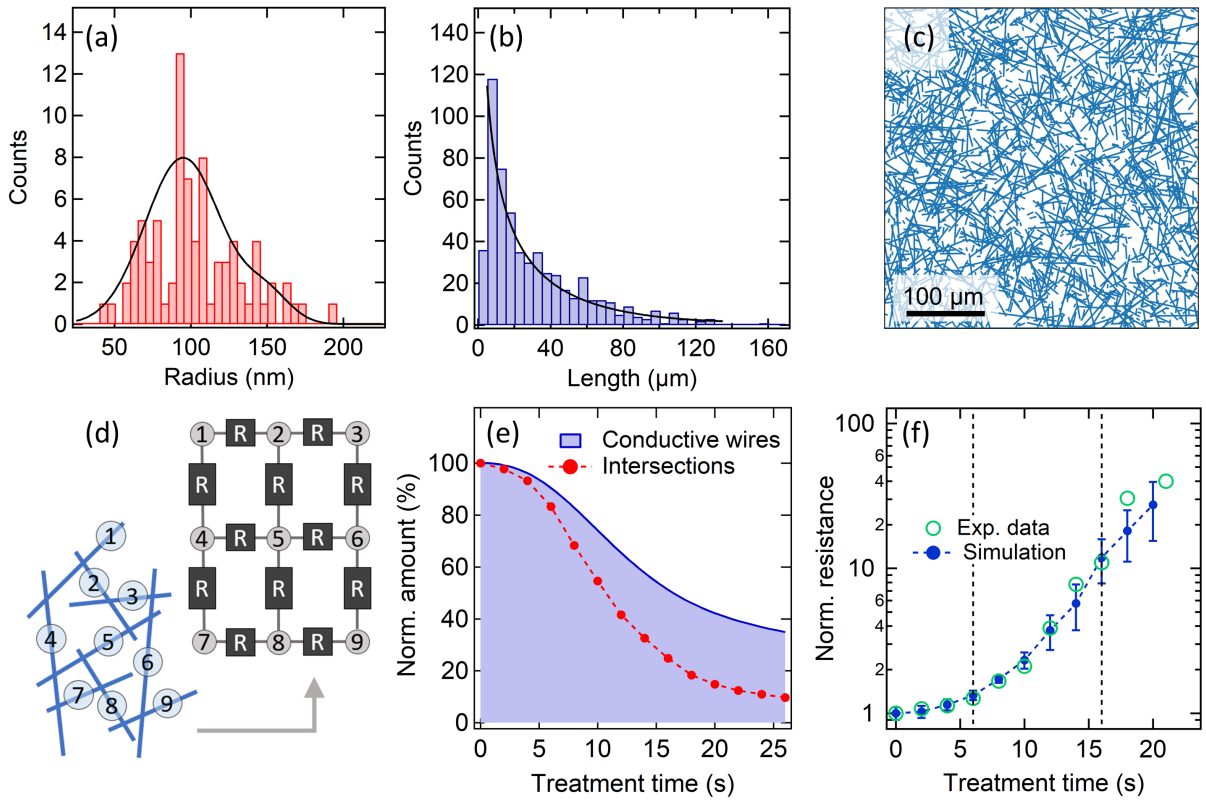

Figure 4.11: (a) Radii of 83 Ag-NWs measured by SEM. (b) Length of 564 Ag-NWs measured by SEM. (c) Exemplary Monte Carlo simulated nanowire network based on the length distribution shown in (b). (d) Schematic illustration of a nanowire network translated into a resistor network. (e) normalized number of conductive wires (blue) and intact nanowire junctions (red) as a function of plasma treatment time. (f) Normalized electrical resistance during plasma treatment. The experimental data is shown in green, the simulated results are depicted in blue. The simulation was carried out with an effective concentration of 11 µg cm^{-2}. The error bars result from five Monte Carlo simulations (n = 5). Reprinted with permission from [97]. Copyright 2021 Elsevier.

characterized by high design flexibility and rapid prototyping.[174] Additive Manufacturing (AM) starts with a 3D computer-aided design (CAD) model of the object, which should be created. The 3D model is then sliced into 2D layers, which will be printed layer by layer.[175] The AM of polymer nanocomposites holds great potential for the production of multifunctional and multidimensional objects.[176] Photopolymers are suitable as matrix material because they can be cured by illumination layer by layer in controlled shapes using e.g. a digital mirror device (DMD).[177] Photopolymers are light sensitive polymer materials, whose polymerization process is initiated by illumintion with light, mostly in the UV range. Usually, a radical or cationic initiation starts the polymerization process. This allows high control on important parameters during device fabrication like the time of polymerization and the shape of the cured area.[178]

An often used photoinitiator is phenylbis(2,4,6-trimethylbenzoyl)phosphine oxide (BAPO). BAPO derivates show a maximum absorption in the range between 365 nm and 416 nm.[179]

Illumination with UV light causes the molecule to split into two radicals. The radicals attack monomer molecules and both together form active chains, which exhibit a radical chain end. By this, the polymer chains are able to grow following the photopolymerization route.[180] Crosslinker molecules with more than one functional group can be used to cross-link the individual polymer chains and to built a network. A typical monomer is 1,6-hexanediol diacrylate (HDDA), which can be used in combination with the cross-linker dipentaerythritol penta-/hexa-acrylate (DPPHA).[181] A recipe for the HDDA-based photopolymer resin used in this work is given in Experimental Details 4.4.

Experimental Details 4.4.

Transparent Photopolymer. 3 mL (n = 0.013 mol) of 1,6-hexanediol diacrylate (HDDA, monomer) were mixed with 0.33 g (n = 0.789 mmol) phenylbis(2,4,6-trimethylbenzoyl)phosphine oxide (BAPO, initiator) and stirred at 40°C for 15 min. Subsequently, 5 mL (n = 0.011 mol) dipentaerythritol penta-/hexa-acrylate (DPPHA, cross-linker) were added and the mixture was stirred until a homogeneous resin was obtained. See also Tab. B.6.

Here, 2D nanowire networks are produced by drop casting (see section 4.1.3) and embedded in a photopolymer matrix.[14, 15, 123] For this purpose, a layer of photoresin is applied to the nanowire networks using a doctor blade. After curing with UV light, the composite sample can be peeled of the substrate. The resulting sample comprises a composite top layer with a thickness of the order of 1 µm consisting of the embedded nanowire network and a pure polymer layer underneath. Experimental details regarding the curing and coating processes are given in Experimental Details 4.5 and 4.6. By using the transparent HDDA-based photopolymer, transparent and conductive Ag-NW composites are fabricated (see section 4.1.9).[14] A flexible photopolymer (Flexible, Formlabs) is utilized to produce flexible Ag-NW electrodes (see section 4.1.8).[14, 15, 123]

Experimental Details 4.5.

Doctor Blading. Doctor blading was used to fabricate photopolymer layers with constant thickness. A blade made from aluminum was moved over the sample with a constant distance to the sample surface. For positioning and movement of sample and blade, micrometer translation stages PT1 (Thorlabs, USA) were used. The final layer thickness was evaluated by light microscopy of cross-sections of the cured layers. Layer thicknesses between 100 µm and 500 µm were fabricated in a controlled fashion. Image taken from [128].

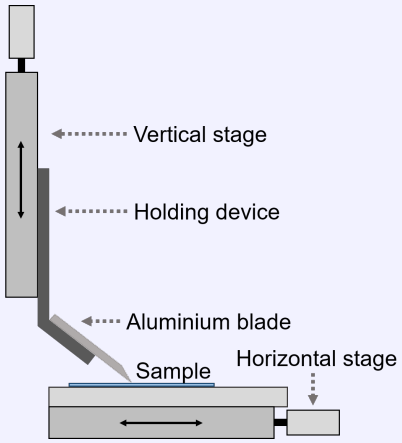

Experimental Details 4.6.

Exposure. A laser driven light source (LDLS) EQ-99X (Energetiq, USA) was used as UV light source to cure the photopolymer. The LDLS exhibit a continuous emission spectrum betweeen 170 nm and 2100 nm.[182] A homogeneous light pattern with a size of (12 × 12) mm^2 was obtained at the sample holder by the illustrated illumination setup. The samples were illuminated for 100 s at 25 mW cm^{-2}. Image taken from [128].

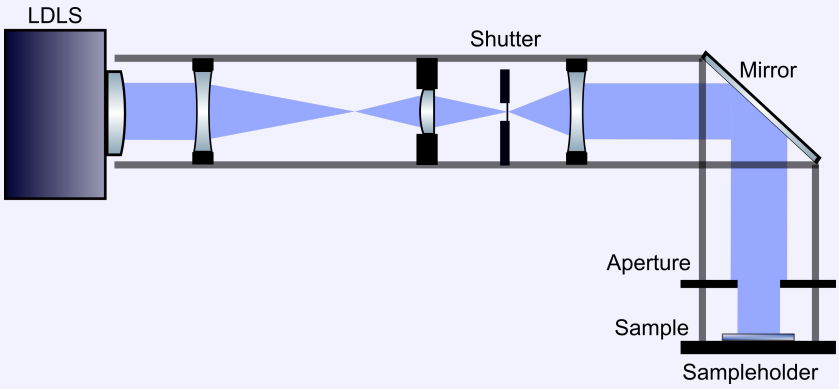

4.1.8 Stretching of Flexible Ag-NW Composites

The question of the behavior of flexible and conductive Ag-NW electrodes under mechanical strain is crucial for their applications in flexible electronics. The matrix material largely determines the mechanical properties of the composite, whereas the electrical properties of the composite are exclusively due to the Ag-NW network. The interaction between

the flexible polymer matrix and the Ag-NW network, therefore, determines how the electrical material properties change during stretching. To understand this, a combination of optical imaging measurements, their quantitative analysis, electrical measurements, and simulations of network morphology and resistance were performed and are presented in the following.[15] Furthermore, studies over several stretching cycles were carried out and the applicability of the material as a strain sensor is demonstrated in section 4.1.9.[123] This section also reports on the printing of a flexible Ag-NW capacitor and a transparent top contact.[14]

Light microscopy and resistance. A sketch of the conducted experiment is shown in Fig. 4.12 (a). A custom-made stretching setup consisting of two motorized linear translation stages is utilized (see section 3.3 for details).[100] The flexible composite samples (see section 4.1.7) are fixed with two polyimide plates, each containing two gold contacts, which enable electrical conductivity measurements in a four-point measurement mode during stretching. Of the 12 mm × 12 mm samples, an area of 3 mm × 12 mm is stretched. The samples are optically observed with a custom-made 50X light microscope (see section 3.1.1). In order to observe morphological changes within the nanowire network as well as changes in electrical conductivity during stretching, the samples are stretched step by step, while conductivity and light microscopy measurements are carried out between the stretching steps. Exemplary light microscopy images for elongations of 3 %, 13 %, and 23 % are shown in Fig. 4.12 (d)-(f). The white arrows denote the stretching direction. In Fig. 4.12 (c) a SEM image of the investigated nanowires is shown. The nanowires form a flexible network by randomly lying above and below one another without being welded or bonded. Fig. 4.12 (b) illustrates the nanowires embedded in the polymer matrix. As described in section 4.1.7, the nanowires were first dropped onto a glass substrate, and then coated with polymer resin. This fabrication process results in a nanowire composite layer that extends up to approximately 1 µm inside the sample. The total sample thickness is 150 µm.

Fig. 4.13 (a) shows the line resistance in stretching direction for three composite samples with a nanowire concentration of 40 µg cm^{-2}, 80 µg cm^{-2}, and 120 µg cm^{-2}, respectively.[15] The resistance is increasing with elongation following a sigmoidal curve for all samples. The lower the nanowire concentration, the higher the relative change in resistance. This can be attributed to the nanowire network interconnectivity, which is propotional to the network concentration (see Fig. 4.7 (b)) and which has a direct and strong influence on the network stability. Fig. 4.13 (b) shows the data presented in (a) normalized to the

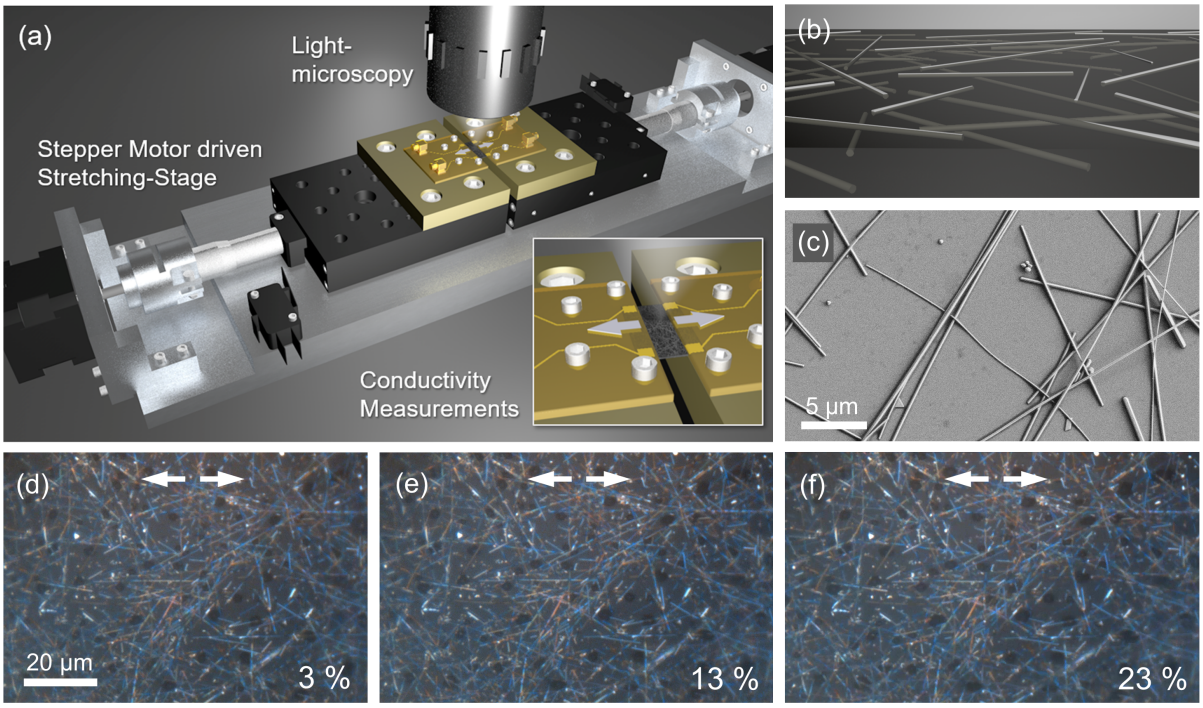

Figure 4.12: (a) Representation of the experimental setup. The flexible composite sample is electrically contacted with two polyimide boards and stretched by two motorized linear translation stages. A light microscope is installed above the sample. The inset shows the clamped sample in stretching mode. The white arrows indicate the stretching direction. Of the 12 mm × 12 mm samples, an area of 3 mm × 12 mm is stretched. (b) Sketch of nanowires embedded in a polymer matrix. (c) SEM image of nanowires forming a network. (d) - (f) Micrographs of a composite sample with a concentration of 120 µg cm^{-2} for three exemplary elongations as indicated in the figure. White arrows indicate the stretching direction. Reprinted from [15]. Licensed under CC BY-NC https://creativecommons.org/licenses/by-nc/3.0/.

resistance value at 3.33 % elongation. Since flat and even samples surfaces are necessary for microscopy studies, the samples were pre-stretched to 3.33 %. In the following, all data are normalized to this value. In order to track changes in the mean nanowire orientation, the micrographs obtained from each stretching step were analyzed by using the Fiber Image Network Evaluation (FINE)[166] algorithm. The FINE algorithm determines the number of fiber families, their orientation and distribution based on a cumulative angular distribution.[165, 166] In Fig. 4.13 (c) the Orientation Index (OI) for the three samples shown in (a) and (b) is presented as a function of elongation. For the 80 µg cm^{-2} and the 120 µg cm^{-2} samples (high concentrated samples), the OI stays constant over stretching. Only for the low concentrated sample (40 µg cm^{-2}), a slight increase in OI was detected. Overall, all measured orientations correspond to isotropic samples for all concentrations and elongations.[15]

In the following paragraph, the resistance change during stretching is modeled based on Monte Carlo simulations. The simulations lead to a physical model that considers

the interaction between the polymer matrix and the tunneling resistances at nanowire junctions.[15] We will further examine how changes in orientation of the nanowires affect the network resistance, and show that alignment effects are small compared to the experimentally observed changes in resistance.

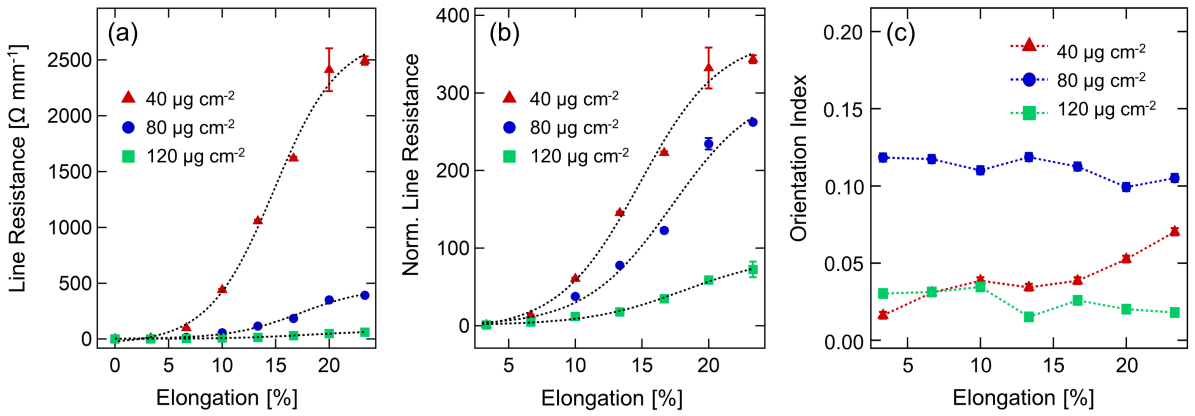

Figure 4.13: (a) Line resistance in stretching direction as a function of elongation of three samples with a Ag-NW concentration of 40 µg cm^{-2} (red), 80 µg cm^{-2} (blue), and 120 µg cm^{-2} (green). The resistance measurements were carried out after each stretching step (3.3 % relative elongation). The dashed line is a sigmoidal guide to the eye. (b) Same experimental data shown in (a) normalized to the value of the pre-stretched sample at 3.3 % elongation. (c) Orientation index of the same samples shown in (a). Adapted from [15]. Licensed under CC BY-NC https://creativecommons.org/licenses/by-nc/3.0/.

Simulation of Ag-NW networks upon mechanical strain. As reported in section 4.1.8, no remarkable alignment of the nanowires is observed during stretching. In the following, simulations are reported in order to confirm that alignment of the nanowires is not the primary effect observed in the experiment. Fig. 4.14 (a) to (d) show simulated nanowire networks with an effective nanowire concentration of 20 µg cm^{-2} and different degrees of orientation. First, an isotropic nanowire network (Fig. 4.14 (a)) is created by a Monte Carlo simulation as described in section 4.1.5. A virtual alignment of the wires during stretching is simulated by changing the x-component $\mathrm{d}x_i$ of a wire i according to the respective elongation $E_{[\%]}$ to $\mathrm{d}\tilde{x}_i = \mathrm{d}x_i \cdot (1 + E_{[\%]}/100)$. The orientation angle Θ_i is then adapted by $\cos(\Theta_i) = \mathrm{d}\tilde{x}_i / L_i$, where L_i is the length of the wire i. In accordance to the change in sample elongation, the positions of the wires are also adapted by $\tilde{x}_i = x_i \cdot (1 + E_{[\%]}/100)$. Fig. 4.14 (b) to (d) show the resulting images for 3.3 %, 13.3 %, and 23.3 % elongation. Again, the FINE algorithm[165, 166] is employed (see section 4.1.8). As demonstrated in Fig. 4.14 (e) we find two fiber families, one isotropic and one anisotropic, which is in contrast to the results from the experiment. For the isotropic network (Fig. 4.14 (a)), the amplitude of the isotropic family is 1.0 whereas the amplitude of the anisotropic family

is 0.0. The virtual alignment causes in a co-existence of the isotropic and anisotropic family with a ratio of 1:1 at 23 % strain. In Fig. 4.14 (f), the orientation index as a function of strain is shown increasing up to 0.5 for 23 % elongation. The impact of fiber alignment on the network resistance is investigated by calculating the network resistance of the simulated networks as described in section 4.1.5. Fig. 4.14 (g) shows the normalized network resistance as a function of elongation for two scenarios. Scenario I (blue) only takes into account the change in the wire position according to the sample elongation ($\tilde{x}_i = x_i \cdot (1 + E_{[\%]}/100)$), while scenario II (red) also takes into account the alignment as shown in Fig. 4.14 (a)-(d). Both only lead to an increase in resistance by a factor of between 2.2 and 2.4, which is much lower than the experimentally observed increase in resistance by a factor of around 300 (see Fig. 4.13 (b) for an experimental concentration of 80 µg cm^{-2}). This results confirm that alignment of nanowires does not lead to the observed two orders of magnitude increase in resistance, and is not the primary effect observed in the experiment.

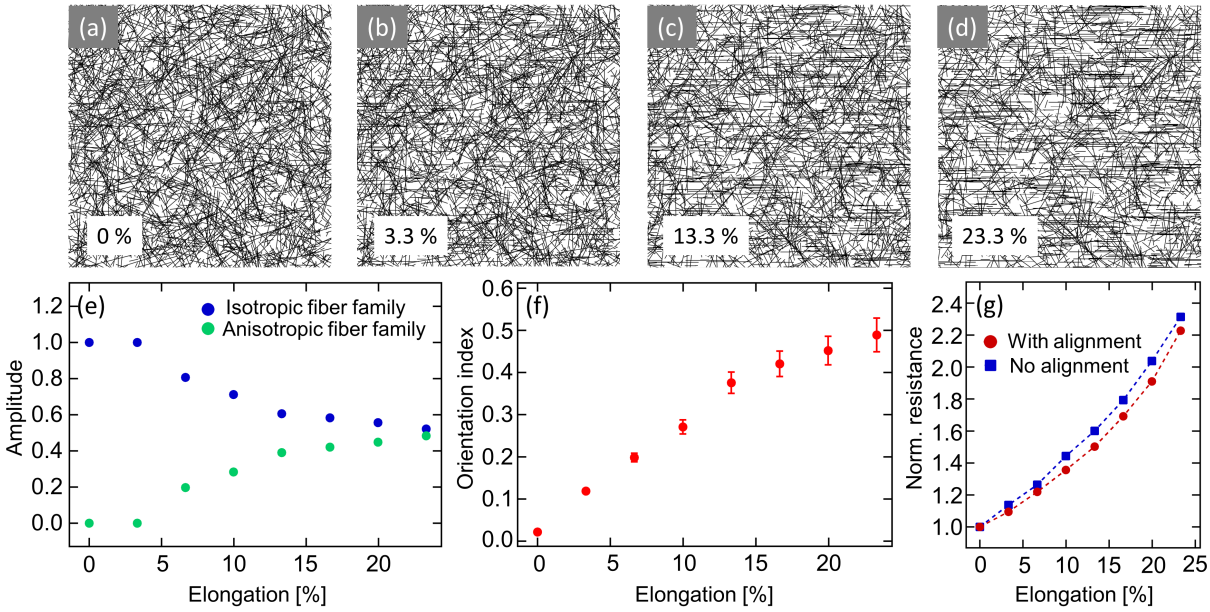

Figure 4.14: (a) Simulated nanowire network with a size of 400 µm × 400 µm, an effective nanowire concentration of 20 µg cm^{-2}, and random nanowire positions and orientations. (b)-(d) The same network shown in (a) for the exemplary virtual stretching steps. The positions and orientations of the wires change in accordance with the elongation of the stretched sample. (e) Amplitudes of the two fiber families found by the FINE algorithm. (f) Orientation index for the simulated networks. (g) Normalized network resistance during stretching of simulated networks. For the blue curve only the change in wire position during stretching was considered. For the red curve also the change in alignment was taken into account. Figure adapted from [15] (Supporting Information). Licensed under CC BY-NC https://creativecommons.org/licenses/by-nc/3.0/.

According to Hooke's Law $F = k \cdot \Delta x$[183], the local elongation Δx_{ij} at a nanowire junction ij is proportional to the force F_{ij} acting on the nanowire junction. A distribution of

local force constants within the polymer matrix is considered, determining the local elongation and, thus, the shifting of the individual nanowires during stretching. For this, we calculate the local elongation Δx_{ij} as the relative movement of the nanowires i and j $\Delta x_{ij} = |{x_i}^1 - {x_j}^1| - |{x_i}^0 - {x_j}^0|$, where ${x_{ij}}^0$ is the initial x-position of the wires i or j and ${x_{ij}}^1$ is their x-position after stretching. In agreement with other works, the cut-off distance for the tunnel current between the nanowires is taken to be 1 nm.[112, 184, 185] Different classes of local force constants can be assumed according to the chemical nature of the polymer matrix material, which serves as the force acting component. Small local force constants lead to large local elongations and, therefore, correspond to physically bonded elastomeric polymer chains (hydrogen and Van-der-Waals bonds). Large local force constants, in contrast, correspond to small local elongations, and are due to chemically bonded short polymer chain elements with less elasticity.[186] Since the nanowires are not welded, a full recovery of the nanowire junctions after relaxation of the material can be assumed.[187]

The flow chart in Fig. 4.15 demonstrates the operating principle of a program that was written to model the behavior of Ag-NW composites upon mechanical stress. In step 1, a Monte Carlo nanowire network is created as described in section 4.1.5. The necessary input parameters are denoted in blue. For creating a nanowire network, the nanowire concentration, which can be calculated by the number of nanowires and the sample size, and the length distribution of the nanowires has to be given. In step 2, the nanowire junctions are found, which represent the quantum mechanical tunneling resistances of the corresponding resistor network. To each nanowire junction a local force constant is then assigned (step 3). The force constant distribution is defined previously according to the respective physical model of the matrix. In order to calculate the electrical network resistance, the Laplace Matrix (Eq. 4.4) is created in step 4, and the resistance is calculated as defined in Eq. 4.5 (step 5). In step 6, local elongations are determined for each nanowire junction in agreement with the respective relative local force constant. If the local elongation is within the cut-off distance for the tunneling current, this junction is counted as intact (step 7). Otherwise, the junction is not counted as a network's connection. With this, the program returns to step 4, and a new Laplace Matrix is created to calculate the network resistance. This process continues until the maximum stretch is reached. As a result, simulated resistance curves are obtained from a random nanowire network during stretching.

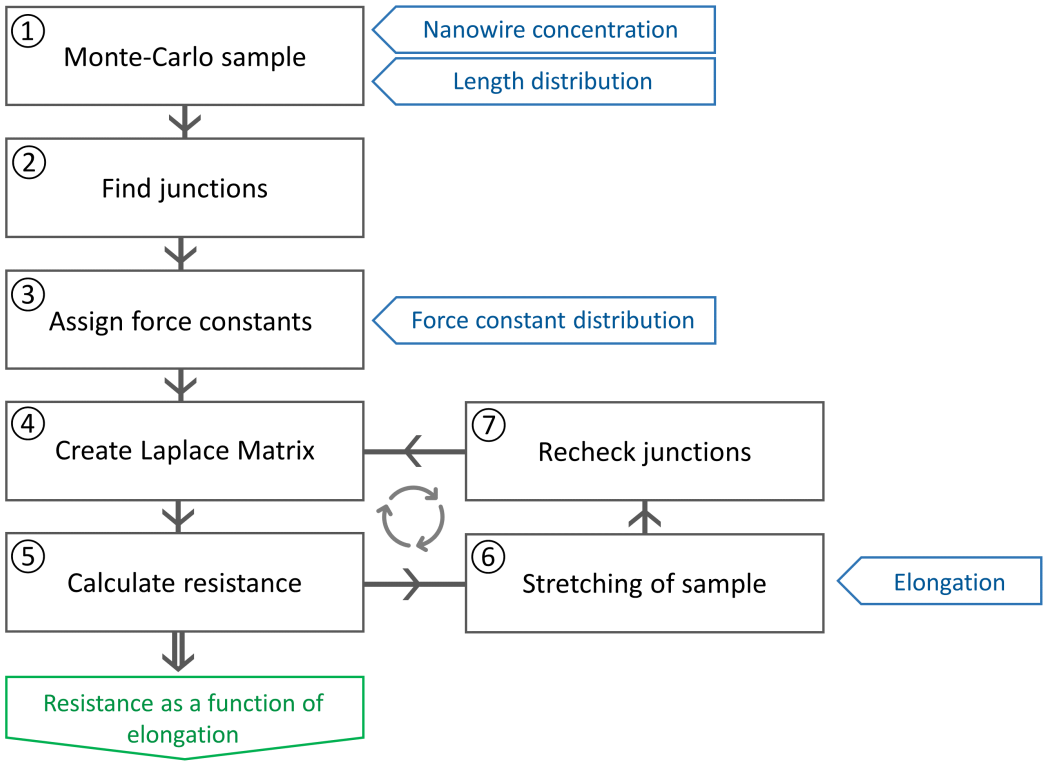

Figure 4.15: Flow chart of the conducted simulation. (1) A random nanowire network is simulated by a Monte Carlo method. The nanowire concentration as well as the length distribution are input parameters (blue). (2) The junctions between the wires are found and saved in an array that contains the two wires for each junction. (3) A critical force is assigned to each junction. A critical force distribution is given as input parameter. (4) The Laplace matrix is created. (5) The resistance is calculated according to the work of F. Y. Wu.[154] (6) The sample is stretched by a specific elongation in x-direction. The x-positions of all wires change accordingly. (7) All junctions are rechecked according to their respective force constants. The program returns to step (4).

In Fig. 4.16 (a) the experimental resistance data as a function of elongation for the $80\,\mu g\,cm^{-2}$ (orange) and the $120\,\mu g\,cm^{-2}$ sample (red) are shown. The results obtained from the Monte Carlo simulation are presented in turquoise ($c_{eff} = 18\,\mu g\,cm^{-2}$), light blue ($c_{eff} = 20\,\mu g\,cm^{-2}$), blue ($c_{eff} = 22\,\mu g\,cm^{-2}$), and dark blue ($c_{eff} = 30\,\mu g\,cm^{-2}$) by lines and markers. As mentioned in the previous sections, the effective concentration (c_{eff}) is by a factor of around 4 lower than the experimental concentration (see Fig. 4.7).[15] The blue arrow on the right shows the direction of increase in the effective nanowire concentration. The resistance for all curves is normalized to the respective value at 3.33 % elongation. For the simulation, four classes of local force constants are assumed, which are randomly assigned to the nanowire junctions of the network. The values for the relative local force constants and their incidences have been determined by fitting of the simulation results to the experimental data. In relation to the weakest class (class I = 1), the relative local force constants are: class II = 1.5, class III = 3.5, and class IV = infinity.

The corresponding incidences of the four classes are $p_{\mathrm{I}} = 75\,\%$, $p_{\mathrm{II}} = 14\,\%$, $p_{\mathrm{III}} = 4\,\%$, and $p_{\mathrm{IV}} = 7\,\%$. This corresponds to three classes of weak and physically bound polymer chain segments, which have a high degree of elasticity and can rearrange themselves in an energetically preferred position while stretching.[186] The forth class represents short and strained polymer chain segments, which are chemically bonded to their neighbors and exhibit less elasticity.[186] High local force constants $k_{ij} \to \infty$ have been chosen for this class, which lead to small local elongations $\Delta x_{ij} \to 0$. Over the observed stretching range between 0 % and 23.3 %, all junctions related to class IV remain intact. The simulated resistance curves show good agreement with the experimental data with regard to the curve shape and the concentration dependent increase in resistance. Fig. 4.16 (b) shows the number of intact junctions (left axis) and the normalized number of wires, which are not connected to the conductive network anymore (right axis), as a function of elongation. The data correspond to the simulated resistance curves illustrated in (a). We observe the number of conductive junctions within the network, which is directly correlated with the connectivity of the network, increasing linearly with the effective nanowire concentration (compare Fig. 4.7 (b)). The curves as a function of elongation are fitted by $y = y_0 + Ax^{-1.3}$, where y represents the number of junctions on the y-axis, y_0 is an offset caused mainly by the junctions assigned to class IV, A is a concentration dependent scaling factor, and x is the elongation. On the right axis of Fig. 4.16 (b), the number of wires, which do not have any conductive connection the network, are plotted. The curves are fitted by $y = y_0 + B\exp(-\alpha x)$, where y is the number of detached wires, y_0 is a constant background of 0.5, B is a concentration dependent scaling factor changing gradually from -0.6 for the lowest concentration to -0.55 for the highest concentration, and α is the decay constant changing from 0.055 for the lowest concentration to 0.025 for the highest concentration. As long as the network connectivity is high (high concentrations/low elongations), large changes in network connectivity cause small changes in network resistance. As soon as the network connectivity approaches the percolation threshold, small changes in the network lead to large changes in the resistance. This leads to a drastic stress sensitivity of the networks. We further observe a flattening of the resistance curves between 20 % and 23 % strain, which can only be explained by a class of highly durable nanowire junctions held together by the polymer matrix (class IV).

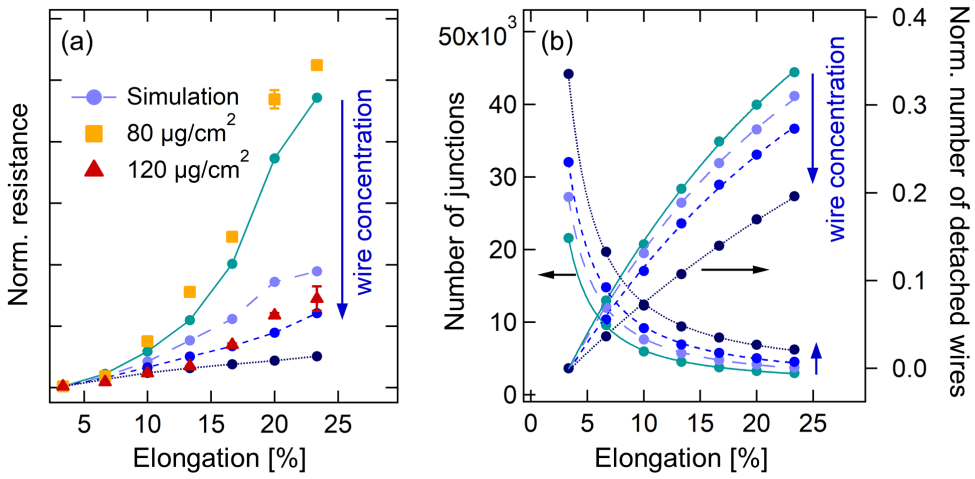

Figure 4.16: (a) Simulation of the experimental data together with the experimental data. The curves were normalized to the resistance of the pre-stretched sample at 3.3 % elongation. The simulation parameters for the critical force distribution are the relative force constants class I = 1, class II = 1.5, class III = 3.5, class IV = infinity, with their incidences $p_I = 75\,\%$, $p_{II} = 14\,\%$, $p_{III} = 4\,\%$, and $p_{IV} = 7\,\%$. The simulated effective concentrations are $18\,\mu g\,cm^{-2}$, $20\,\mu g\,cm^{-2}$, $22\,\mu g\,cm^{-2}$, and $30\,\mu g\,cm^{-2}$. The blue arrow depicts the direction of increasing concentration. (b) Number of tunneling junctions and amount of detached wires (wires without undamaged junctions to other wires) for the simulations shown in (a). The curves were fitted by $y = y_0 + Ax^{-1.3}$ (number of junctions) and $y = y_0 + B\exp(-\alpha x)$ (disconnected wires). Adapted from [15]. Licensed under CC BY-NC https://creativecommons.org/licenses/by-nc/3.0/.

4.1.9 Functional Printing Applications

Functional printing in two and three dimensions has generated great interest in recent years, and is now one of the most promising and revolutionary manufacturing techniques.[188] The smart printed devices can easily be tailored to the respective application due to rapid prototyping. Portable and flexible electronic devices can interact with the human body in a simple manner. Highly sensitive strain sensors that are attached directly to the human body are suitable for motion detection and health monitoring.[118, 189] Different kinds of modern biocompatible sensors have been reported, which are based on nanomaterial fillers and polymers as flexible and stretchable support materials.[190, 191, 192, 193] In the following, Ag-NW composites are utilized and investigated as strain sensors with tunable sensitivity to strain. The strain-resistance relation as a function of stretching cycle is modeled by a Monte Carlo method that considers the local force constant distribution within the polymer matrix as well as the tunneling resistances between the nanowires. We use the same material to print a flexible Ag-NW capacitor as a prototype for a 3D printed functional electronic device. A transparent and conductive cover layer is applied to a solar cell by introducing a transparent and rigid composite.

Composite strain sensor. In this section, the flexible Ag-NW composite studied above is utilized as printable strain sensors. The samples are fabricated as descried in section 4.1.7. Three different nanowire concentrations are reported, leading to different network sensitivities to strain: 40 µg cm^{-2}, 80 µg cm^{-2}, and 120 µg cm^{-2}.

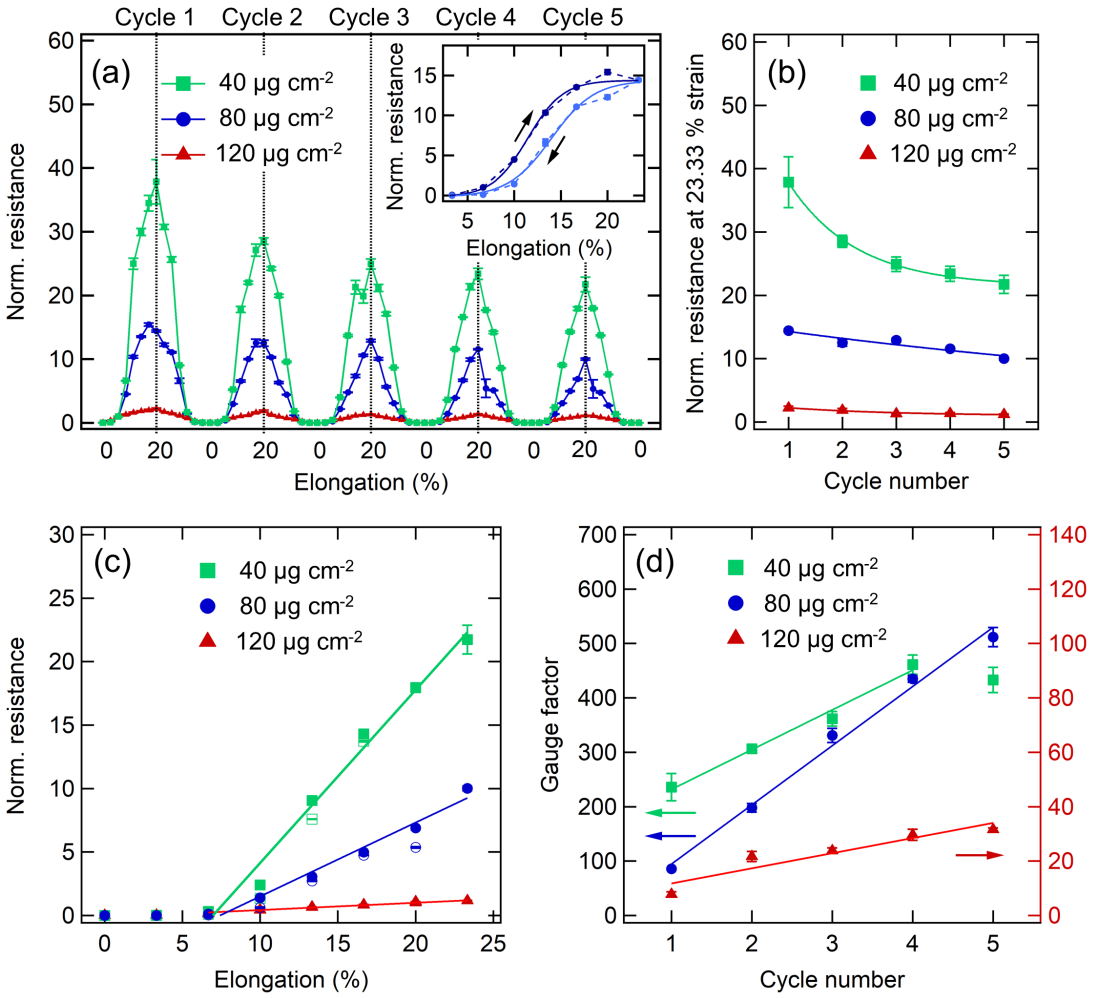

Figure 4.17: (a) Normalized line resistance in stretching direction as a function of elongation for samples with a Ag-NW concentration of 40 µg cm^{-2}, 80 µg cm^{-2}, and 120 µg cm^{-2}, respectively. The resistance was measured over 5 stretching cycles, and normalized to the pre-stretched value at 6.66 % elongation of the first cycle. The inset shows the first stretching (dark blue) and relaxation (light blue) of the 80 µg cm^{-2} sample. (b) Resistance at 23 % elongation normalized to the respective resistance at 6.66 % elongation of the first stretching cycle as a function of cycle. The data is shown for the same samples presented in (a). (c) Normalized resistance for the three investigated samples during the 5$^{\text{th}}$ stretching cycle. Data recorded during stretching is depicted with filled markers, blank points represent the resistances during relaxation. (d) Gauge factor $[(R_{23\%} - R_{6\%})/R_{6\%}]/[(L_{23\%} - L_{6\%})/L_{6\%}]$ as a function of stretching cycle. The solid lines are linear fits to the data. Figure reprinted with permission from [123]. Copyright 2021 IOP Publishing.

The samples consist of a flexible polymer layer with a thickness of 150 µm and a Ag-NW network embedded in the top side of the polymer resulting in a conductive composite top layer with a thickness of the order of 1 µm (see also section 4.1.8).[15, 100, 123] By

using the custom-made stretching setup (see section 3.3), strain-resistance measurements have been carried out for 5 stretching cycles. The normalized resistance as a function of elongation is shown in Fig. 4.17 (a). The data is normalized to the pre-stretched resistance value at 6.66 % elongation of the first stretching cycle, respectively. The lower the nanowire concentration, the larger is the relative change in resistance due to stretching, which can be attributed to a higher sensitivity of the network because of a lower network interconnectivity.[15] The inset in Fig. 4.17 (a) shows the resistance data of the 80 µg cm^{-2} sample during the first stretching cycle. A hysteresis between stretching and relaxation is reproducibly observed, in which the resistance is lower during relaxation than during stretching. Sigmoidal fits to the data are used as guides to the eye. Fig. 4.17 (b) shows the normalized resistance values at 23 % elongation as a function of stretching cycle. For all three nanowire concentrations, the resistance decreases with stretching cycle. In contrast, the gauge factor, which is an often used measure for the sensor sensitivity[189], is increasing as a function of stretching cycle as illustrated in Fig. 4.17 (d). This makes clear that the resistance for all measured elongations between 6.66 % and 23.33 % is decreasing with stretching cycle, whereas the relative resistance change is increasing. The gauge factor (GF) is defined as the slope of the change in electrical resistance or capacitance divided by the applied strain or relative change in elongation[189]

$$GF = \frac{(R - R_0)/R_0}{(L - L_0)/L_0}, \tag{4.6}$$

where R and L denote the resistance and length of the strained sample and R_0 and L_0 are the resistance and length of the unstrained sample, respectively. Nano-composite based strain sensors have been reported with a wide range of GFs. Ag-NW PDMS composites have been demonstrated having GFs between 2 and 14.[118] Crack-induced Ag-NW strain sensor with a GF of 30 at 100 % strain and nanobrush zinc-oxide nanowire polystyrene composites with a GF of 116 have been reported.[194, 195] In order to fabricate ulta-sensitive strain sensors with GFs > 1000, graphene thin films polymer composite have been used.[196] In the case of nanowire composite strain sensors, the sensitivity to strain can be tuned by the nanowire concentration.[189] In this work, GFs between 10 and 500 at 23 % strain were found depending on the nanowire concentration and stretching cycle. This covers a wide range of sensitivities from weakly to ultra-sensitive sensors.

Fig. 4.17 (c) shows the resistance data obtained during the 5$^{\text{th}}$ stretching cycle. The resistances during stretching (filled data points) and relaxation (blank data points) are

almost identical showing no hysteresis any more.[100] A linear strain-resistance relation in the so-called sensor region between 6.66 % elongation and 23.33 % elongation is found for all three nanowire concentrations.

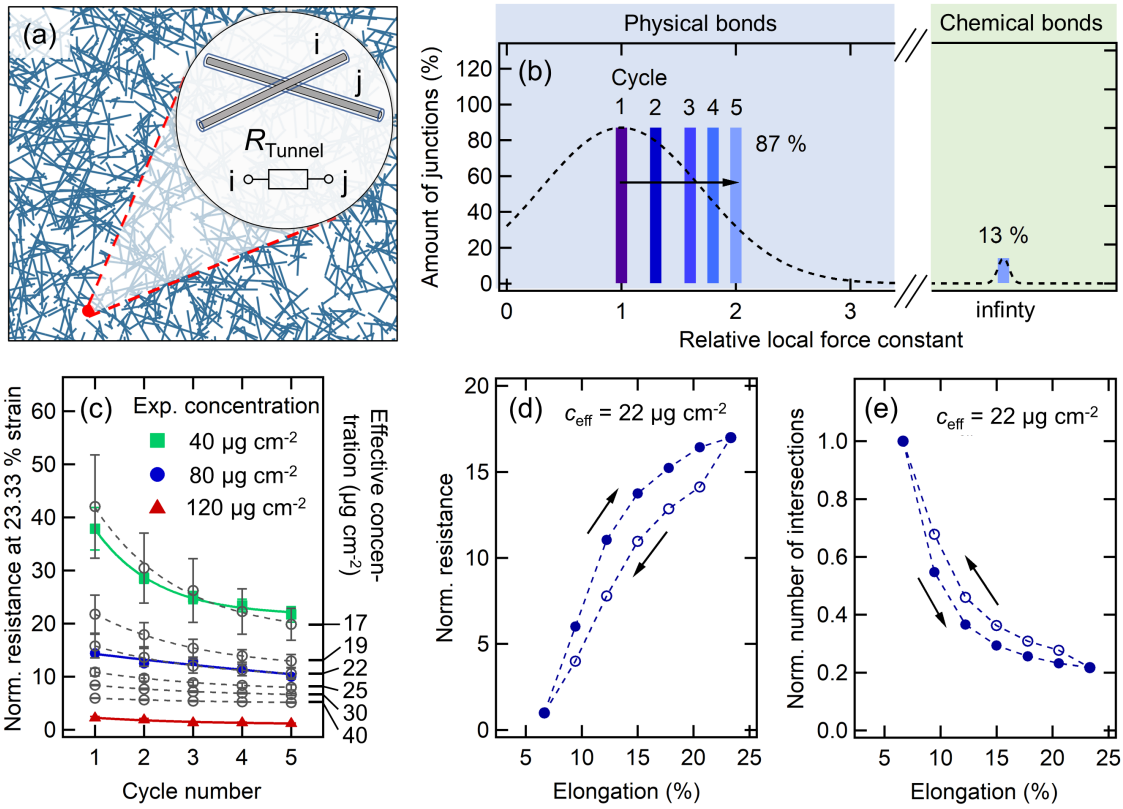

Figure 4.18: (a) Exemplary nanowire network created by a Monte Carlo simulation. The inset shows two schematic nanowires i and j forming a tunneling junction. (b) Histogram of relative local force constants within the polymer matrix used for the simulation. Physical bonds exhibit small local force constants (blue) which change with stretching cycle due to rearrangement of chain elements. Chemical bonds are characterized by large local force constants (green). (c) Experimental normalized resistances at maximum elongation (23.33 %) as a function of stretching cycle (green, blue, red) together with the results from the Monte Carlo simulation (gray). The error bars in the simulated results stem from 5 independent Monte Carlo simulations ($n = 5$). (d) Hysteresis modeled by Monte Carlo simulation for a sample with an effective concentration of 22 µg cm^{-2}. To model the resistance drop during relaxation, the mean local force constant of class I was increased by a factor of 1.5. (e) Normalized number of tunneling junctions within the network during stretching and relaxation for the same sample shown in (d). Figure reprinted with permission from [123]. Copyright 2021 IOP Publishing.

Fig. 4.18 summarized the results from a physical model based on the Monte Carlo method described in section 4.1.8. Fig. 4.18 (a) illustrates a 2D simulated nanowire network. The inset shows two intersecting nanowires i and j. The nanowire networks are translated into resistor networks, where each nanowire junction represents a tunneling resistor, and each nanowire is a node. A local force constant is assigned to each nanowire junction, which determines the local elongation at the respective position. In order to model the experimentally observed resistance behavior as a function of stretching cycle, two local force

constant classes are applied. The first class characterizes weak physical bonds between the polymer chains of the matrix, whereas the second class corresponds to the chemical bonds within the polymer network. Since, in this experiment, stretching was conducted in the elastomeric regime of the matrix material and no irreversible deformation of the material occurred, chemical bonds are assumed to stay intact, and the relative local force constant is taken to be infinity. By fitting the simulation results to the experimental data, class I is assigned to 87 % of all junctions and class II to the remaining 13 %. The observed decrease in network resistance as a function of stretching cycle can now be modeled by a re-arrangement of physically bonded polymer chains leading to an increase in the mean local force constant of class I. This is illustrated in Fig. 4.18 (b). The results obtained from the simulations are presented in Fig. 4.18 (c). The green, blue, and red curves are the experimental data (see Fig. 4.17 (b)). The simulated resistances are depicted in gray for several effective concentrations between $17\,\mu g\,cm^{-2}$ and $40\,\mu g\,cm^{-2}$. As discussed before, the effective network concentration is by a factor of about 4 lower than the experimental concentration (see Fig. 4.7 (a)).[15] Fig. 4.18 (d) shows the hysteresis observed for the first stretching cycles, simulated by the same model. The simulated effective concentration is $22\,\mu g\,cm^{-2}$, according to an experimental concentration of around $80\,\mu g\,cm^{-2}$. The hysteresis is modeled by shifting the mean local force constant of class I by a factor of 1.5 to higher values. The number of tunneling resistors within the network also behave hysteretic as shown in Fig. 4.18 (e). The results indicate that an aging of the polymer matrix due to re-arrangement of physically bonded polymer chains leads to the observed changes in resistance as a function of stretching cycle and elongation.

Transparent top contact. By using the transparent HDDA-based photopolymer (see Experimental Details 4.4 and Tab. B.6), printable and transparent electrodes are fabricated.[14] First, the influence of the polymer coating on the network morphology and resistance has been studied. The GISAXS pattern of the uncoated Ag-NW network on silicon is shown in Fig. 4.19 (a), as it was also discussed in section 4.1.3. A bare HDDA polymer layer on silicon results in a GISAXS pattern as shown in Fig. 4.19 (b) without any horizontal scattering features. Fig. 4.19 (c) shows the result obtained from a Ag-NW polymer composite with a concentration of $7\,\mu g\,cm^{-2}$. We can clearly observe the same intensity flares at 36° to the vertical as for the bare Ag-NW network, stemming from the pentagonal nanowire structure. Horizontal cuts at $q_{z1} = 0.63\,nm^{-1}$, $q_{z2} = 0.78\,nm^{-1}$, and $q_{z3} = 0.96\,nm^{-1}$ for the three samples are presented in Fig. 4.19 (d), (e), and (f).[14] The

intensity peak stemming from the pentagonal nanowire shape is highlighted by arrows. The shift on the q_y axis corresponds to the facet angle.[128] The polymer coating results in a decreased scattering contrast with regard to the Ag-NW contribution in the composite. See Tab. B.7 in the appendix for measurement parameters.

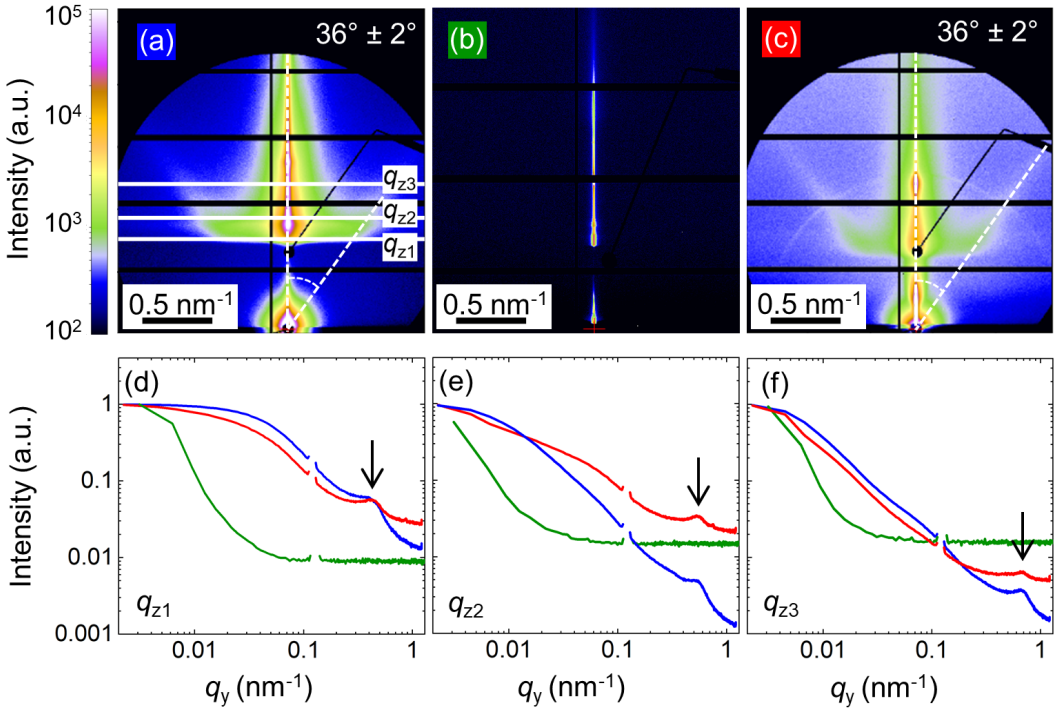

Figure 4.19: (a) 2D GISAXS pattern from Ag-NWs on silicon (58 µg cm^{-2}). See also Fig. 4.3. (b) Bare UV-cured HDDA polymer on a silicon substrate. (c) Ag-NWs (7 µg cm^{-2}) coated with the UV-cured HDDA polymer layer. The intensity scale bar is shown on the left side. Intensity flares at 36° ± 2° are indicated by dashed lines in (a) and (c). (d) Horizontal cuts of the intensity ($I(q_y, q_{z1} = 0.63\,\text{nm}^{-1})$), (h) $I(q_y, q_{z2} = 0.78\,\text{nm}^{-1})$, (i) $I(q_y, q_{z3} = 0.96\,\text{nm}^{-1})$. All cuts are normalized to the intensity at $I(0, q_{z1,2,3})$, correspondingly. The color code corresponds to the colors indicated in (a) to (c). Intensity flares are highlighted by black arrows. Adapted from [14]. Licensed under CC BY, https://creativecommons.org/licenses/by/4.0/.

It is known, that the photoresin shrinks during photocuring.[197] The sheet resistances (see section 3.3 and appendix A) for the three Ag-NW concentrations 26 µg cm^{-2}, 39 µg cm^{-2}, and 65 µg cm^{-2} are shown in Fig. 4.20 (a). For each concentration, three samples are presented, which show different resistances due to statistical deviations. The same samples have been coated with HDDA photoresin and cured by illumination with UV light (see Experimental Details 4.6). After curing, the sheet resistance of all samples is reduced (red data points) due to compression of the Ag-NW networks by the polymer. This is in agreement with our simulation model (see section 4.1.8) based on Hooke's law determining the tunneling distance, which directly influences the network resistance. We further investigate the optical transmission through the Ag-NW networks and composites as illustrated in Fig. 4.20 (b) (see also appendix A). The spectra were corrected by

the transmission through the used glass substrate. Solid lines represent the pure Ag-NW networks as well as the pure polymer. Dashed lines depict the corresponding Ag-NW composites for nanowire concentrations of 26 µg cm^{-2}, 39 µg cm^{-2}, and 65 µg cm^{-2}, respectively. An increased transmission for the composites compared to the bare Ag-NW networks with the same concentration can be observed between 600 nm and 900 nm. Also, the pure polymer layer shows a transmission higher than 100 % in this spectral range. We attribute this effect to a better refractive index matching of the polymer compared to the glass substrate. In Fig. 4.20 (c) layer thickness and mean surface roughness of the HDDA-based samples are presented as determined by profilometry (see appendix A). The three samples are a pure polymer layer, a Ag-NW composite and a polymer - Ag-NW - polymer multilayer structure. The surface roughness is between 110 nm and 160 nm for the composite materials, which is primarily determined by the roughness of the polymer. For all samples, we obtain a thickness to roughness ratio of about 1000.

For the purpose of transparent and conductive printable layers, the influence of a Ag-NW coating, a polymer coating, and a Ag-NW-polymer composite top layer on the functionality of a solar cell was investigated. Photographs and micrographs of the solar panels are shown in Fig. 4.20 (d)-(g). The coated solar cells are exposed with an Ulbricht sphere of calibrated spectral characteristics (DKD, Gigahertz Optik) and the obtained photocurrent is indicated in the figure. For the blank solar cell, as reference, a current of (650 ± 3) µA was measured. A Ag-NW coating with a nanowire concentration of 26 µg cm^{-2} results in a decrease of the current to (613 ± 3) µA. The polymer coating leads to almost no decrease in transmission and a current of (649 ± 3) µA can be obtained. The application of a composite consisting of a Ag-NW layer coated with polymer results in a current of (626 ± 3) µA. Overall, the use of a Ag-NW-polymer electrode on top of the solar cell results in a 4 % decrease of the measured current. This corresponds to a transmission of about 95 %, which is in agreement with the transmission measurements for the composites presented in Fig. 4.20 (b).[14] The sheet resistance of the applied Ag-NW network was determined to be $(75.2 \pm 1.7)\,\Omega$/sq and of the composite $(63.0 \pm 3.5)\,\Omega$/sq. Again, the polymer coating results in an decrease in sheet resistance due to compression of the nanowire network as also shown in Fig. 4.20 (a) and as expected by our models.

Flexible capacitor. Fig. 4.21 (a) shows a schematic view on the cross section of a printed flexible Ag-NW capacitor consisting of two conductive Ag-NW composite layers and an insulating polymer layer in between.[14] A photograph of the capacitor is shown in

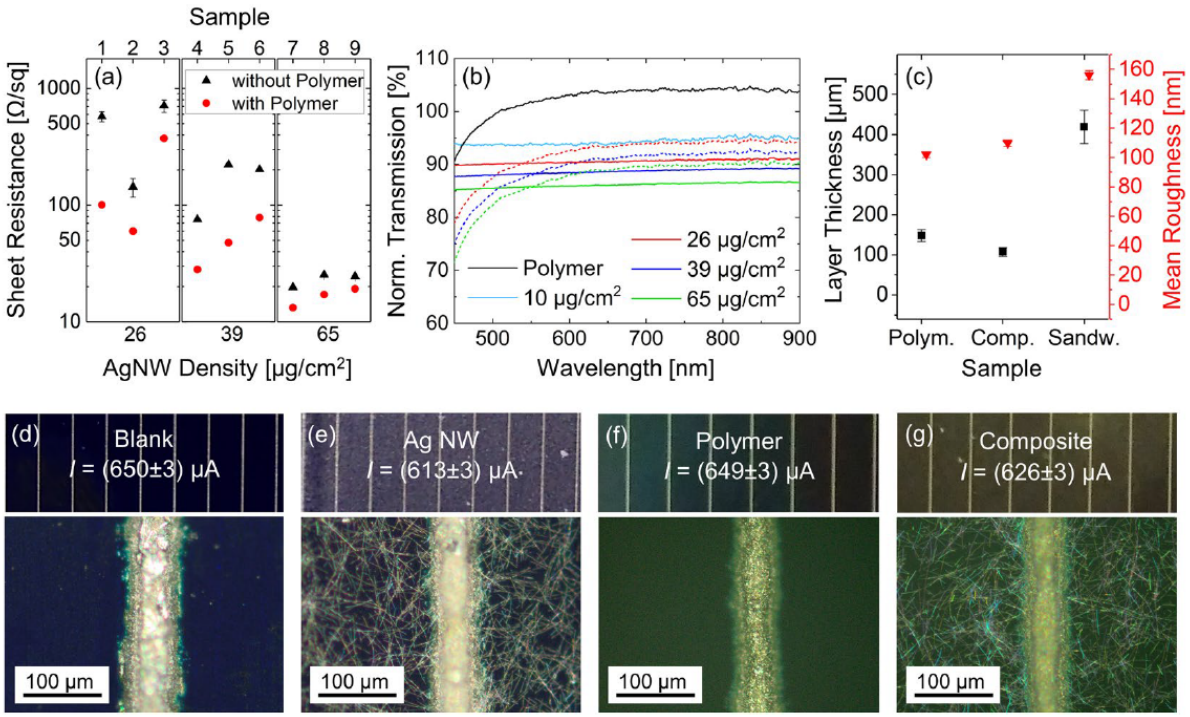

Figure 4.20: (a) Sheet resistance of Ag-NW networks with nanowire concentrations of 26 µg cm^{-2}, 39 µg cm^{-2}, and 65 µg cm^{-2}. For each concentration, three samples were measured, showing different sheet resistances due to statistical deviations. All samples were measured before (black) and after coating with a transparent HDDA-photopolymer resin (red). The sheet resistance is decreasing for all samples after curing of the polymer with UV-light. (b) Optical transmission measured through Ag-NW networks and HDDA-composites deposited on glass substrates. The spectra are corrected by the transmission through the pure glass substrate. The solid lines depict the pure Ag-NW networks and the pure polymer. The dashed lines represent the corresponding composite samples. (c) Layer thickness and mean surface roughness for a pure HDDA photopolymer layer, a composite sample and a polymer-Ag-NW-polymer sandwich sample. (d)-(g) Photographs (top) and micrographs (bottom) of a (d) blank solar cell, (e) a solar cell coated with Ag-NWs (26 µg cm^{-2}), (f) a solar cell coated with HDDA photopolymer, and (g) a solar cell coated with a Ag-NW composite (26 µg cm^{-2}). The respective photocurrents obtained from the samples are given in the upper part of the images. Reprinted from [14]. Licensed under CC BY, https://creativecommons.org/licenses/by/4.0/.

Fig. 4.21 (b). In order to demonstrate its flexibility, the capacitor was bent over a glass rod as shown in Fig. 4.21 (c). The layer thickness of the intermediate polymer layer is (210 ± 5) µm. Fig. 4.21 (d) presents a cross-sectional microscopic view of the intermediate polymer layer with embedded Ag-NWs at the surface. The capacitance of the device can be estimated according to

$$C = \epsilon_r \epsilon_0 \cdot \frac{A}{d} \tag{4.7}$$

where ϵ_r is the vacuum permittivity, ϵ_r is the polymer permittivity, A is the area of the capacitor, and d is the thickness of the insulating intermediate layer.[198] A dielectric

constant of about 4.5 results in an estimated capacitance of 5 pF. In good agreement with the calculation, a capacitance of 7.0 pF and 7.5 pF was measured at 1 kHz and at 100 kHz, respectively.[14] Details on the measurement are given in appendix A.

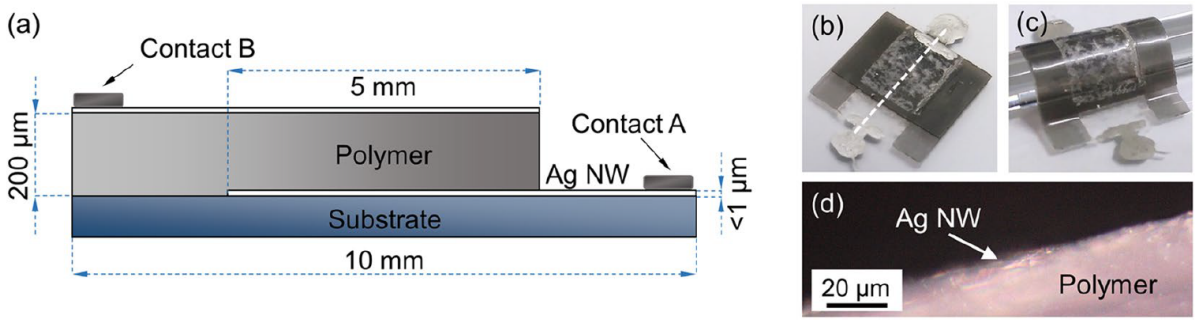

Figure 4.21: (a) Schematic cross-section of the printed and flexible Ag-NW capacitor. The capacitor was printed on top of a glass substrate, and consist of a Ag-NW layer, an insulation polymer layer, and a second Ag-NW layer on top. (b) Photograph of the capacitor with a total size of (10 × 10) mm^2. (c) Ag-NW capacitor bend over a glass rod. (d) Micrograph of a cross-section of the capacitor (see dashed line in (b)) with the Ag-NWs embedded in the polymer. Reprinted from [14]. Licensed under CC BY, https://creativecommons.org/licenses/by/4.0/.

4.1.10 Summary

Networks and composite materials made of silver nanowires (Ag-NWs) were produced and investigated in detail with regard to their application for 3D printing and flexible electronics. The material can be easily manufactured and designed, and is suitable for additive manufacturing. The pure Ag-NW networks have been fabricated by drop casting of a Ag-NW suspension. Due to high mean aspect ratios of the nanowires between 90 and 200, the percolation threshold is low (around 20 µg cm^{-2})[14], and only small amounts of silver are needed to create conductive networks. This makes the process highly efficient, and also enables the electrodes to be transparent. At an optical transmission of 86 %, sheet resistances of $(17.5 \pm 8.1)\,\Omega$/sq were found for networks with a nanowire concentration of 65 µg cm^{-2}.[14] The transmission depends linearly on the nanowire concentration, whereas the network resistance shows an exponential dependency on the concentration, becoming infinity at the percolation threshold. Grazing incidence small angle X-ray scattering (GISAXS) and scanning electron microscopy (SEM) show that the morphology of the randomly oriented nanowires within the network is pentagonal.[14] Furthermore, during synthesis, a shell of polyvinylpyrrolidone (PVP) is formed around the nanowires as a protecting ligand shell.[129, 125] This insulating shell leads to a substantial tunneling current between intersecting nanowires. Using the Monte Carlo method, a model is developed that

describes the properties of the electrical network based on the tunnel resistances between the nanowires. For this, resistor networks are created by random positioning and alignment of virtual nanowires resulting in an exponential dependence of the electrical network resistance on the concentration as also observed in the experiment. The interconnectivity of the networks was found to be a key parameter determining the electrical properties.[15]

In order to develop a post-treatment to modify the electrical network properties, atmospheric plasma treatment was applied.[97] Local etching by atmospheric plasma treatment leads to morphological and chemical changes within the nanowire network, reducing the network interconnectivity. The electrical resistance was tuned over three phases up to a factor of 40. A model that is based on the same Monte Carlo method used before describes plasma etching by considering the individual life times of the nanowires during etching based on their thicknesses. A constant plasma etching rate of $570\,\mathrm{ng\,s^{-1}\,cm^{-2}}$ was found, fitting to the experimental resistance data.[97]

To implement functional devices, a matrix is required that contains and supports the network. Silver-nanowire photopolymer composites were fabricated by embedding a drop-casted 2D nanowire network inside a polymer matrix. The nanowire networks were coated with polymer by doctor blading resulting in 150 µm thick samples with a 1 µm thick composite top layer. Different polymer matrix materials with different mechanical and optical properties were utilized. A flexible polymer matrix leads to stretchable and flexible electronic devices and sensors.[14, 15] A transparent polymer matrix enables the production of transparent and conductive top layers.[14] The flexible composite properties upon mechanical stress were investigated by stretching the composites with a custom-made stretching setup, including four-point resistance measurements and light microscopy.[15] The network resistance in stretching direction increases by a factor of up to 350 at an elongation of 23 % strain, depending on the nanowire concentration. The resistance as a function of elongation follows a sigmoidal curve. We found, that the nanowire orientation within the matrix stays constant during stretching, and no alignment or formation of anisotropy was detected.[15] For this, the obtained micrographs during stretching were analyzed by the FINE algorithm.[165, 166] A physical model based on the Monte Carlo method was derived reproducing the experimentally observed resistance change upon stretching. The model considers a local distribution of force constants within the polymer as well as the tunneling resistances between the nanowires dominating the network resistance.[15] The change in network resistance according to the sensitivity to strain can be tuned by means of the network concentration. We use one-dimensional nanostructures that form two-dimensional

networks without welding of the nanowires. This technique results in flexible networks with excellent sensor properties. A Ag-NW strain sensor was studied over 5 stretching cycles. A hysteresis between the resistances measured during stretching and relaxation was observed, which vanishes completely after the 4^{th} cycle. In the 5^{th} cycle, linear strain-resistance relations occur, the slopes of which depend on the nanowire concentration. Gauge factors between 10 and 500 were obtained depending on the nanowire concentration and stretching cycle. Furthermore, a resistance decrease as a function of stretching cycle was observed and modeled by using the Monte Carlo method. Our model takes into account an increase in the mean local force constants of weakly physically bonded polymer chains, according to a re-arrangement of physically bound polymer chains due to stretching. Finally, the same material was used to print a flexible Ag-NW capacitor by a layer by layer method. This flexible capacitor with a capacitance of 7 pF serves as a prototype for 3D printed flexible electronic devices based on Ag-NW photopolymer composites.

In this work, the production of a silver-nanowire composite material, the tuning of its electrical and optical properties as well as its applicability with regard to 3D printing and flexible electronics were investigated. In agreement with the experimental data, a physical simulation model was developed, which provides deep understanding for different modifications of the electrical nanowire network properties like change in nanowire concentration, atmospheric plasma etching, and the application of mechanical strain. The following publications are attached to this chapter:

(I) Akinsinde, L. O. *et al.* Surface Characterization and Resistance Changes of Silver-Nanowire Networks upon Atmospheric Plasma Treatment. *Applied Surface Science* **2021**, 550, 1493262.

(II) Glier, T. E. *et al.* Electrical and Network Properties of Flexible Silver-Nanowire Composite Electrodes under Mechanical Stain. *Nanoscale* **2020**, 20, 23831-23837.

(III) Glier, T.E. & Betker, M. *et al.* Conductance-Strain Behavior in Silver-Nanowire Composites: Network Properties of a Tunable Strain Sensor. *Nanotechnology* **2021**, 32, 365701.

(IV) Glier, T. E. *et al.* Functional Printing of Conductive Silver-Nanowire Photopolymer Composites. *Scientific Reports* **2019**, 9, 6465.

4.1.11 Outlook

Networks of 1D structures offer great advantages, as individual nanowires can be produced in large quantities using e.g. wet chemical processes, and the networks finally formed in the composite enable a minimum material density with maximum crosslinking, surface coverage, and sheet functionality. Polymer nanowire composites exhibit a large number of possible modifications leading to different functionalities. For example, the network orientation and morphology can be varied. With the aim of ease of manufacture, printability, scale up, and isotropic surfaces, we created random networks. Aligned nanowire arrays and networks offer further potential for specific applications and customized electrical anisotropy.[199] However, the controlled alignment of individual nanowires is a challenge for printing processes. As demonstrated in this thesis, the polymer matrix is interchangeable leading to different mechanical and optical properties. It also interacts in a relevant manner with the effective filler network. On the other hand, the targeted replacement of the nano-filler is particularly promising. The use of a combination of different functional fillers in a layer by layer printing process results in multifunctional materials. For example, composites of semiconducting nanowires can be used for light sensors.[200] The 3D printing p- and n-doped nanowire composite layers is a promising technology towards printed solar cells.[201, 202] Flexible and 3D printed thermoelectric nanogenerator are also subject of nanowire composite research.[203] In general, for various future printed smart electronic devices Ag-NW composites represent a versatile conductive and transparent building block.

With these multifunctional applications in mind, we place a number of requirements on the printing technology. In the past, the processing of nano-composites *via* stereolithography has been reported several times.[204, 205] In most cases, however, stereolithography is not considered a suitable method for making multifunctional parts, because the use of multiple materials leads to contamination of the individual components.[206] Inkjet printing, in comparison, is a material-friendly technology, with which different materials can be printed in one process.[207] However, the physical properties of the ink used, in particular its viscosity and surface tension, must be adapted to the printing process. Furthermore, in the case of nanocomposites, the risk of agglomeration and blockage of the nozzles is high. A future technology, which enables the combination of different filler particles with one polymer matrix in a precise layer by layer printing process would lead to a new era of printing technology.

4.1.12 Publications

Surface Characterization and Resistance Changes of Silver-Nanowire Networks upon Atmospheric Plasma Treatment

Lewis O. Akinsinde*, Tomke E. Glier*, Matthias Schwartzkopf*, Marie Betker, Matz Nissen, Maximilian Witte, Sarah Scheitz, Christian Nweze, Benjamin Grimm-Lebsanft, Marc Gensch, Andrei Chumakov, Ivan Baev, Ulrich Schürmann, Torben Dankwort, Frank Fischer, Michael Martins, Stephan V. Roth, Lorenz Kienle, and Michael Rübhausen*

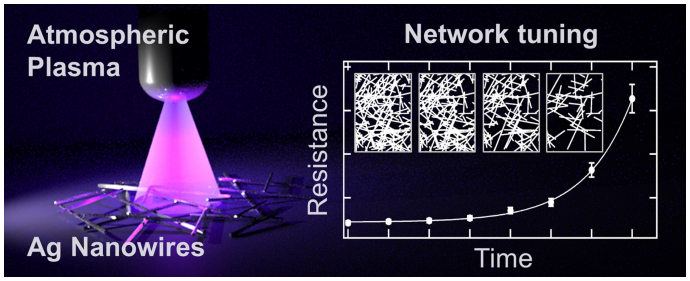

Applied Surface Science - **June 2021**
https://doi.org/10.1016/j.apsusc.2021.149362

Applied Surface Science 550 (2021) 149362

Contents lists available at ScienceDirect

Applied Surface Science

journal homepage: www.elsevier.com/locate/apsusc

Full Length Article

Surface characterization and resistance changes of silver-nanowire networks upon atmospheric plasma treatment

Lewis O. Akinsinde [a,e,*], Tomke E. Glier [a,*], Matthias Schwartzkopf [c,*], Marie Betker [a,c], Matz Nissen [b], Maximilian Witte [d], Sarah Scheitz [a], Christian Nweze [a], Benjamin Grimm-Lebsanft [a], Marc Gensch [c], Andrei Chumakov [c], Ivan Baev [b], Ulrich Schürmann [e], Torben Dankwort [e], Frank Fischer [d], Michael Martins [b], Stephan V. Roth [c,f], Lorenz Kienle [e], Michael Rübhausen [a,*]

[a] Institute for Nanostructures and Solid-State Physics, Center for Free-Electron Laser Science (CFEL), Universität Hamburg, Luruper Chaussee 149, D-22761 Hamburg, Germany
[b] Institute for Experimental Physics, Center for Free-Electron Laser Science (CFEL), Universität Hamburg, Luruper Chaussee 149, D-22761 Hamburg, Germany
[c] Deutsches Elektronen-Synchrotron (DESY), Notkestr. 85, D-22607 Hamburg, Germany
[d] Beiersdorf AG, Unnastraße 48, 20245 Hamburg, Germany
[e] Institute for Materials Science, Kiel University, Kaiserstr.2, D-24143 Kiel, Germany
[f] KTH Royal Institute of Technology, Teknikringen 56-58, SE-100 44 Stockholm, Germany

ARTICLE INFO

Keywords:
Silver nanowire networks
Atmospheric plasma treatment
Crystallinity
In situ X-ray scattering
Monte Carlo simulation
Resistance

ABSTRACT

Highly conductive silver-nanowire (Ag-NW) networks are used in composite materials as conductive channels. Their resistance tuning can be accomplished by changing the Ag-NW concentration, and, therefore, changing the network structure. In this study, an alternative pathway to resistance engineering of conductive Ag-NW networks by local atmospheric plasma treatment is employed. The corresponding changes in nanowire network morphology and crystallinity as a function of plasma etching time are investigated by time-resolved grazing-incidence X-ray scattering, field-effect scanning electron microscopy, and X-ray photoelectron spectroscopy. Three characteristic etching phases are identified. The first two phases enable the controlled engineering of the electrical properties with different rates of resistance change, which results from changes in nanowire shape, network morphology, and different oxidation rates. Phase III is characterized by pronounced fragmentation and destruction of the Ag-NW networks. These results show the feasibility of atmospheric plasma treatments to tune the local electrical properties of conductive Ag-NW networks. Furthermore, we present a physical Monte Carlo model explaining the electrical network properties as a function of plasma etching time based on the network connectivity and a constant plasma etching rate of 570 ng s^{-1} cm^{-2}.

1. Introduction

Nanoparticles and nanowires in metal-polymer composite films have interesting and fascinating physical properties [1–4]. Their outstanding material elasticity, high durability, controllable size, and shapes contribute to their uniqueness [2,5]. The optimization of their synthesis as well as their characterization are highly important to tailor their electrical properties in a controlled fashion. Conductive electrodes consisting of nanowire network composites are used in enhancing the performance of organic light-emitting diodes (OLEDs), solar cells, memory devices, sensors, touch screen devices and opto-electronics [6–14]. In addition, nanowire composites with a printable polymer matrix enable additive manufacturing and, therefore, high design flexibility and rapid prototyping [15]. By using a flexible polymer, flexible and bendable electrodes can be fabricated [15,16]. They represent a competitive counterpart to the existing materials of choice comprising mainly of indium tin oxide (ITO) or doped compounds of tin oxide [6,7], due to their attractive material properties including mechanical flexibility, low sheet resistance, and high optical transparency.

Networks made of silver-nanowires (Ag-NWs) with a well-defined

* Corresponding authors.
E-mail addresses: lakinsin@physnet.uni-hamburg.de (L.O. Akinsinde), tglier@physnet.uni-hamburg.de (T.E. Glier), matthias.schwartzkopf@desy.de (M. Schwartzkopf), ruebhausen@physnet.uni-hamburg.de (M. Rübhausen).

https://doi.org/10.1016/j.apsusc.2021.149362
Received 21 December 2020; Received in revised form 18 February 2021; Accepted 18 February 2021
Available online 25 February 2021

shape, morphology, good crystallinity, and high aspect ratios (length to diameter ratio) of up to 1000 are excellent candidates for modern composite materials with tailored electrical properties [17–19]. Bulk silver exhibits a high electrical and thermal conductivity at room temperature [5,18]. Several publications have highlighted the fabrication of large scale Ag-NW networks by adopting simple and cost-effective chemical methods [17,19–24]. Recent publications show continuous improvements in the optimization of Ag-NW networks and transparent electrodes [13–15,25]. Also, current research focuses on the modification and tailoring of the electrical properties of Ag-NW networks using various techniques such as high-temperature thermal annealing [26], induced current flow [13], washing with solvents [15], mechanical pressing [13,14], and plasma treatment methods [13,25]. A common route to fabricate silver nanowires is the polyol method, which is associated with the formation of a polymer ligand shell (polyvinylpyrrolidone – PVP) around the nanowires [5,17]. The PVP layer has a detrimental effect on the electrical properties of the Ag-NW networks, as it forms an isolating layer at the wire-wire junctions. We, therefore, use a washing procedure with acetone and isopropanol, which causes an improvement in conductivity by a factor of around 100 and, therefore, reduces the PVP layer significantly [15] (see experimental section). In this way, highly conductive nanowire networks with initial sheet resistance in the range of 10–15 Ω/sq. at an optical transmittance of 90% are produced [15].

Traditionally, plasma treatment has been adopted to optimize the conductivity of Ag-NW networks due to the removal of PVP insulating layer as well as to study the degradation mechanism of Ag-NW electrodes [13,25]. Furthermore, several groups have reported on the deterioration phenomena in Ag-NW based electronic devices due to corrosive environment, elevated annealing temperature [14,26], long UV light irradiation exposure [26], induced electrical current [27,28] and humidity [12,29,30]. Here, an atmospheric plasma pen [31–35] is utilized as a versatile, simple, and direct tool to control the electrical properties of polyol grown and washed Ag-NW networks with high conductivities. The local manipulation of Ag-NW networks can enable future complex resistor designs within a premanufactured composite structure. The crystalline nanowires are monitored through a combination of time-resolved grazing-incidence small-and-wide-angle X-ray (GISAXS and GIWAXS) scattering methods during the atmospheric plasma treatment. Moreover, the effects of the applied plasma on the sample morphology are investigated using field-effect scanning electron microscopy (FESEM). The chemical surface composition upon plasma treatment is measured by X-ray photoelectron spectroscopy (XPS). A physical model that explains the electrical network properties as a function of plasma etching time based on the network connectivity is presented. The model is based on a Monte Carlo simulation considering the experimental thickness and length distribution of the nanowires at a constant plasma etching rate and the tunneling resistances at the nanowire junctions.

2. Experimental section

2.1. Materials

⟨100⟩ monocrystalline boron-doped silicon wafers (Si-Mat) with the dimension of 15 × 15 mm^2 were used as substrates, which were acidly cleaned in 1:2 mixture of sulfuric acid (H_2SO_4, 96%, Carl Roth) and hydrogen peroxide (H_2O_2, 30%, Carl Roth) according to the RCA-1 cleaning procedure [36]. More detailed information is given in the supplementary information (SI) S1.1.

The Ag-NWs were synthesized *via* a polyol wet chemical method at a temperature of 155 °C and a reaction time of 3 h. The precursors used were commercially purchased and comprise the following: silver nitrate ($AgNO_3$, 99.9%, Sigma Aldrich), polyvinylpyrrolidone (PVP, molecular weight, $M_w = 55$ kg mol^{-1}, Sigma Aldrich, and PVP $M_w = 360$ kg mol^{-1}, Carl Roth), anhydrous ethylene glycol (EG 99.8%, Sigma Aldrich) and copper chloride ($CuCl_2$ 99.999% purity, Sigma Aldrich). A detailed description of the synthesis is given in Ref. [15].

After synthesis, the Ag-NW suspension was consecutively washed twice with isopropanol (99.5%, Sigma Aldrich), twice with acetone (99.8%, VWR), and finally again twice with isopropanol to eliminate remaining precursors and PVP from the synthesis. After each washing step, the suspension was centrifuged at 2000 rpm at 20 °C for 10 min. The final product was stored in isopropanol (99.5%, Sigma Aldrich). The synthesis yields silver nanowires with pentagonal cross-sections and were analyzed *via* TEM verifying the pentagonal shape [17] as well as the crystallinity as displayed in Figure S2 in the SI.

2.2. Ag-NW network preparation

20 µl of the Ag-NW suspension were drop casted on a 15 × 15 mm^2 clean ⟨100⟩ monocrystalline silicon substrate at room temperature leading to a network of silver nanowires with a density of around 26 µg cm^{-2}. After 5 min the solvent was evaporated. The film thickness of each sample is estimated to be approximately 1 µm and typically averaged initial line resistances of (1.3 ± 0.5) Ω mm^{-1} are found. A commercial hand-held atmospheric plasma pen device (Plasma Wand, Plasma Etch, Inc.) was adopted to treat the samples with varying treatment times from 0 s to 26 s (see SI S1.2). The plasma pen uses a piezo crystal to create very high voltages and is driven by a 30 W plasma generator with an integrated power supply ionizing surrounding gas. We use air from the surrounding atmosphere. Since the plasma temperature is smaller than 50 °C, ozone (O_3) predominantly contributes to the plasma etching [private communication Plasma Etch Inc.] [37]. The setup enables various types of materials to be locally modified in the sub-micrometer to millimeter range. The treatment area is determined by the nozzle diameter, which was 10 mm for the presented experiments. For enabling the electrical discharge from the atmospheric plasma to attain the sample surface, a nozzle-to-sample height (NSH) of (10.5 ± 0.5) mm was used.

2.3. Grazing-incidence small-and-wide-angle X-ray scattering

For the structural investigation and the verification of the Ag-NW oxidation, *in situ* GISAXS/GIWAXS experiments were conducted at the Micro-and-Nanofocus X-ray scattering (MiNaXS) beamline P03 of the high-brilliance light source PETRA III at DESY, Hamburg [38]. We used an X-ray beam with a wavelength λ = (0.965 ± 0.002) Å and a focus size of around 20 × 30 $µm^2$. The sample-to-detector distance (SDD) for GISAXS was (4380 ± 2) mm and for GIWAXS (116.5 ± 0.5) mm. The incident angle was $\alpha_i = 0.425°$. A Pilatus 300 k detector (Dectris Ltd.) with an image dimension of 487 × 619 pixels and a pixel size of 172 × 172 $µm^2$ was used. GIWAXS data were acquired with a LAMBDA 750k detector (X-Spectrum GmbH) yielding an image dimension of 512 × 1536 pixels and a pixel size of 55 × 55 $µm^2$. Lateral y-scans with a scan rate of 100 ms, step-width of 100 µm and an overall length of 7 mm were carried out. In situ GISAXS and GIWAXS scans were carried out simultaneously on the sample before and after each atmospheric plasma treatment step.

2.4. Field emission scanning electron microscopy

The morphology of the Ag-NW networks (treated and untreated sample) and the shape of the nanowires were investigated by a field emission scanning electron microscope setup (Zeiss company) at an accelerating voltage of 3 kV and a focus distance of 7 mm.

2.5. X-ray photoelectron spectroscopy

The chemical surface composition was measured by using an X-ray photoelectron spectroscopy (XPS) with a hemispherical electron analyzer SES2002 (Scienta) measuring system.

2.6. Resistance measurements

After each atmospheric plasma treatment step, *in situ* GISAXS/GIWAXS scans and electrical resistance measurements using a Keithley 2000 multimeter (Tektronix) in a two-point resistance configuration were carried out [39]. The effects of the contact resistances of the electrical cables on the measured line resistances were considered. For the measurements, two coaxial cables with an insulating shield were connected to a lithographically patterned pad structure with gold contacts with a distance of 10 mm. Pieces of indium foil (max 1 × 1 mm^2) were utilized to obtain a gapless contact between the Ag-NWs and the gold contacts. At least 10 data points were recorded for each atmospheric plasma treatment time and averaged.

3. Results and discussion

In order to obtain a direct overview of the Ag-NW network changes upon atmospheric plasma etching, SEM images were recorded for different plasma treatment times. In Fig. 1 exemplary FESEM images of Ag-NW networks with a concentration of 26 μg cm^{-2} after different atmospheric plasma treatment times are shown. An untreated (pristine) Ag-NW network (0 s) consisting of pentagonal nanowires with aspect ratios of up to 1000 can be observed in Fig. 1a. Small treatment times lead to marginal changes in the nanowire morphology like rounding of the nanowire facets as shown in Fig. 1b and 1f. Here, the robustness of the Ag-NW networks can be attributed to a strong wire-wire interconnectivity within the percolation network of the Ag-NWs [16,40–42]. However, for longer treatment times, enhanced destruction and fragmentation of the Ag-NW networks is observable [26,28] as shown in Fig. 1c −1f, which finally leads to the failure of the conductive Ag-NW networks. The degradation observed with longer treatment times is caused by mechanical ablation induced by the atmospheric plasma pen (see Fig. 1f (26 s)). In comparison, Li et al. [25] reported a low energy (45 W) plasma treatment in argon inert gas resulting in a decrease in Ag-NW network resistance due to the removal of PVP and welding of nanowires in the first 20 min. A degradation of the Ag-NW electrode occurred after a prolonged treatment time of more than 20 min. Kim et al. [13] also used argon inert gas to treat Ag-NW networks at a power of 200 W, resulting in a rapid decrease in resistance after 2 min, which can be attributed to welding of the nanowires. Atmospheric plasma, however, is known to generate reactive oxygen species (ROS) [31–35] after air ionization and is also very versatile in applications for composite 3D printing. Here, the plasma treatment of the network can be used to manipulate the electrical properties locally. ROS enable ultrafast morphological changes as well as surface oxidation that can be observed already after 10 sec treatment time.

In order to obtain a measure of the morphological network changes during plasma treatment, the Fiber Image Network Evaluation (FINE) algorithm [16,43,44] was used. Based on the SEM images for different plasma treatment times, the FINE algorithm determines the number of fiber families, their amplitudes, mean orientation, and dispersion, based on the cumulative angular orientation distribution (see SI S2.5 for details). Nanowires contribute to an anisotropic class of fiber families, whereas particle-like structures are detected as an isotropic contribution. Therefore, the FINE algorithm is a relevant tool for the quantitative analysis of the destruction, fragmentation, and melting of nanowires. The results are shown in Fig. 1g, where the amplitude of the isotropic fiber family is displayed in red. Blue denotes the amplitudes of the anisotropic class. Sigmoidal curves are used as guides to the eye. After 6 s plasma treatment, a clear increase in the isotropic family and a corresponding decrease in the anisotropic fiber family can be observed. This indicates a transition from slight changes on the nanowire surface to stronger morphological changes including an onset of fragmentation and melting of the nanowires. These morphological changes have a strong influence on the interconnectivity of the network and, thus, on the electrical network resistance.

Fig. 2a and b show exemplary XPS spectra of oxygen (O 1 s) and silver (Ag 3d) for plasma-treated Ag-NW networks. For a treatment time of 0 s and 6 s, the Ag 3d spectra display two characteristic peaks at (368.4 ± 0.2) eV and (374.4 ± 0.2) eV, which correspond to the Ag $3d_{5/2}$

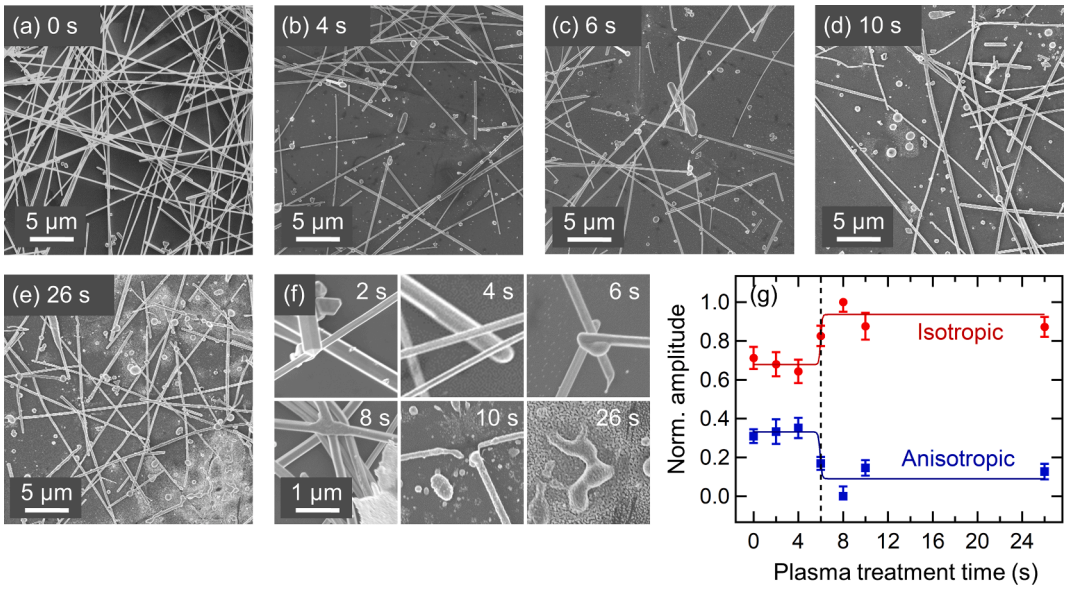

Fig. 1. (a)–(e) Exemplary scanning electron microscopy images of the investigated Ag-NW sample with a nanowire concentration of 26 μg cm^{-2} after different atmospheric plasma treatment times (0 s to 26 s). Please note that different areas of the same sample are shown. Longer treatment times (>8 s) lead to enhanced fragmentation, melting, and destruction of the Ag-NWs. (f) Collage of six SEM images at high magnification for a plasma treatment time of 2 s, 4 s, 6 s, 8 s, 10 s, and 26 s, respectively. After 2 s, the pentagonal shape of the wires can still be observed. After 4 s, rounding is visible on individual wires. Further changes in the nanowire shape are observable after 6 s. After 8 s, welding of the nanowire junctions occurs and local destruction is already visible after 10 s. After 26 s, parts of the network are completely destroyed. (g) Amplitudes for the isotropic (red) and the anisotropic fiber family (blue) determined by the FINE algorithm based on the SEM images. Sigmoidal curves are guides to the eye. A clear increase in the isotropic particle class (particle-like structures, fragmented and melted nanowires) after 6 s plasma treatment (phase I) and a corresponding decrease in the anisotropic class can be observed.

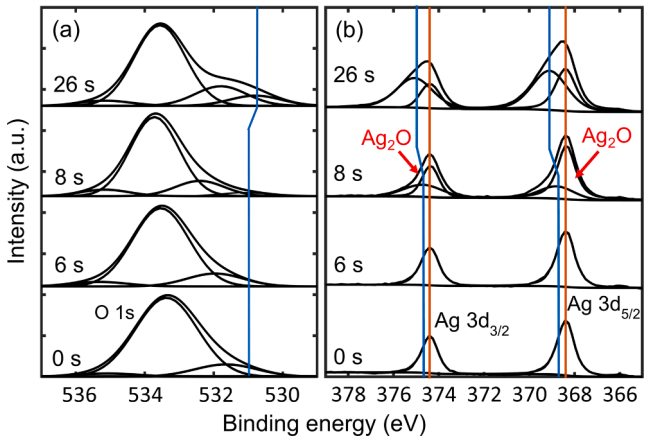

Fig. 2. Exemplary XPS spectra of the Ag-NW sample highlighting the characteristic oxygen (O 1s) (a) and silver (Ag $3d_{3/2}$ and Ag $3d_{5/2}$) (b) peak positions for a plasma treatment time of 0 s, 6 s, 8 s, and 12 s, respectively.

and $3d_{3/2}$ binding energy of metallic Ag^0 (orange line) [45]. After 8 s treatment, peaks at (368.8 ± 0.2) eV and (374.7 ± 0.2) eV are observed and are attributed to oxidized species Ag_2O (see red arrows in Fig. 2b) [45–47]. This oxidation process indicates the crossover between two characteristic phases induced by the atmospheric plasma treatment. Phase I lasts up to 6 s, where phase II begins. This also correlates strongly with the observation from the SEM analysis (see Fig. 1g).

Similarly, the O 1s spectra displayed in Fig. 2a exhibit three different oxygen species with peaks at (532.0 ± 0.2) eV, (533.6 ± 0.2) eV, and (535.0 ± 0.2) eV, which we attribute to C=O, C-O, and H_2O [48–53], respectively. These peaks are not unambiguous and presumably contain overlapping hydroxides or carboxyl groups from the PVP precursor [46,52,54]. Above 8 s treatment time, a peak at (531.0 ± 0.2) eV is observed and is attributed to Ag_2O [46,49,55]. The further shift in the O 1s spectra to lower binding energies at 26 s prolonged treatment time confirms the formation of AgO, which is characteristic for phase III of the treatment [48,49,55,56]. This view is also supported by an enhanced shoulder seen in Fig. 2b after 26 s treatment [46,47]. A detailed information on the XPS experimental information is given in the SI and also, an overview of all the identified elements as well as the Carbon 1s spectra are shown in Figure S6.

Surface-sensitive X-ray scattering using high flux X-ray beams enables time-resolved measurements and, thus, allows in-depth observation of morphological and nanostructural changes in a variety of processes [57–60]. In order to observe morphological and crystallinity changes, as well as changes in electrical properties of the Ag-NW networks during plasma treatment, *operando* GISAXS, GIWAXS and resistance measurements were carried out. The used measurement setup is illustrated in Fig. 3j. Further detailed experimental information is given in the experimental part and in the SI in Fig. S1.

GISAXS pattern of Ag-NW networks during atmospheric plasma treatment for exemplary treatment times are shown in Fig. 3a–d. The GISAXS pattern of the untreated Ag-NW network (Fig. 3a) is dominated by intensity streaks at around (36 ± 2)° starting from the direct beam as a consequence of the pentagonal shape of the Ag-NWs [15]. Upon plasma treatment the intensity of these streaks decreases monotonically. The streaks vanish completely after 8 s treatment time as shown in Fig. 3c and d. This indicates the rounding of the pentagonal Ag-NWs in the initial phase of the plasma treatment (phase I). Long treatment times (16 s – 26 s, Phase III) lead to melting, fragmentation, and degradation of the Ag-NWs as observed in Fig. 1, which is contributing to increased two-point resistance measurements.

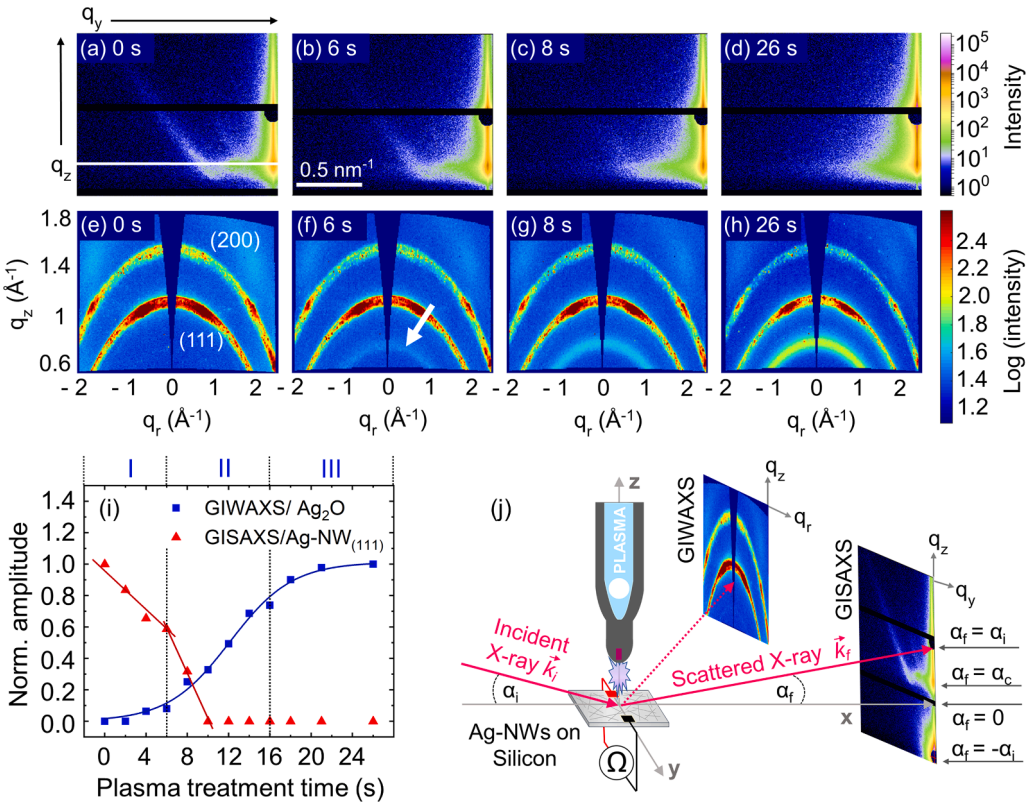

Fig. 3. (a)–(d) 2D GISAXS pattern for (26 µg cm^{-2} Ag-NW concentration) exemplary atmospheric plasma treatment times of 0 s, 6 s, 8 s, and 26 s. The position of the line cuts is shown in (a) as a white line for the horizontal line cut $I(q_y)$ at q_z = 0.885 nm^{-1}. (e)–(h) GIWAXS data showing the reciprocal space maps (RSM) [61] for a (26 µg cm^{-2} Ag-NW concentration) plasma treatment time of 0 s, 6 s, 8 s and 26 s, respectively. The characteristic face-centred-cubic (fcc) silver (111), (200) Miller's indices and oxidized Ag-NWs (Ag_2O) reflections are indicated. The white arrow in (f) indicates the Bragg peak corresponding to the Ag_2O diffractions [62–64]. (i) Normalized comparison of the Ag-NW flare intensity obtained by GISAXS (red), and the Ag_2O Bragg intensity obtained by GIWAXS (blue) as a function of atmospheric plasma treatment time. Three characteristic phases can be observed as marked in blue in the upper part of the figure. (j) Schematic view on the experiment showing the *operando* atmospheric plasma pen above the Ag-NW/SiO_x sample. The incident X-ray beam with an incident angle α_i, the scattered X-ray beams in GIWAXS geometry (dashed line) and GISAXS mode (solid line) with a scattering angle α_f, as well as two exemplary detector images for GIWAXS and GISAXS are shown. The digital multimeter represents the *in situ*

diffuse scattering based on pronounced surface roughness as shown in Fig. 3d.

The reciprocal space maps (RSM) shown in Fig. 3e–h for different atmospheric plasma treatment times were obtained from the GIWAXS measurements. The original GIWAXS scattering patterns were transformed using the GIXSGUI [61] software. The pristine Ag-NW sample shown in Fig. 3e exhibit two anisotropic Bragg diffraction peaks stemming from X-ray diffraction at the characteristic face-centered-cubic (fcc) crystalline lattices of silver (111) and (200), respectively. After 6 s of atmospheric plasma treatment, the intensity of those two key features reduces gradually and the evolution of a crescent-like isotropic Bragg peak corresponding to the Ag_2O diffraction (see white arrow in Fig. 3f) can be observed. This observation indicates the more significant oxidation of Ag to Ag_2O in phase II in line with the XPS data (see Fig. 2) [62–64].

In Fig. 3i, the extracted amplitudes (see Fig. S3 in the SI for details) representing the streak intensity and corresponding pentagonal shape of the Ag-NW from GISAXS (red), and the Bragg intensity corresponding to the Ag_2O signal obtained by GIWAXS (blue) of the Ag-NW sample upon atmospheric plasma treatment are shown. The extracted amplitudes are normalized to the maximum values, for GISAXS (0 s Fig. 3a) and GIWAXS (26 sec, Fig. 3h). In phase I rounding of the nanowires occurs resulting in a decrease of the GISAXS flare intensity with treatment time. These small changes in nanowire morphology as well as a weak oxidation (GIWAXS Ag_2O) hardly affect the interconnectivity of the network and, thus, the electrical resistance (see Fig. 4f). The Bragg intensities for Ag_2O determined by GIWAXS (blue curve) follow a sigmoidal shape with only small changes in phase I, drastic changes in phase II, and attaining a saturation in phase III. Phase III represents the destructive melting and pronounced fragmentation of the Ag-NW network upon atmospheric plasma treatment (see Fig. 1). The XPS and GIWAXS data show that this phase is characterized by the enhanced oxidation of Ag to Ag_2O. The analyzed data show that the most relevant effect of the atmospheric plasma treatment is the etching of the silver nanowires from the surface to the core and selective oxidation of the nanowires [65]. Since the nanowires are thoroughly washed and highly conductive (see experimental section), no notable influence of a ligand layer (PVP) can be observed. Thus, we do not observe any increase in conductivity for short plasma treatment times, which is typically observed to the removal of a PVP ligand shell [13,25].

4. Electrical resistance & Monte Carlo simulation

The electrical behavior of Ag-NW networks can be simulated using a Monte Carlo method, in which the network resistance is calculated considering the tunnel resistances between the nanowires [16]. Fig. 4(a) shows the experimental radii of the Ag-NWs measured by SEM. The data are fitted using two Gaussian functions. In Fig. 4(b) the length distribution, also measured by SEM, is shown. Due to the high aspect ratio of the used nanowires, the lengths of the nanowires strongly dominate the network connectivity and the percolation threshold, while the exact thickness distribution of nanowires is not significant for the network. Atmospheric plasma etching, however, has a direct impact on the nanowires as shown earlier in the previous section. It can be assumed that the durability of a single nanowire during plasma treatment correlates strongly with its thickness. We, therefore, adopt a simplified model for simulating the electrical resistance of Ag-NW networks that is based on the lifetime of the nanowires during plasma treatment as a function of their thickness. For this, a constant plasma etching rate R_{Etch} is given, which indicates the etched mass of silver per unit of time t and sample area A_{Sample}. In order to calculate the life time of a wire upon plasma etching, a critical wire radius is required, from which the wire is counted as no longer functional. For the following simulation, the critical radii of all wires are assumed to be $r_{i,crit} = 0.5r_{0,i}$ according to a critical mass of $m_{i,crit} = 0.25m_{0,i} = 0.25\rho\pi r_{0,i}^2 \cdot L_i$, where L_i is the length of wire i and $r_{0,i}$ and $m_{0,i}$ are the radius and mass of wire i at the time $t =$

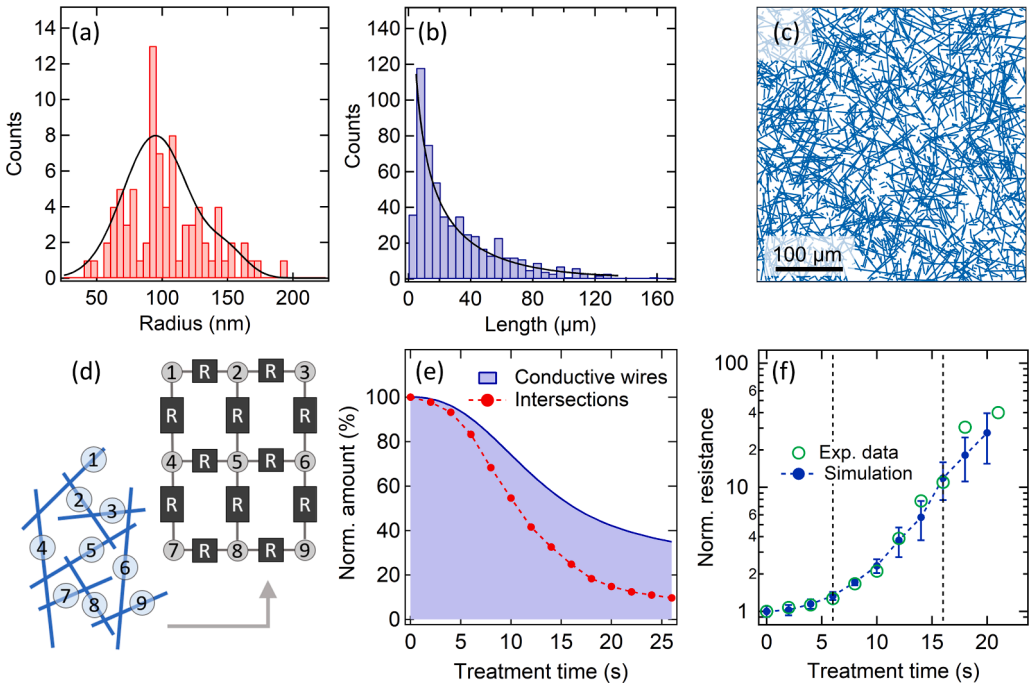

Fig. 4. (a) Radii of 83 Ag-NWs measured by SEM and represented as a histogram. The black solid line shows the sum of two Gaussian functions that were fitted to the data. (b) Length distribution of 564 Ag-NWs measured by SEM. The data was fitted by $y_0 + A\exp\left(-(\ln(x/x_0)\cdot 1/width)^2\right)$ (solid line). (c) Exemplary Monte Carlo simulated nanowire network with an effective concentration of 11 μg cm^{-2} and a sample size of (400 × 400) μm^2. The nanowire lengths correspond to the length distribution shown in (b). (d) Translation of a nanowire network (blue) into a resistor network (gray). Every wire is a node (circles), and every nanowire junction is a tunnel resistor (black squares). (e) Normalized number of intact wires (blue) and nanowire junctions (red) during plasma treatment obtained from Monte Carlo simulations for an etching rate of 570 ng s^{-1} cm^{-2} and Ag-NW concentration of 11 μg cm^{-2}. It is assumed that 28% of all wires are not affected by plasma etching. The number of intact wires as a function of plasma treatment time results directly from the radius distribution shown in (a). (f) Normalized resistance as a function of plasma treatment time. The experimental data is shown in green and the simulated results are given in blue (n = 5). The dashed lines denote the three characteristic plasma treatment phases. An etching rate of 570 ng s^{-1} cm^{-2} was used with an effective Ag-NW concentration of 11 μg cm^{-2}.

0, respectively. We also assume that each unit length element of the wires in the network is etched at the same rate. The rate for etching an individual wire can therefore be expressed as $R_{Etch} \cdot A_{Sample} \cdot L_i L_{ges}^{-1}$, where L_{ges} is the sum of the lengths of all wires. This leads to Eq. (1), which determines the critical live time of wire *i*.

$$t_{i,crit} = \frac{(m_{i,0} - m_{i,crit}) \cdot L_{ges}}{R_{Etch} \cdot L_i \cdot A_{Sample}} = \frac{0.75 \rho \pi r_{0,i}^2 \cdot L_{ges}}{R_{Etch} \cdot A_{Sample}} \quad (1)$$

Fig. 4(c) shows an exemplary Monte Carlo nanowire sample with an effective nanowire concentration of 11 μg cm^{-2} and a sample size of (400 × 400) μm^2. The effective concentration of nanowires, which contribute to the final network, is lower than the experimentally used concentration due to side products and the effective distribution of the nanowires [16]. In the case of drop-cast nanowires on a silicon surface, the effective concentration was found to be by a factor of around 2.4 lower than the experimental concentration. In addition to the nanowire lengths and concentration, the position and orientation of the nanowires are important parameters for defining a sample, as shown in Fig. 4(c). The positions are determined randomly within the size of the sample and the orientations are randomly distributed between −90° and 90° in order to create an isotropic network. To determine the electrical network resistance, the nanowire networks have to be translated into resistor networks as illustrated in Fig. 4(d). For this, every wire is considered as a node and every wire junction presents a tunneling resistor with a unit resistance of $r_{ij} = 1$ [16]. The resistance of a resistor network between two nodes can now be calculated as shown by F.Y. Wu [16,66].

Fig. 4(e) shows the normalized number of wires that were stable to the atmospheric plasma and the number of tunnel junctions within the network as a function of the plasma etch time. The number of intact wires as function of time results directly from the thickness distribution shown in Fig. 4(a). The presented simulation was carried out with an effective Ag-NW concentration of 11 μg cm^{-2}, which corresponds to the used experimental concentration of 26 μg cm^{-2}. In order to model the residual conductance in phase III, we assume that 28% of all wires remain conductive. The corresponding change in network resistances of the Ag-NW sample upon atmospheric plasma treatment together with the experimental data are shown in Fig. 4(f). By fitting the simulation results to the experimental data, an etching rate of 570 ng s^{-1} cm^{-2} was found. For an exemplary nanowire with a mean radius of 100 nm and a mean length of 25 μm, this etching rate corresponds to $2.4 \cdot 10^9$ atoms s^{-1}. The simulated resistances and its error bars result from five Monte Carlo simulations (n = 5).

Overall, we can identify three characteristic phases as indicated by nearly linear slopes on a logarithmic scale outlining exponential growths of the resistance as a function of plasma treatment time as highlighted in Fig. 4f. The initial phase I with relatively small resistance changes lasting until 6 s and exhibits a typical slope of the order of Ω s^{-1}. In phase II the resistance change upon plasma pen treatment time is approximately one order of magnitude larger than in phase I. Thus, in phase I and phase II it is possible to build a voltage divider with an exemplary voltage ratio of U_{in}:U_{out} = 3:2 after 10 s treatment. After 16 s of atmospheric plasma treatment (phase III), an extreme increase in resistance can be observed, leading to a nearly infinite resistance and subsequent breakdown and failure of the Ag-NW network for treatment times beyond 26 s. The theoretical data show a strong match with the experiment for the analyzed resistance of the Ag-NW networks. The ultra-fast fragmentation and degradation observed in the giant resistance with the longer treatment at time scale above 16 s is attributed to aggressive etching mechanism induced by the reactive oxygen species (ROS) generated by the plasma during the treatment.

5. Conclusions

The effect of atmospheric plasma treatment on the electrical and structural properties of highly conductive silver-nanowire (Ag-NW) networks as a function of treatment time was investigated. The results obtained provide a strong correlation between the changes in electrical resistance of the Ag-NW networks during plasma treatment and the selective oxidation of the Ag-NWs as well as the morphological network changes. Phase I (0 s to 6 s atmospheric plasma treatment) is characterized by the rounding of the pentagonal nanowires and by small and controlled changes in resistance. XPS and GIWAXS data confirm a pronounced evolution of silver oxide (Ag_2O) in phase II (6 s to 16 s atmospheric plasma treatment), which is correlated with drastic but controllable resistance changes. Thus, phase I and II allow a controlled manipulation of the network resistance with an exponential dependence between resistance and atmospheric plasma treatment time with different rates of resistance change upon etching. After 16 s, phase III leads to an enhanced oxidation, fragmentation, and destruction of the Ag-NW network as validated by FESEM, XPS, GIWAXS and GISAXS. For the presented study, Ag-NWs were thoroughly washed before use leading to a nearly ligand free suspension and correspondingly low resistances of the untreated samples. We, therefore, observe no decrease in resistance upon plasma treatment according to a removal of an isolating ligand shell. In contrast, we initiate a controlled oxidation of our wires and offer an alternative approach to manipulate the local resistance of Ag-NW networks at a controllable rate for technological applications such as sensors, transparent electrodes, and integrated circuits. We simulate the electrical properties of the investigated nanowire networks upon plasma etching by a Monte Carlo method resulting in a physical model explaining the dependence between network resistance, connectivity, and etching rate.

Author contributions

MS, LOA, TEG, SVR and MR designed the study and supervised the project. MB, LOA, and TEG fabricated the samples. MB, TEG, MS, MG, BG-L, LOA, SVR and MR conceived the experiment and facilitated the *in situ* conductivity setup. MB, LOA, MS, MG, and AC conducted the GIWAXS and GISAXS measurements. XPS measurements and data analysis were done by MN, IB and MM. SS, CN and LOA carried out FESEM studies on the samples. TEM studies and analysis were done by US, TD, and LK. MW and FF conducted FINE analysis. TEG conducted the Monte Carlo simulations. TEG, LOA and MR analyzed the data and wrote the manuscript. All authors contributed to the preparation of the manuscript. All authors have approved the final version of the manuscript.

Funding

This work was supported by the Deutsche Forschungsgemeinschaft (DFG, German Research Foundation; grant number MA2561/6-1) and the Helmholtz society through DESY. This work was funded by the BMBF via 05K19GU5.

Declaration of Competing Interest

The authors declare no competing financial or conflict of interest.

Acknowledgements

The authors would like to thank Jan Rubeck, Anca Ciobanu, Milena Lippmann and André Rothkirch (DESY, Hamburg) and Stephan Martens (Universität Hamburg) for the technical support and helpful discussions. We are further thankful to Nils Huse and Robert Frömter for the usage of their scanning electron microscopes. We thank Christin Szillus for the ultramicrotome preparation of the TEM cross-sections of the pentagonal silver nanowires.

Appendix A. Supplementary material

Supplementary data to this article can be found online at https://doi.org/10.1016/j.apsusc.2021.149362.

References

[1] M.C. Daniel, D. Astruc, Gold nanoparticles: assembly, supramolecular chemistry, quantum-size-related properties, and applications toward biology, catalysis, and nanotechnology, Chem. Rev. 104 (2004) 293–346, https://doi.org/10.1021/cr030698+.

[2] Y. Xia, Y. Xiong, B. Lim, S. Skrabalak, Shape-controlled synthesis of metal nanocrystals: Simple chemistry meets complex physics? Angew. Chemie - Int. Ed. 48 (1) (2009) 60–103, https://doi.org/10.1002/anie.200802248.

[3] F. Faupel, V. Zaporojtchenko, T. Strunskus, M. Elbahri, Metal-polymer nanocomposites for functional applications, Adv. Eng. Mater. 12 (12) (2010) 1177–1190, https://doi.org/10.1002/adem.201000231.

[4] H. Yang, Y. Wang, X. Chen, X. Zhao, L. Gu, H. Huang, J. Yan, C. Xu, G. Li, J. Wu, A. J. Edwards, B. Dittrich, Z. Tang, D. Wang, L. Lehtovaara, H. Häkkinen, N. Zheng, Plasmonic twinned silver nanoparticles with molecular precision, Nat. Commun. 7 (2016) 1–8, https://doi.org/10.1038/ncomms12809.

[5] Y. Sun, Y. Yin, B.T. Mayers, T. Herricks, Y. Xia, Uniform silver nanowires synthesis by reducing AgNO3 with ethylene glycol in the presence of seeds and poly(vinyl pyrrolidone), Chem. Mater. 14 (11) (2002) 4736–4745, https://doi.org/10.1021/cm020587b.

[6] D.S. Hecht, L. Hu, G. Irvin, Emerging transparent electrodes based on thin films of carbon nanotubes, graphene, and metallic nanostructures, Adv. Mater. 23 (13) (2011) 1482–1513, https://doi.org/10.1002/adma.201003188.

[7] A. Kim, Y. Won, K. Woo, S. Jeong, J. Moon, All-solution-processed indium-free transparent composite electrodes based on Ag nanowire and metal oxide for thin-film solar cells, Adv. Funct. Mater. 24 (17) (2014) 2462–2471, https://doi.org/10.1002/adfm.201303518.

[8] S. De, T.M. Higgins, P.E. Lyons, E.M. Doherty, P.N. Nirmalraj, W.J. Blau, J. J. Boland, J.N. Coleman, Silver nanowire networks as flexible, transparent, conducting films: extremely high DC to optical conductivity ratios, ACS Nano 3 (7) (2009) 1767–1774, https://doi.org/10.1021/nn900348c.

[9] E. Braun, Y. Eichen, U. Sivan, G. Ben-Yoseph, DNA-templated assembly and electrode attachment of a conducting silver wire, Nature 391 (6669) (1998) 775–778, https://doi.org/10.1038/35826.

[10] Y. Kim, J.W. Kim, Silver nanowire networks embedded in urethane acrylate for flexible capacitive touch sensor, Appl. Surf. Sci. 363 (2016) 1–6, https://doi.org/10.1016/j.apsusc.2015.11.052.

[11] B. Yoo, Y. Kim, C.J. Han, M.S. Oh, J.W. Kim, Recyclable patterning of silver nanowire percolated network for fabrication of flexible transparent electrode, Appl. Surf. Sci. 429 (2018) 151–157, https://doi.org/10.1016/j.apsusc.2017.07.285.

[12] C. Mayousse, C. Celle, A. Fraczkiewicz, J.-P. Simonato, Stability of silver nanowire based electrodes under environmental and electrical stresses, Nanoscale. 7 (5) (2015) 2107–2115, https://doi.org/10.1039/C4NR06783E.

[13] D.G. Kim, J. Kim, S.B. Jung, Y.S. Kim, J.W. Kim, Electrically and mechanically enhanced Ag nanowires-colorless polyimide composite electrode for flexible capacitive sensor, Appl. Surf. Sci. 380 (2016) 223–228, https://doi.org/10.1016/j.apsusc.2016.01.130.

[14] G. Deignan, I.A. Goldthorpe, The dependence of silver nanowire stability on network composition and processing parameters, RSC Adv. 7 (57) (2017) 35590–35597, https://doi.org/10.1039/C7RA06524H.

[15] T.E. Glier, L. Akinsinde, M. Paufler, F. Otto, M. Hashemi, L. Grote, L. Daams, G. Neuber, B. Grimm-Lebsanft, F. Biebl, D. Rukser, M. Lippmann, W. Ohm, M. Schwartzkopf, C.J. Brett, T. Matsuyama, S.V. Roth, M. Rübhausen, Functional printing of conductive silver-nanowire photopolymer composites, Sci. Rep. 9 (2019) 6465, https://doi.org/10.1038/s41598-019-42841-3.

[16] T.E. Glier, M. Betker, M. Witte, T. Matsuyama, L. Westphal, B. Grimm-Lebsanft, F. Biebl, L.O. Akinsinde, F. Fischer, M. Rübhausen, Electrical and network properties of flexible silver-nanowire composite electrodes under mechanical strain, Nanoscale. 12 (46) (2020) 23831–23837, https://doi.org/10.1039/D0NR05734G.

[17] Y. Sun, B. Mayers, T. Herricks, Y. Xia, Polyol synthesis of uniform silver nanowires: a plausible growth mechanism and the supporting evidence, Nano Lett. 3 (2003) 955–960, https://doi.org/10.1021/nl034312m.

[18] S.H. Park, M.W. Prior, T.H. LaBean, G. Finkelstein, Optimized fabrication and electrical analysis of silver nanowires templated on DNA molecules, Appl. Phys. Lett. 89 (2006) 2004–2007, https://doi.org/10.1063/1.2234282.

[19] J. Chen, B.J. Wiley, Y. Xia, One-dimensional nanostructures of metals: Large-scale synthesis and some potential applications, Langmuir 23 (2007) 4120–4129, https://doi.org/10.1021/la063193y.

[20] F. Fievet, J.P. Lagier, M. Figlarz, Preparing monodisperse metal powders in micrometer and submicrometer sizes by the polyol process, MRS Bull. 14 (12) (1989) 29–34, https://doi.org/10.1557/S0883769400060930.

[21] K.E. Korte, S.E. Skrabalak, Y. Xia, Rapid synthesis of silver nanowires through a CuCl- or CuCl2-mediated polyol process, J. Mater. Chem. 18 (4) (2008) 437–441, https://doi.org/10.1039/B714072J.

[22] L.D. Marks, Experimental studies of small particle structures, Reports Prog. Phys. 57 (6) (1994) 603–649, https://doi.org/10.1088/0034-4885/57/6/002.

[23] X. Tang, M. Tsuji, Syntheses of Silver Nanowires in Liquid Phase, in: Nanowires Sci. Technol., InTech, 2010. https://doi.org/10.5772/39491.

[24] S. Coskun, B. Aksoy, H.E. Unalan, Polyol synthesis of silver nanowires: An extensive parametric study, Cryst. Growth Des. 11 (11) (2011) 4963–4969, https://doi.org/10.1021/cg200874g.

[25] J. Li, Y. Tao, S. Chen, H. Li, P. Chen, M.Z. Wei, H. Wang, K. Li, M. Mazzeo, Y. Duan, A flexible plasma-treated silver-nanowire electrode for organic light-emitting devices, Sci. Rep. 7 (2017) 1–9, https://doi.org/10.1038/s41598-017-16721-7.

[26] D.C. Choo, T.W. Kim, Degradation mechanisms of silver nanowire electrodes under ultraviolet irradiation and heat treatment, Sci. Rep. 7 (2017) 1–12, https://doi.org/10.1038/s41598-017-01843-9.

[27] H.H. Khaligh, I.A. Goldthorpe, Failure of silver nanowire transparent electrodes under current flow, Nanoscale Res. Lett. 8 (2013) 2–7, https://doi.org/10.1186/1556-276x-8-235.

[28] T. Sannicolo, N. Charvin, L. Flandin, S. Kraus, D.T. Papanastasiou, C. Celle, J.P. Simonato, D. Muñoz-Rojas, C. Jiménez, D. Bellet, Electrical Mapping of Silver Nanowire Networks: A Versatile Tool for Imaging Network Homogeneity and Degradation Dynamics during Failure, ACS Nano. 12 (2018) 4648–4659. https://doi.org/10.1021/acsnano.8b01242.

[29] J. Jiu, J. Wang, T. Sugahara, S. Nagao, M. Nogi, H. Koga, K. Suganuma, M. Hara, E. Nakazawa, H. Uchida, The effect of light and humidity on the stability of silver nanowire transparent electrodes, RSC Adv. 5 (35) (2015) 27657–27664, https://doi.org/10.1039/C5RA02722E.

[30] J.L. Elechiguerra, L. Larios-Lopez, C. Liu, D. Garcia-Gutierrez, A. Camacho-Bragado, M.J. Yacaman, Corrosion at the nanoscale: The case of silver nanowires and nanoparticles, Chem. Mater. 17 (2005) 6042–6052, https://doi.org/10.1021/cm051532n.

[31] A. Kuzminova, T. Kretková, O. Kylián, J. Hanuš, I. Khalakhan, V. Prukner, E. Doležalová, M. Šimek, H. Biederman, Etching of polymers, proteins and bacterial spores by atmospheric pressure DBD plasma in air, J. Phys. D. Appl. Phys. 50 (13) (2017) 135201, https://doi.org/10.1088/1361-6463/aa5c21.

[32] G. Bauer, D. Sersenová, D.B. Graves, Z. Machala, Cold atmospheric plasma and plasma-activated medium trigger RONS-based tumor cell apoptosis, Sci. Rep. 9 (2019) 1–28, https://doi.org/10.1038/s41598-019-50291-0.

[33] A. Sonawane, M.A. Mujawar, S. Bhansali, Effects of cold atmospheric plasma treatment on the morphological and optical properties of plasmonic silver nanoparticles, Nanotechnology. 31 (36) (2020) 365706, https://doi.org/10.1088/1361-6528/ab9788.

[34] I.-M. Chan, W.-C. Cheng, F.C. Hong, Enhanced performance of organic light-emitting devices by atmospheric plasma treatment of indium tin oxide surfaces, Appl. Phys. Lett. 80 (1) (2002) 13–15, https://doi.org/10.1063/1.1428624.

[35] C. Tendero, C. Tixier, P. Tristant, J. Desmaison, P. Leprince, Atmospheric pressure plasmas: a review, Spectrochim. Acta Part B. 61 (2006) 2–30, https://doi.org/10.1016/j.sab.2005.10.003.

[36] W. Kern, Evolution of silicon wafer cleaning technology, Proc. - Electrochem. Soc. 90 (1990) 3–19.

[37] Plasma Etch, Inc., (n.d.). https://www.plasmaetch.com/atmospheric-plasma-wand-cleaner.php.

[38] A. Buffet, A. Rothkirch, R. Döhrmann, V. Körstgens, M.M. Abul Kashem, J. Perlich, G. Herzog, M. Schwartzkopf, R. Gehrke, P. Müller-Buschbaum, S.V. Roth, P03, the microfocus and nanofocus X-ray scattering (MiNaXS) beamline of the PETRA III storage ring: the microfocus endstation, J. Synchrotron Radiat. 19 (4) (2012) 647–653, https://doi.org/10.1107/S0909049512016895.

[39] M. Gensch, M. Schwartzkopf, W. Ohm, C.J. Brett, P. Pandit, S.K. Vayalil, L. Bießmann, L.P. Kreuzer, J. Drewes, O. Polonskyi, T. Strunskus, F. Faupel, A. Stierle, P. Müller-Buschbaum, S.V. Roth, Correlating nanostructure, optical and electronic properties of nanogranular silver layers during polymer-template-assisted sputter deposition, ACS Appl. Mater. Interfaces. 11 (32) (2019) 29416–29426, https://doi.org/10.1021/acsami.9b08594.

[40] J. Li, S.L. Zhang, Finite-size scaling in stick percolation, Phys. Rev. E - Stat. Nonlinear, Soft Matter Phys. 80 (2009) 1–4, https://doi.org/10.1103/PhysRevE.80.040104.

[41] S.M. Bergin, Y.H. Chen, A.R. Rathmell, P. Charbonneau, Z.Y. Li, B.J. Wiley, The effect of nanowire length and diameter on the properties of transparent, conducting nanowire films, Nanoscale. 4 (2012) 1996–2004, https://doi.org/10.1039/c2nr30126a.

[42] M. Marus, A. Hubarevich, R.J.W. Lim, H. Huang, A. Smirnov, H. Wang, W. Fan, X. W. Sun, Effect of silver nanowire length in a broad range on optical and electrical properties as a transparent conductive film, Opt. Mater. Express. 7 (3) (2017) 1105, https://doi.org/10.1364/OME.7.001105.

[43] M. Witte, S. Jaspers, H. Wenck, M. Rübhausen, F. Fischer, Noise reduction and quantification of fiber orientations in greyscale images, PLoS One. 15 (2020) 1–21. https://doi.org/10.1371/journal.pone.0227534.

[44] M. Witte, S. Jaspers, H. Wenck, M. Rübhausen, F. Fischer, General method for classification of fiber families in fiber-reinforced materials: application to in-vivo human skin images, Sci. Rep. 10 (2020) 1–11, https://doi.org/10.1038/s41598-020-67632-z.

[45] A.M. Ferraria, A.P. Carapeto, A.M. Botelho do Rego, X-ray photoelectron spectroscopy: silver salts revisited, Vacuum 86 (12) (2012) 1988–1991, https://doi.org/10.1016/j.vacuum.2012.05.031.

[46] Z. Hui, Y. Liu, W. Guo, L. Li, N. Mu, C. Jin, Y. Zhu, P. Peng, Chemical sintering of direct-written silver nanowire flexible electrodes under room temperature, Nanotechnology. 28 (28) (2017) 285703, https://doi.org/10.1088/1361-6528/aa76ce.

[47] J. Zhang, Y. Li, B.o. Wang, H. Hu, B. Wei, L. Yang, High brightness organic light-emitting diodes with capillary-welded hybrid diameter silver nanowire/graphene

layers as electrodes, Micromachines. 10 (8) (2019) 517, https://doi.org/10.3390/mi10080517.
[48] Thermo Scientific,XPS Database, (n.d.). https://xpssimplified.com/elements/oxygen.php.
[49] L.Q. Zhou, C. Ling, M. Jones, H. Jia, Selective CO2 reduction on a polycrystalline Ag electrode enhanced by anodization treatment, Chem. Commun. 51 (100) (2015) 17704–17707, https://doi.org/10.1039/C5CC06752A.
[50] N.J. Firet, M.A. Blommaert, T. Burdyny, A. Venugopal, D. Bohra, A. Longo, W. A. Smith, Operando EXAFS study reveals presence of oxygen in oxide-derived silver catalysts for electrochemical CO2 reduction, J. Mater. Chem. A. 7 (6) (2019) 2597–2607, https://doi.org/10.1039/C8TA10412C.
[51] G. Beamson, D. Briggs, High-Resolution XPS of Organic Polymers: The Scienta ESCA300 Database, WILEY, Chichester (England); New York, 1993. https://doi.org/doi.org/10.1021/ed070pA25.5.
[52] X. Kong, D. Castarède, A. Boucly, L. Artiglia, M. Ammann, T. Bartels-Rausch, E. S. Thomson, J.B.C. Pettersson, Reversibly physisorbed and chemisorbed water on carboxylic salt surfaces under atmospheric conditions, J. Phys. Chem. C. 124 (9) (2020) 5263–5269, https://doi.org/10.1021/acs.jpcc.0c00319.
[53] X-ray Photoelectron Spectroscopy (XPS) Reference Pages, (n.d.). http://www.xpsfitting.com/2013/08/oxygen-1s-for-organic-compounds.html.
[54] Y. Wu, P. Jiang, M. Jiang, T.-W. Wang, C.-F. Guo, S.-S. Xie, Z.-L. Wang, The shape evolution of gold seeds and gold@silver core-shell nanostructures, Nanotechnology. 20 (30) (2009) 305602, https://doi.org/10.1088/0957-4484/20/30/305602.
[55] W. Wei, X. Mao, L.A. Ortiz, D.R. Sadoway, Oriented silver oxide nanostructures synthesized through a template-free electrochemical route, J. Mater. Chem. 21 (2) (2011) 432–438, https://doi.org/10.1039/C0JM02214D.
[56] J.A. McMillan, Magnetic properties and crystalline structure of AgO, J. Inorg. Nucl. Chem. 13 (1-2) (1960) 28–31, https://doi.org/10.1016/0022-1902(60)80231-X.
[57] G. Santoro, S. Yu, M. Schwartzkopf, P. Zhang, S. Koyiloth Vayalil, J.F.H. Risch, M. A. Rübhausen, M. Hernández, C. Domingo, S.V. Roth, Silver substrates for surface-enhanced Raman scattering: correlation between nanostructure and Raman scattering enhancement, Appl. Phys. Lett. 104 (24) (2014) 243107, https://doi.org/10.1063/1.4884423.
[58] S.V. Roth, G. Herzog, V. Körstgens, A. Buffet, M. Schwartzkopf, J. Perlich, M. M. Abul Kashem, R. Döhrmann, R. Gehrke, A. Rothkirch, K. Stassig, W. Wurth, G. Benecke, C. Li, P. Fratzl, M. Rawolle, P. Müller-Buschbaum, In situ observation of cluster formation during nanoparticle solution casting on a colloidal film, J. Phys. Condens. Matter. 23 (25) (2011) 254208, https://doi.org/10.1088/0953-8984/23/25/254208.
[59] C.J. Brett, S. Montani, M. Schwartzkopf, R.A.T.M. van Benthem, J.F.G.A. Jansen, G. Griffini, S.V. Roth, M.K.G. Johansson, Revealing structural evolution occurring from photo-initiated polymer network formation, Commun. Chem. 3 (2020) 1–7, https://doi.org/10.1038/s42004-020-0335-9.
[60] M. Witte, S. Jaspers, H. Wenck, M. Rübhausen, F. Fischer, Noise reduction and quantification of fiber orientations in greyscale images, PLoS One. 15 (2020) 1–21. https://doi.org/10.1371/journal.pone.0227534.
[61] Z. Jiang, GIXSGUI: A MATLAB toolbox for grazing-incidence X-ray scattering data visualization and reduction, and indexing of buried three-dimensional periodic nanostructured films, J. Appl. Crystallogr. 48 (2015) 917–926, https://doi.org/10.1107/S1600576715004434.
[62] P. Norby, R. Dinnebier, A.N. Fitch, Decomposition of silver carbonate; the crystal structure of two high-temperature modifications of Ag2CO3, Inorg. Chem. 41 (14) (2002) 3628–3637, https://doi.org/10.1021/ic0111177.
[63] A. Werner, H.D. Hochheimer, High-pressure X-ray study of Cu2O and Ag2O, Phys. Rev. B - Condens. Matter Mater. Phys. 2 (1982) 2–7.
[64] T. Wada, T. Sakuma, R. Sakai, H. Uehara, Xianglian, H. Takahashi, O. Kamishima, N. Igawa, S.A. Danilkin, Inter-atomic force constants of Ag2O from diffuse neutron scattering measurement, Solid State Ionics 225 (2012) 18–21, https://doi.org/10.1016/j.ssi.2012.02.007.
[65] H. Seidel, L. Csepregi, A. Heuberger, H. Baumgärtel, Anisotropic etching of crystalline silicon in alkaline solutions: I. Orientation dependence and behavior of passivation layers, J. Electrochem. Soc. 137 (11) (1990) 3612–3626, https://doi.org/10.1149/1.2086277.
[66] F.Y. Wu, Theory of resistor networks: The two-point resistance, Exactly Solved Model. A Journey Stat. Mech. Sel. Pap. with Comment. (2009) 489–509. https://doi.org/10.1088/0305-4470/37/26/004.

Electrical and Network Properties of Flexible Silver-Nanowire Composite Electrodes under Mechanical Strain

Tomke E. Glier*, Marie Betker, Maximilian Witte, Toru Matsuyama, Lea Westphal, Benjamin Grimm-Lebsanft, Florian Biebl, Lewis O. Akinsinde, Frank Fischer, and Michael Rübhausen*

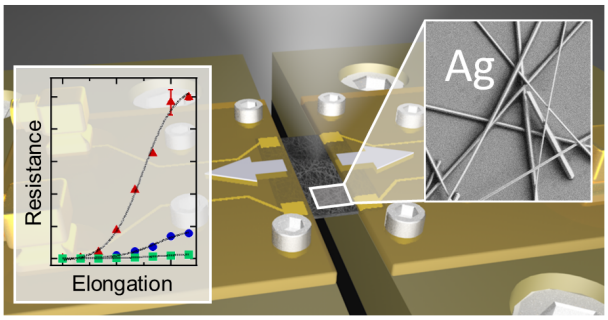

Nanoscale - **November 2020**
https://doi.org/10.1039/D0NR05734G

Nanoscale

PAPER

View Article Online
View Journal | View Issue

Cite this: *Nanoscale*, 2020, **12**, 23831

Electrical and network properties of flexible silver-nanowire composite electrodes under mechanical strain†

Tomke E. Glier, *[a] Marie Betker,[a] Maximilian Witte, [a,b] Toru Matsuyama, [c] Lea Westphal,[a] Benjamin Grimm-Lebsanft, [a] Florian Biebl, [a] Lewis O. Akinsinde,[a] Frank Fischer[b] and Michael Rübhausen*[a]

Flexible and conductive silver-nanowire photopolymer composites are fabricated and studied under mechanical strain. The initial resistances of the unstretched flexible composites are between 0.27 Ω mm^{-1} and 1.2 Ω mm^{-1} for silver-nanowire concentrations between 120 μg cm^{-2} and 40 μg cm^{-2}. Stretching of the samples leads to an increased resistance by a factor of between 72 for 120 μg cm^{-2} and 343 for 40 μg cm^{-2} at elongations of 23%. In order to correlate network morphology and electrical properties, micrographs are recorded during stretching. The Fiber Image Network Evaluation (FINE) algorithm determines morphological silver-nanowire network properties under stretching. For unstretched and stretched samples, an isotropic nanowire network is found with only small changes in fiber orientation. Monte-Carlo simulations on 2D percolation networks of 1D conductive wires and the corresponding network resistance due to tunneling of electrons at nanowire junctions confirm that the elastic polymer matrix under strain exhibits forces in agreement with Hooke's law. By variation of a critical force distribution the resistance curves are accurately reproduced. This results in a model that is dominated by quantum-mechanical tunneling at nanowire junctions explaining the electrical behavior and the sensitivity of nanowire-composites with different filler concentrations under mechanical strain.

Received 3rd August 2020,
Accepted 23rd September 2020

DOI: 10.1039/d0nr05734g

rsc.li/nanoscale

Introduction

Functional polymer composites have caught the attention of materials science and industry due to their enormous versatility for applications in *e.g.* medicine, electronics, and functional printing.[1–3] Conductive films are of great interest because of their various electronic and optical applications in solar cells and OLEDs.[4–6] Silver-nanowire polymer composites are a promising alternative to indium tin oxide. They offer a scalable process for large scale, flexible, conductive materials, as used in integrated photovoltaics, touch screens, and flexible electronics.[7–11] Furthermore, the embedding of metal nanoparticles in a printable polymer matrix enables a fabrication process with a high design flexibility and allows rapid prototyping. Additive manufacturing of components has developed over the last 25 years to be an important and innovative part of the industrial process.[12–14] As a matrix material, photopolymers have tunable viscosities, are curable by illumination with UV-light, and are well suited to create three dimensional structures *via* layer by layer additive manufacturing. For example, a flexible silver-nanowire composite capacitor was built and demonstrated recently.[15] Due to the fact, that the matrix material of the composite is exchangeable and tunable in *e.g.* color, optical, and mechanical properties, the composites can easily be tailored to their respective application.[15] Bending and stretching of silver nanowire composite electrodes have been investigated from many different perspectives.[16–22] Flexible electrodes as used in foldable touch displays are some of the most demanding applications of these materials.

We have investigated flexible electrodes, which are based on silver nanowires embedded in a flexible and photocurable polymer matrix. In order to test their deformation and durability, we performed mechanical strain tests, *in situ* conductivity, and light microscopy measurements. The conductivity measurements monitor the functionality of the films. By light microscopy, the nanowire network morphology was observed.

[a]*Institut für Nanostruktur- und Festkörperphysik, Center for Free Electron Laser Science (CFEL), Universität Hamburg, Luruper Chaussee 149, 22761 Hamburg, Germany. E-mail: tglier@physnet.uni-hamburg.de, ruebhausen@physnet.uni-hamburg.de*

[b]*Beiersdorf AG, Unnastraße 48, 20245 Hamburg, Germany*

[c]*Max-Planck Institute for the Structure and Dynamics of Matter, Luruper Chaussee 149, 22761 Hamburg, Germany*

†Electronic supplementary information (ESI) available: Analysis of light microscopy images and Monte-Carlo simulated nanowire networks using the FINE algorithm. See DOI: 10.1039/d0nr05734g

In order to obtain quantitative information on the network structure change upon stretching, the Fiber Image Network Evaluation (FINE) algorithm was employed.[23,24] Based on the micrographs, the FINE algorithm determines the number of fiber families, their amplitudes, mean orientation and dispersion, based on the cumulative angular orientation distribution. Monte-Carlo simulations on the nanowire networks and the corresponding network resistance confirm that the elastic polymer matrix under strain exhibits forces acting on the nanowire junctions in agreement with Hooke's law. The experimental data were reproduced by variation of a critical force distribution leading to a model explaining the electrical behavior of nanowire-composites with different concentrations under mechanical strain.

Experimental part

Sample preparation

Ag NWs were synthesized as described in ref. 15. After the synthesis, the Ag-NW suspension was washed successively twice with isopropanol, twice with acetone and twice with isopropanol. After each washing step, the suspension was centrifuged at 2000 rpm for 10 min. The supernatant was removed and replaced with fresh solvent. No further post-processing or welding was carried out to ensure a flexible nanowire network. The resulting Ag-NW isopropanol suspension was drop-casted on a solvent-cleaned glass substrate using a 3 cm^2 template. The dried Ag-NW networks were coated with the liquid polymer resin Flexible (Formlabs, USA) by using a doctor blade, which was moved over the sample in a defined distance to the glass substrate. The polymer layer with a thickness of around 150 μm was cross-linked with a laser driven UV light source EQ-99X (Energetiq, USA) for 100 s. Remaining resin was removed after the curing process with isopropanol and acetone. Finally, the samples were removed from the substrate.

Characterization and stretching

For scanning electron microscopy measurements, a commercial field emission scanning electron microscope (FE-SEM Zeiss, Germany) was used. For conductivity measurements a DC voltage/current source GS200 (Yokogawa, Japan) and the 34401A 6 $\frac{1}{2}$ Digit Multimeter (Keysight, USA) were used. A constant current of 0.6 mA was applied to the nanowire composite samples and the voltage drop across the sample in stretching direction was measured. This measurement mode allows the measurement of line- and sheet resistances without the influence of the contact resistance. The resistance measurements were carried out after each stretching step (3.3% relative elongation). The time between each stretching step was 10 min. Light microscopy was carried out using a custom-made microscope with a magnification of 50× consisting of the infinity corrected 50× objective Plan Apo NA = 0.55 (Mitutoyo, Japan) in combination with the MT-40 accessory tube lens (Mitutoyo, Japan), a color industrial camera DFK 37AUX264 (The Imaging Source, Germany), and a LED lamp QTH10/M (Thorlabs, USA). The stretching-setup consists of an aluminum base plate on which two single-axis translation stages PT1/M (Thorlabs, USA) are mounted. Both have a travel range of 25 mm with a translation of 0.5 mm per revolution. Each stage is driven by a stepping motor 0.9-NEMA 17 (Nanotec, Germany). The stepping motors are controlled by a closed-loop-stepping motor-controller SMCI33-2 (Nanotec, Germany) with an encoder controlled guaranteed resolution of 2 μm.

Results and discussion

Fig. 1(a) shows the experiment. Flexible silver-nanowire (Ag-NW) composite films were clamped in a stretching setup, which is based on two linear translation stages motorized with two stepper motors. Two isolating polyether ether ketone (PEEK) base plates were mounted on top of the linear translation stages. The composite samples, behaving like thin rubber like foils, are placed on the PEEK plates and clamped on each site with a small polyimide plate, which contains two gold electrodes. By doing so, the electrical conductivity of the samples can be measured in a four-point geometry.

The samples consist of Ag-NW networks, which were embedded in a flexible photopolymer matrix as described in the Experimental section. The samples have a size of 12 mm × 12 mm and a total thickness of 150 μm. The embedded nanowires extend up to 1 μm into the polymer matrix, resulting in a conductive composite layer at the top site of the sample, which is shown in Fig. 1(b). In Fig. 1(c) a SEM image of Ag NWs drop-casted on a bare silicon wafer is shown. One can see how the nanowire networks are formed and how the thinner wires are flexibly above and below other wires. Nanoparticles (spheres, triangles and plates) arise as marginal side products during the synthesis. The Ag NWs were synthesized by a polyol route and have a pentagonal cross section as discussed in detail in ref. 15. The Ag-NW networks are produced by drop-casting of a Ag-NW suspension on a clean and smooth substrate like silicon or glass. Homogeneous networks of randomly orientated nanowires are formed, which show high conductivities even at small amounts of silver.[15] This is a consequence of a percolative process, which is determined by the high aspect ratio of the used wires. Compared to composites of spherical fillers, anisotropic sticklike fillers reach the percolation threshold at a lower amount of the filler material, decreasing with increasing aspect ratio (length/diameter).[25–28] Furthermore, by using one-dimensional (1D) structures, conductive pathways with a minimum number of terminations can be obtained, which minimizes the influence of the tunneling resistance on the total resistance of the system. Therefore, 1D nano-structures with high aspect ratio are highly desirable for the formation of conductive 2D films. In addition, the small amount of necessary conductive filler material facilitates the fabrication of transparent and conductive composites.[15] In order to fabricate the composites, the drop-casted networks were coated with a photocurable resin. After curing the

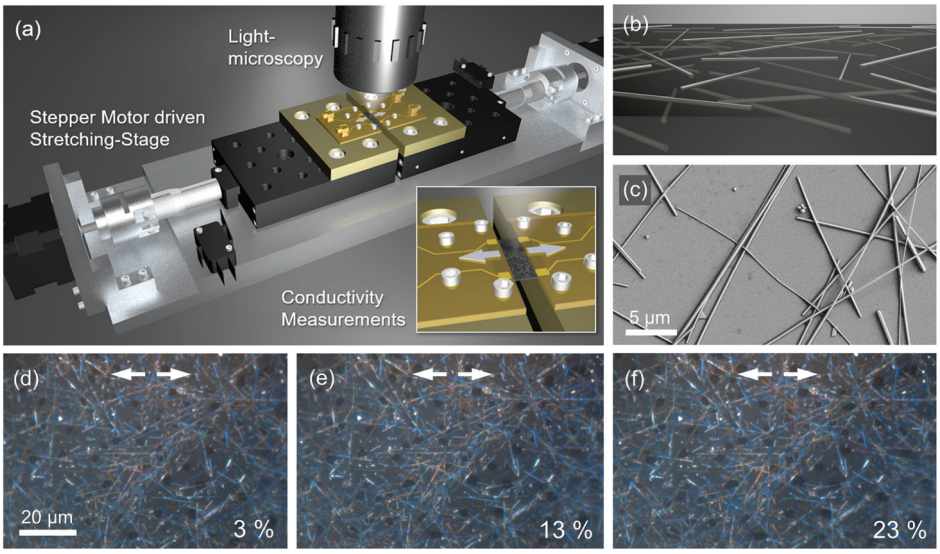

Fig. 1 (a) Representation of the experimental setup. The sample is fixed and contacted with two circuit boards and stretched by two motorized linear translation stages. A custom-made light microscope is installed above the sample. The inset shows the clamped sample in stretching mode. Of the 12 mm × 12 mm samples, an area of 3 mm × 12 mm is stretched. (b) Sketch of Ag NWs, which are embedded in the polymer matrix. (c) SEM image of drop-casted Ag NWs on a silicon wafer without polymer matrix. (d)–(f) Excerpts from light microscopy images of a Ag-NW composite with a Ag-NW concentration of 120 µg cm^{-2} for 3 exemplary stretching steps at 3%, 13%, and 23% elongation, respectively. The elongation is given in relative units (distance of the translation stages after stretching divided by initial distance). The stretching direction is depicted as white arrows.

polymer layer with UV-light, the composite film can be detached from the substrate and subsequently investigated in our stretching setup. Fig. 1(d) shows three micrographs of a Ag-NW composite film during stretching at different elongations. The stretching direction is horizontal and the width of the images corresponds to the relative lengthening of the film during stretching.

In Fig. 2(a) the line resistance of three samples with nanowire concentrations of 40 µg cm^{-2}, 80 µg cm^{-2}, and 120 µg cm^{-2} are shown. The line resistance was measured along the stretching direction and the measured values were divided by the length of the sample, respectively. The initial resistances of the unstretched flexible composites are (0.269 ± 0.002) Ω mm^{-1} for the 120 µg cm^{-2} sample, (0.387 ± 0.001) Ω mm^{-1} for the 80 µg cm^{-2} sample, and (1.193 ± 0.002) Ω mm^{-1} for the 40 µg cm^{-2} sample. The samples were stretched stepwise. Each stretching step corresponds to a relative elongation of 3.3%. One can observe an increase in line resistance for samples with lower Ag-NW concentrations. The increase in resistance during stretching follows a sigmoidal shape with a higher relative increase for lower nanowire concentrations. All curves are saturated after 20% stretching. Since optical measurements require flat sample surfaces, pre-stretching of the samples by 3.3% elongation was necessary. In the following, we, therefore, analyze all our data normalized to the pre-stretched value at 3.3% elongation. The line resistance upon stretching for the

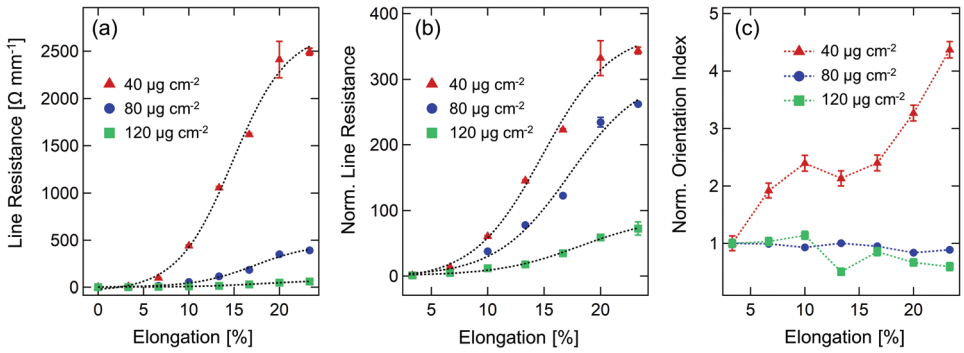

Fig. 2 (a) Line resistance in stretching direction as function of elongation of three samples with a Ag-NW concentration of 40 µg cm^{-2} (red), 80 µg cm^{-2} (blue) and 120 µg cm^{-2} (green). The resistance measurements were carried out after each stretching step (3.3% relative elongation). The dashed line is a sigmoidal guide to the eye. (b) Same experimental data shown in (a) normalized to the value of the pre-stretched sample at 3.3% elongation. (c) Orientation index of the same samples shown in (a). The data was normalized to the value of the pre-stretched sample at 3.3% stretching.

samples shown in Fig. 2(a) normalized to the resistance value at 3.3% are shown in Fig. 2(b). For the 120 μg cm^{-2} sample, an increase by a factor of 72 after stretching by 23% elongation in relation to the value of the pre-stretched sample at 3.3% elongation was observed. A sample with a Ag-NW concentration of 80 μg cm^{-2} shows an increase by a factor of 262 and the resistance of the 40 μg cm^{-2} sample was increased by a factor of 343.

For each stretching step, a light microscopy image was recorded as shown in Fig. 1(d)–(f). These images were analyzed using an algorithm that determines the number of fiber families, their amplitudes, mean orientation and dispersion, based on the cumulative angular orientation distribution, the FINE algorithm.[23] The analysis clearly shows that the nanowire networks consist of one isotropic fiber family (see ESI SI 1† for details). Upon stretching, changes in the overall network morphology are observed by the orientation index as shown in Fig. 2(c).[29] The orientation index represents the degree of fiber orientation in the angular distribution function. A completely isotropic distribution leads to a vanishing orientation index, while a full alignment of the fibers yields an orientation index of one.[23,29] Samples with high concentrations (80 μg cm^{-2} and 120 μg cm^{-2}) show no remarkable changes in orientation, whereas for the 40 μg cm^{-2} sample a change in orientation index by a factor of 4.5 was observed. However, no emerging anisotropic fiber family could be found by the FINE algorithm (see ESI†). The lower the concentration, the greater the impact of individual changes and alignments within the network. Overall, the orientation indices for all samples and all stretching conditions are small (≤0.1) and in the isotropic region. From these results, it becomes clear that changes in network morphology and mean fiber orientation are not the primary effect leading to the observed drastic resistance changes of several orders of magnitude depending on the Ag-NW concentration.

When considering a percolation of randomly orientated 1D wires, the position of the wires, their length, number and orientation, as well as their length distribution are critical parameters. The behavior of a percolation network during stretching conditions can be calculated by a Monte-Carlo simulation on the resistor network formed by overlapping wires in a 2D network. In Fig. 3(a), a sample (350 μm × 350 μm) with a typical length distribution corresponding to the synthesized nanowires and a concentration of 10 μg cm^{-2} is shown. The orientation of the wires was chosen randomly between $-90° \le \theta_i \le 90°$, which results in an isotropic sample. Intersections of the wires were found by using two criteria: if the distance between the centers of two wires i and j is larger than the sum of half the length of wire i and wire j (eqn (1)), an intersection can be excluded. If eqn (1) is fulfilled, the distances A_i and A_j were calculated (see eqn (2) and Fig. 3(b)).[25,26] If $A_i \le L_i/2$ and $A_j \le L_j/2$, an intersection is found.

$$\begin{aligned} d_{ij} &= [(x_i - x_j)^2 + (y_i - y_j)^2]^{1/2} \\ d_{ij} &< \frac{L_i}{2} + \frac{L_j}{2} \end{aligned} \tag{1}$$

$$\begin{aligned} A_i &= d_{ij}\left|\cos(\theta_j + \gamma)/\sin(\theta_j - \theta_i)\right| \\ A_j &= d_{ij}\left|\cos(\theta_i + \gamma)/\sin(\theta_j - \theta_i)\right| \\ \gamma &= \arctan[(y_i - y_j)/(x_i - x_j)] \end{aligned} \tag{2}$$

Due to the fact, that the Ag NW itself is an excellent conductor, the tunneling junctions between the wires determine the total resistance of the network. A sample consisting of N wires (see Fig. 3(c)) can be considered as a resistor network with N nodes and the quantum-mechanical tunneling resistance r_{ij} of the resistor connecting nodes i and j (see Fig. 3(d)).[30–33] For the simulation all tunneling resistances r_{ij} of intersecting wires were assumed to be equal to 1, resulting in a conductance of $c_{ij} = r_{ij}^{-1} = 1$. The resistance between wires, which are not intersecting, is infinity resulting in a conductance of 0. With V_i being the electric potential at the i-th node and I_i being the current flowing in the system at the i-th node, Kirchhoff's Law can be written as

$$\boldsymbol{L}\vec{V} = \vec{I} \tag{3}$$

where $\boldsymbol{L}$ is the Laplace matrix as given in eqn (4):[30]

$$\boldsymbol{L} = \begin{pmatrix} c_{11} & -c_{12} & \cdots & -c_{1N} \\ -c_{21} & c_{22} & \cdots & -c_{2N} \\ \vdots & \vdots & \ddots & \vdots \\ -c_{N1} & -c_{N2} & \cdots & c_{NN} \end{pmatrix}. \tag{4}$$

According to the method presented by Wu *et al.*[30] the resistance of a resistor network between two nodes can be calculated by eqn (5), where ψ_i are the eigenvectors and λ_i are the eigenvalues of $\boldsymbol{L}$.[30]

$$R_{\alpha\beta} = \sum_{i=1}^{N} \frac{1}{\lambda_i} \left|\psi_{i\alpha} - \psi_{i\beta}\right|^2 \tag{5}$$

Wires representing the contacts at the left and the right side of the sample were assumed spanning the whole length of the simulated width. Fig. 3(e) shows the resistance as a function of Ag-NW concentration. The concentration was determined by calculating the silver mass per square centimeter using a mean wire diameter of 200 nm and a silver density of 10.49 g cm^{-3}. The resistance shows an exponential dependence on the concentration, as discussed in previous simulations and experimental studies.[15,16,34] The red solid line depicts an exponential curve as guide to the eye. For an experimental realization of a Ag-NW network, Ag-NW concentrations of 40 μg cm^{-2}–120 μg cm^{-2} were used. These experimental concentrations are by a factor of about 4 higher than the corresponding effective concentrations used for the simulation. We have benchmarked the effective concentration against the silver nanowire concentration observed in the experimental micrographs. The effective concentration of silver that contributes to a conductive percolation network of nanowires is lower due to side products (particles and rods, see Fig. 1(c)) in the Ag-NW suspension used for the experiments and its effective distribution in the composite.

In order to simulate the fiber morphology during stretching of a composite material, one has to consider that the distances

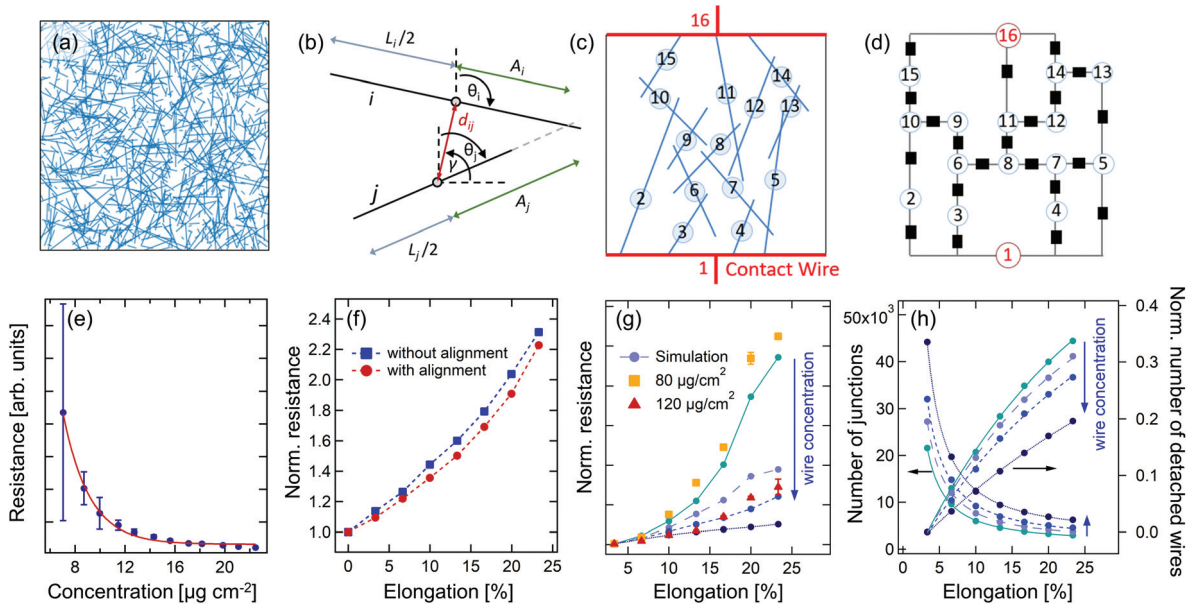

Fig. 3 (a) Exemplary two-dimensional nanowire network with a size of 350 µm × 350 µm and a concentration of 10 µg cm^{-2}. The wires have random angles and positions. The lengths of the wires follow the length distributions that was determined by the analysis of SEM images of real samples. (b) Geometrical quantities, which were used in eqn (1) and (2) to check whether two wires i and j are intersecting. (c) Network of 14 wires and 2 contact wires. The resistance will be calculated between the contact wires 1 and 16. (d) Resistor network corresponding to the network shown in (b). Every node (numbered) represents a wire and every resistor (black squares) depict a wire-to-wire junction with the tunneling resistance r_{ij}. (e) Simulated resistance as a function of nanowire concentration. Each datapoint is the average of 16 simulated samples with a size of 200 µm × 200 µm. (f) Resistance change during simulated stretching conditions based on morphological changes, for elongations between 0 and 23% and a nanowire concentration of 20 µg cm^{-2}. The wire positions were changed according to the changed sample dimensions during stretching. For the red curve, an alignment of the wires was considered. (g) Simulation of the experimental data (circular points in cyan to dark blue) together with the experimental data (yellow squares and red triangles). The curves were normalized to the resistance of the pre-stretched sample at 3.3% elongation. The simulation parameters for the critical force distribution are k_{ij}(A) = 200 N nm^{-1}, k_{ij}(B) = 300 N nm^{-1}, k_{ij}(C) = 700 N nm^{-1}, k_{ij}(D) = 50 000 N nm^{-1}, and p_A = 75%, p_B = 14%, p_C = 4%, and p_D = 7%. The simulated effective concentrations are 18 µg cm^{-2}, 20 µg cm^{-2}, 22 µg cm^{-2} and 30 µg cm^{-2}. The blue arrow depicts the direction of increasing concentration. (h) Number of tunneling junctions and amount of detached wires (wires without undamaged junctions to other wires) for the simulations shown in (g). The curves were fitted by $y = y_0 + Ax^{-1.3}$ (number of junctions) and $y = y_0 + B\exp(-\alpha x)$ (disconnected wires).

between the filler particles in the stretching direction become larger, based on the assumption that the particles follow the matrix. This aspect was simulated by changing the positions of the wires according to the respective elongation. Thus, an increase in resistance by a factor of between 2 and 2.5 was reproducibly observed at an elongation of 23%, see Fig. 3(f) for an exemplary sample with an effective concentration of 20 µg cm^{-2}. In a second step, the impact of wire alignment during stretching was investigated. For this purpose, the x-component dx of the vector that describes a wire was adapted in accordance with the respective elongation to $d\tilde{x} = dx(1 + E_{[\%]}/100)$. The orientation angle of the wire θ_i was then adapted by $\cos(\theta_i) = d\tilde{x}/L_i$, where L_i is the fixed length of a wire i. With these assumptions, the simulation results, in contrast to the experiment, in the formation of an anisotropic fiber family upon stretching as analyzed by the FINE algorithm (see ESI SI 2†). The initial, unstretched samples consist of a single isotropic fiber family and have an orientation index of smaller than 0.05. After stretching, an anisotropic fiber family with orientation in stretching direction is formed, resulting in an orientation index of around 0.5. Both, the isotropic and the anisotropic fiber families co-exist with equal amplitudes. The red curve in Fig. 3(f) represents a sample for which the stretching conditions were simulated by the described changes in terms of position and alignment. We can conclude, that an alignment of the wires in stretching direction does not lead to the drastic resistance changes observed in the experiment. Furthermore, the findings obtained from the microscopy images clearly show, that the simulated alignments are much higher than the observed alignments in the experiment.

The force F used to stretch an elastic polymer matrix can be described by Hooke's law $F = k{\cdot}\Delta x$, where k is a constant factor characteristic for the elastic polymer matrix and Δx is the elongation. This force acts on the nanowire tunneling junctions yielding a strong dependence of the resistance on the quantum-mechanical tunneling matrix element. In order to explain the drastic increase in resistance during stretching observed in the experiments, a critical force at which the individual junctions break and disconnect was introduced implying that the tunneling matrix element becomes infinitesimal small. Considering two wires with the x-positions (x is stretching direction) x_i^0 and x_j^0 before stretching and the positions

after stretching x_i^1 and x_j^1, the acting force F is proportional to the relative movement of the wires, or rather the distance change $F \propto \Delta x_{ij} = |x_i^1 - x_j^1| - |x_i^0 - x_j^0|$. The proportionality constant is the force constant k_{ij}. The critical force for each nanowire tunneling junction should depend on the embedding polymer matrix of the two intersecting nanowires. The top nanowires at the surface of the sample are not completely covered with polymer resulting in a weaker connection to the matrix and the wires embedded in it. The simulated results together with the experimental data for different concentrations are shown in Fig. 3(g). For the simulation shown in Fig. 3(g), a force constant k_{ij} normalized to a critical distance Δx = 1 nm from four junction classes A, B, C, and D with the frequencies p_A, p_B, p_C, and p_D was assigned to each wire-wire junction. They represent the critical forces required to break the respective tunneling junction. The qualitative behavior of the experimental data such as the increase in resistance and the shape of the curves was successfully simulated with k_{ij}(A) = 200 N nm^{-1}, k_{ij}(B) = 300 N nm^{-1}, k_{ij}(C) = 700 N nm^{-1}, k_{ij}(D) = 50 000 N nm^{-1}, and p_A = 75%, p_B = 14%, p_C = 4%, and p_D = 7% (see Fig. 3(g)). We can not only describe the shape of the resistance curves upon stretching but also its change upon concentration and stretching. The simulated networks consist of a total number of wires between 4400 wires for the lowest concentration and 7350 wires for the highest concentration, resulting in an effective concentration between 18 μg cm^{-2} and 30 μg cm^{-2} and a number of tunneling junctions of the wires between 21 700 and 60 500. The number of effectively functional tunneling junctions as well as the normalized number of completely disconnected wires with vanishing tunneling probability (wires that no longer have undamaged connections to other wires) for the simulations in Fig. 3(g) are shown in Fig. 3(h). The number of tunneling junctions was fitted by $y = y_0 + Ax^{-1.3}$ with the same decay constant of −1.3 for all nanowire concentrations. The variable x is the elongation. The lower the nanowire concentration, the lower is the number of junctions in the network resulting in a respective change in offset y_0 and amplitude A. The number of detached wires was fitted by $y = y_0 + B\exp(-\alpha x)$, where y_0 is a constant background of 0.5 and x is the elongation. The amplitude B changes gradually from −0.6 for the lowest concentration to −0.55 for the highest concentration. The decay constant α is also changing from 0.055 for the lowest concentration to 0.025 for the highest concentration.

These results demonstrate and explain the strong concentration dependence and sensitivity of the investigated nanocomposite material under stretching conditions. The decrease of the number of tunneling junctions in the network results in an enhanced sensitivity towards mechanical strain. Even small changes in the number of connections at high elongations lead to large changes in resistance. The observed saturation in the resistance curves can be explained by the existence of a class of tunneling junctions with an infinitely high critical force constant (class D), representing wire-wire connections, which are well embedded in the polymer matrix and highly durable. The lower the concentration, the lower is the number of tunneling junctions of an individual wire to other wires, which is a measure for the connectivity of the network. By looking at the relative number of wires without undamaged junctions to the nanowire network after 23% stretching, we found a linear decrease of this number with increasing concentration. This linear decrease in connectivity leads to drastic changes in the resistivity as shown in Fig. 3(g) and (e).

Conclusions

In conclusion, we have shown that the electrical behavior of Ag-NW networks in flexible polymer composites can be controlled by the Ag-NW concentration and lead to resistance changes of up to three orders of magnitude upon stretching. The samples were investigated by an integrated light microscopy setup that allows to image the Ag-NW composite during stretching. The micrographs were analyzed in terms of changes in network morphology and fiber orientation. Furthermore, we were able to model the composite conductance as a function of concentration and stretching by a Monte-Carlo simulation that considers a resistor network consisting of the resistances resulting from the tunneling junctions between the wires. Moreover, we model and quantitively reproduce the experimentally observed resistance changes upon stretching by means of the interaction between the nanowire network and the polymer matrix. For this, Hooke's Law and a critical force distribution of the nanowire junctions within the composite were derived.

Author contributions

T. E. G. and M. R. designed and supervised the study. M. B. and T. E. G. conducted the experiments and fabricated the samples. M. B., L. W., B. G-L., F. B., L. O. A., T. M., T. E. G., and M. R. designed the experimental setup including the stretching setup, the programming, the light microscope and the conductivity measurements. M. W., F. F, and M. R. analyzed the light microscopy images by the FINE algorithm. T. E. G. conducted the Monte-Carlo simulations. T. E. G. wrote the manuscript with input from all coauthors. All coauthors reviewed the manuscript.

Conflicts of interest

There are no conflicts to declare.

Acknowledgements

The authors thank Birger Höhling and Boris Fiedler for making the circuits boards. We thank Sarah Scheitz, Nils Huse, and Robert Frömter for supporting the SEM measurements and Stephan Roth and Matthias Schwarzkopf for their input and support. This work is funded by the Helmholtz

Society through DESY and by BMBF (Bundesministerium für Bildung und Forschung) 05K19GU5.

References

1 R. Dermanaki Farahani and M. Dubé, *Adv. Eng. Mater.*, 2018, **20**, 1700539.
2 J. F. Tressler, S. Alkoy, A. Dogan and R. E. Newnham, *Composites, Part A*, 1999, **30**, 477–482.
3 S.-B. Park, E. Lih, K.-S. Park, Y. K. Joung and D. K. Han, *Prog. Polym. Sci.*, 2017, **68**, 77–105.
4 S. Lu, Y. Sun, K. Ren, K. Liu, Z. Wang and S. Qu, *Polymers*, 2017, **10**, 5.
5 Y. Xu, X. Wei, C. Wang, J. Cao, Y. Chen, Z. Ma, Y. You, J. Wan, X. Fang and X. Chen, *Sci. Rep.*, 2017, **7**, 45392.
6 W. U. Huynh, J. J. Dittmer and A. P. Alivisatos, *Science*, 2002, **295**, 2425–2427.
7 M. S. Miller, J. C. O'Kane, A. Niec, R. S. Carmichael and T. B. Carmichael, *ACS Appl. Mater. Interfaces*, 2013, **5**, 10165–10172.
8 J. Li, Y. Tao, S. Chen, H. Li, P. Chen, M. Z. Wei, H. Wang, K. Li, M. Mazzeo and Y. Duan, *Sci. Rep.*, 2017, **7**, 1–9.
9 X.-Y. Zeng, Q.-K. Zhang, R.-M. Yu and C.-Z. Lu, *Adv. Mater.*, 2010, **22**, 4484–4488.
10 X. He, F. Duan, J. Liu, Q. Lan, J. Wu, C. Yang, W. Yang, Q. Zeng and H. Wang, *Materials*, 2017, **10**, 1362.
11 T. Sannicolo, M. Lagrange, A. Cabos, C. Celle, J.-P. Simonato and D. Bellet, *Small*, 2016, **12**, 6052–6075.
12 E. MacDonald and R. Wicker, *Science*, 2016, **353**, aaf2093.
13 M. Hofmann, *ACS Macro Lett.*, 2014, **3**, 382–386.
14 A. D. Valentine, T. A. Busbee, J. W. Boley, J. R. Raney, A. Chortos, A. Kotikian, J. D. Berrigan, M. F. Durstock and J. A. Lewis, *Adv. Mater.*, 2017, **29**, 1703817.
15 T. E. Glier, L. Akinsinde, M. Paufler, F. Otto, M. Hashemi, L. Grote, L. Daams, G. Neuber, B. Grimm-Lebsanft, F. Biebl, D. Rukser, M. Lippmann, W. Ohm, M. Schwartzkopf, C. J. Brett, T. Matsuyama, S. V. Roth and M. Rübhausen, *Sci. Rep.*, 2019, **9**, 6465.
16 A. R. Madaria, A. Kumar, F. N. Ishikawa and C. Zhou, *Nano Res.*, 2010, **3**, 564–573.
17 W. Hu, X. Niu, L. Li, S. Yun, Z. Yu and Q. Pei, *Nanotechnology*, 2012, **23**, 344002.
18 R. Wang, H. Zhai, T. Wang, X. Wang, Y. Cheng, L. Shi and J. Sun, *Nano Res.*, 2016, **9**, 2138–2148.
19 W. Xu, L. Zhong, F. Xu, W. Shen, W. Song and S. Chou, *ACS Appl. Nano Mater.*, 2018, **1**, 3859–3866.
20 X. Crispin, F. L. E. Jakobsson, A. Crispin, P. C. M. Grim, P. Andersson, A. Volodin, C. van Haesendonck, M. Van der Auweraer, W. R. Salaneck and M. Berggren, *Chem. Mater.*, 2006, **18**, 4354–4360.
21 J. Liang, L. Li, K. Tong, Z. Ren, W. Hu, X. Niu, Y. Chen and Q. Pei, *ACS Nano*, 2014, **8**, 1590–1600.
22 W. Xu, L. Zhong, F. Xu, W. Song, J. Wang, J. Zhu and S. Chou, *Small*, 2019, **15**, 1805094.
23 M. Witte, S. Jaspers, H. Wenck, M. Rübhausen and F. Fischer, *Sci. Rep.*, 2020, **10**, 10888.
24 M. Witte, S. Jaspers, H. Wenck, M. Rübhausen and F. Fischer, *PLoS One*, 2020, **15**, e0227534.
25 I. Balberg and N. Binenbaum, *Phys. Rev. B: Condens. Matter Mater. Phys.*, 1983, **28**, 3799–3812.
26 G. E. Pike and C. H. Seager, *Phys. Rev. B: Solid State*, 1974, **10**, 1421–1434.
27 S. H. Munson-McGee, *Phys. Rev. B: Condens. Matter Mater. Phys.*, 1991, **43**, 3331–3336.
28 S. I. White, R. M. Mutiso, P. M. Vora, D. Jahnke, S. Hsu, J. M. Kikkawa, J. Li, J. E. Fischer and K. I. Winey, *Adv. Funct. Mater.*, 2010, **20**, 2709–2716.
29 C. Bayan, J. M. Levitt, E. Miller, D. Kaplan and I. Georgakoudi, *J. Appl. Phys.*, 2009, **105**, 102042.
30 F. Y. Wu, *J. Phys. A: Math. Gen.*, 2004, **37**, 6653–6673.
31 S.-H. Yook, W. Choi and Y. Kim, *J. Korean Phys. Soc.*, 2012, **61**, 1257–1262.
32 X. Ni, C. Hui, N. Su, W. Jiang and F. Liu, *Nanotechnology*, 2018, **29**, 075401.
33 I. Balberg, N. Binenbaum and C. H. Anderson, *Phys. Rev. Lett.*, 1983, **51**, 1605–1608.
34 K. K. Kim, S. Hong, H. M. Cho, J. Lee, Y. D. Suh, J. Ham and S. H. Ko, *Nano Lett.*, 2015, **15**, 5240–5247.

Conductance-Strain Behavior in Silver-Nanowire Composites: Network Properties of a Tunable Strain Sensor

Tomke E. Glier*, Marie Betker*, Benjamin Grimm-Lebsanft, Sarah Scheitz, Toru Matsuyama, Lewis O. Akinsinde, and Michael Rübhausen*

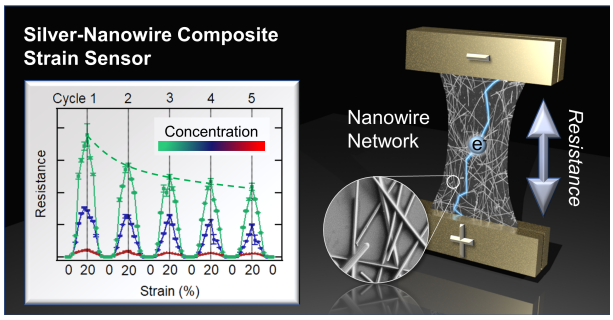

Nanotechnology - **June 2021**

Conductance-Strain Behavior in Silver-Nanowire Composites: Network Properties of a Tunable Strain Sensor

Tomke E. Glier[1*†], Marie Betker[1*†], Benjamin Grimm-Lebsanft[1], Sarah Scheitz[1], Toru Matsuyama[2], Lewis O. Akinsinde[1] and Michael Rübhausen[1*]

[1] Institut für Nanostruktur- und Festkörperphysik, Center for Free Electron Laser Science (CFEL), Universität Hamburg, Luruper Chaussee 149, 22761, Hamburg, Germany.
[2] Max-Planck-Institut für Struktur und Dynamik der Materie, Luruper Chaussee 149, 22761 Hamburg, Germany.

E-mail: TEG tglier@physnet.uni-hamburg.de; MB marie.betker@desy.de; MR mruebhau@physnet.uni-hamburg.de

Received xxxxxx
Accepted for publication xxxxxx
Published xxxxxx

Abstract

Highly flexible and conductive nano-composite materials are promising candidates for stretchable and flexible electronics. We report on the strain-resistance relation of a silver-nanowire photopolymer composite during repetitive stretching. Resistance measurements reveal a gradual change of the hysteretic resistance curves towards a linear and non-hysteretic behavior. Furthermore, a decrease in resistance and an increase in electrical sensitivity to strain over the first five stretching cycles can be observed. Sensitivity gauge factors between 10 and 500 at 23 % strain were found depending on the nanowire concentration and stretching cycle. We model the electrical behavior of the investigated silver nanowire composites upon repetitive stretching considering the strain induced changes in the local force distribution within the polymer matrix and the tunnel resistance between the nanowires by using a Monte Carlo method.

Keywords: silver-nanowire composite, strain sensor, strain-resistance behavior, flexible electronics, functional printing, Monte Carlo simulation

1. Introduction

Flexible electronic devices are subject of recent research as they can be used in a wide spectrum of applications such as displays[1–3], piezoelectric generators[4], energy storage devices[5], in various fields like health care[6], and renewable energy[7]. The combination of flexible substrates like PDMS or PET with conducting/semiconducting nanomaterials such as silicon, graphene, or metallic nanotubes, -dots, and -wires is a promising way to manufacture flexible and conductive composites.[8,9] Silver-nanowire (Ag-NW) networks have proven to be a suitable conductive filler due to their excellent conductivity, high transparency, and potential to develop flexibility.[10,11] High aspect ratios are advantageous for a high network connectivity and a low percolation threshold and, therefore, enable 2D network properties even with a small amount of material.[12,13] A 3D printable polymer matrix enables functional additive manufacturing of these materials.[14] However, the resilience of elastomeric nanowire

polymer composites is still crucial for the later performance. The embedding of 2D nanowire networks in a polymer matrix leads to highly conductive and thin composite layers. For this purpose, the nanowires are usually applied from a suspension to an auxiliary substrate, then covered with a liquid polymer resin, and peeled off after curing.[15–17] In nanowire networks without post-treatment, the nanowire junctions remain flexible when stretched and the network conductivity recovers after the material has been relaxed.[18] During the wet-chemical and scalable Ag-NW synthesis, a stabilizing polymer ligand shell around the nanowires is created.[19] Thus, no direct contact between nanowires within the network can be achieved and the tunneling resistances between the nanowires dominate the network conductivity.[20] Great efforts have been made to produce modern strain sensors based on carbon nanotubes or metal nanowire composites with high sensitivity, biocompatibility, ease of manufacture, and high stability.[17,21–27] The gauge factor (GF), which is defined as the slope of the change in electrical resistance or capacitance divided by the applied strain, is an often-used measure for the sensitivity of a strain sensor. Nano-composite based strain sensors exhibit GFs in a wide range. Typical Ag-NW PDMS composites have been reported to have tunable GFs in the range of 2-14.[17] In general, the GFs are controlled by the density of the used nanowire networks.[21] Crack-induced Ag-NW strain sensors with GFs of 30 at 100 % strain have been reported.[22] For zinc oxide (ZnO) nanowire polystyrene composites with nanobrush ZnO-NWs a GF of 116 has been found.[28] Ultra-sensitive strain sensors with GFs > 1000 have been fabricated based on graphene thin film polymer composites.[29]

In this article, we report on the strain-resistance performance of highly conductive, flexible and printable Ag-NW photopolymer composites with different nanowire concentrations (40 µg cm^{-2}, 80 µg cm^{-2}, and 120 µg cm^{-2}) under repetitive strain by using a customized stretching-setup. The composites consist of drop-casted Ag-NW networks, which are embedded in a flexible and printable polymer matrix.[14,20] Our composites show a gradual change of the hysteretic resistance curves to a linear dependence and an improved conductivity after 5 stretching cycles. GFs between 10 and 500 at 23.33 % strain were found depending on the nanowire concentration. We model the strain-resistance behavior of the Ag-NW composites based on the local force distribution within the polymer matrix and the tunneling resistance between the nanowires by a Monte Carlo method.

2. Materials and Methods

Figure 1(a) shows a thin layer of Ag-NWs drop-casted on a silicon wafer forming a nanowire network with a concentration of around 50 µg cm^{-2}. The Ag-NWs were synthesized *via* a polyol route and stored in isopropanol with a concentration of 2 g L^{-1}.[14,19,20,30] By stepwise washing with acetone and isopropanol remaining educts, mainly polyvinylpyrrolidone (PVP), were removed from the nanowire reaction solution.[14,20] Initial sheet resistances of the drop-casted nanowire networks in the range of 10 – 15 Ω/sq at an optical transmission of 90 % have been obtained without further post-treatment.[14] Figure 1(b) shows nanowires of the same synthesis batch shown in (a) at a higher magnification. Networks are formed by nanowires laying above and below each other without welding or bonding between nanowires. This allows flexible sliding of the nanowires during stretching and a full recovering of the network resistance after relaxation.[18]

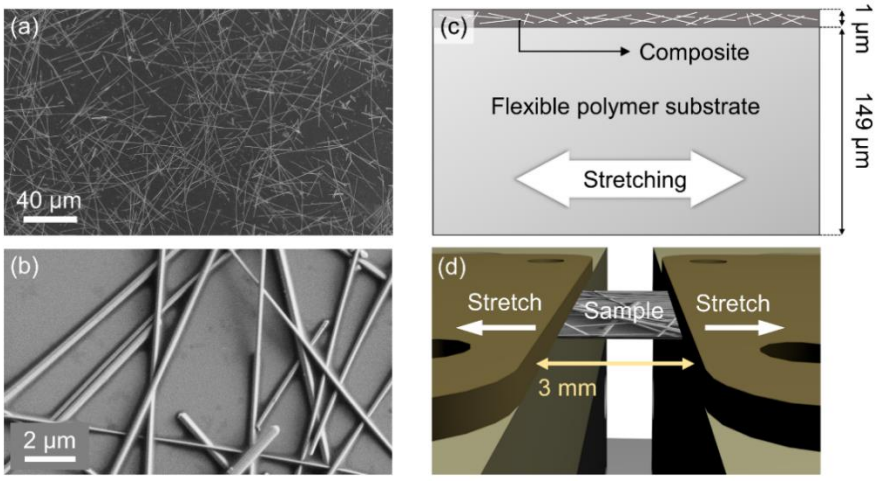

Figure 1. Stretching of Ag-NW composite samples. (a) Scanning electron micrograph of Ag-NWs deposited on a silicon wafer (before coating with polymer, $c_{NW} \approx 50$ µg cm^{-2}). (b) High magnification scanning electron micrograph of Ag-NWs deposited on a silicon wafer. (c) Cross-sectional schematic view on the composite samples. The samples exhibit a total thickness of around 150 µm with a 1 µm composite top layer. (d) Sketch of the stretching experiment. The sample is clamped by two electrodes for conductivity measurements. Uniaxial strain is applied by two stepper-motor driven translation stages.

The overall sample structure used in our experiments is shown in Figure 1(c). The nanowire suspension was first drop-casted on an auxiliary substrate like silicon or glass to create two-dimensional nanowire networks. In a next step, these networks were coated with a liquid urethane-acrylate based photopolymer resin (Formlabs Flexible). A constant layer thickness was obtained by using a doctor blade, which was moved over the sample in a defined distance to the substrate. The polymer layer was cured by illumination with UV light (laser driven light source EQ-99X Energetiq) for 100 s and the sample was peeled off from the substrate resulting in a conductive composite top layer with a thickness of around 1 µm. The total sample size was (12 x 12) mm^2. More details are given in the supporting information (SI 1 and SI 2). The use of the flexible and 3D printable polymer matrix (Formlabs Flexible) enables functional printing of the investigated material as already demonstrated in [14] by printing a flexible Ag-NW capacitor.

A sketch of the used stretching setup is illustrated in Figure 1(d). The samples were clamped between the gold contacts of polyimide plates for conductivity measurements. The free-standing sample area between the two clamps had a size of (3 x 12) mm^2. Uniaxial strain was applied to the sample by two encoder-controlled stepper-motors (0.9-NEMA 17, Nanotec) driving micrometer translation stages (PT1/M, Thorlabs). The composites were stretched uniformly from both sides in 100 µm steps up to a maximum elongation of 23.33 %. Subsequently, the composites were relaxed in 100 µm steps back to the starting position (see SI 3). After each step the electrical resistance was measured (see SI 4 for details) by using a DC voltage/current source (GS200, Yokogawa Japan) and a digital multimeter (34401A 6 12, Keysight USA). A constant current of 0.6 mA was applied to the nanowire composite samples and the voltage drop across the sample in stretching direction was measured.

For scanning electron microscopy measurements, a commercial field emission scanning electron microscope (FE-SEM Zeiss, Germany) was used.

3. Results

3.1 Experimental Results

Figure 2(a) shows the line resistances in stretching direction for five stretching cycles as a function of elongation for three samples with a nanowire concentration of 40 µg cm^{-2}, 80 µg cm^{-2}, and 120 µg cm^{-2}, respectively. The initial resistances of the investigated samples before stretching are 0.9 Ω mm^{-1} (R_{Sheet} = 31.9 Ω sq^{-1}) for a concentration of 40 µg cm^{-2}, 2.9 Ω mm^{-1} (R_{Sheet} = 67.4 Ω sq^{-1}) at 80 µg cm^{-2}, and 0.7 Ω mm^{-1} (R_{Sheet} = 21.7 Ω sq^{-1}) at 120 µg cm^{-2}. The deposition of the nanowires and, thus, the network formation is a stochastic process and the initial network resistances are distributed for different samples of the same concentration.[14] However, the qualitative behavior of the samples during stretching and relaxation was reproducible for more than 30 individual samples. We, therefore, normalize the data to the resistance values of the pre-stretched samples at 6.66 % elongation of the first stretching cycle. The detailed shape of a single stretching curve of the same material has been analyzed and modelled in [20].

The inset in Figure 2(a) shows the first stretching cycle of the 80 µg cm^{-2} sample, which exhibits a hysteresis between the resistance curve upon stretching (dark blue) and relaxation (light blue), respectively. The solid lines depict sigmoidal fits to the data. In Figure 2(a), the hysteresis can also clearly be seen in the non-symmetrical shape of the resistance curves for all three concentrations in the first two stretching cycles. We observe a decrease in hysteresis for all samples as a function of stretching cycle up to the fifth cycle (see SI Table S1 and Figure S3 – S5), resulting in a symmetric stretching and relaxation after 4 cycles. Beside the decrease of the hysteresis width, the resistance values itself are decreasing systematically as a function of stretching. Figure 2(b) shows the resistances at 23.33 % strain depending on concentration normalized to the respective resistance of the pre-stretched samples at 6.66 % of the first cycle. Samples with a lower concentration show a higher sensitivity of the network and correspondingly a higher change in resistance upon stretching due to the lower network connectivity. The resistance recovers after a full relaxation for all three concentrations as shown in Figure 2(a).

In Figure 2(c) the normalized line resistances as a function of elongation during the fifth stretching cycles of the three samples are shown. The data are normalized to the initial pre-stretched line resistance at 6.66 % elongation of the first stretching cycle. During further stretching and relaxation a transition is observed, where the resistance changes are concentration dependent. In this so-called sensor region, the line resistance of each sample increases and decreases linearly. Their slopes increase with decreasing Ag-NW concentration. A measure for the sensitivity of a strain sensor is the Gauge Factor (GF), which is defined as

$$GF = \frac{(R - R_0)/R_0}{(L - L_0)/L_0} \ , \qquad (1)$$

where R and L denote the resistance and length of the strained sample and R_0 and L_0 are the resistance and length of the unstrained sample, respectively. Figure 2(d) shows the GF for the resistance and length at 23 % elongation in respect of the resistance and length at 6.66 % strain. The GF is increasing for all three samples as a function of stretching cycle, which is attributed to the stronger decrease in resistance at small elongations compared to the decrease in resistance at 23 % elongation. During the first stretching cycle, the GF scales

with the silver nanowire concentration linearly with an increased GF for lower network density. For additional stretching cycles, a clear cross-over between the high-concentration sample (120 µg cm^{-2}) and samples with lower concentration (40 µg cm^{-2} and 80 µg cm^{-2}) can be observed. The high concentration sample has a GF of 7.8 for the sample in the first stretching cycle and 31 in the fifth cycle. However, the low-concentration samples (40 µg cm^{-2} and 80 µg cm^{-2}) converge at cycle 4 with a mean GF of around 450. Thus, we can conclude that the composite resistance is decreasing over multiple stretching cycles. Their hysteretic behavior is reduced over the first five stretching cycles and the sensitivity is increased.

3.2 Numerical Modeling

In the following, the electrical properties of Ag-NW composites upon stretching are simulated by a Monte Carlo method. For this purpose, networks of randomly oriented nanowires ($-90° \leq \theta \geq 90°$) with a random position (x_i, y_i) within a certain sample size and a length L according to the length distribution determined by SEM analysis (see [20]) are created as illustrated in Figure 3(a). In a next step, these networks are translated into resistor networks, where each nanowire is a node and each nanowire junction is a tunnel resistor with a normalized tunneling resistance of $r_{ij} = 1$, resulting in a conductance of $c_{ij} = r_{ij}^{-1} = 1$ (see Figure 3(a)). The tunneling resistance between all wires, which are not intersecting, is infinity resulting in a conductance of zero.

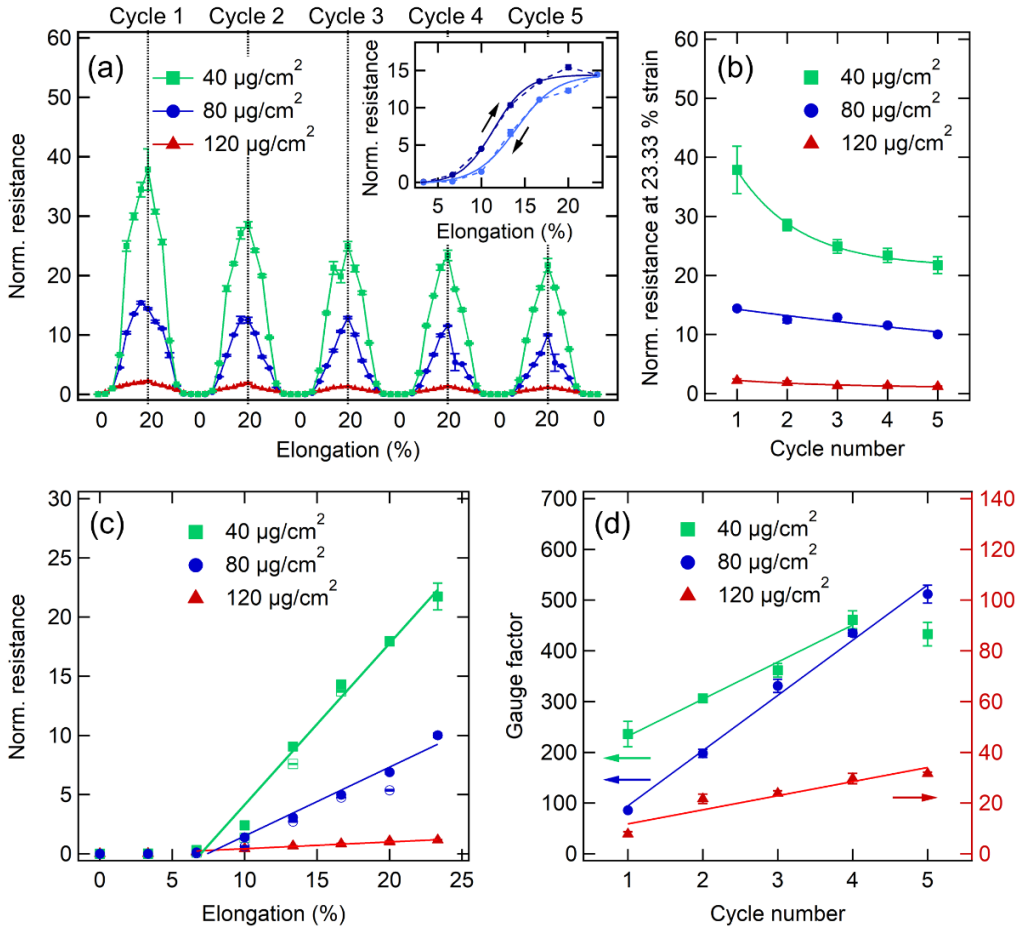

Figure 2. (a) Normalized line resistance in stretching direction as a function of elongation for five stretching cycles. Three samples with Ag-NW concentrations of 40 µg cm^{-2} (green), 80 µm cm^{-2} (blue), and 120 µm cm^{-2} (red) are shown. The inset shows the line resistance during the first stretching (dark blue) and relaxation (light blue) of the sample with a nanowire concentration of 80 µg cm^{-2}. (b) Amplitude (max. resistance) as a function of stretching cycle for the same samples shown in (a). (c) Normalized line resistance for the three samples during the fifth stretching cycle. Filled markers depict the data during stretching and blank markers represent the data during relaxation. Linear fits (solid lines) between 6.66 % strain and 23.33 % strain are used as guide to the eye. (d) Gauge factor as a function of stretching cycle for the three investigated nanowire concentrations. The gauge factor is defined as $[(R_{23\%}-R_{6\%})/R_{6\%}]/[(L_{23\%}-L_{6\%})/L_{6\%}]$. The solid lines represent linear fits to the data.

Since silver is an excellent conductor, the resistance of the nanowire itself can be neglected and accordingly the tunnel resistance between the nanowires dominate the network resistance. The network resistance of the random resistor network is calculated as demonstrated by Wu *et al.*.[31] More detailed information on the simulation principle is given in [20].

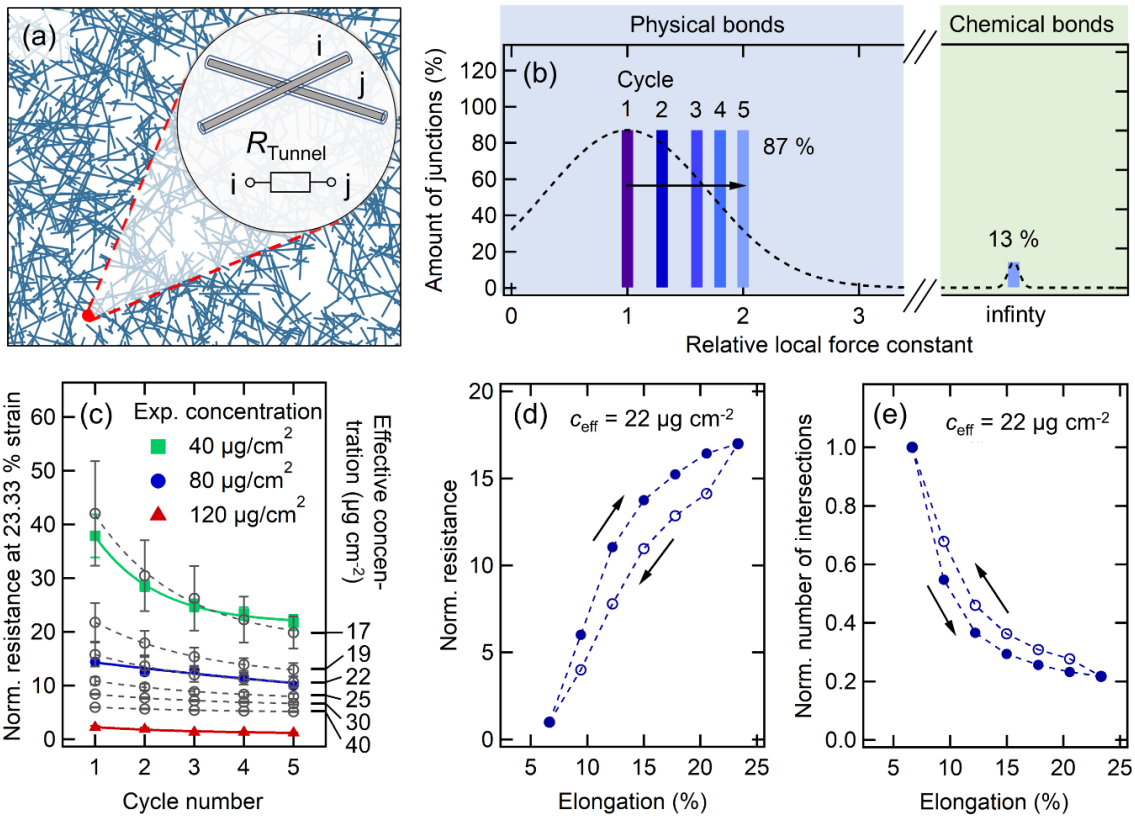

Figure 3. (a) Illustration of Monte Carlo simulated Ag-NW networks. Nanowires with random positions, random orientations, and lengths randomly drawn from a given length distribution are forming a 2D network. Each nanowire junction *ij* represents a tunnel resistor as shown in the inset. (b) Local force constant histogram. Class I (87 %) represents the class of weak bonds within the polymer matrix (hydron bonds). Class II (13 %) is taken to be infinity representing chemical bonds. The mean force constant of class I is shifting to higher values as a function of stretching cycle (black arrow). (c) Resistance at 23.33 % strain normalized to the resistance value of the first stretching cycle at 6.66 % as a function of stretching cycle for different nanowire concentrations. The filled markers (red, blue, and green) depict the experimental data (see Figure 2(b)). Simulated results (n = 8) are presented in gray for effective concentrations between 17 µg cm^{-2} and 40 µg cm^{-2} (see right axis). (d) Simulated normalized resistance as a function of elongation during stretching and relaxation, demonstrating the hysteretic behavior (see Figure 2(a) inset). (e) Normalized number of intersections within the simulated sample shown in (d).

In order to model the change in network resistance upon stretching, the corresponding changes in network connectivity have to be considered. First, each individual nanowire junction of the initial Monte Carlo simulated network is identified. We consider a distribution of local force constants within the polymer matrix, determining the local elongation and, thus, the local shifting of the nanowires upon stretching. For two intersecting wires i and j with the positions x_i and x_j, the local elongation Δx_{local} at the nanowire junction is defined as the relative movement of the nanowires $\Delta x_{ij} = \left|x_i^1 - x_j^1\right| - \left|x_i^0 - x_j^0\right|$. Here, x_{ij}^0 is the initial x-position of the wires i and j, respectively, and x_{ij}^1 is the respective x-position after stretching. In agreement with other publications, the cut-off distance for the tunnel current was taken to be 1 nm.[21,32,33] We assume two classes of local force constants: Class I is characterized by elastomeric polymer chains bonded physically by hydrogen and Van-der-Waals bonds. Class II represents short chain elements with less elasticity dominated mainly by chemical bonds between the chain elements and, therefore, exhibits a much higher local force constant. In order to simulate the network properties within the polymer matrix, the nanowire junctions are randomly assigned to the two force

constant classes. The higher the local force constant at a nanowire junction, the lower the local elongation following Hooke's law $F_{global} = k_{local} \cdot \Delta x_{local}$. As a consequence, nanowire junctions of class II remain intact over the complete stretching. This is the reason why the mean force constant of class II is set to infinity. Nanowire junctions of class I easily exceed the cut-off distance ($F_{global}/k_{local} = \Delta x_{crit} = 1$ nm) at a certain elongation making the network less connected and conductive. This approach allows a local mapping of the matrix force distribution on the scale of the nanowire network junctions. The lack of welded intersections leads to the elasticity of the network allowing us to assume a full recovery of nanowire junctions after relaxation, which agrees with the experimental data. In contrast to this, it is assumed that the polymer matrix ages upon stretching. Mechanical stress can lead to a rearrangement of physically bound polymer chains and, thus, to changes in the local force distribution.[34–36]

The force constant distribution is illustrated in Figure 3(b). The mean force constants of the two classes, which were used for the simulation, are depicted as blue bars. The dashed line represents a possible force distribution in class I for the first stretching. A shift in the mean force constant with stretching cycle can be attributed to a rearrangement of polymer chains, in which strong bonds remain and weak bonds are energetically unfavorable and are changed during stretching. As can be seen in Figure 3(c), we can successfully model the concentration dependent resistance change as a function of cycle number and, therefore, the aging of the polymer matrix. The relative distribution of class I to class II was 87 % to 13 %. The mean force constants of class I normalized to the first cycle are 1.3 for the second cycle, 1.6 for the third cycle, 1.8 for the 4th, and 2.0 for the 5th cycle. On the right axis, the effective nanowire concentrations used for the simulations are given. As shown in [20], the effective concentrations are by a factor of about 4 lower than the experimental concentrations. The different concentrations for experiment and simulation can be attributed to a small amount of side products like silver particles in the reaction solution, the effective distribution of the nanowires in the composites as well as a coffee ring at the edge of the auxiliary substrate after drop-casting of the Ag-NW suspension. In Figure 3(d), we model the hysteretic resistance curve for a sample with an effective concentration of 22 µg cm^{-2}, corresponding to the experimental concentration of 80 µg cm^{-2}. We can model the hysteretic behavior after stretching by shifting the mean force constant of class I by a factor of 1.5 (see Figure 2(a)). This leads to the corresponding hysteretic number of intersections in the simulated network normalized to the number of intersections of the pre-stretched sample at 6.66 % strain as shown in Figure 3(e). These results indicate an aging in the polymer matrix due to the weak physical bonds. This behavior explains the changes in both, the network properties upon repetitive stretching cycles and the hysteretic behavior.

4. Discussion

Stretching and relaxation of Ag-NW polymer composites affect their electrical properties depending on the Ag-NW concentration. This can mainly be attributed to the connectivity of the networks, since the nanowire junctions are the dominant resistors. The inter-connectivity, which we define as the mean number of junctions per nanowire, is therefore an important measure for the network resistance.[20] In order to understand the percolative properties of networks of 1D nano-structures, Monte Carlo methods have been used in many studies.[37–40] It is also known that the tunnel resistance at the nanowire junctions dominate the network resistance in most cases.[32,41]

The comparison of our experimental data with other studies shows that both, the nanowire network and the polymer matrix have a major influence on the electrical behavior under mechanical stress.[15,16,21,42–46] The matrix material strongly interacts with the network during stretching, since it is the force-acting component. Many different mostly macroscopic models exist on the stress-strain behavior of polymers and the influence of nanofillers.[47,48] The model used in this work offers a combination of matrix and filler network properties, explaining the influence of the local force distribution within the polymer matrix upon stretching, which has a direct impact on the network inter-connectivity. The respective change in the force constant distribution as a function of the stretching cycle, therefore, depends on the properties of the matrix material. The 3D printable photo-resin used in this study enables the unique property that upon repetitive stretching the network resistance decreases and the electrical sensitivity to strain increases. Our results demonstrate prototypes for a tunable 3D printable strain sensor with tailored sensitivity. Furthermore, we are able to understand this behavior due to the combined properties of the Ag-NW composite under mechanical strain.

Acknowledgements

The authors thank Birger Höhling and Boris Fiedler for making the circuits boards. We thank Florian Biebl, Matthias Schwartzkopf, and Stephan Roth for their support and helpful discussions, and Robert Frömter and Nils Huse for using the scanning electron microscope. This research was funded by Bundesministerium für Bildung und Forschung (BMBF), grant number 05K19GU5 and the Helmholtz-Gemeinschaft Deutscher Forschungszentren through DESY.

Current address of M.B.: Deutsches Elektronen-Synchrotron, Notkestrasse 85, 22607 Hamburg, Germany; KTH, Royal Institute of Technology, 10044 Stockholm, Sweden.

Author Contributions:

Conceptualization, T.E.G. and M.R.; software, M.B., B.G.L., and T.E.G.; validation, T.E.G., M.B. and M.R.; formal analysis, T.E.G. and M.R.; investigation, M.B., T.E.G., L.O.A, T.M.; writing - original draft preparation, M.B. and T.E.G.; visualization, M.B. and T.E.G.; supervision, T.E.G and M.R.; project administration, M.R.; funding acquisition, M.R. All authors have read and agreed to the published version of the manuscript. † M.B. and T.E.G. contributed equally.

References

[1] Ju, S.; Facchetti, A.; Xuan, Y.; Liu, J.; Ishikawa, F.; Ye, P.; Zhou, C.; Marks, T.J.; Janes, D.B. Fabrication of fully transparent nanowire transistors for transparent and flexible electronics. *Nat. Nanotechnol.* **2007**, *2*, 378–384, doi:10.1038/nnano.2007.151.

[2] Liang, J.; Li, L.; Chen, D.; Hajagos, T.; Ren, Z.; Chou, S.-Y.; Hu, W.; Pei, Q. Intrinsically stretchable and transparent thin-film transistors based on printable silver nanowires, carbon nanotubes and an elastomeric dielectric. *Nat. Commun.* **2015**, *6*, 7647, doi:10.1038/ncomms8647.

[3] Gelinck, G.H.; Huitema, H.E.A.; van Veenendaal, E.; Cantatore, E.; Schrijnemakers, L.; van der Putten, J.B.P.H.; Geuns, T.C.T.; Beenhakkers, M.; Giesbers, J.B.; Huisman, B.-H.; et al. Flexible active-matrix displays and shift registers based on solution-processed organic transistors. *Nat. Mater.* **2004**, *3*, 106–110, doi:10.1038/nmat1061.

[4] Park, K.-I.; Lee, M.; Liu, Y.; Moon, S.; Hwang, G.-T.; Zhu, G.; Kim, J.E.; Kim, S.O.; Kim, D.K.; Wang, Z.L.; et al. Flexible Nanocomposite Generator Made of BaTiO3 Nanoparticles and Graphitic Carbons. *Adv. Mater.* **2012**, *24*, 2999–3004, doi:10.1002/adma.201200105.

[5] Pushparaj, V.L.; Shaijumon, M.M.; Kumar, A.; Murugesan, S.; Ci, L.; Vajtai, R.; Linhardt, R.J.; Nalamasu, O.; Ajayan, P.M. Flexible energy storage devices based on nanocomposite paper. *Proc. Natl. Acad. Sci.* **2007**, *104*, 13574–13577, doi:10.1073/pnas.0706508104.

[6] Liu, Y.; Pharr, M.; Salvatore, G.A. Lab-on-Skin: A Review of Flexible and Stretchable Electronics for Wearable Health Monitoring. *ACS Nano* **2017**, *11*, 9614–9635, doi:10.1021/acsnano.7b04898.

[7] Pagliaro, M.; Ciriminna, R.; Palmisano, G. Flexible Solar Cells. *ChemSusChem* **2008**, *1*, 880–891, doi:10.1002/cssc.200800127.

[8] Rogers, J.A.; Someya, T.; Huang, Y. Materials and Mechanics for Stretchable Electronics. *Science (80-.).* **2010**, *327*, 1603–1607, doi:10.1126/science.1182383.

[9] Nathan, A.; Ahnood, A.; Cole, M.T.; Sungsik Lee; Suzuki, Y.; Hiralal, P.; Bonaccorso, F.; Hasan, T.; Garcia-Gancedo, L.; Dyadyusha, A.; et al. Flexible Electronics: The Next Ubiquitous Platform. *Proc. IEEE* **2012**, *100*, 1486–1517, doi:10.1109/JPROC.2012.2190168.

[10] Hu, L.; Kim, H.S.; Lee, J.-Y.; Peumans, P.; Cui, Y. Scalable Coating and Properties of Transparent, Flexible, Silver Nanowire Electrodes. *ACS Nano* **2010**, *4*, 2955–2963, doi:10.1021/nn1005232.

[11] De, S.; Higgins, T.M.; Lyons, P.E.; Doherty, E.M.; Nirmalraj, P.N.; Blau, W.J.; Boland, J.J.; Coleman, J.N. Silver Nanowire Networks as Flexible, Transparent, Conducting Films: Extremely High DC to Optical Conductivity Ratios. *ACS Nano* **2009**, *3*, 1767–1774, doi:10.1021/nn900348c.

[12] Pike, G.E.; Seager, C.H. Percolation and conductivity: A computer study. I. *Phys. Rev. B* **1974**, *10*, 1421–1434, doi:10.1103/PhysRevB.10.1421.

[13] Munson-McGee, S.H. Estimation of the critical concentration in an anisotropic percolation network. *Phys. Rev. B* **1991**, *43*, 3331–3336, doi:10.1103/PhysRevB.43.3331.

[14] Glier, T.E.; Akinsinde, L.; Paufler, M.; Otto, F.; Hashemi, M.; Grote, L.; Daams, L.; Neuber, G.; Grimm-Lebsanft, B.; Biebl, F.; et al. Functional Printing of Conductive Silver-Nanowire Photopolymer Composites. *Sci. Rep.* **2019**, *9*, 6465, doi:10.1038/s41598-019-42841-3.

[15] Yun, S.; Niu, X.; Yu, Z.; Hu, W.; Brochu, P.; Pei, Q. Compliant Silver Nanowire-Polymer Composite Electrodes for Bistable Large Strain Actuation. *Adv. Mater.* **2012**, *24*, 1321–1327, doi:10.1002/adma.201104101.

[16] Xu, F.; Zhu, Y. Highly Conductive and Stretchable Silver Nanowire Conductors. *Adv. Mater.* **2012**, *24*, 5117–5122, doi:10.1002/adma.201201886.

[17] Amjadi, M.; Pichitpajongkit, A.; Lee, S.; Ryu, S.; Park, I. Highly Stretchable and Sensitive Strain Sensor Based on Silver Nanowire–Elastomer Nanocomposite. *ACS Nano* **2014**, *8*, 5154–5163, doi:10.1021/nn501204t.

[18] Wu, J.; Zang, J.; Rathmell, A.R.; Zhao, X.; Wiley, B.J. Reversible Sliding in Networks of Nanowires. *Nano Lett.* **2013**, *13*, 2381–2386, doi:10.1021/nl4000739.

[19] Sun, Y.; Yin, Y.; Mayers, B.T.; Herricks, T.; Xia, Y. Uniform Silver Nanowires Synthesis by Reducing AgNO 3 with Ethylene Glycol in the Presence of Seeds and Poly(Vinyl Pyrrolidone). *Chem. Mater.* **2002**, *14*, 4736–4745, doi:10.1021/cm020587b.

[20] Glier, T.E.; Betker, M.; Witte, M.; Matsuyama, T.; Westphal, L.; Grimm-Lebsanft, B.; Biebl, F.; Akinsinde, L.O.; Fischer, F.; Rübhausen, M. Electrical and network properties of flexible silver-nanowire composite electrodes under mechanical strain. *Nanoscale* **2020**, *12*, 23831–23837, doi:10.1039/D0NR05734G.

[21] Amjadi, M.; Kyung, K.-U.; Park, I.; Sitti, M. Stretchable, Skin-Mountable, and Wearable Strain Sensors and Their Potential Applications: A Review. *Adv. Funct. Mater.* **2016**, *26*, 1678–1698, doi:10.1002/adfm.201504755.

[22] Lee, C.-J.; Park, K.H.; Han, C.J.; Oh, M.S.; You, B.; Kim, Y.-S.; Kim, J.-W. Crack-induced Ag nanowire networks for transparent, stretchable, and highly sensitive strain sensors. *Sci. Rep.* **2017**, *7*, 7959, doi:10.1038/s41598-017-08484-y.

[23] Hu, N.; Li, J.H.; Shi, D.J.; Liu, X.Y.; Chen, M.Q. Synthesis and self-assembly behaviors of four-armed amphiphilic polystyrene-b-poly(N-isopropylacrylamide) copolymers. *Polym. Sci. Ser. B* **2013**, *55*, 69–76, doi:10.1134/S1560090413020073.

[24] Alamusi; Hu, N.; Fukunaga, H.; Atobe, S.; Liu, Y.; Li, J. Piezoresistive Strain Sensors Made from Carbon Nanotubes Based Polymer Nanocomposites. *Sensors* **2011**, *11*, 10691–10723, doi:10.3390/s111110691.

[25] Yao, S.; Zhu, Y. Wearable multifunctional sensors using printed stretchable conductors made of silver nanowires. *Nanoscale* **2014**, *6*, 2345, doi:10.1039/c3nr05496a.
[26] Choi, S.; Han, S.I.; Jung, D.; Hwang, H.J.; Lim, C.; Bae, S.; Park, O.K.; Tschabrunn, C.M.; Lee, M.; Bae, S.Y.; et al. Highly conductive, stretchable and biocompatible Ag–Au core–sheath nanowire composite for wearable and implantable bioelectronics. *Nat. Nanotechnol.* **2018**, *13*, 1048–1056, doi:10.1038/s41565-018-0226-8.
[27] Xu, H.; Lv, Y.; Qiu, D.; Zhou, Y.; Zeng, H.; Chu, Y. An ultra-stretchable, highly sensitive and biocompatible capacitive strain sensor from an ionic nanocomposite for on-skin monitoring. *Nanoscale* **2019**, *11*, 1570–1578, doi:10.1039/C8NR08589G.
[28] Xiao, X.; Yuan, L.; Zhong, J.; Ding, T.; Liu, Y.; Cai, Z.; Rong, Y.; Han, H.; Zhou, J.; Wang, Z.L. High-Strain Sensors Based on ZnO Nanowire/Polystyrene Hybridized Flexible Films. *Adv. Mater.* **2011**, *23*, 5440–5444, doi:10.1002/adma.201103406.
[29] Li, X.; Zhang, R.; Yu, W.; Wang, K.; Wei, J.; Wu, D.; Cao, A.; Li, Z.; Cheng, Y.; Zheng, Q.; et al. Stretchable and highly sensitive graphene-on-polymer strain sensors. *Sci. Rep.* **2012**, *2*, 870, doi:10.1038/srep00870.
[30] Sun, Y.; Mayers, B.; Herricks, T.; Xia, Y. Polyol Synthesis of Uniform Silver Nanowires: A Plausible Growth Mechanism and the Supporting Evidence. *Nano Lett.* **2003**, *3*, 955–960, doi:10.1021/nl034312m.
[31] Wu, F.Y. Theory of resistor networks: The two-point resistance. In Exactly Solved Models: A Journey in Statistical Mechanics: Selected Papers with Commentaries (1963-2008); 2009 ISBN 9789812813893.
[32] Li, C.; Thostenson, E.T.; Chou, T.-W. Dominant role of tunneling resistance in the electrical conductivity of carbon nanotube–based composites. *Appl. Phys. Lett.* **2007**, *91*, 223114, doi:10.1063/1.2819690.
[33] Balberg, I. Tunneling and nonuniversal conductivity in composite materials. *Phys. Rev. Lett.* **1987**, *59*, 1305–1308, doi:10.1103/PhysRevLett.59.1305.
[34] Qi, H.J.; Boyce, M.C. Stress–strain behavior of thermoplastic polyurethanes. *Mech. Mater.* **2005**, *37*, 817–839, doi:10.1016/j.mechmat.2004.08.001.
[35] Harwood, J.A.C.; Payne, A.R.; Whittaker, R.E. Stress-Softening and reinforcement of rubber. *J. Macromol. Sci. Part B - Phys.* **1971**, *5*, 473–486, doi:10.1080/00222347108212551.
[36] Lorenz, H.; Klüppel, M.; Heinrich, G. Microstructure-based modelling and FE implementation of filler-induced stress softening and hysteresis of reinforced rubbers. *ZAMM - J. Appl. Math. Mech. / Zeitschrift für Angew. Math. und Mech.* **2012**, *92*, 608–631, doi:10.1002/zamm.201100172.
[37] Yook, S.-H.; Choi, W.; Kim, Y. Conductivity of stick percolation clusters with anisotropic alignments. *J. Korean Phys. Soc.* **2012**, *61*, 1257–1262, doi:10.3938/jkps.61.1257.
[38] Ni, X.; Hui, C.; Su, N.; Jiang, W.; Liu, F. Monte Carlo simulations of electrical percolation in multicomponent thin films with nanofillers. *Nanotechnology* **2018**, *29*, 075401, doi:10.1088/1361-6528/aaa0be.
[39] Balberg, I.; Binenbaum, N.; Anderson, C.H. Critical Behavior of the Two-Dimensional Sticks System. *Phys. Rev. Lett.* **1983**, *51*, 1605–1608, doi:10.1103/PhysRevLett.51.1605.
[40] Kumar, A. Electrical Percolation in Metal Wire Network-Based Strain Sensors. *IEEE Sens. J.* **2019**, *19*, 10373–10378, doi:10.1109/JSEN.2019.2933239.
[41] Bao, W.S.; Meguid, S.A.; Zhu, Z.H.; Weng, G.J. Tunneling resistance and its effect on the electrical conductivity of carbon nanotube nanocomposites. *J. Appl. Phys.* **2012**, *111*, 093726, doi:10.1063/1.4716010.
[42] Chen, Y.; Carmichael, R.S.; Carmichael, T.B. Patterned, Flexible, and Stretchable Silver Nanowire/Polymer Composite Films as Transparent Conductive Electrodes. *ACS Appl. Mater. Interfaces* **2019**, *11*, 31210–31219, doi:10.1021/acsami.9b11149.
[43] Hu, W.; Niu, X.; Li, L.; Yun, S.; Yu, Z.; Pei, Q. Intrinsically stretchable transparent electrodes based on silver-nanowire–crosslinked-polyacrylate composites. *Nanotechnology* **2012**, *23*, 344002, doi:10.1088/0957-4484/23/34/344002.
[44] Kim, J.; Park, J.; Jeong, U.; Park, J.-W. Silver nanowire network embedded in polydimethylsiloxane as stretchable, transparent, and conductive substrates. *J. Appl. Polym. Sci.* **2016**, *133*, 1–7, doi:10.1002/app.43830.
[45] Lee, C.; Oh, Y.; Yoon, I.S.; Kim, S.H.; Ju, B.-K.; Hong, J.-M. Flash-induced nanowelding of silver nanowire networks for transparent stretchable electrochromic devices. *Sci. Rep.* **2018**, *8*, 2763, doi:10.1038/s41598-018-20368-3.
[46] Lee, P.; Lee, J.; Lee, H.; Yeo, J.; Hong, S.; Nam, K.H.; Lee, D.; Lee, S.S.; Ko, S.H. Highly Stretchable and Highly Conductive Metal Electrode by Very Long Metal Nanowire Percolation Network. *Adv. Mater.* **2012**, *24*, 3326–3332, doi:10.1002/adma.201200359.
[47] Michler, G.H.; Baltá-Calleja, F.J. *Mechanical Properties of Polymers based on Nanostructure and Morphology*; Michler, G.H., Balta-Calleja, F.J., Eds.; CRC Press, 2016; ISBN 9780429118609.
[48] Frankland, S.J.V.; Harik, V.M.; Odegard, G.M.; Brenner, D.W.; Gates, T.S. The stress-strain behavior of polymer-nanotube composites from molecular dynamics simulation. *Compos. Sci. Technol.* **2003**, doi:10.1016/S0266-3538(03)00059-9.

Functional Printing of Conductive Silver-Nanowire Photopolymer Composites

Tomke E. Glier*, Lewis Akinsinde, Malwin Paufler, Ferdinand Otto, Maryam Hashemi, Lukas Grote, Lukas Daams, Gerd Neuber, Benjamin Grimm-Lebsanft, Florian Biebl, Dieter Rukser, Milena Lippmann, Wiebke Ohm, Matthias Schwartzkopf, Calvin J. Brett, Toru Matsuyama, Stephan V. Roth*, and Michael Rübhausen*

Scientific Reports - **April 2019**
https://doi.org/10.1038/s41598-019-42841-3

SCIENTIFIC REPORTS

OPEN

Functional Printing of Conductive Silver-Nanowire Photopolymer Composites

Received: 28 November 2018
Accepted: 8 April 2019
Published online: 23 April 2019

Tomke E. Glier[1], Lewis Akinsinde[1], Malwin Paufler[1], Ferdinand Otto[1], Maryam Hashemi[1], Lukas Grote[1], Lukas Daams[1], Gerd Neuber[1], Benjamin Grimm-Lebsanft[1], Florian Biebl[1], Dieter Rukser[1], Milena Lippmann[2], Wiebke Ohm[2], Matthias Schwartzkopf[2], Calvin J. Brett[2,3,4], Toru Matsuyama[5], Stephan V. Roth[2,6] & Michael Rübhausen[1]

We investigated the fabrication and functional behaviour of conductive silver-nanowire-polymer composites for prospective use in printing applications. Silver-nanowires with an aspect ratio of up to 1000 were synthesized using the polyol route and embedded in a UV-curable and printable polymer matrix. Sheet resistances in the composites down to 13 Ω/sq at an optical transmission of about 90% were accomplished. The silver-nanowire composite morphology and network structure was investigated by electron microscopy, atomic force microscopy, profilometry, ellipsometry as well as surface sensitive X-ray scattering. By implementing different printing applications, we demonstrate that our silver nanowires can be used in different polymer composites. On the one hand, we used a tough composite for a 2D-printed film as top contact on a solar cell. On the other hand, a flexible composite was applied for a 3D-printed flexible capacitor.

Functional printing of films and additive manufacturing of components have developed over the last 25 years to be an important and innovative part of the industrial process[1]. From a scientific point of view, the limited physical properties of polymers used mainly for 3D printing represent one of the largest challenges[2]. For electronic applications, conductive layers with good printability are of key importance. Conductive polymers such as PEDOT:PSS have been used for conductive layers[3–5]. Functionalized composite resins are an important alternative as they are also photopolymers and therefore 3D-printable. In this case, the polymer matrix determines the structural and mechanical properties that can be tuned e.g. from tough to flexible. Composites of spherical nanoparticles have to overcome the tunnelling resistance when electrons move from one metallic nanoparticle to the next. Hence, previous approaches to establish resins with good conductivity based on spherical nanoparticles suffer from problems of agglomeration and strong photon absorption at high nanoparticle concentrations. Therefore, they are often unsuitable for optical applications requiring transparent contacts[6,7].

Nanowires offer an alternative approach, which circumvents the tunnelling resistance in the direction of the wire. Silver-nanowire (Ag-NW) electrodes can be realized by various routes, including printing and spray-coating[8–11]. Ag-NW composites offer a scalable process for large scale, flexible, conductive media, as used in e.g. integrated photovoltaics, touch screens, and flexible electronics[12–19]. The plasmonic effects of metallic nanoparticles and nanowires render them useful as advanced optoelectronic devices and biosensors[20–25]. The sheet resistances of spray-coated Ag-NW layers are between 10 Ω/sq and 30 Ω/sq at transparencies of around 90%[10,26]. Thus, they are potential candidates for replacing indium tin oxide in, for example, solar cells[27]. Due to their high aspect ratio, ordered arrangements are possible, leading to an anisotropic conductive behavior[28,29]. Furthermore, the development of flexible electronics based on silver nanowires is progressing[30–34]. Printable flexible Ag-NW

[1]Institut für Nanostruktur- und Festkörperphysik, Center for Free Electron Laser Science (CFEL), Universität Hamburg, Luruper Chaussee 149, 22761, Hamburg, Germany. [2]DESY, Notkestrasse 85, 22607, Hamburg, Germany. [3]Department of Mechanics, KTH Royal Institute of Technology, Teknikringen 8, 100 44, Stockholm, Sweden. [4]Wallenberg Wood Science Center, Teknikringen 56-58, 100 44, Stockholm, Sweden. [5]Max-Planck Institute for the Structure and Dynamics of Matter, Luruper Chaussee 149, 22761, Hamburg, Germany. [6]Department of Fiber and Polymertechnology, KTH Royal Institute of Technology, Teknikringen 56-58, 100 44, Stockholm, Sweden. Correspondence and requests for materials should be addressed to T.E.G. (email: tglier@physnet.uni-hamburg.de) or S.V.R. (email: stephan.roth@desy.de) or M.R. (email: ruebhausen@physnet.uni-hamburg.de)

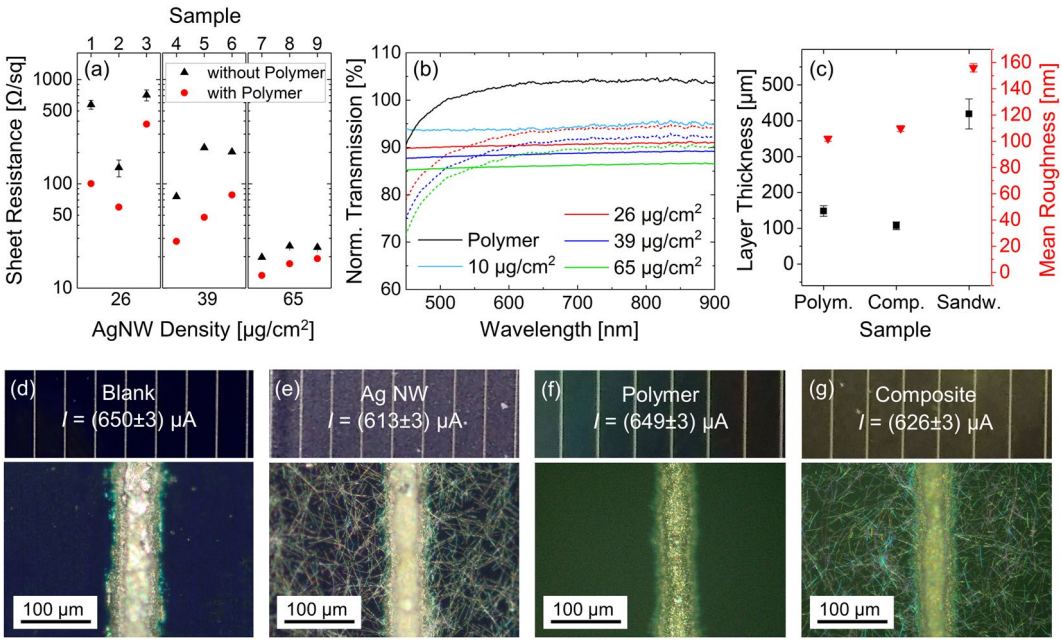

Figure 1. Characterization and 2D printing of the tough Ag-NW-polymer composite. (**a**) Impact of the polymer crosslinking on the Ag-NW composite conductivity by comparing the sheet resistances of Ag-NW networks (black dots) and Ag-NW composites (red dots) for 3 different Ag-NW densities (26 µg/cm^2, 39 µg/cm^2 and 65 µg/cm^2). At high Ag-NW densities, the reproducibility of the measured sheet resistances is enhanced, but the impact of the polymer coating on the conductivity is reduced. (**b**) Transmission of visible to near infrared light through Ag-NWs and Ag-NW composites. Solid lines indicate pure polymer or Ag-NW films, whereas dashed lines indicate Ag-NW composites. The transmission is larger than 87% for all composites between 600 nm and 800 nm normalized to a bare glass substrate. The polymer coating decreases scattering and reflection at the glass interface resulting in an enhanced transmission compared to a bare glass slide. (**c**) Exemplary layer thickness and roughness of the produced polymer samples: pure polymer layer, Ag-NW (7 µg/cm^2) composite and polymer-Ag-NW (22 µg/cm^2)-polymer multilayer sample. Please note that layer thicknesses between 20–300 µm represent typical thicknesses in functional printing. The thickness to surface roughness ratio is >1000:1. (**d**) Photograph and optical microscopy image of a blank solar cell (monocrystalline, 60010, Sol-Expert). A photocurrent *I* of 650 µA was measured during exposure with an Ulbricht sphere. (**e**–**g**) Photographs, optical microscopy images and measured photocurrents of coated solar cells ((**e**) Ag-NWs, (**f**) polymer, (**g**) composite).

composites enable the fabrication of flexible electronic devices with complex geometric shapes, rapid prototyping, and high design flexibility due to additive manufacturing[1,35]. Therefore, we study photopolymer-based silver-nanowire composites. For characterization, we utilized grazing incidence small angle X-ray scattering (GISAXS), scanning electron microscopy (SEM), profilometry, optical transmission, electrical conductivity measurements, energy dispersive X-ray spectroscopy (EDX), atomic force microscopy (AFM), and ellipsometry. By using a tough and a flexible polymer matrix, we demonstrate the application of our Ag-NW composites as a solar cell top contact and as a 3D-printed flexible capacitor.

Results and Discussion

We demonstrate the application of our Ag-NWs within a tough polymer matrix as transparent and conductive top contact in Fig. 1. Figure 1(a) shows the conductivities of the Ag-NW networks and the corresponding composites after photopolymerization. The samples were prepared by coating of an Ag-NW layer with 1,6-Hexanediol diacrylate (HDDA) based resin (see Supplementary Information S1.4) and curing with UV-light (see Supplementary Information S1.5). The HDDA-based polymer matrix has a resistance of above 1 MΩ. We synthesized the Ag-NWs *via* the polyol route[36,37] resulting in nanowires with high aspect ratios (length/diameter) between 100 and up to 1000. The influence of the polymer layer on the conductivity of the nanowire network is shown in Fig. 1(a). The Ag-NW network alone has a decreasing sheet resistance with increasing nanowire concentration from about 500 Ω/sq at 26 µg/cm^2 down to 13 Ω/sq at 65 µg/cm^2. The polymer deposition and cross-linking have a positive impact on the conductivity. It is known that resins compress during the curing procedure[38,39]. Shrinking of the polymer matrix presumably also compresses the nanowire network upon polymerization. This decreases the sheet resistance close to the critical nanowire concentration by a factor of about 2–5 as can be seen in Fig. 1(a). The impact of the compression decreases with increasing nanowire concentration from several 100% at 26 µg/cm^2 to a few percent at 65 µg/cm^2. The reason is the already enhanced nanowire density resulting in higher conductivities at higher concentrations. Reducing the nanowire density leads also to a higher sensitivity on how the nanowires connect to form a conductive network (see Supplementary Fig. S9).

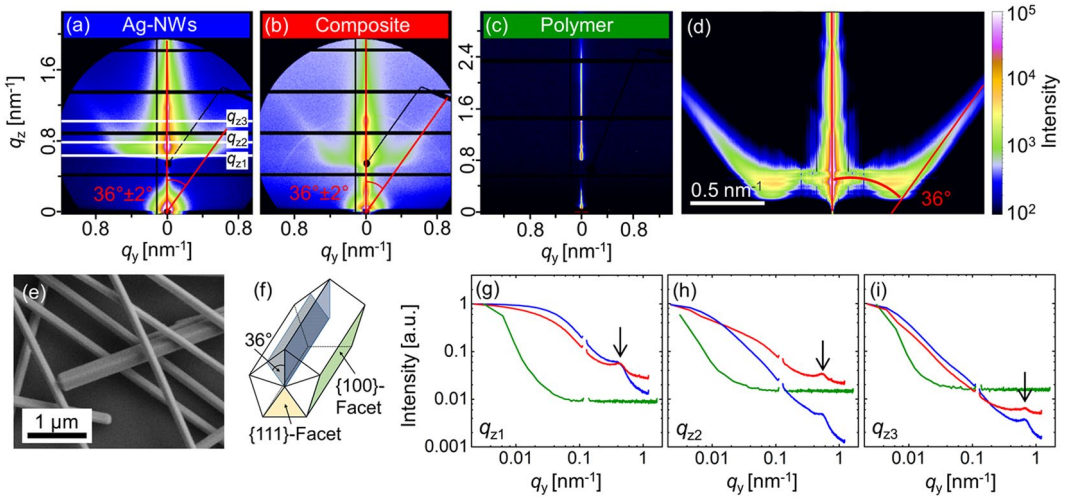

Figure 2. Two-dimensional (2D) GISAXS pattern from the samples. (**a**) Ag-NWs (58 µg/cm^2). (**b**) Ag-NWs (7 µg/cm^2) coated with UV-cured polymer layer. (**c**) Bare UV-cured polymer. Intensity scale bar is shown on the right side. Clear flares at 36° ± 2° (indicated by red lines) stemming from the facets of the pentagon morphology starting from the sample horizon are visible for (**a**,**b**). (**d**) Simulation of the key scattering features of Ag-NWs. (**e**) SEM image of Ag-NWs on a silicon substrate (Ag-NW density around 120 µg/cm^2). (**f**) Sketch of the faceted Ag-NW (adapted from[44,45]). (**g**) Horizontal cuts of the intensity ($I(q_y,q_{z1} = 0.63\,\text{nm}^{-1})$), (**h**) $I(q_y,q_{z2} = 0.78\,\text{nm}^{-1})$, (**i**) $I(q_y,q_{z3} = 0.96\,\text{nm}^{-1})$. All cuts are normalized to the intensity at $I(0,q_{z1,2,3})$ correspondingly. The colour code corresponds to (**a**–**c**).

The transmission spectra of bare Ag-NW networks and Ag-NW composites in reference to a bare glass substrate are shown in Fig. 1(b). At a nanowire concentration of 26 µg/cm^2 of the composite, we find a transmission of 94% at 700 nm and a sheet resistance of up to several 100 Ω/sq. At 65 µg/cm^2 the transmission drops to about 90% and the sheet resistance decreases down to 13 Ω/sq. These results are compatible with previous studies[40–43]. Due to its intermediate refractive index, the bare polymer already enhances the transmission through the glass substrate. As expected, we observe a reduced transmittance with increasing nanowire concentration. The relevance of optimizing the conductivities at relatively low nanowire concentrations, where the compressive effects of the composite are the largest, becomes apparent. This indicates the delicate interplay between the optimization of the polymer matrix and the Ag-NW network when an application is intended as a transparent top contact.

The typical layer thicknesses used in our study are in agreement with typical layer thicknesses used for functional printing ranging between 20 and 300 µm. For optical applications, a control of the surface roughness is of high relevance. Figure 1(c) depicts the layer thickness and surface roughness as determined by profilometry of the polymer, the Ag-NW composite, and a multilayer structure. The latter serves as model for 3D-printed multilayers, which places an Ag-NW layer between different polymer layers. Remarkably, the surface roughness is about 110–160 nm for the Ag-NW composite materials, which is primarily determined by the roughness of the polymer. The thickness to surface roughness ratio is about 1000. Thus, we can expect reduced losses due to diffuse scattering effects. These results show that the composite Ag-NW-polymer materials can act as competitive materials for conducting and light-transparent electrodes.

In order to demonstrate an application of the composite as potential top contact we have printed a conductive Ag-NW composite film (26 µg/cm^2) on top of a monocrystalline solar cell. For comparative purposes, we have also printed a bare polymer layer and a bare conductive Ag-NW-network. Figure 1(d–g) shows the blank solar cell (d), the Ag-NW coated solar cell (e), the polymer coated solar cell (f), and the solar cell coated with the Ag-NW composite (g) with their corresponding photocurrents under identical illumination conditions. The photocurrent decreases only slightly from the blank solar cell ((650 ± 3) µA) to the Ag-NW composite ((626 ± 3) µA). The composite showed a better transmission than the pure Ag-NW layer due to better phase index matching according to Fig. 1(b). Overall, the use of an Ag-NW-polymer electrode on top of the solar cell resulted in a 4% decrease of the measured current. The sheet resistance in the particular configuration of the Ag-NW network was (75.2 ± 1.7) Ω/sq and of the Ag-NW composite was (63.0 ± 3.5) Ω/sq, also in agreement with Fig. 1(a).

In order to characterize the Ag-NW composites we apply grazing incidence small angle X-ray scattering (GISAXS). GISAXS enables the investigation of structural properties of the Ag-NW network embedded in the HDDA-based polymer matrix with statistical relevance. The results are summarized in Fig. 2 and the following samples were investigated: Ag-NWs (Fig. 2(a)), the Ag-NW composite (Fig. 2(b)), and the pure polymer layer (Fig. 2(c)). As reference substrate, a silicon wafer was used. The polymer pattern of Fig. 2(c) is essentially featureless. In Fig. 2(a) and (b) two intensity flares with an angle of around 36° to the vertical direction can be seen outlining a contribution from the Ag-NWs. Figure 2(g–i) depict horizontal cuts at different q_z positions for the different samples (green polymer, blue Ag-NW network, and red Ag-NW composite, compare Fig. 2(a–c)) as indicated by the white lines in Fig. 2(a). A side maximum in the region 0.4–0.8 nm^{-1} occurs when a flare is present in the GISAXS pattern (labelled with an arrow in Fig. 2(g–i)). The shift corresponds to the facet angle of around

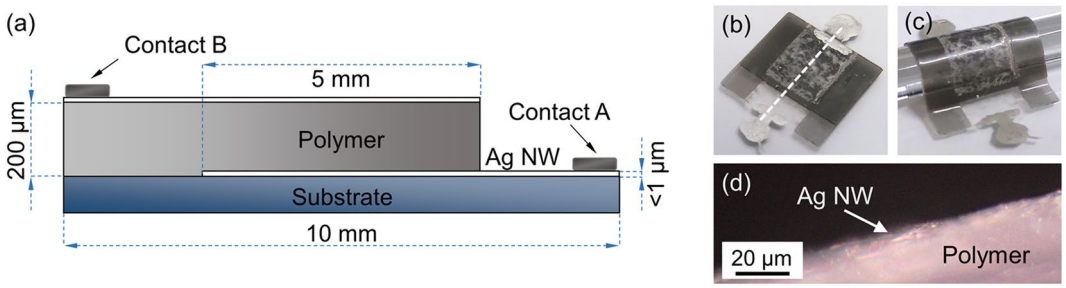

Figure 3. Flexible Ag-NW composite capacitor. (**a**) Illustration of the cross-section of the capacitor. (**b**) Photograph of a produced Ag-NW capacitor (10×10 mm^2). The dashed white line depicts the position of the cross-section, which is presented in (**a**). (**c**) Photograph of the capacitor bent over a glass rod in order to demonstrate its flexibility. (**d**) Cross-sectional view of the lower part of the stripped off capacitor with Ag-NWs.

36°. The polymer coating decreases the scattering contrast between the Ag-NWs and the surrounding medium, thus at higher q_z the peak of the Ag-NW polymer composite appears smaller.

To understand the origin of the flares, Fig. 2(f) depicts a sketch of the Ag-NW with pentagonal cross-section[44,45]. Ag-NWs, synthesized *via* the polyol method, exhibit a pentagonal structure. In the early state of the synthesis, five-fold twinned seeds are formed, which grow in <110> direction[46]. The pentagonal structure and fivefold twinned tip of our Ag-NWs were also verified by SEM studies (Fig. 2(e)). However, SEM studies are not applicable to the composite. The pentagonal morphology is confirmed by simulating the key features of the observed GISAXS pattern using the software IsGISAXS[47] (for details of the modelling, see Supplementary Information S2.6), as shown in Fig. 2(d). The deduced angle of the intensity flares is 36° and compares well with the facets of the pentagonal morphology. Additionally, the enhancement of the diffuse scattering around the Yoneda peak ($\alpha_c = 0.14°$ for Si) can also be reproduced.

The further development of the 2D functional printing into the third dimension is fairly straightforward and can be accomplished within a 3D printing process. A capacitor consisting of Ag-NWs and a flexible photopolymer (Flexible, Formlabs) was prepared in order to demonstrate the feasibility of our approach for 3D-printed flexible electronics. It also highlights the relevance of the polymer of composite for improving the functional properties of the printed object. In order to print the capacitor, six layers along the third dimension were used. A glass slide was coated with resin. The resin and the composite were illuminated and cured by using a combination of three proximity illumination patterns with an area of 10×10 mm^2. The remaining uncured resin was washed off with acetone and isopropanol. An illustration of the cross-section and a photograph of the resulting capacitor with two conductive Ag-NW composite plates and a resin dielectric are shown in Fig. 3(a,b). In order to contact the capacitor two silver-lacquer contacts were applied. The produced capacitor is made up of two 5×5 mm^2 Ag-NW layers with an Ag-NW density of about 100 µg/cm^2. In Fig. 3(c) a photograph of our stripped off capacitor bent over a glass rod is shown in order to demonstrate its flexibility. A total layer thickness of the intermediate polymer layer of (210 ± 5) µm was found by optical microscopy. Figure 3(d) shows an optical microscopic cross-sectional view of the capacitor with Ag-NWs at the surface.

The capacitance was estimated according to Eq. (1), where ε_0 is the vacuum permittivity, ε_r is the polymer permittivity, A is the area of the capacitor and d is the layer thickness of the intermediate polymer layer. The estimated capacitance is 5 pF taking the dielectric constant to about 4.5. In good agreement with the estimation, a capacitance of 7.0 and 7.5 pF was reproducibly measured at 1 kHz and at 100 kHz, respectively.

$$C = \varepsilon_0 \varepsilon_r \times \frac{A}{d} \tag{1}$$

Experimental Section

Synthesis. We synthesized the Ag-NWs *via* the polyol route[36,37]. The used chemicals are listed in Table 1. Initially, an oil bath was heated up to 165 °C or 155 °C. In an unsealed vial, 6 mL of ethylene glycol (EG) was heated for 50 min in the oil bath and stirred at 600 rpm. In the meantime, 0.03 g silver nitrate ($AgNO_3$) was added to 2 mL EG and polyvinylpyrrolidone (PVP) (0.03 g PVP 55000 + 0.06 g PVP 360000) was dissolved in 3 mL EG. After complete dissolution of the PVP, 3 µL copper(II) chloride ($CuCl_2$) solution ($c = 0.0519$ mol/L containing $CuCl_2 \cdot 2H_2O$ + 2 mL EG) was added to the PVP solution. After 50 min preheating, PVP in solution was added to the preheated EG and was heated further for 15 min. The solution was stirred at 600 rpm. The $AgNO_3$ solution was injected into the reaction solution using a syringe pump (neMESYS, CETONI GmbH) and a flow rate of 1.88 mL/h. No stirring was applied during the addition of $AgNO_3$. The reaction was quenched with 16 °C water after 180 min (165 °C) or 235 min (155 °C). After synthesis, the Ag-NWs were washed consecutively three times with acetone and three times with isopropanol. The suspension was centrifuged at 200 rpm at 20 °C for 20 min each time.

Sample preparation. For the sample preparation, cleaned substrates either of silicon or glass (see Supplementary Information S1.1) were used. Pure Ag-NW networks were fabricated by deposition of a drop of nanowire suspension in isopropyl alcohol leading to randomly orientated Ag-NWs forming a percolation

Chemical			Amount
Ethylene glycol	EG	anhydrous, 99.8% purity, S. Aldrich	$V_{total} = 11$ mL, $n = 0.20$ mol
Silver nitrate	$AgNO_3$	>99.9% purity, Carl Roth	$m = 0.03$ g, $n = 0.18$ mmol
Polyvinylpyrrolidone	PVP 55000 MW	Sigma Aldrich	$m = 0.03$ g, $n = 0.55$ µmol
	PVP 360000 MW	Carl Roth	$m = 0.06$ g, $n = 0.17$ µmol
Copper(II) chloride	$CuCl_2$	99.999% purity, Sigma Aldrich	$V = 3$ µL of solution ($c = 0.0519$ mol/L), $n = 0.156$ µmol

Table 1. Chemicals used for silver-nanowire synthesis.

network with a nanowire surface density between 6.5–120 µg/cm^2 (see Supplementary Information S1.2). To fabricate the polymer films, 10 µL of a 1,6-Hexanediol diacrylate (HDDA) based resin (see Supplementary Information S1.4) or a flexible resin (Formlabs) was dropped on the surface of a cleaned substrate. The resin was cross-linked by illumination with a laser diode ($\lambda = 405$ nm, see Supplementary Information S1.5) for 10 min. The fabrication process of a composite sample combines the Ag-NW network and a polymer layer. Firstly, an Ag-NW network was produced. Secondly, the Ag-NWs were coated with resin, which was finally cured with UV-light. Multilayer structures were fabricated by a three-step process with an Ag-NW layer between two polymer layers. A summary of the composite materials and their key properties is given in the Supplementary Table S2.

Characterization methods. For scanning electron microscopy measurements, a commercial field emission scanning electron microscopy (FE-SEM) equipment (Zeiss, Germany) was used (see Supplementary Information S2.1). Resistivity was determined in Van der Pauw[48] geometry by utilizing a four probe measurement setup with DPP 105-M/V-Al-S positioners (CascadeMicrotech, USA) (see Supplementary Information S2.3). Transmission spectra were recorded with an Ulbricht sphere of calibrated spectral characteristics (DKD, Gigahertz Optik) coupled to a QE65000 spectrometer (Ocean optics, USA) in a spectral range between 400 nm and 900 nm. In order to measure the photocurrent of a coated solar cell, the same light source was used. A circular area with a diameter of approximately 5 mm was exposed with a power of about 20 mW/cm^2, and the setup was sealed off from ambient light. The photocurrent was measured with a digital multimeter (Voltcraft, VC 850). Profilometry measurements were performed with a Dektak XT equipment (Bruker, USA). The capacitance of our flexible capacitor was experimentally determined with a programmable HM8118 LCR bridge (Rohde & Schwarz, Germany). GISAXS[49–51] measurements were performed at the beamline P03 at PETRA III @ DESY[52] with a wavelength of 0.972 Å. The sample-to-detector distance (SDD) was SDD = (4990 ± 1) mm calibrated using silver behenate, and the beam size (horizontal × vertical) was 25 × 15 µm^2. The polymer sample was measured at an SDD of (3600 ± 1) mm with a beam size of 30 × 36 µm^2. For detection, a 2D Pilatus 1 M (Dectris Ltd.) detector was used (981 × 1043 pixels, pixel size 172 µm). The flight path between sample and detector was evacuated to reduce scattering. An incident angle of around 0.5° was chosen (see Supplementary Information S2.5). Data reduction was performed using the software package DPDAK[53]. Our methods were selected such that the nanowire network in functional polymer-Ag-NW composites can be studied towards its critical parameters, namely network interconnectivity, optical transmission, sheet resistance, as well as thickness, and roughness.

Conclusion

We have manufactured conductive silver-nanowire (Ag-NW) networks with use in functional printing. By applying two different polymers, we have fabricated composites with different properties that were tested for two specific applications. Firstly, we have optimized Ag-NW composites for use as transparent top contacts by tuning the Ag-NW concentration within a tough and transparent HDDA-based polymer matrix. We have accomplished a sheet resistance of 13 Ω/sq and a corresponding transmission at 700 nm of 90%. Secondly, we have used a flexible polymer matrix in the composite for a 3D-printed flexible capacitor. The capacity of around 7 pF agrees well with the estimated value of about 5 pF. Our characterization involves GISAXS, which enables the investigation of embedded nanostructures and interfaces with high statistical relevance. This shows that GISAXS can develop further to an excellent technique for the investigation of embedded nanostructures in 3D-printed and technically relevant films.

Data Availability

The data of this study are available within the article and its Supplementary Information.

References

1. MacDonald, E. & Wicker, R. Multiprocess 3D printing for increasing component functionality. *Science* **353**, aaf2093 (2016).
2. Hofmann, M. 3D printing gets a boost and opportunities with polymer materials. *ACS Macro Lett.* **3**, 382–386 (2014).
3. Crispin, X. *et al*. The Origin of the High Conductivity of Poly(3,4-ethylenedioxythiophene)−Poly(styrenesulfonate) (PEDOT−PSS) Plastic Electrodes. *Chem. Mater.* **18**, 4354–4360 (2006).
4. Frackowiak, E., Khomenko, V., Jurewicz, K., Lota, K. & Béguin, F. Supercapacitors based on conducting polymers/nanotubes composites. in. *Journal of Power Sources* **153**, 413–418 (2006).
5. Huynh, W. U., Dittmer, J. J. & Alivisatos, A. P. Hybrid nanorod-polymer solar cells. *Science (80-.).* **295**, 2425–2427 (2002).

6. Gonon, P. & Boudefel, A. Electrical properties of epoxy/silver nanocomposites. *J. Appl. Phys.* **99**, 024308 (2006).
7. Nam, S. *et al.* Effects of silica particles on the electrical percolation threshold and thermomechanical properties of epoxy/silver nanocomposites. *Appl. Phys. Lett.* **99**, 043104 (2011).
8. Park, J. S., Kim, T. & Kim, W. S. Conductive Cellulose Composites with Low Percolation Threshold for 3D Printed Electronics. *Sci. Rep.* **7**, 1–10 (2017).
9. Choi, H. W., Zhou, T., Singh, M. & Jabbour, G. E. Recent developments and directions in printed nanomaterials. *Nanoscale* **7**, 3338–3355 (2015).
10. Ding, Z., Stoichkov, V., Horie, M., Brousseau, E. & Kettle, J. Spray coated silver nanowires as transparent electrodes in OPVs for Building Integrated Photovoltaics applications. *Sol. Energy Mater. Sol. Cells* **157**, 305–311 (2016).
11. Cui, Z., Han, Y., Huang, Q., Dong, J. & Zhu, Y. Electrohydrodynamic printing of silver nanowires for flexible and stretchable electronics. *Nanoscale* **10**, 6806–6811 (2018).
12. Hemmati, S., Barkey, D. P., Gupta, N. & Banfield, R. Synthesis and Characterization of Silver Nanowire Suspensions for Printable Conductive Media. *ECS J. Solid State Sci. Technol.* **4**, P3075–P3079 (2015).
13. He, X. *et al.* Transparent electrode based on silver nanowires and polyimide for film heater and flexible solar cell. *Materials (Basel).* **10**, 1–11 (2017).
14. Park, J. S., Kim, B. J., Park, J. S. & Hwang, Y. J. Characteristics of silver meshes coated with carbon nanotubes via spray-coating and electrophoretic deposition for touch screen panels. in. *Thin Solid Films* **596**, 68–71 (2015).
15. Leem, D.-S. *et al.* Efficient Organic Solar Cells with Solution-Processed Silver Nanowire Electrodes. *Adv. Mater.* **23**, 4371–4375 (2011).
16. Gaynor, W., Lee, J.-Y. & Peumans, P. Fully Solution-Processed Inverted Polymer Solar Cells with Laminated Nanowire Electrodes. *ACS Nano* **4**, 30–34 (2010).
17. Zhang, D. *et al.* Silver Nanowires for Reconfigurable Bloch Surface Waves. *ACS Nano* **11**, 10446–10451 (2017).
18. Li, J. *et al.* Healable Capacitive Touch Screen Sensors Based on Transparent Composite Electrodes Comprising Silver Nanowires and a Furan/Maleimide Diels–Alder Cycloaddition Polymer. *ACS Nano* **8**, 12874–12882 (2014).
19. Karakawa, M., Tokuno, T., Nogi, M., Aso, Y. & Suganuma, K. Silver Nanowire Networks as a Transparent Printable Electrode for Organic Photovoltaic Cells. *Electrochemistry* **85**, 245–248 (2017).
20. Rycenga, M. *et al.* Controlling the synthesis and assembly of silver nanostructures for plasmonic applications. *Chem. Rev.* **111**, 3669–3712 (2011).
21. Piazza, L. *et al.* Simultaneous observation of the quantization and the interference pattern of a plasmonic near-field. *Nat. Commun.* **6**, 6407 (2015).
22. Kawata, S. Plasmonics for Nanoimaging and Nanospectroscopy. *Appl. Spectrosc.* **67**, 117–125 (2013).
23. Dregely, D. *et al.* Imaging and steering an optical wireless nanoantenna link. *Nat. Commun.* **5**, 4354 (2014).
24. Davies, M. *et al.* Synchronous Emission from Nanometric Silver Particles through Plasmonic Coupling on Silver Nanowires. *ACS Nano* **6**, 6049–6057 (2012).
25. Santoro, G. *et al.* Silver substrates for surface enhanced Raman scattering: Correlation between nanostructure and Raman scattering enhancement. *Appl. Phys. Lett.* **104**, 243107 (2014).
26. Bergin, S. M. *et al.* The effect of nanowire length and diameter on the properties of transparent, conducting nanowire films. *Nanoscale* **4**, 1996–2004 (2012).
27. Xu, Y. *et al.* Silver Nanowires Modified with PEDOT: PSS and Graphene for Organic Light-Emitting Diodes Anode. *Sci. Rep.* **7**, 45392 (2017).
28. Hu, H., Pauly, M., Felix, O. & Decher, G. Spray-assisted alignment of Layer-by-Layer assembled silver nanowires: a general approach for the preparation of highly anisotropic nano-composite films. *Nanoscale* **9**, 1307–1314 (2017).
29. Yan, Z. *et al.* Controlling the Position and Orientation of Single Silver Nanowires on a Surface Using Structured Optical Fields. *ACS Nano* **6**, 8144–8155 (2012).
30. Wang, J. *et al.* A highly sensitive and flexible pressure sensor with electrodes and elastomeric interlayer containing silver nanowires. *Nanoscale* **7**, 2926–2932 (2015).
31. Lee, H., Kim, M., Kim, I. & Lee, H. Flexible and Stretchable Optoelectronic Devices using Silver Nanowires and Graphene. *Adv. Mater.* **28**, 4541–4548 (2016).
32. Bobinger, M. *et al.* Solution processing of silver nanowires for transparent heaters and flexible electronics. In *2017 13th Conference on Ph.D. Research in Microelectronics and Electronics (PRIME)* 9–12, https://doi.org/10.1109/PRIME.2017.7974094 (IEEE, 2017).
33. Miller, M. S., O'Kane, J. C., Niec, A., Carmichael, R. S. & Carmichael, T. B. Silver Nanowire/Optical Adhesive Coatings as Transparent Electrodes for Flexible Electronics. *ACS Appl. Mater. Interfaces* **5**, 10165–10172 (2013).
34. Liu, Z., Xu, J., Chen, D. & Shen, G. Flexible electronics based on inorganic nanowires. *Chem. Soc. Rev.* **44**, 161–192 (2015).
35. Valentine, A. D. *et al.* Hybrid 3D Printing of Soft Electronics. *Adv. Mater.* **29**, 1703817 (2017).
36. Sun, Y., Gates, B., Mayers, B. & Xia, Y. Crystalline Silver Nanowires by Soft Solution Processing. *Nano Lett.* **2**, 165–168 (2002).
37. Korte, K. E., Skrabalak, S. E. & Xia, Y. Rapid synthesis of silver nanowires through a CuCl- or CuCl 2 -mediated polyol process. *J. Mater. Chem.* **18**, 437–441 (2008).
38. Bailey, W. J. Synthesis of Monomers That Expand on Polymerization. *J. Elastoplast.* **5**, 142–152 (1973).
39. Ji, L., Chang, W., Cui, M. & Nie, J. Photopolymerization kinetics and volume shrinkage of 1,6-hexanediol diacrylate at different temperature. *J. Photochem. Photobiol. A Chem.* **252**, 216–221 (2013).
40. Hu, W. *et al.* Intrinsically stretchable transparent electrodes based on silver-nanowire–crosslinked-polyacrylate composites. *Nanotechnology* **23**, 344002 (2012).
41. Zeng, X.-Y., Zhang, Q.-K., Yu, R.-M. & Lu, C.-Z. A New Transparent Conductor: Silver Nanowire Film Buried at the Surface of a Transparent Polymer. *Adv. Mater.* **22**, 4484–4488 (2010).
42. Yu, Z., Li, L., Zhang, Q., Hu, W. & Pei, Q. Silver Nanowire-Polymer Composite Electrodes for Efficient Polymer Solar Cells. *Adv. Mater.* **23**, 4453–4457 (2011).
43. Xu, W. *et al.* Silver Nanowire-Based Flexible Transparent Composite Film for Curvature Measurements. *ACS Appl. Nano Mater.* **1**, 3859–3866 (2018).
44. Sun, Y., Mayers, B., Herricks, T. & Xia, Y. Polyol Synthesis of Uniform Silver Nanowires: A Plausible Growth Mechanism and the Supporting Evidence. *Nano Lett.* **3**, 955–960 (2003).
45. Lofton, C. & Sigmund, W. Mechanisms Controlling Crystal Habits of Gold and Silver Colloids. *Adv. Funct. Mater.* **15**, 1197–1208 (2005).
46. Xia, Y., Xiong, Y., Lim, B. & Skrabalak, S. E. Shape-Controlled Synthesis of Metal Nanocrystals: Simple Chemistry Meets Complex Physics? *Angew. Chemie Int. Ed.* **48**, 60–103 (2009).
47. Lazzari, R. IsGISAXS: a program for grazing-incidence small-angle X-ray scattering analysis of supported islands. *J. Appl. Crystallogr.* **35**, 406–421 (2002).
48. van der Pauw, L. J. A method of measuring the resistivity and Hall coefficient on lamellae of arbitrary shape. *Philips Technical Review* **20**, 220–224 (1958).
49. Hexemer, A. & Müller-Buschbaum, P. Advanced grazing-incidence techniques for modern soft-matter materials analysis. *IUCrJ* **2**, 106–125 (2015).

50. Roth, S. V. A deep look into the spray coating process in real-time—the crucial role of x-rays. *J. Phys. Condens. Matter* **28**, 403003 (2016).
51. Schwartzkopf, M. & Roth, S. Investigating Polymer–Metal Interfaces by Grazing Incidence Small-Angle X-Ray Scattering from Gradients to Real-Time Studies. *Nanomaterials* **6**, 239 (2016).
52. Buffet, A. *et al*. P03, the microfocus and nanofocus X-ray scattering (MiNaXS) beamline of the PETRA III storage ring: the microfocus endstation. *J. Synchrotron Radiat.* **19**, 647–653 (2012).
53. Benecke, G. *et al*. A customizable software for fast reduction and analysis of large X-ray scattering data sets: applications of the new DPDAK package to small-angle X-ray scattering and grazing-incidence small-angle X-ray scattering. *J. Appl. Crystallogr.* **47**, 1797–1803 (2014).

Acknowledgements

We thank the group of H.P. Oepen for SEM usage and B. Beyersdorff (DESY) for assistance. Furthermore, we thank B. Fiedler for his support in characterization of our flexible capacitor. Parts of this research were carried out at the light source PETRA III at DESY, a member of the Helmholtz Association (HGF). Our funding source is BMBF VUV-Fast (05K2014). C.J.B. and S.V.R. thank the DESY strategic fund (DSF) for financial support *via* the project "Investigation of processes for spraying and spray-coating of hybrid cellulose-based nanostructures".

Author Contributions

S.V.R., M.R. and T.E.G. designed the experiment and wrote the manuscript; L.A., M.P., M.H., L.G., L.D., F.O. and T.E.G. manufactured the samples; Transmission spectroscopy was carried out by T.E.G., G.N., F.B., D.R. and B.G.L.; M.P., T.E.G., L.A. and F.O. did SEM and EDX measurements; Profilometry measurements were carried out by L.A. and AFM measurements were carried out by M.L.; Conductivity measurements were done by L.A., B.G.L. and T.E.G.; Plasma treatment was performed by M.L., L.A., M.P., F.O. and T.E.G.; Our flexible capacitor was characterized by T.M. and ellipsometry measurements (Supplementary Information) were done by G.N.; W.O., C.B., T.E.G., L.A., M.S., S.V.R., M.H. and M.R. did GISAXS measurements as well as GISAXS analysis; IsGISAXS-simulations were carried out by W.O., S.V.R. and M.S.; All authors reviewed the manuscript.

Additional Information

Supplementary information accompanies this paper at https://doi.org/10.1038/s41598-019-42841-3.

Competing Interests: The authors declare no competing interests.

Publisher's note: Springer Nature remains neutral with regard to jurisdictional claims in published maps and institutional affiliations.

4.2 Quantum Confinement in 1D Nanostructures studied by Surface Enhanced Raman Scattering

4.2.1 Introduction

Surface-enhanced Raman scattering (SERS) is an effect that occurs in a variety of sample systems, with the common property of increasing the Raman intensity at an interface. The origin of enhancement can be completely different. There are many studies following SERS of single molecules[24, 208, 209] as well as SERS of solids[22, 210]. SERS describes the enhancement of the often weak Raman cross-section, leading to an enhanced Raman signal, which can be used for fingerprinting of single molecules and the observation of single layer adsorbates on surfaces.[211, 212] SERS is of great interest in analytical chemistry and biological physics, and is used, for example, in the sensing of molecules, medicine, and forensics.[213] The first observation was made by Fleischmann *et al.* in 1974 investigating pyridine deposited on rough silver electrodes.[214] According to today's understanding, there are two main routes of SERS: plasmonic enhancement and chemical SERS.[215, 216] Both variants place special requirements on the respective SERS substrate. In chemical SERS, charge transfer resonances between the molecule and a semiconductor or insulator representing the substrate are used. This process is highly chemically selective, as electronic transitions between occupied and unoccupied states take place. A high surface roughness enables a maximum SERS active area. In this work, chemical SERS of 4-mercaptopyridine on nanostructured zinc oxide microrod arrays is studied (section 4.2.2).[24] For plasmonic SERS, metallic nanostructures are typically used. Here, the nanostructure size and shape play a decisive role as surface plasmons of the SERS substrate enhance the excitation of the Raman process. In section 4.2.3, plasmonic enhancement of the Raman intensity in 1D confined surface states of the topological insulator bismuth selenide is investigated.[22]

4.2.2 Chemical SERS of 4-Mercaptopyridine on Nanostructured ZnO Micro-Rods

Experiment. Fig. 4.22 (a) represents the used sample system for chemical SERS in a schematic view.[24, 217, 218] Zinc oxide (ZnO) micro-rods are arranged in 8 × 8 arrays (see Fig. 4.22 (b)). Each square array has a size of (60 × 60) µm^2. The micro-rods have an inner nano-needle structure, which leads to a large surface roughness and a corresponding

large SERS active area (see Fig. 4.22 (c)). The underlying substrate is silicon, covered with a multilayer graphene layer. A SiO_2 growth mask depicted in gray enable the patterned growth.[217, 218] The outer diameter of the single microrods is 4 µm and their relative height to the SiO_2 layer is 5 µm. A monolayer of 4-mercaptopyridine (4-Mpy) molecules is applied to the ZnO substrate by immersing the substrate into a solution of 4-Mpy. More experimental details are given in Experimental Details 4.7.

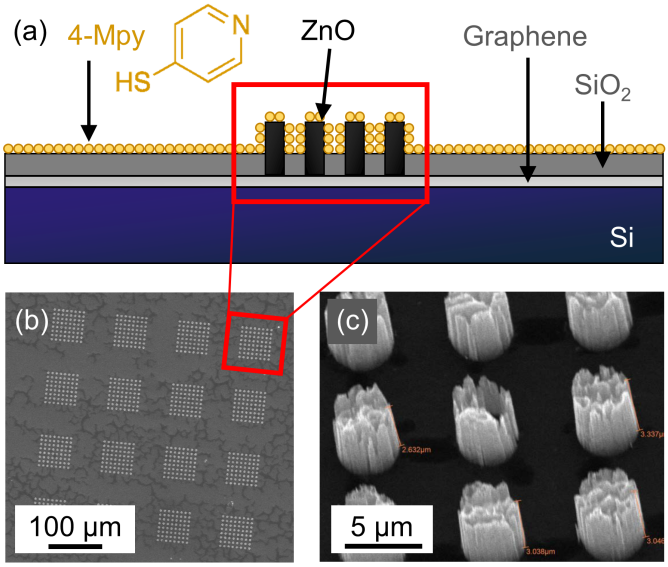

Figure 4.22: (a) Sketch of the sample system. 4-mercaptopyridine (4-Mpy, orange) is adsorbed on nanostructured ZnO micro-rod arrays (black). (b) SEM image of the SERS substrate at low magnification. A pattern of regularly arranged micro-rod arrays can be seen. Each array has a size of 60 µm × 60 µm consisting of 8 × 8 micro-rods. (c) High magnification SEM image of the micro-rods, showing their internal nanostructured nature. Reprinted with permission from [24] (Supporting Information). Copyright 2019 American Chemical Society.

Experimental Details 4.7.

ZnO micro-rod arrays. Zinc oxide (ZnO) SERS substrates made from nanostructured ZnO micro-rod arrays were obtained from J. Kim, N.-J. Kim, H. Kim, and S. Yoon (Seoul).[217, 218] They have been grown on chemical vapor deposition (CVD) graphene films through a catalyst-free CVD process. An silicon dioxide growth mask was used to obtain position-controlled patterned micro-rod arrays.[217, 218] A monolayer of 4-mercaptopyridine (4-Mpy) molecules was applied to the ZnO substrate by immersing the substrate into a solution of 4-Mpy in methanol ($c = 10^{-4}$ M) for 2 h. The sample was subsequently washed with deionized water.[24]

Raman measurements were carried out with different excitation wavelengths from the deep UV (220 nm) to the visible (633 nm). The UT-3 spectrometer was used in macro-Raman configuration (see section 3.1).[90] The laser spot at the sample had a diameter of around

20 µm, illuminating a quarter of one micro-rod array. For the measurements, the laser spot was positioned in the middle of a micro-rod array.

Results and Model. Exemplary Raman spectra of a monolayer of 4-Mpy adsorbed on the nanostructured ZnO substrate for 8 excitation wavelength out of 15 covering the UV and visible spectral range are presented in Fig. 4.23.[24] The raw Raman spectra are corrected for the spectral response of the Raman spectrometer and normalized to the used laser power and integration time. Since a monolayer of molecules is sampled, the obtained Raman intensity directly corresponds to the Raman susceptibility, since no corrections have to be made for the scattering volume. We observe the 4-Mpy ring-breathing mode at around 1000 cm^{-1}, marked by the gray dashed line.[219] Modes stemming from the substrate are highlighted by blue dashed lines. The 4-Mpy breathing mode is clearly enhanced at an excitation energy of around 5.14 eV (241 nm). Other modes from the sample can be observed in the visible, but, in the UV, only get weakly enhanced, outlining a mode selective enhancement of the chemical SERS effect.

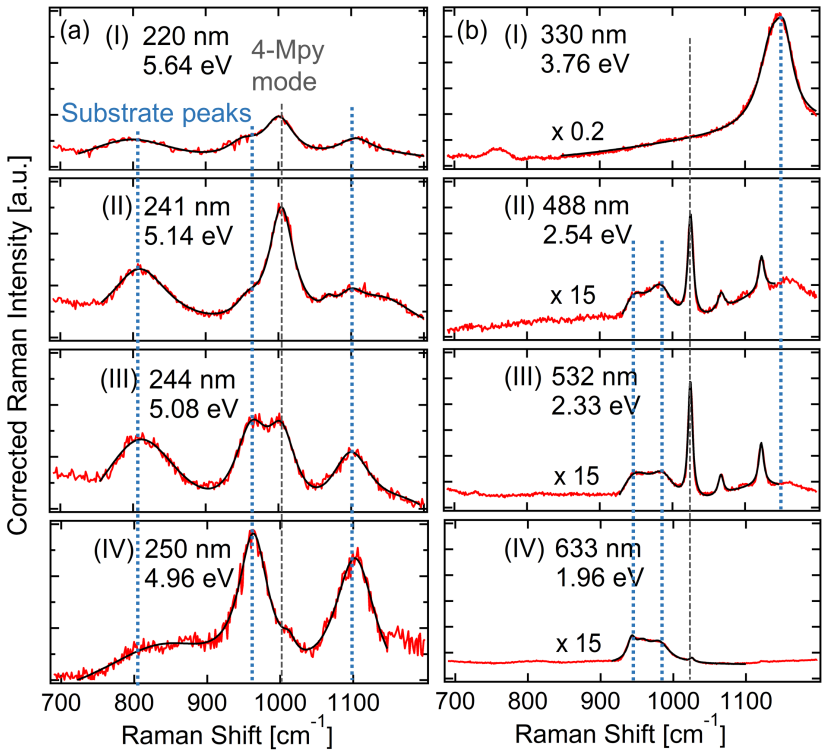

Figure 4.23: (a) UV Raman spectra of a monolayer of 4-Mpy deposited on nanostructured ZnO rods. Spectra are shown for four exemplarily laser energies in the deep UV range as indicated in the figure (I)-(IV). The gray dashed line highlights the breathing mode of the pyridine ring at around 1000 cm^{-1}[219], which is strongest enhanced at 5.14 eV (241 nm). Blue dashed lines show modes stemming from the substrate. (b) Raman spectra of a monolayer of 4-Mpy deposited on ZnO rods for excitation energies covering the mid UV to visible spectral range. Reprinted with permission from [24]. Copyright 2019 American Chemical Society.

In order to understand the observed Raman intensity as a function of incidence laser energy, we consider the resonant Raman process as a Four-Photon Greens Function following the work of A. Kawabata[76] (see also section 2.2.1). Fig. 4.24 shows the respective Feynman diagrams for the resonant Raman process. We illustrate two processes, as two major electronic transitions are expected. The first is the transition from the valence band (VB) from the ZnO to the lowest unoccupied molecular orbital (LUMO) of the 4-Mpy. The second transition corresponds to crossing from the highest occupied molecular orbital (HOMO) to the ZnO conduction band (CB). The combination of the sample molecule with a chemical SERS substrate, in this study, enables the enhancement of the Raman cross-section by cross transitions between molecule and semiconductor yielding resonances in the spectral range used for resonant Raman spectroscopy.

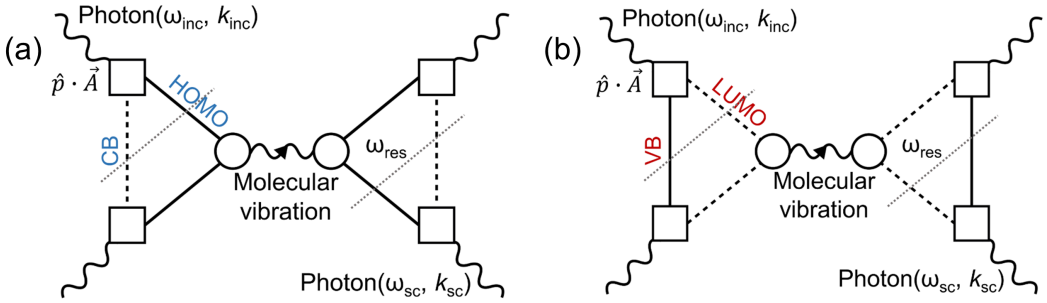

Figure 4.24: Feynman diagrams representing the Four-Photon Greens Function for the resonant SERS Raman process. Incident photons with frequency ω_{inc} and wave vector $\vec{k}_{\text{inc}}$ couple to the electronic system *via* the $\hat{p} \cdot \vec{A}$ matrix element depicted as square (see Eq. 2.37). Circles denote the electron-vibration coupling constants. The molecular vibration is shown in the middle of the diagram as wavy line and arrow. (a) shows the resonance in the UV corresponding to the electronic transition between the HOMO and the CB. The dashed lines represent the resonance frequencies. (b) represents the VIS resonance from the VB to the LUMO. Adapted with permission from [24]. Copyright 2019 American Chemical Society.

As introduced in section 2.2.1 we use a semi-phenomenological model for calculating the Raman response as a function of laser excitation energy. For this, we assume the vibrational excitation to be independent of the electronic susceptibility and the coupling constants to be real, constant, and independent of the momentum.[24] It follows for the scattering intensity corrected to the scattering volume and for constant temperatures

$$I(\omega, \omega_{\text{inc}}) = -\text{Im}(\tilde{R}(\omega, \omega_{\text{inc}})) = -\text{Im}(T_e^4 \, g^2 \, \pi_0(\omega_{\text{inc}})^2 \, D^0) \tag{4.8}$$

where T_e is the photon-electron coupling *via* the $\hat{p} \cdot \vec{A}$ matrix element, g is the electron-vibration coupling constant, π_0 is the polarization bubble, and D^0 is the vibration propagator.[24] D^0 can be expressed by the phonon propagator as given in Eq. 2.39

(see section 2.2.1). π_0, the electronic susceptibility, can be expressed by a real ($R(\omega_{\mathrm{inc}})$) and imaginary part ($\rho(\omega_{\mathrm{inc}})$), which are plotted in Fig. 4.25. The polarization of the electronic system can be understood as a collective excitation between the HOMO and CB, and the VB and LUMO, respectively. The molecule represents discrete molecular states, which are considered by a constant polarization C. For the VB and CB, we use the free electron propagator as introduced in Eq. 2.36. This results in the following relationship for the scattering intensity

$$I(\omega,\omega_{\mathrm{inc}}) = \sum_i \alpha_i \cdot [R_i^2(\omega_{\mathrm{inc}}) + \rho_i^2(\omega_{\mathrm{inc}})] \cdot \frac{2\Gamma_{\mathrm{vib}}\,\omega}{(\omega^2-\omega_0^2)^2 + (2\Gamma_{\mathrm{vib}}\,\omega)^2}, \tag{4.9}$$

with $\alpha_i = T_{e,i}^4\, g_i^2\, C_i^2$ and Eq. 4.10 and 4.11 for the real and imaginary part of the polarization bubble. The inverse electronic lifetime is denoted as Γ_e and also indicated in Fig. 4.25.[24]

$$R^2(\omega_{\mathrm{inc}}) = \left(\frac{(\omega_{\mathrm{res}}-\omega_{\mathrm{inc}})}{(\omega_{\mathrm{inc}}-\omega_{\mathrm{res}})^2+\Gamma_e^2}\right)^2 \tag{4.10}$$

$$\rho^2(\omega_{\mathrm{inc}}) = \left(\frac{\Gamma_e}{(\omega_{\mathrm{inc}}-\omega_{\mathrm{res}})^2+\Gamma_e^2}\right)^2. \tag{4.11}$$

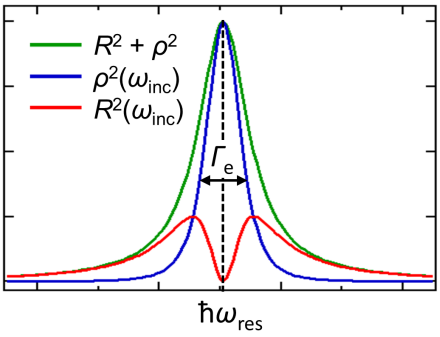

Figure 4.25: Real ($R^2(\omega_{\mathrm{inc}})$, red) and imaginary part ($\rho^2(\omega_{\mathrm{inc}})$, blue) of the electronic polarizability, and the sum of both parts (green) as a function of energy. The green curve represents the resonance enhancement of the Raman susceptibility. $\Gamma_e/\hbar\omega_{\mathrm{res}}$ was set to 0.02. Adapted with permission from [24]. Copyright 2019 American Chemical Society.

The Raman susceptibility determined from the experiment as a function of incidence photon energy is shown in Fig. 4.26 (a).[24] Strong fluorescence between 2.7 eV - 3.7 eV superimposes the Raman signal leading to no reasonable data in this range. As expected, we observe two main resonances, one in the visible and one the UV spectral range. Surprisingly, the data show an additional sharp resonance in the UV, which peaks at around 400 meV below the ZnO conduction band. We fitted our model (Eq. 4.9) to the data. The result is represented as dashed line in Fig. 4.26 (a). The three resonance energies, determined from

the fit, are at (5.152 ± 0.0068) eV, (5.551 ± 0.053) eV, and 2.435 eV. The visible resonance is supported by literature.[217] Further fit parameters are listed in Tab. 4.1. An energy model corresponding to our experimental findings is illustrated in Fig. 4.26 (b). The sharp resonance with a damping of only 0.0967 eV located 400 meV below the CB can be related to an excitonic state. As shown by A. A. Mosquera *et al.*, the bulk ZnO excitonic level is shifted from 50 meV below the CB to up to 400 meV due to confinement within the nanostructures.[42] This excitonic resonance surprises with its high intensity enhancement, which is by a factor of 15 higher than the resonance in the visible. This knowledge leads to new possibilities in optimization of the chemical SERS to detect single molecules or molecule monolayers on ZnO substrates.

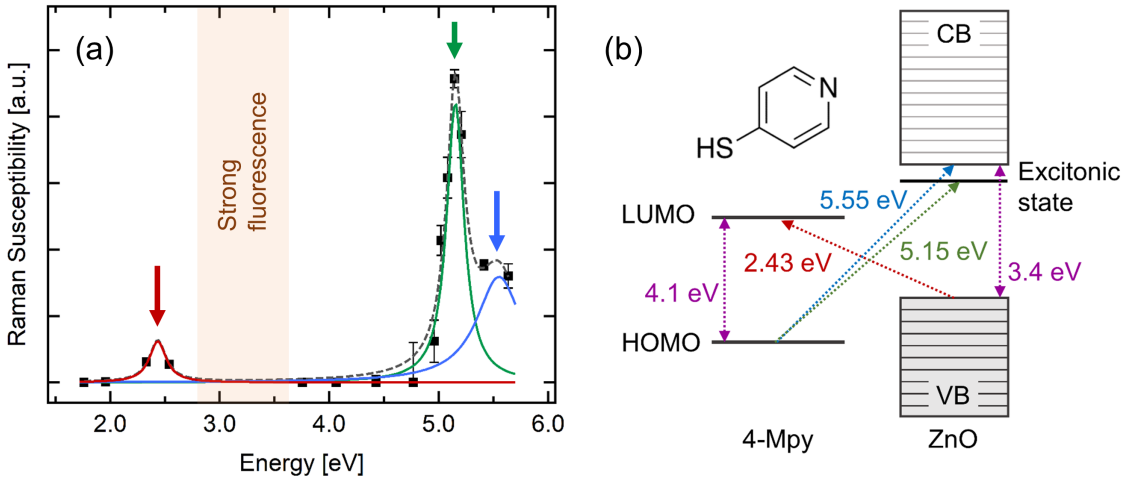

Figure 4.26: (a) Raman susceptibility derived from the experiment (black data points) together with the fit corresponding to Eq. 4.9 (dashed line) as a function of excitation energy $\hbar\omega_{\text{inc}}$. Three resonances are observed and highlighted in red, green, and blue. The fit parameters are listed in Tab. 4.1. (b) Energy model according to the experimental data presented in (a). The discrete molecular energy level (left) and the VB and CB of the ZnO (right) are schematically shown. The resonances observed in the Raman measurements are highlighted by red, green, and blue arrows. Most importantly, we assign the UV resonance at 5.15 eV to an excitonic state 400 meV below the conduction band. Adapted with permission from [24]. Copyright 2019 American Chemical Society.

Table 4.1: Fit parameters corresponding to Fig. 4.26 and Eq. 4.9. UV 1, UV 2, and Vis denote the three observed resonances.

	$\hbar\omega_{\text{res}}$ (eV)	$\hbar\Gamma_e$ (eV)	$\tilde{\alpha}$
UV 1	$5.152 \pm 6.76\times10^{-3}$	$0.09667 \pm 1.15\times10^{-2}$	$4.433\times10^{-3} \pm 0.487\times10^{-3}$
UV 2	$5.551 \pm 53.1 \times10^{-3}$	0.2500	$7.046\times10^{-3} \pm 0.565\times10^{-3}$
Vis	2.435	0.09282 ± 1.16	$1.636\times10^{-3} \pm 8.92\times10^{-3}$

4.2.3 Topological Insulator Nanowires

Bismuth selenide (Bi_2Se_3) is one of the most frequently studied 3D topological insulators (TIs) with a single Dirac cone at the Γ-point (see section 2.1.3). Bi_2Se_3 crystallizes in a rhombohedral crystal structure that grows in multiples of so-called quintuple layers of alternating Bi and Se layers (see Fig. 4.27 (b)).[220, 66] For crystals of Bi_2Se_3 with 3D and 2D geometry (thin films, nanoflakes), surface states with spin polarized linear dispersion branches are observed.[34] The confinement of a TI into a 1D cylinder, however, results in a band gap opening and splitting of the surface state band structure into sub-bands with spin degeneration (see section 2.1.3). The opened band gap is inversely proportional to the wire diameter.[59] The cross-over from a 2D to a 1D geometry of the TI crystal results in a Spin Berry Phase induced by the curved surface (see also section 2.1.3).[61] This cross over is investigated in the following by means of micro-focus Raman scattering on single Bi_2Se_3 nanowires with diameters ranging from 40 nm to 400 nm.

Experiment. Bi_2Se_3 nanowires are synthesized based on a vapour liquid solid (VLS) method by using a two-zone tube furnace. Details are given in the Supporting Information of Ref. [22]. The nanowires are grown on silicon <100> substrates, and are single crystalline with a growth direction of [11-20] as determined by transmission electron microscopy (TEM).[22] We further observe an amorphous oxide shell with a thickness of 1-2 nm around the nanowires, protecting the TI surface states. The amorphous shell can clearly be seen in Fig. 4.27 (c) and is investigated in detail in the Supporting Information of Ref. [22]. The diameters of the synthesized and investigated nanowires range from 40 nm to 400 nm. Their quintuple layer stacking is schematically shown in Fig. 4.27 (b).

The nanowires are studied by Raman spectroscopy using the UT-3 spectrometer as well as the custom-made micro-Raman setup (see section 3.1). The micro-Raman spot size of around 540 nm enables ultra-high local resolution and an optimized sample to substrate ratio in the obtained Raman spectra. For the measurements, the spot was positioned on the nanowires by using the integrated light microscope (see section 3.1 and Fig. 4.27 (a) and (b)). In order to avoid sample damage due to heating of the wires, scanning along the wire axis is employed by using a piezo stage. The nanowires are aligned parallel to the polarization of the incident laser. An incidence laser energy of 2.33 eV (532 nm) and a power of 140 µW at the sample are used. In Fig. 4.27 (d) and (e) light microscopy images taken with the integrated light microscope of two investigated wires with diameters of

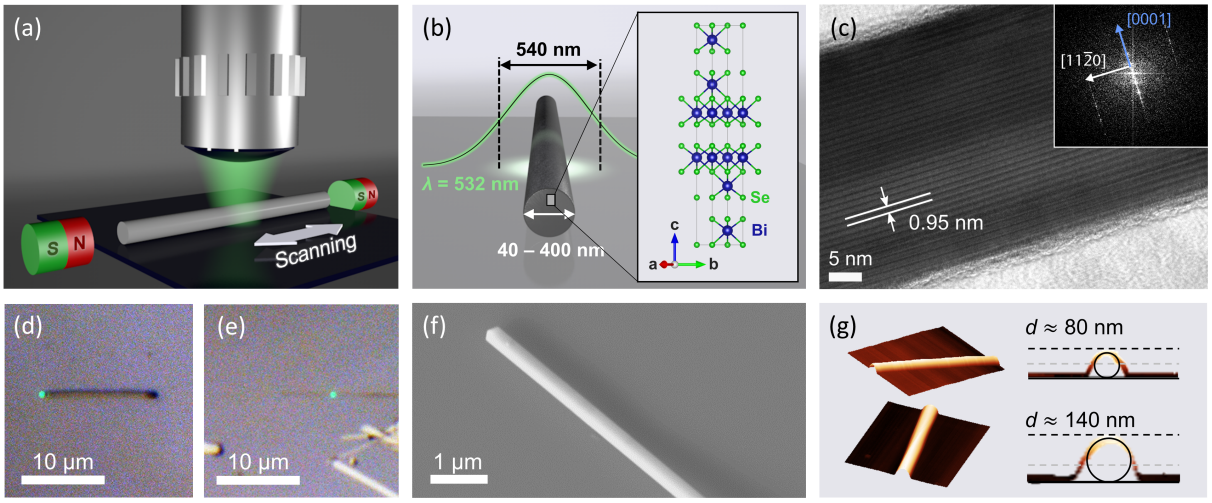

Figure 4.27: (a) Sketch of the conducted experiment. Bi_2Se_3 nanowires with different diameters are studies by micro-Raman spectroscopy. The laser spot is focused on the wire using a microscope objective (see also section 3.1). Two permanent magnets are used to apply a constant magnetic field along the wire axis. (b) Experiment configuration showing the quintuple layer stacking within the Bi_2Se_3 crystal. The probe laser has a wavelength of 532 nm and a spot width (FWHM) of (544 ± 13) nm. (c) HRTEM image of an exemplary nanowire with a diameter of 42 nm along the [11-20] direction. The quintuple layer stacking with a spacing of 0.95 nm can be seen. (d) Light microscope image of the 411 nm wire together with the laser spot (green). (e) Light microscopy image of the 73 nm wire together with the laser spot. (f) SEM image of an exemplary wire (316 nm diameter). (g) AFM measurements showing the cross sections of the wires exemplary shown for a 80 nm and a 140 nm wire. The shape can be approximated by circles. Figure adapted from [22].

411 nm and 73 nm together with the green laser spot are shown. An SEM image of an exemplary Bi_2Se_3 nanowire is also presented in Fig. 4.27 (f). The wires appear circular, which is also indicated by the AFM measurements as shown in Fig. 4.27 (g).

Results. Fig. 4.28 summarizes the Raman results as a function of wire diameter. In Fig. 4.28 (a) the Raman spectra for 8 nanowires with diameters between 42 nm and 411 nm are shown. The spectrum of a 2D Bi_2Se_3 nanoflake is shown for comparison. We observe the E_g^2 and the A_{1g}^2 modes at Raman shifts of around 130 cm^{-1} and 170 cm^{-1}, respectively.[220, 66] The Raman spectrum obtained from the 411 nm wire and the 2D nanoflake are comparable and can be considered as the 2D or bulk limit.

With decreasing wire diameter a clear decrease in mode intensity can be observed, which can be attributed to the decrease in scattering volume. At 200 nm diameter, the Raman signal completely vanishes. Surprisingly, the signal increases again with further decrease in wire diameter. A maximum intensity at 60 nm diameter is observed. The difference between the positions of the E_g^2 and the A_{1g}^2 modes on an energy scale are plotted in Fig. 4.28 (b) clearly indicating a shift of the modes to each other from a diameter of 100 nm to

smaller wire diameters. Fig. 4.28 (c) and (d) show the intensities of the E_g^2 mode and the A_{1g}^2 mode corrected by the scattering volume scaling with the square of the wire diameter, normalized to the 411 nm wire. The enhancement of the Raman susceptibility clearly peaks for the E_g^2 mode at 55 nm, which is also highlighted by a Lorentzian fit (dashed line). For the A_{1g}^2 mode a Lorentzian with a maximum at 36 nm is plotted as guide to the eye.

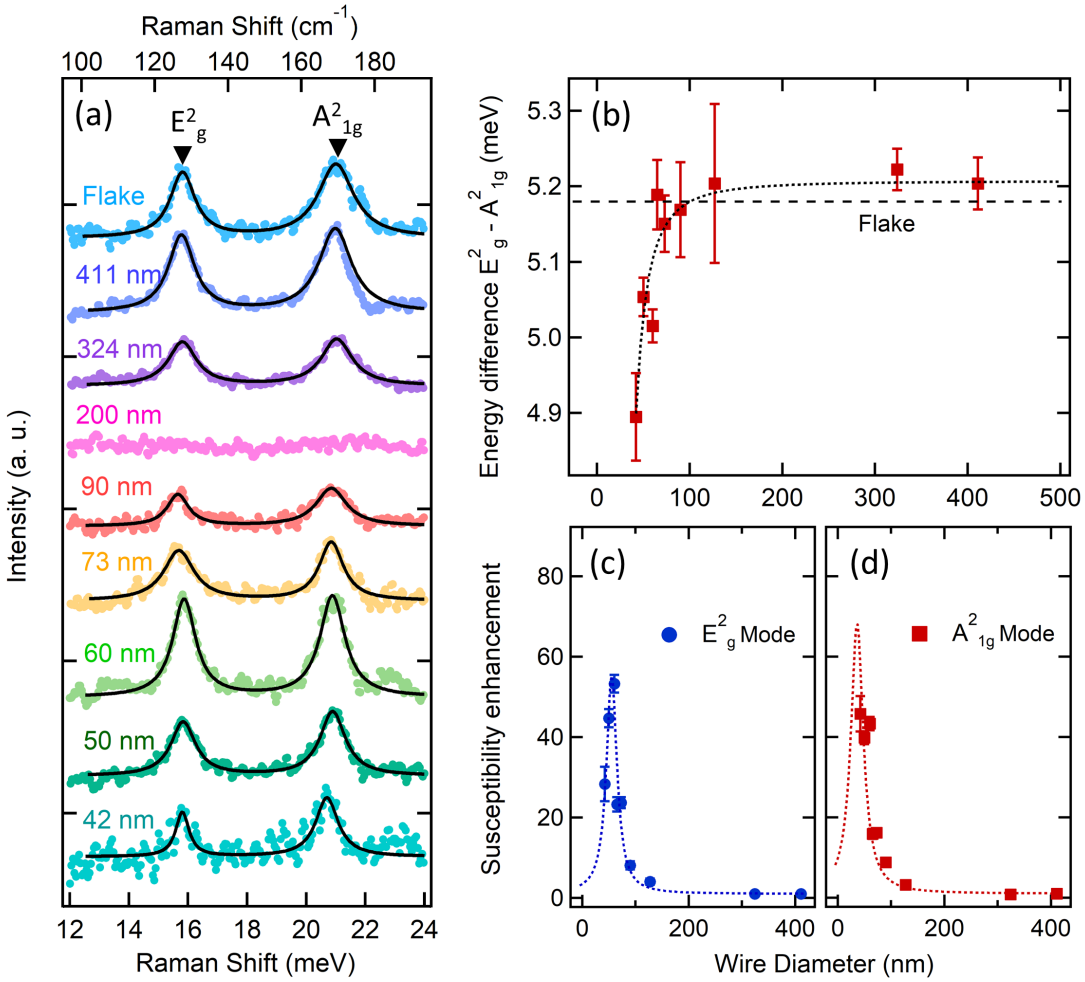

Figure 4.28: (a) Raman spectra for 8 Bi_2Se_3 nanowires with diameters ranging from 42 nm to 411 nm and an exemplary 2D flake. Between 411 nm and 200 nm, the signal decreases with decreasing diameter according to the decrease in scattering volume. From 100 nm, the signal starts to increase again peaking at 60 nm diameter. (b) Difference in mode position of the E_g^2 mode and the A_{1g}^2 mode as a function of wire diameter. The energy difference obtained from a 2D flake is depicted as dashed line. (c) Susceptibility enhancement for the E_g^2 mode as a function of wire diameter. The mode intensities from (a) were normalized to the respective scattering volume and the susceptibility of the 411 nm wire. A Lorentzian with its maximum at 55 nm is fitted to the data. (d) Susceptibility enhancement for the A_{1g}^2. A Lorentzian with maximum at 36 nm is used as guide to the eye. Figure taken from [22].

As outlined in section 2.2.1, the line-shape of phonon modes can be described either with a Lorentzian or a Fano profile.[27] In the case of interaction of phonons with plasmonic excitations for smaller wire diameters, one would expect the formation of an asymmetric

Fano line-shape. For this reason, we carried out a line-shape analysis for the signals with the highest intensities and fitted a simplified Fano profile[221] to the data, which is given as

$$I(\omega)_{\mathrm{Fano}} = C_{\mathrm{Fano}} \frac{(q+\epsilon)^2}{(1+\epsilon^2)}, \tag{4.12}$$

with $\epsilon = \frac{\omega-\omega_0}{\Gamma}$. q represents the Fano parameter, ω is the scattering frequency, ω_0 is the phonon frequency corresponding to the mode positions, and Γ denotes the phonon damping. Two exemplary fits for the 411 nm and the 50 nm wires are shown in Fig. 4.29. The 411 nm wire, which we define as the 2D limit, shows sharp and symmetric phonon modes. We found Fano parameters of -67 and 109 for the E_g^2 mode and A_{1g}^2 mode, respectively. In the limit of large Fano parameters, this indicates Lorentzian line-shapes for the 2D samples. For the 1D wires (50 nm and 60 nm), we observe clear asymmetry in the E_g^2 mode resulting in a decrease in Fano parameter down to -10.3 and -11.6. We further observe changes in the phonon width and frequency, which is also expected from the phonon self-energy corrections resulting from the interaction with plasmonic excitations.[27] All fit parameters are listed in Tab. 4.2. Data with low intensity and accordingly high signal to noise ratio allow no reasonable Fano fit which is the reason why we limit the line-shape analysis on the spectra with high intensity. Please also note that we use a simplified Fano for this analysis, which is aimed to give an indication on the existence of plasmonic excitations within the TI surface states. A detailed analysis of the Fano line shape would require high signal to noise ratio since the parameters C_{Fano} and q are coupled. In this study, the signal to noise ratio is limited due to very small scattering volumes.

Table 4.2: Wire diameter and Fano fit parameters of the samples with the strongest signal.

Wire diameter (nm)	**E_g^2 mode fit parameters**	**A_{1g}^2 mode fit parameters**
411 nm (2D)	$q = -67.0 \pm 0.009$	$q = 109.3 \pm 0.005$
	$\omega = 125.3 \pm 0.005$ cm^{-1}	$\omega = 166.99 \pm 0.004$ cm^{-1}
	$\Gamma = 5.07 \pm 0.005$ cm^{-1}	$\Gamma = 6.2 \pm 0.004$ cm^{-1}
60 nm (1D)	$q = -11.6 \pm 2.52$	$q = 140 \pm 286$
	$\omega = 127.04 \pm 0.24$ cm^{-1}	$\omega = 168.6 \pm 0.29$ cm^{-1}
	$\Gamma = 5.5 \pm 0.247$ cm^{-1}	$\Gamma = 7.3 \pm 0.28$ cm^{-1}
50 nm (1D)	$q = -10.30 \pm 1.9$	$q = 156 \pm 338$
	$\omega = 126.27 \pm 0.23$ cm^{-1}	$\omega = 167.51 \pm 0.22$ cm^{-1}
	$\Gamma = 5.5 \pm 0.236$ cm^{-1}	$\Gamma = 6.98 \pm 0.23$ cm^{-1}

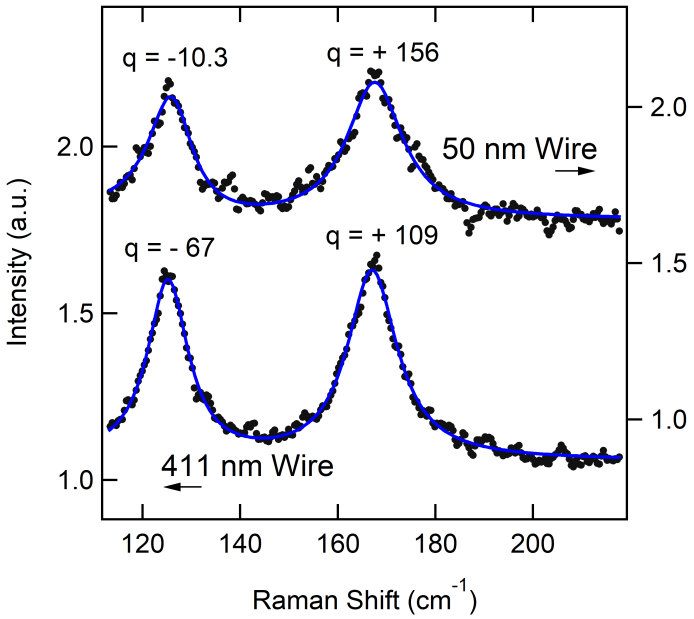

Figure 4.29: Raman intensity as a function of Raman shift for the 50 nm and the 411 nm wire. The data are fitted by a simplified Fano profile (Eq. 4.12). The obtained Fano parameters q are given in the figure. Figure taken from [22] (Supporting Information).

Discussion and Model. For the interpretation of the experimental data, we consider the Raman process to be in the non-resonant limit and the coupling constants to be enhanced by plasmons at the TI surface. Plasmonic SERS can enhance the Raman response by factors of 10^2 to 10^9 if the Raman process takes place in the plasmon resonance of metallic nanoparticles.[222] However, since the frequency of optical phonons and the plasmon frequency of the TI are expected to differ by two orders of magnitude, a non-resonant picture is reasonable for this experiment. Fig. 4.30 shows a Feynman diagram representing the Four-Photon Greens Function[76] for a non-resonant phononic Raman process as introduced in section 2.2.1.

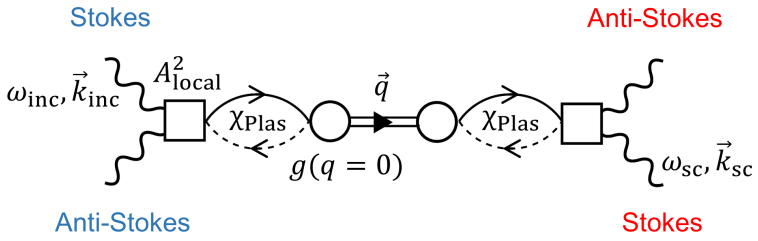

Figure 4.30: Feynman diagram representing the Four-Photon Greens Function for a Raman process in the non-resonant limit.

The incident photon with frequency ω_{inc} and wave vector $\vec{k}_{inc}$ couples to the electronic system *via* the A^2 matrix element (see Eq. 2.37). We consider a plasmonic excitation leading to a local field enhancement. This is expressed by an enhanced coupling called

A^2_{local}, which we assume to be of the order of 10 A^2.[22] For the plasmonic excitation, the polarization bubble in Fig. 4.30 denotes the plasmon susceptibility, which can be written as[26]

$$\chi_{\mathrm{Plas}}(R_0) = \frac{1}{\omega^2 - (2\,\epsilon_{\mathrm{k,m,r}}(R_0))^2 + 2i\frac{\epsilon_{\mathrm{k,m,r}}(R_0)}{\tau_k}} = \chi^{\mathrm{Re}}_{\mathrm{Plas}} + i\cdot\chi^{\mathrm{Im}}_{\mathrm{Plas}}, \tag{4.13}$$

where R_0 is the wire radius, and τ_k denotes the plasmonic tife time. $\epsilon_{k,m,r}$ is the electronic dispersion relation, which has been introduced by Iorio and co-workers for TI cylinders as[59]

$$\epsilon_{k,m,r}(R_0) = \pm C_2\sqrt{k^2 + (1+2m-2r)^2\tilde{\Delta}^2(R_0)}, \tag{4.14}$$

with k being the momentum and m the sub-band index. r equals to the ratio between a magnetic flux applied to the sample Φ and the quantum flux $\Phi_0 = \hbar/2e$. $\tilde{\Delta}(R_0)$ denotes the electronic band gap, which is proportional to R_0^{-1}.[59]

$$\tilde{\Delta}(R_0) = \frac{C_1}{C_2}\frac{1}{2R_0} = \frac{\alpha}{d} \tag{4.15}$$

C_1 and C_2 represent the inter-spin and inter-orbit couplings, respectively, which are identical for exact particle-hole symmetry.[59] $d = 2R_0$ is the wire diameter.

The coupling of the plasmonic excitation to a phonon excitation is considered by means of a constant coupling constant g. Since a Raman probe at $q \approx 0$ is utilized, we view the process in the $q = 0$ limit. The phonon propagator can be descried by the following Greens Function

$$\chi_{\mathrm{pho}}(\omega) = \frac{1}{\omega^2 - \Omega_0^2 + 2i\Gamma}. \tag{4.16}$$

From the Feynman diagram in Fig. 4.30 we get with a semi-phenomenological approach (compare section 2.2.1)

$$I(\omega, R_0) = -\mathrm{Im}[\tilde{R}(\omega, R_0)] = -\mathrm{Im}\left[\left(\frac{A^2_{\mathrm{local}}}{A^2}\right)^2 g^2\,\chi^2_{\mathrm{plas}}(R_0)\,\chi_{\mathrm{pho}}\right]. \tag{4.17}$$

In Fig. 4.31 (a), the square of the plasmonic susceptibility according to Eq. 4.13 corrected by the scattering value scaling with R_0^2 is plotted as a function of energy (ω in Raman shift).

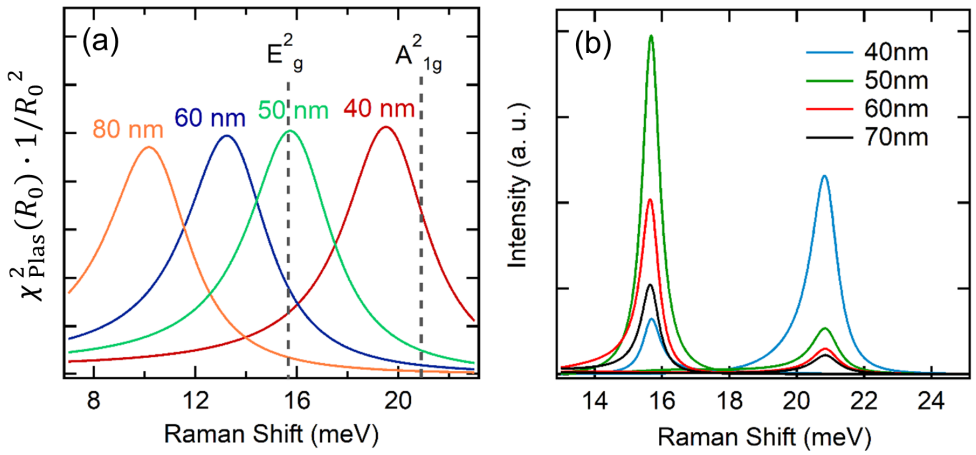

Figure 4.31: (a) Plasmon susceptibility $\chi^2_{\text{plas}}(R_0,\omega)$ as a function of Raman shift for different wire diameters between 40 nm and 80 nm. The Bi_2Se_3 E^2_g mode and the A^2_{1g} mode are marked as dashed lines. (b) Calculated Raman intensity as a function of energy for different wire diameters between 40 nm and 70 nm. The E^2_g mode peaks at around 50 nm, whereas the A^2_{1g} mode is most enhanced for smaller diameters. Figure adapted from [22].

A plasmonic life time of 500 ps was estimated. For the dispersion relation $\epsilon_{k,m,r}(R_0)$ (Eq. 4.14) m was set to 0 (first sub band), α was 0.866, and a finite momentum $k = 0.0005\,\text{Å}^{-1}$ was used, which is compatible with the averaged photon momentum transferred to the electrons along the wire axis.[22] The positions of the E^2_g mode and the A^2_{1g} mode are marked on the same energy axis as dashed lines. This clearly indicates a maximum plasmonic enhancement for the E^2_g mode at a wire diameter of around 50 nm. For the A^2_{1g} mode, the plasmon energy matches the phonon energy for a wire diameter of less than 40 nm (see also Fig. 4.32 (a)). The Raman intensity of the two phonon modes are calculated in Fig. 4.32 (b) according to Eq. 4.17.

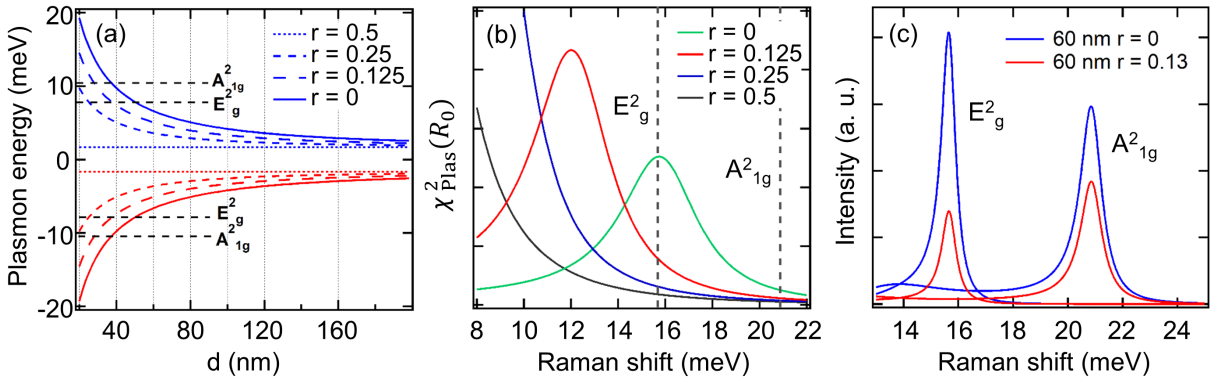

Figure 4.32: (a) Plasmon energy as a function of wire diameter. The curves are shown for different magnetic flux ratios r. The critical value corresponds to $r = 0.5$. The phonon energies of the E^2_g mode and the A^2_{1g} mode are marked by dashed lines. (b) Plasmon susceptibility as a function of energy for a 50 nm diameter wire for different magnetic flux ratios. (c) Simulated Raman spectra for a 60 nm wire for a magnetic flux ratio of 0 (blue) and 0.13 (red). Figure adapted from [22].

Fig. 4.32 (a) represents the dispersion relation $\epsilon_{k,m,r}(R_0)$ for the first sub band ($m = 0$) and finite momentum $k = 0.0005\,\text{Å}^{-1}$ as a function of wire diameter. Curves for varying magnetic flux ratio r between 0 and 0.5 are shown. The figure illustrates the sensitivity of the electric dispersion relation to the magnetic flux, yielding a flat line for $r = 0.5$. This value corresponds to the magnetic phase shift canceling the π-Berry phase of the cylinder.[62, 63, 64] Dashed straight lines mark the phonon energies. For wire diameters smaller than 100 nm, the electronic band gap opens, and the phonons interacting with surface plasmon excitations get enhanced. This SERS effect is completely quenched for $r = 0.5$. For further illustration, $\chi^2_{\text{Plas}}(R_0)$ is shown as a function of Raman shift for different values of r in Fig. 4.32 (b) assuming a plasmon lifetime of 500 ps. The dashed lines depict the positions of the Raman modes observed in the experiment. The calculated Raman modes for a magnetic flux ratio of $r = 0$ compared to $r = 0.13$ are presented in Fig. 4.32 (c) for an exemplary nanowire diameter of 60 nm.

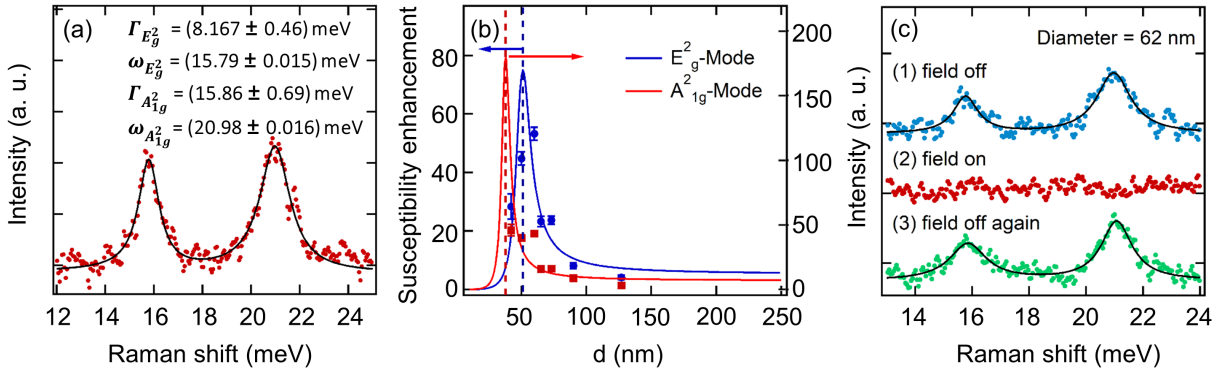

Figure 4.33: (a) Exemplary Raman spectra (50 nm wire) representing the fitting of two Lorentzians to the data. The fit parameters are given in the figure. (b) Obtained Raman susceptibility enhancement (see also Fig. 4.28 (c) and (d)) together with the calculation (solid line) as a function of wire diameter. (c) Raman intensity of a 62 nm diameter wire without magnetic field (blue), with magnetic field in wire direction (80 mT) (red), and again without magnetic field (green). Figure adapted from [22].

In order to fit the Raman spectra, which, to some extent, exhibit low intensity due to very small scattering volumes, Lorentzians are fitted to the data (compare Fig. 4.29 for a Fano analysis). Fig. 4.33 (a) shows an exemplary fit of two Lorentzians to the Raman spectrum for the 50 nm diameter wire. The fit parameters are given in the figure. In Fig. 4.33 (b) the susceptibility enhancements (see also Fig. 4.28 (c) and (d)) are shown together with the calculation (solid line) for $m = 0$ and $r = 0$. Our simplified model is in good agreement with the experimental data. Finally, the quenching of the SERS signal by the application of a magnetic flux along the wire axis is presented in Fig. 4.33 (c). The measurement has been conducted on a nanowire with a diameter of 62 nm, representing a diameter in the

range of maximum plasmonic enhancement. The Raman spectrum of the sample without magnetic field is shown in the first row (blue). In a next step, a magnetic field of 80 mT corresponding to a magnetic flux ratio of $r \approx 0.23$ was applied by using two permanent magnets (see Fig. 4.27 (a)). With this, the Raman signal completely disappears within the noise (red). The magnets have been removed in a third step resulting in a recovery of the Raman signal in a third measurement (green). A similar result has been obtained for a nanowire with a diameter of 90 nm ($r \approx 0.45$).[22] This experiments proof the existence of a non-trivial spin-Berry phase within the topological insulator surface states of the 1D nanowires, which is compensated by magnetic flux as theoretically predicted.[59, 62, 63, 64]

4.2.4 Summary

Two main effects of quantum confinement in 1D nanostructures were studied by surface enhanced Raman scattering (SERS). Chemically selective SERS of 4-mercaptopyridine (4-Mpy) deposited on nanostructured zinc oxide (ZnO) substrates was observed showing resonances for excitation energies in the visible (2.43 eV) and in the UV (5.15 eV and 5.55 eV). The resonances can be attributed to the cross transitions from the ZnO valence band to the 4-Mpy lowest unoccupied molecular orbital (LUMO) and the highest occupied molecular orbital (HOMO) to the conduction band, respectively. A sharp resonance was found in the UV, which is located 400 meV below the ZnO conduction band corresponding to an excitonic state in the quantum confined ZnO and which is by a factor of 15 stronger than the resonance in the visible. The Raman susceptibility enhancements as a function of excitation energy were modeled by a semi-phenomenological model based on a Four-Photon Greens Function method. Chemical SERS represents a route for detecting very few amounts of molecules. The results presented here show new opportunities for the optimization of molecule detection in the UV.

The investigation of Bi_2Se_3 topological insulator nanowires as a function of wire diameter by micro-Raman spectroscopy revealed confinement of the quasi-relativistic surface states on the curved nanowire surface leading to a Spin-Berry phase. We observe plasmonic enhancements of the Bi_2Se_3 Raman signal at the cross-over from the 2D limit to the 1D geometry at nanowire diameters of 100 nm, as well as the quenching of the SERS due to a magnetic flux along the wire axis. The maximum susceptibility enhancement of a factor of 53 compared to the 2D limit was measured for a wire diameter of 50 nm. The key features

of the experiment were successfully modeled by the coupling between spin-polarized 1D plasmons of the TI with phonons.

In conclusion, one-dimensional nanostructures as examined in this thesis, lead us to investigate the consequences of anisotropy in nanosciences and nanotechnology. The formation of conductive networks under different conditions was discussed in section 4.1. In addition, surface effects such as the confinement of topological insulator surface states in a cylinder are of essential importance for the characterization of 1D nanostructures. Overall, it becomes clear that the applicability of individual nanowires can be completely different depending on their composition, arrangement and environment. In addition, it is of great importance to find suitable experimental characterization methods. The high aspect ratios of nanowires do not make this easy, as the observable sizes are in different orders of magnitude. This leads to a wide range of experimental techniques in the research community, which are presented in this work by (I) a Raman microscope with diffraction-limited spot sizes of down to 200 nm - 300 nm to resolve the weak inelastic light scattering signal of small scattering volumes and (II) the use of surface-sensitive X-ray scattering to study random networks within a large sample area. Appropriate models have been found that lead to physical pictures understanding the key properties of the investigated systems.

The following publications are attached to this chapter:

(V) Kim, J. & Glier, T. E. *et al.* Quantum Confinement Induced Excitonic Mechanism in Zinc-Oxide-Nanowalled Microrod Arrays for UV-Vis Surface-Enhanced Raman Spectroscopy. *Journal of Physical Chemistry C* **2019**, 123, 24957-24962.

(VI) Nweze, C. & Glier, T. E. *et al.* Quantum Confinement of the Spin-Berry Phase on 1D Topological Surfaces of Single Bi_2Se_3 Nanowires. Submitted to *Nano Letters*.

4.2.5 Outlook

Surface enhanced Raman scattering has great potential to become a substantial part in sensors for medicine, forensics, and analytical chemistry. Chemical selective SERS is molecule specific, and, therefore, of high interest for chemical industry.

With regard to the fundamental research of the low-energy excitation spectrum of condensed matter, SERS is also a seminal technique. Huge interest is attracted by the different types of Dirac materials, from graphene to Weyl semi-metals, realizing quasi-relativistic

electronic states within a crystal lattice. The manipulation of the topological insulator surface states by geometrical confinement and external fields was outlined in this thesis by means of Bi_2Se_3 nanowires. 2D Bi_2Se_3 nanoflakes represent a suitable system for studying the thickness dependency of a 3D topological insulator in a 2D geometry with two opposite surfaces.[66, 220, 223] Local manipulation of the surface states by single metal nanoparticles leading to local charge transfer and plasmonic effects will be of high interest.[224] Magnetic nanoparticles also represent a promising way to manipulate the spin-polarized surface states with a local magnetic field. The ultra-small diffraction limited spot sizes of the presented Raman-microscope enable the investigation of local and nanoscale phenomena in the low-energy excitation spectrum, as well as the interplay between excitations of the electronic system with the crystal vibrations.

4.2.6 Publications

Quantum Confinement Induced Excitonic Mechanism in Zinc-Oxide-Nanowalled Microrod Arrays for UV-Vis Surface-Enhanced Raman Spectroscopy

Jayeong Kim*, Tomke E. Glier*, Benjamin Grimm-Lebsanft, Sören Buchenau, Melissa Teubner, Florian Biebl, Nam-Jung Kim, Heehun Kim, Gyu-Chul Yi, Michael Rübhausen*, and Seokhyun Yoon*.

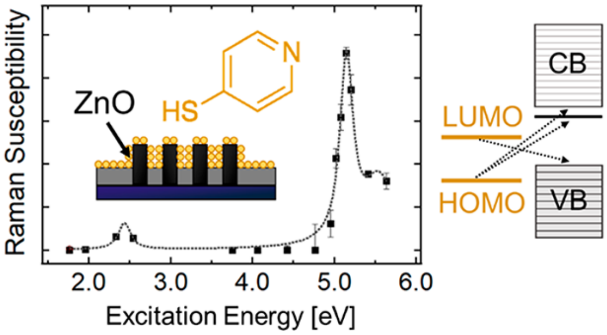

Journal of Physical Chemistry C - **September 2019**
https://doi.org/10.1021/acs.jpcc.9b07329

THE JOURNAL OF PHYSICAL CHEMISTRY C

Article

Cite This: J. Phys. Chem. C 2019, 123, 24957−24962

pubs.acs.org/JPCC

Quantum Confinement Induced Excitonic Mechanism in Zinc-Oxide-Nanowalled Microrod Arrays for UV−Vis Surface-Enhanced Raman Scattering

Jayeong Kim,*[,†,∥] Tomke E. Glier,*[,‡,∥] Benjamin Grimm-Lebsanft,[‡] Sören Buchenau,[‡] Melissa Teubner,[‡] Florian Biebl,[‡] Nam-Jung Kim,[§] Heehun Kim,[§] Gyu-Chul Yi,[§] Michael Rübhausen,*[,‡] and Seokhyun Yoon*[,†]

[†]Department of Physics, Ewha Womans University, 52 Ewhayeodae-gil, Seodaemun-gu, Seoul 03760, Korea

[‡]Institut für Nanostrukturforschung, Center for Free Electron Laser Science (CFEL), Universität Hamburg, Luruper Chaussee 149, Hamburg 22761, Germany

[§]Department of Physics and Astronomy, Institute of Applied Physics, and Research Institute of Advanced Materials (RIAM), Seoul National University, 1 Gwanak-ro, Gwanak-gu, Seoul 08826, Korea

Supporting Information

ABSTRACT: We studied surface-enhanced Raman spectroscopy (SERS) in 4-mercaptopyridine (4-Mpy) deposited on zinc oxide (ZnO) nanostructures, by using resonance Raman scattering covering a range of incident photon energies from 1.7 to 5.7 eV. We investigated all primary routes of the energy-specific resonances that are associated with the electronic transitions between the ZnO valence band (VB) to the lowest unoccupied molecular orbital (LUMO) and the highest occupied molecular orbital (HOMO) to the ZnO conduction band (CB), respectively. Two resonances at 5.55 and 5.15 eV in the ultraviolet (UV) spectral range can be associated with transitions into the CB and most importantly into an excitonic-related state below the ZnO CB, respectively. The energy difference between the UV resonances is 0.4 eV corresponding to the excitonic binding energy as a result of excitonic quantum confinement in the 10−20 nm thick ZnO nanowalls. The observed excitonic SERS resonance enhancement of the ring-breathing mode of 4-Mpy is about 15 times stronger than for the VB resonance observed at 2.43 eV and free of luminescence background. Hence, we outline new pathways of improving the detectability of molecules by chemical SERS due to tuning of the quantum confinement in the excitonic resonance enhancement.

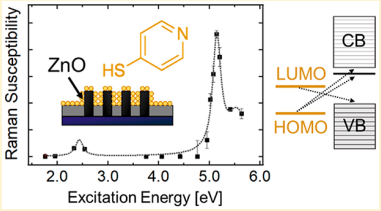

INTRODUCTION

Since its first observation, surface-enhanced Raman scattering (SERS) has been widely used to enhance the often relatively weak Raman cross section.[1−12] SERS has been a subject of intense research in various disciplines such as nanoscale physics, analytical chemistry, and biological physics.[13−15] Very importantly, its extremely high sensitivity makes it possible to realize Raman fingerprinting of a single molecule.[16] This makes SERS a very attractive technique, which can be applied to diverse areas including pharmacy, biological sciences, and forensics.[17,18] However, SERS involves light−matter interaction on a small scale, where quantum mechanical confinement effects could be important.[19] It is generally accepted that there are two main pathways to apply SERS.

Plasmonic SERS involves surface plasmon resonances yielding an electric field enhancement in metallic nanostructures of, e.g., silver and gold, leading to typical enhancement factors (EF) of 10^6.[7−9,20] The near-field enhancement is strongly associated with the shape of the nanoparticles[9] and their geometric arrangement, leading to the strongest enhancement when the gap between the nanostructure reaches molecular dimensions.[21] It is reported that the EF can reach giant values as high as 10^{12} in some cases.[13]

The other pathway is associated with a resonance enhancement mechanism. In general, this effect is the result of charge-transfer resonances between a molecule and a semiconductor or insulator. Since these resonances have to occur between occupied and unoccupied states, they are chemically highly selective, coining the term chemical SERS.[22,23] This effect has no specific constraints regarding the arrangement of the used nanostructures. Here, the nanostructuring is known to enhance the SERS active area.[22−25] Moreover, since substrates for chemical SERS are not metals, there is no intense heating of the nanostructure due to light absorption during the Raman measurements.[26,27]

There are two charge-transfer processes between a molecule and a semiconductor that can lead to resonance Raman enhancement. The first process is associated with transitions between the valence band (VB) of the semiconductor and the

Received: August 1, 2019
Revised: September 13, 2019
Published: September 16, 2019

DOI: 10.1021/acs.jpcc.9b07329
J. Phys. Chem. C 2019, 123, 24957−24962

lowest unoccupied molecular orbital (LUMO). The second process occurs between the highest occupied molecular orbital (HOMO) and the conduction band (CB) of the semiconductor. Moreover, it is known that particularly sharp in-gap excitonic states show strong resonance Raman enhancements,[28] making them prime candidates for enhancing the chemical SERS effect. Excitonic states are also subject to many interesting design options to change their properties that relate, e.g., to doping, to the size of the nanostructure, especially quantum confinement, and to external parameters such as temperature.[29]

Within this Article we report on the nature of the expected charge-transfer resonances between a molecule and a nanostructured semiconductor substrate in chemical SERS. For the case of 4-mercaptopyridine (4-Mpy) on zinc oxide (ZnO) one would expect the VB to LUMO resonance in the visible, which is commonly used in many studies[25] and the HOMO to CB resonance in the deep ultraviolet spectral range, which has not been utilized before. Most importantly, we identify a novel contribution to the UV resonance that can be tracked down to excitonic states. These states can be tuned by the thickness of the ZnO. Due to quantum confinement in the 10−20 nm thick ZnO nanowalls the expected exciton binding energy is shifted from 50 meV in the bulk to 400 meV below the band gap, as also seen in photoluminescence spectra.[30] In order to study all resonance pathways, we utilize a unique resonance Raman setup that is equipped with a fully reflective parabolic entrance objective and a broad range of 15 different laser energies covering the visible to UV spectral range.[31−33]

EXPERIMENTAL METHODS

For the nanostructured ZnO SERS substrates, position-controlled ZnO microrod structures with nanowalls inside were grown on chemical vapor deposition (CVD) graphene films through the catalyst-free CVD process. We obtained ZnO nanowall growth selectivity by depositing an SiO_2 growth mask on the graphene films. The SiO_2 growth masks were prepared by plasma-enhanced CVD (PECVD). Dimensional parameters including the height and diameter of the obtained microrods can be controlled by modifying the lithographic pattern mask or varying the growth parameters of the catalyst-free CVD process. In this work, highly oriented and ordered ZnO mircrorods with an outer diameter of 4 μm and a height of 5 μm were typically employed. The detailed process for growing ZnO nanostructures is described in previous reports.[23,34,35]

For molecule deposition, we immersed the substrates in a 4-Mpy molecular solution ($c = 10^{-4}$ M in methanol) for 2 h and subsequently washed the samples with deionized water.

Raman measurements in the UV and visible spectral range were obtained by the UT-3 Raman spectrometer,[31] which is equipped with a fully reflective custom-made entrance objective allowing an all achromatic focusing of light in the studied spectral range. A Tsunami Ti:sapphire laser system, model 3950-X1BB (Spectra Physics Lasers Inc., California), which was pumped with a green Millennia Pro Xs 10sJS diode laser (Spectra Physics Lasers Inc., California) was used as primary laser source. The fundamental laser line was frequency doubled, tripled, or quadrupled with second harmonic generation, third harmonic generation or fourth harmonic generation (Spectra Physics Lasers Inc., California), respectively. The pulse width of the laser was monitored with an auto correlator (APE GmbH, Berlin) and around 1.7 ps. A gray filter unit enables power reduction of the laser. The laser beam was widened with a spatial filter and then focused on the sample by the main parabola of the objective also collecting the backscattered Raman signal. Measurements at 532 nm were carried out by using a green CW Millennia laser.

For Raman measurement in the visible, we used two additional setups. Measurements at 488 nm (diode laser) and 532 nm (diode-pumped solid state (DPSS) laser) were carried out by using a McPherson 207 spectrometer equipped with a nitrogen-cooled charge-coupled-device (CCD) array detector. A LabRam HREvo 800 spectrometer and a helium−neon laser were used for the 632.8 nm measurement. The excitation power was less than 0.2 mW to avoid laser heating.

The raw Raman spectra were corrected for the spectral response of the Raman spectrometer and normalized to the used laser power and integration time,[31] yielding the Raman susceptibility. The measured intensity of 4-Mpy deposited on ZnO-rods directly represents the Raman susceptibility since a monolayer of molecules was measured.

RESULTS AND DISCUSSION

Figure 1 shows measured corrected Raman intensities (see Experimental Methods for details) of a monolayer of 4-Mpy adsorbed on nanostructured ZnO-rods for eight exemplarily selected excitation energies out of 15 from 1.96 to 5.64 eV. These excitation energies cover both expected resonances from the molecular HOMO level to the semiconductor CB (deep ultraviolet (UV) spectral range) and the semiconductor VB to the molecular LUMO (visible). In Figure 1a we can observe that the 4-Mpy ring-breathing mode at around 1000 cm^{-1} [23,36,37] is strongly enhanced when tuning the incident photon energy from 4.96 to 5.14 eV, showing an extremely sharp resonance directly below the CB minimum. At

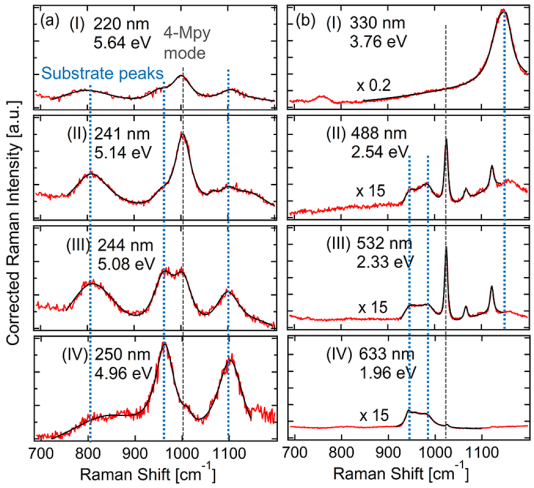

Figure 1. (a) Raman spectra of a monolayer of 4-Mpy deposited on nanostructured ZnO rods for four exemplarily laser energies in the deep UV range between 5.64 eV (220 nm) and 4.96 eV (250 nm). Around 1000 cm^{-1}, the breathing mode of the pyridine ring can be observed. The maximum measured Raman response of this mode was reached at 5.14 eV (241 nm). Other modes only get weakly enhanced, outlining the mode selective enhancement of the chemical SERS effect. (b) Raman spectra of a monolayer of 4-Mpy deposited on ZnO rods for excitation energies covering the mid UV to visible spectral range, i.e., of 3.76 eV (I), 2.54 eV (II), 2.44 eV (III), and 1.96 eV (IV). At 3.76 eV, no 4-Mpy mode can be observed, but at 2.54, 2.33, and 1.96 eV, it can be observed.

DOI: 10.1021/acs.jpcc.9b07329
J. Phys. Chem. C 2019, 123, 24957−24962

even higher incident photon energies up to 5.64 eV, we still find a substantial resonance enhancement of this mode due to transitions into the continuous CB states. In Figure 1b resonance of the ring-breathing mode in the visible can be observed. At 3.76 eV (330 nm), i.e., in the mid UV, no 4-Mpy mode can be detected, while the ZnO mode is resonant according to the expected VB-CB transition close to 3.4 eV (see also Figure 3).[30] However, concomitantly with the proximity to this interband transition, we observe enhanced fluorescence making Raman measurements between 330 and 488 nm very difficult or even impossible. At 488 nm we can already observe the 4-Mpy modes, which get slightly further enhanced toward 532 nm and then again strongly suppressed at 633 and 704 nm (not shown). Therefore, the maximum Raman response of the ring-breathing mode in the visible can be estimated to be around 2.4 eV. Note that the visible and the UV resonance have different mode-selective couplings since for the UV the coupling to the molecular vibration occurs through the molecular HOMO, whereas the visible resonance occurs through the molecular LUMO. When comparing Figure 1a,b one can also observe a significant line width broadening in the UV, which is attributed to the difference in coupling between HOMO and LUMO states, respectively. It is also noteworthy to mention that the measurements in the UV are highly reproducible due to the lack of any fluorescence backgrounds. In order to discuss the resonance Raman effect that is responsible for the chemical SERS effect, we utilize a simplified Feynman diagram approach of Kawabata.[38]

The Feynman diagram in Figure 2 illustrates the resonant Raman scattering process due to molecular vibrations. For the UV resonance shown in Figure 2a, the light couples to electrons via the $\hat{p}\cdot\vec{A}$ matrix element of a photon with energy $\hbar\omega_{inc}$ and momentum $\hbar k_{inc}$, exciting an electron from the 4-Mpy HOMO to levels near the ZnO CB. The holes of the HOMO in turn couple mode selectively to molecular vibrations. After recombination of the electrons with the holes in the HOMO, photons with ω_{sc} and k_{sc} are emitted. Equivalently, Figure 2b shows the transition of electrons from the VB to the LUMO, which also couple mode selectively to the molecular vibrations of 4-Mpy. The resonance energies are determined by the transitions between HOMO and CB and between VB and LUMO, respectively (see Figure 3b).

The measured intensity of the scattered light $I(\omega)$ is proportional to the imaginary part of the Raman response function $\tilde{R}(\omega)$. For resonance Raman scattering the response function depends on the incidence photon energy $\hbar\omega_{inc}$. After correction for the scattering volume and for a constant temperature, we can calculate the scattering intensity as[31]

$$I(\omega,\omega_{inc}) = -\mathrm{Im}(\tilde{R}(\omega,\omega_{inc})) \quad (1)$$

We can express eq 1 in terms of the Feynman diagram representing the four-photon Green's function, as shown in Figure 2a,b as a resonant Raman response function.[38] In order to derive a simple expression for the modeling of our results, the Feynman diagram can be approximated with the following simplifying assumptions:

- The vibrational excitation itself is independent of the electronic susceptibility requiring that the energy scales of electronic degrees of freedom (a few eV) are decoupled from the molecular vibrational degrees of freedom (smaller than 0.1 eV).

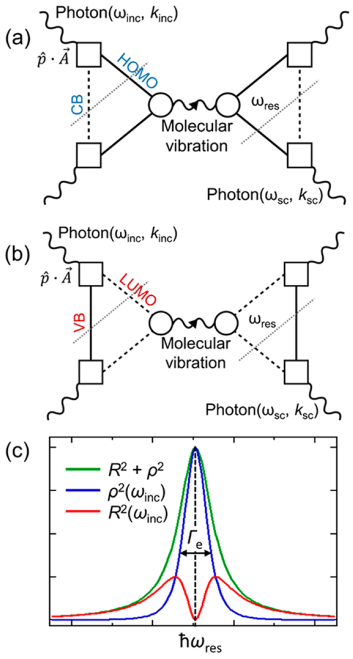

Figure 2. Feynman diagram illustrating the four-photon Green's function of the resonant Raman scattering process coupling electronic states to vibrations. (a) shows the UV resonance occurring between the molecular HOMO level and the semiconductor CB, whereas (b) shows the visible resonance occurring between the semiconductor VB and the molecular LUMO. Both resonances are denoted as dotted lines. Squares depict the photon−electron interaction, where $\hat{p}\cdot\vec{A}$ denotes the matrix element that is linear in the vector potential $\vec{A}$. Photons are represented by wavy lines. The electronic transitions occur between occupied states (solid lines, HOMO, VB) and unoccupied states (dashed lines, CB, LUMO). Circles represent the coupling between electrons and the molecular vibration, which is shown in the middle of the diagram as a wavy line with a rightward arrow. (c) Representation of the squared real part $R^2(\omega)$ (red) and the squared imaginary part $\rho^2(\omega)$ (blue) of the polarization as expressed in eqs 4, 7a, and 7b. The sum of both parts shown in green represents the resonance enhancement of the Raman susceptibility. We have set $\Gamma_e/\hbar\omega_{res}$ equal to 0.02.

- Couplings are constant, real, and independent of the momentum.

Then, we can simplify the Feynman diagram to the following expression

$$\tilde{R}(\omega,\omega_{inc}) = T_e{}^4 g_{ep}{}^2 \left(\;\right)^2 D_0\,, \quad (2)$$

where T_e is the photon−electron interaction, g_{ep} denotes the electron−phonon coupling constant, D_0 is the vibrational excitation, and denotes the electronic polarizability. Since g_{ep} represents the coupling between an electronic state and molecular vibration, mode selective enhancement can be induced by this factor. The vibrational excitation D_0 with an eigenfrequency of ω_0 and a damping Γ_{vib}, consisting of an imaginary part D_0^{Im} and a real part D_0^{Re} is given by eq 3. The electronic polarizability consists of imaginary and real parts as shown in eq 4, where ω_{inc} is the frequency of the incident photons.

$$D_0 = \frac{1}{\omega^2 - \omega_0{}^2 + 2i\Gamma_{vib}\omega} = D_0^{Re} + iD_0^{Im} \quad (3)$$

DOI: 10.1021/acs.jpcc.9b07329
J. Phys. Chem. C 2019, 123, 24957−24962

$$\left(\vec{\ }\right)^2 = [R(\omega_{inc}) + i\rho(\omega_{inc})]^2 = R^2(\omega_{inc}) + \rho^2(\omega_{inc}) \quad (4)$$

After substitution eqs 4 and 3 into eq 2 and calculating the imaginary part to obtain the scattering intensity according to eq 1, we find the following expression:

$$I(\omega,\omega_{inc}) = T_e^4 g_{ep}^2 \cdot [R^2(\omega_{inc}) + \rho^2(\omega_{inc})] \cdot \frac{2\Gamma_{vib}\omega}{(\omega^2 - \omega_0^2)^2 + (2\Gamma_{vib}\omega)^2} \quad (5)$$

In order to find an expression for the polarization, we have to understand it as a collective excitation between the HOMO and CB, or VB and LUMO, respectively. In discrete molecular states, the polarization is given by a constant C_{max}. The general form of the propagator in the CB or VB is given in eq 6, where ε_k is the respective dispersion relation of electrons and holes in the semiconductor, ω_{elec} is the electronic energy, and δ_k represents the electronic damping.

$$G_0(\vec{k},\omega_{elec}) = \frac{1}{\omega_{elec} - \varepsilon_k + i\delta_k} \quad (6)$$

The real part $R(\omega_{inc})$ and imaginary part $\rho(\omega_{inc})$ of the polarization (see eq 4) can now be written as shown in eqs 7a and 7b. From eq 6 we can derive that the maximum contribution to the transition within the semiconductor occurs at the top of the VB and the bottom of the CB. Note that with the experimentally observed lifetime of the electronic states and the small energy difference between ingoing and outgoing resonances, as shown in Figure 2 as dotted lines cannot be resolved. Hence, we set the resonance energy as simply $E_{HOMO} - E_{CB,min} = \hbar\omega_{res}$ (see also Figure 3b).[39] The inverse lifetime of this electronic excitation is denoted as Γ_e. Figure 2c shows the square of the real and imaginary parts of the electronic susceptibility, $R^2(\omega_{inc})$ and $\rho^2(\omega_{inc})$, to which the phonon couples, respectively. The sum of both parts yields the resonance enhancement factor, $R^2(\omega_{inc}) + \rho^2(\omega_{inc})$. We use this for fitting the resonance profile, as shown in Figure 3a. It is interesting to observe that the enhancement gets significantly widened by considering the real part of the electronic susceptibility and that this is also generating the dominant "off-resonance" contribution.

$$C_{max}^2 \cdot R^2(\omega_{inc}) = C_{max}^2 \cdot \left(\frac{(\omega_{res} - \omega_{inc})}{(\omega_{inc} - \omega_{res})^2 + \Gamma_e^2}\right)^2 \quad (7a)$$

$$C_{max}^2 \cdot \rho^2(\omega_{inc}) = C_{max}^2 \cdot \left(\frac{\Gamma_e}{(\omega_{inc} - \omega_{res})^2 + \Gamma_e^2}\right)^2 \quad (7b)$$

In the case of several resonance levels, a simple superposition of the Feynman diagram in Figure 2 leads after a similar calculation to eq 8, where $\tilde{\alpha}_i = T_{e,i}^4 g_{ep,i}^2 C_{max,i}^2$.

$$I(\omega,\omega_{inc}) = \sum_i \tilde{\alpha}_i \cdot [R_i^2(\omega_{inc}) + \rho_i^2(\omega_{inc})] \cdot \frac{2\Gamma_{vib}\omega}{(\omega^2 - \omega_0^2)^2 + (2\Gamma_{vib}\omega)^2} \quad (8)$$

Our model is in agreement with the approach by others representing the effective resonance process as product of electronic and vibrational wave functions.[39,40]

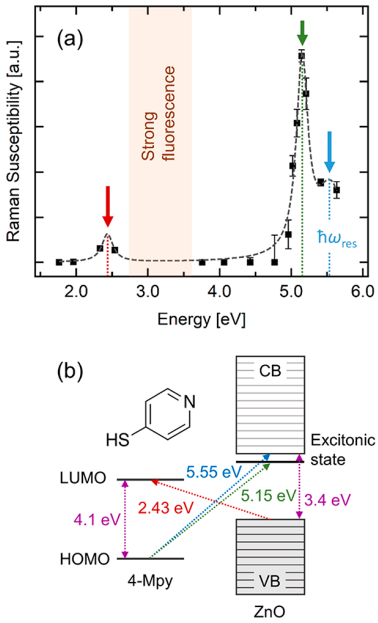

Figure 3. (a) SERS Raman susceptibility (intensity of the Raman response of a 4-Mpy monolayer on ZnO rods) of the mode at 1000 cm^{-1} plotted against the excitation energy. We found a resonance at 2.43 eV and two further resonance levels in the ultraviolet spectral range at 5.15 and 5.55 eV. The resonance profile was fitted by eq 8 (detailed information in the text). (b) Pictorial energy model of the investigated system, outlining the observed resonances in (a) due to the indicated optical transitions. The intrinsic resonance transition of 4-Mpy from HOMO to LUMO (4.1 eV) and the band gap of ZnO (3.4 eV) are shown in violet.

Figure 3a shows the results of our fit to the vibrational intensities, i.e., the resonance Raman profile of the 4-Mpy ring-breathing mode according to the resonance enhancement factors in eq 8. As expected we observe two main resonances, which we can attribute to transitions from the molecular HOMO to the CB in the UV and from the semiconductor VB to the molecular LUMO in the visible. Surprisingly, the UV resonance consists of two contributions. The initial resonance at 5.15 eV is very sharp and responsible for the strong resonance enhancement observed at 5.14 eV in Figure 1a. Above 5.25 eV we observe a shoulder with substantial scattering intensity, as evidenced by the 5.64 eV measurement in Figure 1a. The fit of these resonance levels shows that they are split by about 400 meV. This corresponds in good agreement to the energy difference between the CB and the quantum confined excitonic state in 10−20 nm thick ZnO.[30] As shown in Table 1, the excitonic state exhibits a long lifetime resulting in a damping of only 0.0967 eV, leading to a surprisingly sharp resonance. It is shifted from 50 meV to about 400 meV below the band gap due to confinement effects in thin films. In our case the internal structure of the nanowalled microrods is about 10−20 nm, leading to an enhanced binding energy and stabilization of the exciton.[29,30] Since ZnO has a polar termination surface, one would expect that the direct interface of ZnO is passivated by environmental gases such as H_2O and CO_2 adsorbed directly after the manufacturing process, which prevents the formation of hybrid states with the adsorbed molecule.[30]

Thus, the sharp resonance enhancement in the deep UV is dominated by the presence of an excitonic state induced by the

DOI: 10.1021/acs.jpcc.9b07329
J. Phys. Chem. C 2019, 123, 24957−24962

Table 1. Fit Parameters Corresponding to Figure 2a and Eqs 7a, 7b, and 8 for the Two Observed Resonance in the UV and the Visible[a]

resonance	$\hbar\omega_{res}$ [eV]	σ_E [eV]	$\hbar\Gamma_e$ [eV]	σ_Γ [eV]	$\tilde{\alpha}$	σ_α
UV 1	5.152	6.76×10^{-3}	0.09667	1.15×10^{-2}	4.433×10^{-3}	0.487×10^{-3}
UV 2	5.551	53.1×10^{-3}	0.2500		7.046×10^{-3}	0.565×10^{-3}
Vis	2.435		0.09282	1.16	1.636×10^{-3}	8.92×10^{-3}

[a] σ_E, σ_Γ, and σ_α denote the standard deviations of $\hbar\omega_{res}$, $\hbar\Gamma_e$, and $\tilde{\alpha}$, respectively.

quantum confinement of the 10−20 nm thick ZnO. In the visible the resonance is by a factor of 15 weaker and occurs due to the transition between the semiconductor VB and molecular LUMO without the involvement of any excitonic states. The competing resonance phenomena are summarized in Figure 3b. The red arrow shows the transition at 2.43 eV between the VB and the LUMO, whereas the green and blue arrows denote the deep UV transitions from the HOMO to the excitonic states and the CB. However, it is also clear that the deep UV excitation energies are above the intrinsic "bulk" resonance energies in 4-Mpy, specifically the HOMO to LUMO transition. In Figure 3b the energy splitting of both the molecular HOMO−LUMO levels that is expected to be around 4.1 eV and the ZnO CB to VB splitting that is expected to be around 3.4 eV are shown in violet.[30] The mid UV resonance enhancement of the ZnO modes can be exemplarily seen in Figure 1b for the measurement at 3.76 eV. The presence of intramolecular resonances and charge-transfer resonances between molecule and semiconductor will modify the nominal SERS enhancement factor. Details on the SERS enhancement can be found in the Supporting Information.

CONCLUSION

We studied the SERS effect of 4-mercaptopyridine adsorbed on an array of nanostructured zinc-oxide microrods by resonance Raman spectroscopy in the ultraviolet and visible spectral range. We described the observed resonances by using a phenomenological model based on a four-photon Green's function calculation of the Raman intensity. Two resonances in the UV at 5.15 and 5.55 eV as well as one resonance in the visible at around 2.43 eV were observed. The strongest resonance is found in the UV at 5.15 eV and results from transitions into an excitonic-related state below the ZnO CB. This excitonic resonance is the result of quantum confinement effects in the 10−20 nm thick ZnO nanowalls and the signal enhancement exceeds the visible resonance by a factor of 15. Our results lead to a better detectability and new opportunities to optimize the chemical SERS effect of molecules adsorbed on semiconductor nanostructured rods.

ASSOCIATED CONTENT

Supporting Information

The Supporting Information is available free of charge on the ACS Publications website at DOI: 10.1021/acs.jpcc.9b07329.

Details on the experimental section (SERS substrate preparation and Resonance Raman setup) and the phonon fitting, as well as an estimate on the UV SERS factor (PDF)

AUTHOR INFORMATION

Corresponding Authors

*jayeongkim93@gmail.com.
*tglier@physnet.uni-hamburg.de.
*ruebhausen@physnet.uni-hamburg.de.
*syoon@ewha.ac.kr.

ORCID

Jayeong Kim: 0000-0003-3975-0856
Tomke E. Glier: 0000-0001-8943-1509
Seokhyun Yoon: 0000-0002-4533-646X

Author Contributions

J.K., T.E.G., B.G.L., S.B., M.T., F.B., M.R., and S.Y. conducted the UV−vis Raman measurements. T.E.G., M.R., J.K., and S.Y. analyzed the data and wrote the manuscript. N.J.K., H.K., G.C.Y., and J.K. produced the samples. All authors reviewed the manuscript and did approve submission.

Author Contributions

‖These authors contributed equally.

Notes

The authors declare no competing financial interest.

ACKNOWLEDGMENTS

This work is supported by Basic Science Research Program (NRF-2016R1D1A1B01009032, NRF-2018R1A6A1A03025340) through the National Research Foundation of Korea (NRF) and the Global Research Laboratory Program through the National Research Foundation of Korea (NRF) funded by the Ministry of Science, ICT, and Future Planning (NRF-2015K1A1A2033332 and NRF-2015R1A5A1037627). T.E.G. is partially funded by the Helmholtz Society through DESY, DFG (Deutsche Forschungs Gesellschaft) RU773/8-1.

ABBREVIATIONS

4-Mpy, 4-mercaptopyridine; CB, conduction band; CCD, charge-coupled device; CVD, chemical vapor deposition; EF, SERS enhancement factor; HOMO, highest occupied molecular orbital; LUMO, lowest unoccupied molecular orbital; SERS, surface-enhanced Raman spectroscopy; SiO_2, silicon dioxide; UV, ultraviolet; VB, valence band; vis, visible; ZnO, zinc oxide

REFERENCES

(1) Fleischmann, M.; Hendra, P. J.; McQuillan, A. J. Raman Spectra of Pyridine Adsorbed at a Silver Electrode. *Chem. Phys. Lett.* **1974**, *26*, 163−166.
(2) Moskovits, M. Surface-Enhanced Spectroscopy. *Rev. Mod. Phys.* **1985**, *57*, 783−826.
(3) Jeanmaire, D. L.; Van Duyne, R. P. Surface Raman Spectroelectrochemistry. *J. Electroanal. Chem. Interfacial Electrochem.* **1977**, *84*, 1−20.
(4) Smith, E.; Dent, G. *Modern Raman Spectroscopy - A Practical Approach*; John Wiley & Sons, Ltd.: Chichester, U.K., 2005.
(5) Otto, A. Surface-Enhanced Raman Scattering of Adsorbates. *J. Raman Spectrosc.* **1991**, *22*, 743−752.
(6) Moskovits, M. Surface-Enhanced Raman Spectroscopy: A Brief Retrospective. *J. Raman Spectrosc.* **2005**, *36*, 485−496.

DOI: 10.1021/acs.jpcc.9b07329
J. Phys. Chem. C 2019, 123, 24957−24962

(7) Stiles, P. L.; Dieringer, J. A.; Shah, N. C.; Van Duyne, R. P. Surface-Enhanced Raman Spectroscopy. *Annu. Rev. Anal. Chem.* **2008**, *1*, 601−626.
(8) Xu, H.; Bjerneld, E. J.; Käll, M.; Börjesson, L. Spectroscopy of Single Hemoglobin Molecules by Surface Enhanced Raman Scattering. *Phys. Rev. Lett.* **1999**, *83*, 4357−4360.
(9) Nie, S.; Emory, S. R. Probing Single Molecules and Single Nanoparticles by Surface-Enhanced Raman Scattering. *Science* **1997**, *275*, 1102−1106.
(10) Li, J. F.; Huang, Y. F.; Ding, Y.; Yang, Z. L.; Li, S. B.; Zhou, X. S.; Fan, F. R.; Zhang, W.; Zhou, Z. Y.; Wu, D. Y.; et al. Shell-Isolated Nanoparticle-Enhanced Raman Spectroscopy. *Nature* **2010**, *464*, 392−395.
(11) Tao, A.; Kim, F.; Hess, C.; Goldberger, J.; He, R.; Sun, Y.; Xia, Y.; Yang, P. Langmuir−Blodgett Silver Nanowire Monolayers for Molecular Sensing Using Surface-Enhanced Raman Spectroscopy. *Nano Lett.* **2003**, *3*, 1229−1233.
(12) Santoro, G.; Yu, S.; Schwartzkopf, M.; Zhang, P.; Koyiloth Vayalil, S.; Risch, J. F. H.; Rübhausen, M. A.; Hernández, M.; Domingo, C.; Roth, S. V. Silver Substrates for Surface Enhanced Raman Scattering: Correlation between Nanostructure and Raman Scattering Enhancement. *Appl. Phys. Lett.* **2014**, *104*, 243107.
(13) David, C.; Guillot, N.; Shen, H.; Toury, T.; Chapelle, M. L. de la SERS Detection of Biomolecules Using Lithographed Nanoparticles towards a Reproducible SERS Biosensor. *Nanotechnology* **2010**, *21*, 475501.
(14) Fan, M.; Andrade, G. F. S.; Brolo, A. G. A Review on the Fabrication of Substrates for Surface Enhanced Raman Spectroscopy and Their Applications in Analytical Chemistry. *Anal. Chim. Acta* **2011**, *693*, 7−25.
(15) Kneipp, K.; Kneipp, H.; Itzkan, I.; Dasari, R. R.; Feld, M. S. Surface-Enhanced Raman Scattering and Biophysics. *J. Phys.: Condens. Matter* **2002**, *14*, R597−R624.
(16) Kneipp, K.; Wang, Y.; Kneipp, H.; Perelman, L. T.; Itzkan, I.; Dasari, R. R.; Feld, M. S. Single Molecule Detection Using Surface-Enhanced Raman Scattering (SERS). *Phys. Rev. Lett.* **1997**, *78*, 1667−1670.
(17) Fini, G. Applications of Raman Spectroscopy to Pharmacy. *J. Raman Spectrosc.* **2004**, *35*, 335−337.
(18) Izake, E. L. Forensic and Homeland Security Applications of Modern Portable Raman Spectroscopy. *Forensic Sci. Int.* **2010**, *202*, 1−8.
(19) Xue, X.; Ji, W.; Mao, Z.; Mao, H.; Wang, Y.; Wang, X.; Ruan, W.; Zhao, B.; Lombardi, J. R. Raman Investigation of Nanosized TiO_2: Effect of Crystallite Size and Quantum Confinement. *J. Phys. Chem. C* **2012**, *116*, 8792−8797.
(20) Stockman, M. I. Electromagnetic Theory of SERS. In *Surface-Enhanced Raman Scattering*; Kneipp, K., Moskovits, M., Kneipp, H., Eds.; Springer: Berlin, Heidelberg, 2006; pp 47−65.
(21) Santoro, G.; Yu, S.; Schwartzkopf, M.; Zhang, P.; Koyiloth Vayalil, S.; Risch, J. F. H.; Rübhausen, M. A.; Hernández, M.; Domingo, C.; Roth, S. V. Silver Substrates for Surface Enhanced Raman Scattering: Correlation between Nanostructure and Raman Scattering Enhancement. *Appl. Phys. Lett.* **2014**, *104*, 243107.
(22) Alessandri, I.; Lombardi, J. R. Enhanced Raman Scattering with Dielectrics. *Chem. Rev.* **2016**, *116*, 14921−14981.
(23) Kim, N.-J.; Kim, J.; Park, J.-B.; Kim, H.; Yi, G.-C.; Yoon, S. Direct Observation of Quantum Tunnelling Charge Transfers between Molecules and Semiconductors for SERS. *Nanoscale* **2019**, *11*, 45−49.
(24) Wang, X.; Shi, W.; She, G.; Mu, L. Surface-Enhanced Raman Scattering (SERS) on Transition Metal and Semiconductor Nanostructures. *Phys. Chem. Chem. Phys.* **2012**, *14*, 5891−5901.
(25) Shin, H.-Y.; Shim, E.-L.; Choi, Y.-J.; Park, J.-H.; Yoon, S. Giant Enhancement of the Raman Response Due to One-Dimensional ZnO Nanostructures. *Nanoscale* **2014**, *6*, 14622−14626.
(26) Ding, S.-Y.; You, E.-M.; Tian, Z.-Q.; Moskovits, M. Electromagnetic Theories of Surface-Enhanced Raman Spectroscopy. *Chem. Soc. Rev.* **2017**, *46*, 4042−4076.
(27) Caldarola, M.; Albella, P.; Cortés, E.; Rahmani, M.; Roschuk, T.; Grinblat, G.; Oulton, R. F.; Bragas, A. V.; Maier, S. A. Non-Plasmonic Nanoantennas for Surface Enhanced Spectroscopies with Ultra-Low Heat Conversion. *Nat. Commun.* **2015**, *6*, 7915.
(28) Yu, P. Y.; Cardona, M. *Fundamentals of Semiconductors*, 4th ed.; Springer: Heidelberg, Dordrecht, London, New York, 1996.
(29) Ramsay, A. J. A. Review of the Coherent Optical Control of the Exciton and Spin States of Semiconductor Quantum Dots. *Semicond. Sci. Technol.* **2010**, *25*, 103001.
(30) Mosquera, A. A.; Horwat, D.; Rashkovskiy, A.; Kovalev, A.; Miska, P.; Wainstein, D.; Albella, J. M.; Endrino, J. L. Exciton and Core-Level Electron Confinement Effects in Transparent ZnO Thin Films. *Sci. Rep.* **2013**, *3*, 1714.
(31) Schulz, B.; Bäckström, J.; Budelmann, D.; Maeser, R.; Rübhausen, M.; Klein, M. V.; Schoeffel, E.; Mihill, A.; Yoon, S. Fully Reflective Deep Ultraviolet to near Infrared Spectrometer and Entrance Optics for Resonance Raman Spectroscopy. *Rev. Sci. Instrum.* **2005**, *76*, 073107.
(32) Krüger, R.; Schulz, B.; Naler, S.; Rauer, R.; Budelmann, D.; Bäckström, J.; Kim, K. H.; Cheong, S.-W.; Perebeinos, V.; Rübhausen, M. Orbital Ordering in $LaMnO_3$ Investigated by Resonance Raman Spectroscopy. *Phys. Rev. Lett.* **2004**, *92*, 097203.
(33) Hoffmann, A.; Binder, S.; Jesser, A.; Haase, R.; Flörke, U.; Gnida, M.; Salomone Stagni, M.; Meyer-Klaucke, W.; Lebsanft, B.; Grünig, L. E.; et al. Catching an Entatic State-A Pair of Copper Complexes. *Angew. Chem., Int. Ed.* **2014**, *53*, 299−304.
(34) Park, S. I.; Tchoe, Y.; Baek, H.; Heo, J.; Hyun, J. K.; Jo, J.; Kim, M.; Kim, N.-J.; Yi, G.-C. Growth and Optical Characteristics of High-Quality ZnO Thin Films on Graphene Layers. *APL Mater.* **2015**, *3*, 016103.
(35) Kim, Y.-J.; Yoo, H.; Lee, C.-H.; Park, J. B.; Baek, H.; Kim, M.; Yi, G.-C. Position- and Morphology-Controlled ZnO Nanostructures Grown on Graphene Layers. *Adv. Mater.* **2012**, *24*, 5565−5569.
(36) Zhang, L.; Bai, Y.; Shang, Z.; Zhang, Y.; Mo, Y. Experimental and Theoretical Studies of Raman Spectroscopy on 4-Mercaptopyridine Aqueous Solution and 4-Mercaptopyridine/Ag Complex System. *J. Raman Spectrosc.* **2007**, *38*, 1106−1111.
(37) Hu, H.; Song, W.; Ruan, W.; Wang, Y.; Wang, X.; Xu, W.; Zhao, B.; Ozaki, Y. Fabrication of One-Dimensional ZnO/4-Mpy/Ag Assemblies and Their Spectroscopic Studies. *J. Colloid Interface Sci.* **2010**, *344*, 251−255.
(38) Kawabata, A. Green Function Theory of Raman Scattering. *J. Phys. Soc. Jpn.* **1971**, *30*, 68−85.
(39) Galperin, M.; Ratner, M. A.; Nitzan, A. Raman Scattering in Current-Carrying Molecular Junctions. *J. Chem. Phys.* **2009**, *130*, 144109.
(40) Lombardi, J. R.; Birke, R. L. Theory of Surface-Enhanced Raman Scattering in Semiconductors. *J. Phys. Chem. C* **2014**, *118*, 11120−11130.

DOI: 10.1021/acs.jpcc.9b07329
J. Phys. Chem. C 2019, 123, 24957−24962

Quantum Confinement of the Spin-Berry Phase on 1D Topological Surfaces of Single Bi_2Se_3 Nanowires

Christian Nweze*, Tomke E. Glier*, Sarah Scheitz, Lea Westphal, Florian Biebl, Sören Buchenau, Lewis O. Akinsinde, Niklas Kohlmann, Lorenz Kienle, Isabel González Díaz-Placio, Robert Frömter, Robert Zierold, Robert Blick, Nils Huse, Michael Rübhausen*.

Submitted to Nano Letters

Quantum Confinement of the Spin Berry Phase on 1D Topological Surfaces of Single Bi_2Se_3 Nanowires

Christian Nweze[‡1], Tomke E. Glier[*‡1], Sarah Scheitz[1], Lea Westphal[1], Florian Biebl[1], Sören Buchenau[1], Lewis O. Akinsinde[1,2], Niklas Kohlmann[2], Lorenz Kienle[2], Isabel González Díaz-Placio[3], Robert Frömter[3], Robert Zierold[3], Robert Blick[3], Nils Huse[3], and Michael Rübhausen[*‡1]*

[1] Institut für Nanostruktur- und Festkörperphysik, Center for Free Electron Laser Science (CFEL), Universität Hamburg, Luruper Chaussee 149, 22761, Hamburg, Germany

[2] Institute for Materials Science, Faculty of Engineering, Kiel University, Kaiserstrasse 2, 24143 Kiel, Germany

[3] Institut für Nanostruktur- und Festkörperphysik, Center for Hybrid Nanostructures (CHyN), Universität Hamburg, Luruper Chaussee 149, 22761, Hamburg, Germany

Topological insulators (TIs) exhibit unconventional quantum phases that can be tuned by external quantum confinements. The geometrical crossover from 2D to 1D in a TI results in a novel state with a Spin Berry Phase (SBP). We use Raman scattering on single crystalline Bi_2Se_3-TI nanowires to track the geometrical crossover from quasi 2D to quasi 1D. It is marked by the sudden appearance of plasmonic surface-enhanced Raman scattering (SERS) in nanowires below 100 nm diameter. A magnetic field applied along the wire axis results in a quenched SERS, providing clear evidence that spin-polarized plasmonic excitations of the SBP dominate the electronic excitation spectrum.

Topological insulators (TIs) exhibit Dirac cones, segments of nearly linear dispersion, where both dispersion branches have opposite spin orientation.[1–3] The spin-polarized bands make TIs interesting candidates for many applications such as room-temperature spintronics, quantum computing, and thermoelectric generators.[4] Experimental studies report on the investigation of electrical transport properties from nano-ribbons.[5–11] TIs offer an exciting avenue to study physical anomalies and unconventional states in matter.[6] In particular, geometric quantum confinement leads to exciting effects. For instance, morphing a 3D TI such a Bi_2Se_3 into a 1D cylinder leads to a splitting of the 2D conical Dirac band structure of the SS into 1D discrete subbands.[12,13] As a consequence, 1D plasmonic bands are formed with gaps in the electronic excitation spectrum due to self-interference of the electronic wave functions around the cylinder perimeter. These gaps are inversely proportional to the wire diameter.[12,14] Electronic bands of the TI are spin-polarized and consequently a Spin Berry Phase (SBP) is formed. The application of a magnetic field along the wire axis adds an additional phase shift to the electronic wave function yielding a high sensitivity to small magnetic fluxes and as a consequence the restoration of the Dirac cone for magnetic fields of the order of a single flux quantum.[12,14,15]

In 3D TIs with planar geometry, such as 2D-flakes and thin films, optical studies of plasmons have provided a deep insight into their electronic structure.[16–22] Raman scattering on TIs has revealed the thickness-dependent quantum confinement of phonons in Bi_2Se_3 flakes and thin films.[20–23] Plasmonic excitations at surfaces can enhance the Raman scattering cross-section by surface-enhanced Raman scattering (SERS).[24,25] Thus, Raman scattering is a powerful tool to study the low-energy excitation spectrum, which is determined by novel plasmonic states, and to understand the coupling between spin, charge, and lattice degrees of freedom in TIs.

Low-energy 1D plasmonic excitations of TIs have an energy scale of the order of 10 meV.[12,13] Direct absorption measurements of the plasmonic excitations will fail, as these low energies correspond to electromagnetic wavelengths of more than 100 μm exceeding the nanowire diameter by far. In this letter, we report on the study of single nanowires in a diameter range suitable to study the geometrical crossover from 2D to 1D TI SS and provide evidence for the presence of a SBP in nanowires with a diameter below 100 nm. We have designed a micro-Raman setup[26] that uses a circular diffraction limited spot with a diameter of (544 ± 13) nm within a magnetic field provided by two permanent magnets (Fig. 1(a) and (b), see SI 4). The heating of the wire even for powers of 140 μW from a 532 nm diode laser, was mitigated by scanning along the nanowire axis (see Fig. 1(a)). We have synthesized circular Bi_2Se_3 nanowires with lengths from 5 μm to 35 μm (see Fig. 1(d)-(f)) and diameters ranging from 22 nm to 800 nm (see SI 2). Bi_2Se_3 nanowires with diameters down to 42 nm together with the laser focus were observed in the custom-made optical microscope, enabling a precise control of the scanning procedure (see Fig. 1(d)). The cylindrical shape of the nanowires is demonstrated by scanning electron microscopy (SEM) and atomic force microscopy (AFM) images (Fig. 1(e) and (f), see SI 2). High-resolution transmission electron

microscopy (HRTEM) confirms the single crystallinity of the wires and a 1D wire growth perpendicular to c-axis direction along the [11-20] axis (Fig. 1(c)) in agreement with previous growth mechanisms.[8,27] The wires exhibit an amorphous oxide shell as can be seen in Fig. 1(c), which is also evident in energy filtered TEM maps of the Oxygen-K edge (see lower inset and SI 2). Energy-dispersive X-ray spectroscopy (EDX) studies shown in the SI (SI 2) support the 2:3 (Bi:Se) stoichiometry. The wire, its quintuple layers, and orientation during the experiment are shown in Fig. 1(b) with the c-axis being perpendicular to the wire axis. We expect a Raman spectrum of phonons that is essentially comparable to that of a conventional 2D-flake of Bi_2Se_3.[23,28] Magneto-transport measurements on devices as shown in Fig. 1(g) obtained from a 260 nm diameter wire reveal the presence of metallic SS. Weak anti-localization effects prove the strong spin-orbit coupling, which is prerequisite for the band inversion and the formation of Dirac-like SS. The measurements show a magnetic field-dependent crossover between 2D- and 1D-electrical transport in agreement with previous observations.[29–31] From the transport measurements the Fermi vectors can be estimated to be $k_F = (1.24 \pm 0.42) \cdot 10^{-2}$ Å^{-1} leading to an effective carrier concentration $n = (k_F)^2/2\pi = 4.9 \cdot 10^{11}$ cm^{-2} in good agreement with the 2:3 stoichiometry. More details are given in SI 8.

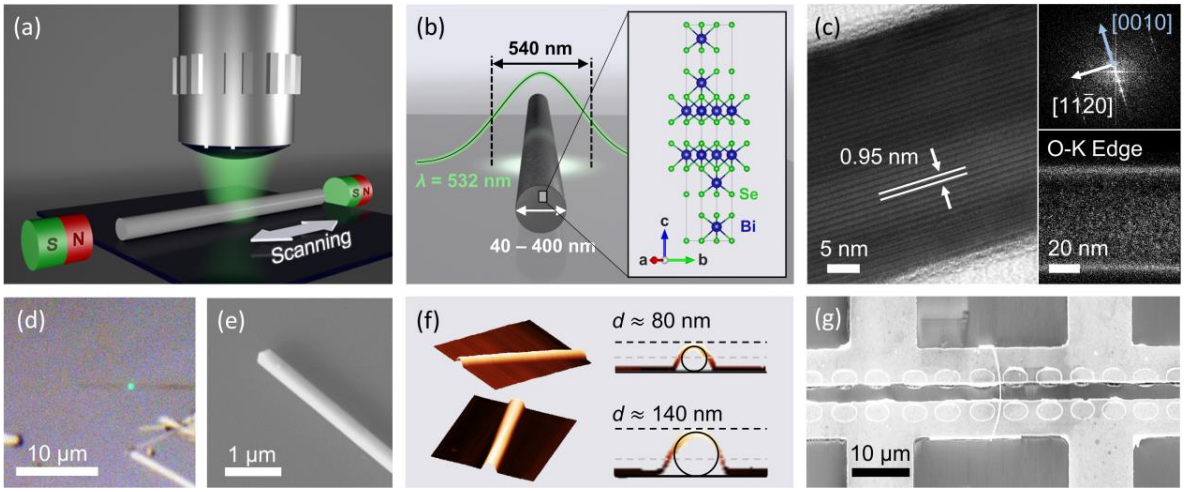

Figure 1. Experimental setup and sample characterization: (a) Sketch of the experimental Raman setup. A 532 nm diode laser beam is focused on a single Bi_2Se_3 nanowire. The scan direction along the wire axis is shown (white arrow). A magnetic field can be applied along the wire axis. (b) Schematic illustration of the quintuple layers and the wire growth in relation to the Raman experiments. (c) HRTEM micrograph of a wire (42 nm diameter). The wire is viewed along [2-1-10] showing the quintuple layer stacking. The FFT shown in the upper inset reveals a growth direction of [11-20] orthogonal to the c-axis. The lower inset presents an exemplary EFTEM elemental map of the O-K edge at approx. 530 eV. (d) Microscopy image of a wire with 73 nm diameter and the laser spot (green). (e) SEM image of a 316 nm wire. (f) Cross-sections as determined by AFM on wires with 80 nm and 140 nm diameter, respectively. The shapes are approximated by circles. (g) Device for transport measurements. The SEM image shows the 260 nm wire connected to the Cr contacts.

The results of the Raman measurements as a function of nanowire diameter are shown in Fig. 2. In Fig. 2(a) we observe the E^2_g- and A^2_{1g}-modes of the Bi_2Se_3 phonons characteristic for the structure building quintuple layers.[32] The measurements of the 2D flake and the 411 nm nanowire show nearly identical phonon modes, which is in agreement with the stacking of the quintuple layers perpendicular to the wire elongation. The observed Raman intensity decreases proportional to the square of the wire diameter reflecting the decreased scattering volume. Finally, at around 200 nm, the signal strength of the nanowires is lost. Four nanowires with diameters between 180 nm and 225 nm were measured confirming this result. Surprisingly, the intensity of the Raman signal from wires smaller than 100 nm starts to increase again, peaking around 60 nm. This observation marks a clear crossover from a 2D to a 1D behaviour. In order to model the contributing phonons, the line shape can be described by Lorentz- or Fano-profiles.[33–36] The details of the line shape analysis are given in SI 6. For the sake of clarity, we fit Lorentz-profiles to the phonons. In Fig. 2(b) we plot the energy difference between the E^2_g- and A^2_{1g}-modes, which is reduced by about 0.3 meV as the wire diameter is decreased. The simultaneous changes in intensity and relative phonon position point clearly towards the interaction of the phonon with an electronic mode that is characteristic for a 1D confined TI (see SI 7). The intensities of the E^2_g- and A^2_{1g}-modes divided by the square of the wire diameter and normalized to the susceptibility of the 411 nm wire are plotted in Fig. 2(c) and (d). While the E^2_g-mode intensity peaks at a wire diameter of 55 nm the A^2_{1g}-modes intensity continues to rise indicating that the highest intensity of the A^2_{1g}-mode occurs below 40 nm. These results suggest a coupling of these phonons to an electronic low-energy excitation with an excitation energy depending on the diameter of the wire.

For circular 3D TIs, surface charges build up with decreasing wire diameter.[12] The resulting electric field can couple to the photon field in Raman scattering. Surface enhanced Raman scattering (SERS) shows Raman enhancements between 10^2 and 10^9 in resonance with surface plasmons of metallic nanoparticles.[24,25] Since the frequency of the optical photons and the frequency of the plasmons in TIs are expected to be different by two orders of magnitude, we adopt a non-resonant picture of the Raman process. This assumption is supported by the fact that the spectra in the 1D regime reveal the same contributing phonons that are present in the 2D limit, suggesting that a local field enhancement effect amplifies the conventional response. This mechanism is pictorially shown in Fig. 3(a). For 3D TI SS that are confined in 1D a photon excites plasmons and the phonons coupling to them get enhanced. In this context, the phonons act as low-energy probe of the electronic excitation spectrum. The energies of the E^2_g-mode and the A^2_{1g}-mode are 15.6 meV and 20.86 meV matching the expected energy scale of the plasmon in the 1D confined SS.[12] The largest effect is expected when the energy of the plasmon matches the phonon energy. Note, the same plasmon that is responsible for the enhancement of the Raman process also interacts with the phonon so that we would expect changes in the phonon frequencies as observed in Fig. 2(b). As shown in SI 6, the E_g^2-mode exhibits a distinctive enhancement of the Fano-

parameter at smaller NW diameter concomitantly with an enhanced width (broadening) and shift in mode frequency (hardening) clearly indicating the presence of a novel low-energy mode.[33–35]

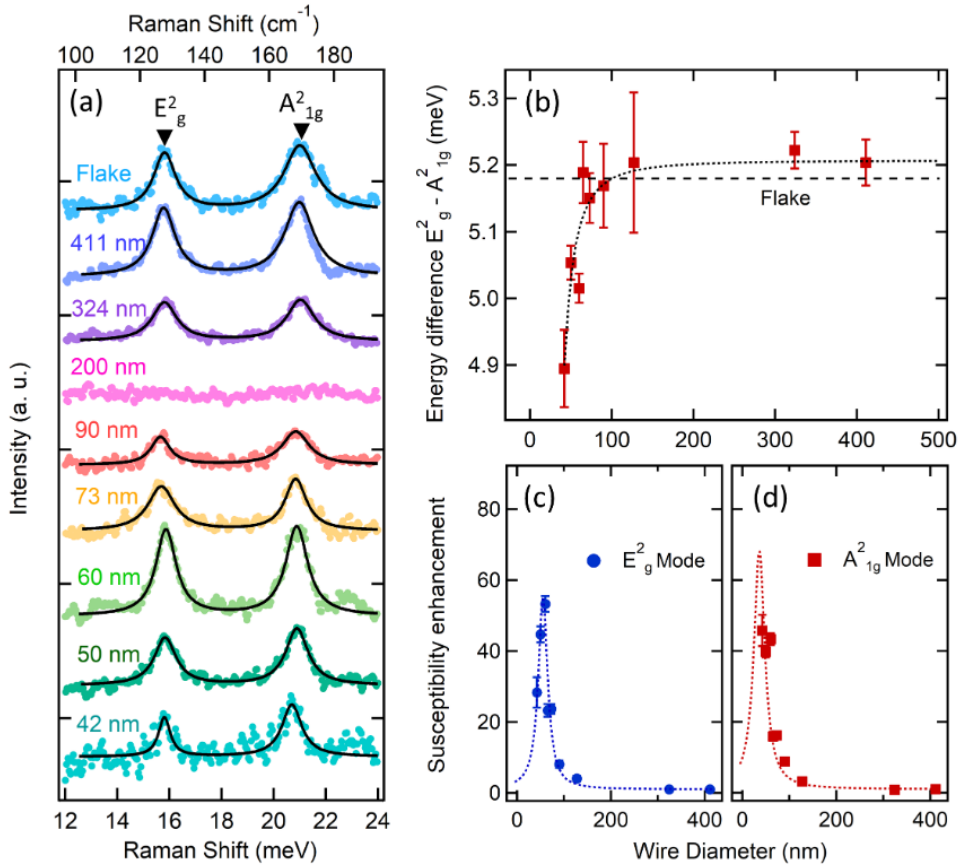

Figure 2. Experimental Raman data: (a) Raman spectra of Bi_2Se_3 nanowires with diameters from 411 nm to 42 nm, as well as from a Bi_2Se_3 flake with a thickness of 10 nm. (b) Energy difference between the E^2_g- and the A^2_{1g}-modes as function of wire diameter. The dashed line guides the eye. (c) Raman susceptibility of the E^2_g-mode and (d) Raman susceptibility of the A^2_{1g}-mode as function of wire diameter. Curves were normalized to their respective susceptibilities at 411 nm. A Lorentzian with a maximum at a wire diameter of 55 nm models the E^2_g-mode susceptibility. (d) A Lorentzian with a maximum at 36 nm was added as guide to the eye.

A novel quasi-particle excitation in an unconventional quantum state reveals itself by its dispersion relation. Experimentally, one would vary the momentum to probe the dispersion relation. However, the plasmonic dispersion relation depends strongly on the wire diameter. Therefore, our study on single nanowires as a function of wire diameter is suitable to track the dispersion of electronic excitations in the SBP. The dispersion relation of electronic states of a 1D cylinder in a magnetic field is given by[12,37],

$$\varepsilon_{k,m,r}(R_0) = \pm C_2\sqrt{k^2 + (1 + 2m - 2r)^2\,\tilde{\Delta}^2(R_0)} \quad , \tag{1}$$

with a gap opening in the electronic excitation spectrum that is inversely proportional to the wire diameter

$$\tilde{\Delta}(R_0) = \frac{C_1}{C_2}\frac{1}{2R_0} = \frac{\alpha}{d} \quad . \tag{2}$$

C_1 and C_2 are the inter-spin and inter-orbital coupling constants. R_0 and d are the radius and diameter of the wire, respectively. k is the momentum, m is the sub-band quantum number, and r is the magnetic flux ratio along the wire axis in units of an elementary flux quantum. We take the following values. $m = 0$ assuming that only one sub-band is occupied. This is motivated by the 2:3 stoichiometry (see EDX analysis in SI 2) and transport studies (see SI 8). $k = 0.0005$ Å^{-1} is compatible with the averaged photon momentum transferred to the electrons along the wire axis. From Ref. [12] one obtains $C_2 = C_1 = 3.33$ eV Å. However, we have obtained $\alpha = 0.866$ leading to $C_1 = 2.88$ eV Å. With these parameters, we plot the electronic energies of the first sub-band as a function of wire diameter in Fig. 3(b). The energies of the E^2_g- and A^2_{1g}-phonons are marked by straight lines. Two essential conclusions can be made: Firstly, the impact of the cylindrical quantum confinement becomes relevant for wire diameters below 100 nm and, secondly, the energies of E^2_g-mode and the A^2_{1g}-mode match the excitation energies of the 1D plasmon at slightly different wire diameters of 55 nm and 36 nm, respectively. Both observations are well in line with the key findings in our experiment (Fig. 2(c) and (d)), strongly suggesting that the phonons couple to the photons by means of the electronic SS of the cylindrical TI. Note, with increasing magnetic flux parallel to the NW axis, it is possible to quench these plasmonic excitations, which vanish for a fractional magnetic flux quantum of $r = 0.5$.[12] Since the topological properties are dominated by the centre of the Brillouin Zone and as we apply a $q \approx 0$ Raman probe, we will evaluate the Feynman diagram in the $k = q \approx 0$ limit. From the Feynman diagram shown in Fig. 3(a)[38] we obtain:

$$I(\omega, R_0) = -\mathrm{Im}\left[M_0^2\,\chi^2_{\mathrm{Plas}}(R_0)\,\chi_{\mathrm{Phon}}\right] \quad , \tag{3}$$

where $M_0^2 = \left|\frac{A^2_{\mathrm{local}}}{A^2}\right|^2 g^2$, with A^2 being the first order non-resonant term of the light-matter interaction to a free electronic particle and g being the electron-phonon coupling constant. A^2_{local} is representing the local field enhancement, which we estimate to be of the order of 10 A^2. The plasmonic susceptibility depends now critically on R_0 due to the dispersion relation (equation (1)). The real and imaginary parts of the plasmonic susceptibility can be modelled by[39]

$$\chi_{\mathrm{Plas}}(R_0) = \frac{1}{\omega^2 - \left(2\varepsilon_{k,m,r}(R_0)\right)^2 + 2i\frac{\varepsilon_{k,m,r}(R_0)}{\tau_k}} \quad , \tag{4}$$

with τ_k being the plasmon lifetime. The phonon susceptibility is given by

$$\chi_{\mathrm{Phon}}(\omega_0, \Gamma) = \frac{1}{\omega^2 - \omega_0^2 + 2i\Gamma} \ . \qquad (5)$$

The observed Raman intensity depends on the radius of a nanowire *via* the dispersion relation (equation (1)) in the susceptibility of the 1D-plasmon. The required input parameters were fixed in the following way. The bare phonon frequencies ω_0 and damping constants Γ for both phonons were taken from the 2D limit, i.e. fits to the phonon spectrum of the flake. The dispersion in equation (4) was identical to the one shown in Fig. 3(b). The only unknown parameter is the plasmon lifetime. It determines the width of the resonance as a function of wire diameter. For the calculations shown in Fig. 3(c) we have assumed an interaction of both phonons with one and the same plasmonic excitation and an estimated plasmon lifetime of 500 ps. When comparing Fig. 2(c) and (d) with Fig. 3(d), it is evident that our simplified calculation can reproduce the experimentally derived different resonance behaviours of the E^2_g- and A^2_{1g}-modes by considering a single plasmonic mode that obeys the dispersion relation of equation (1) with $m = 0$ and $r = 0$ (for more details see SI 7).

If these plasmons originate from the proposed SBP they should be very sensitive to the application of even small magnetic fields, as indicated by the sensitivity of the dispersion (equation (1)) to an applied magnetic field (see Fig. 3(b)). The critical value is half a flux quantum.[12] For wires of 90 nm and 62 nm diameter this corresponds to magnetic fields of about 165 mT and 350 mT, respectively. We have applied a field in axial geometry as outlined in Fig. 1(a). The results are shown for a 62 nm wire in Fig. 3(e) with a field of 80 mT corresponding to $r = 0.13$ in equation (1). The effect was reproduced for a wire with a diameter of 90 nm (see SI 4). The SERS is completely quenched with an applied magnetic field and recovers to the original results without field. This behaviour is even more dramatic than anticipated by our model. The calculation in Fig. 3(f), performed with the same parameters as the calculations in Fig. 3(c), would indicate a strongly suppressed E^2_g -mode but only a 40 % suppression on the high energy A^2_{1g}-mode. Yet, we could not find any sign of the A^2_{1g}-mode in magnetic field measurements on wires with diameters of 62 nm and 90 nm. The extraordinarily strong magnetic field suppression clearly supports the presence of the SBP in 1D quantum confined TIs. Furthermore, the strong dependence suggest that magnetic fields applied along the wire axis influence parameters such as the ratio α indicating changed inter-spin or inter-orbital coupling constants.

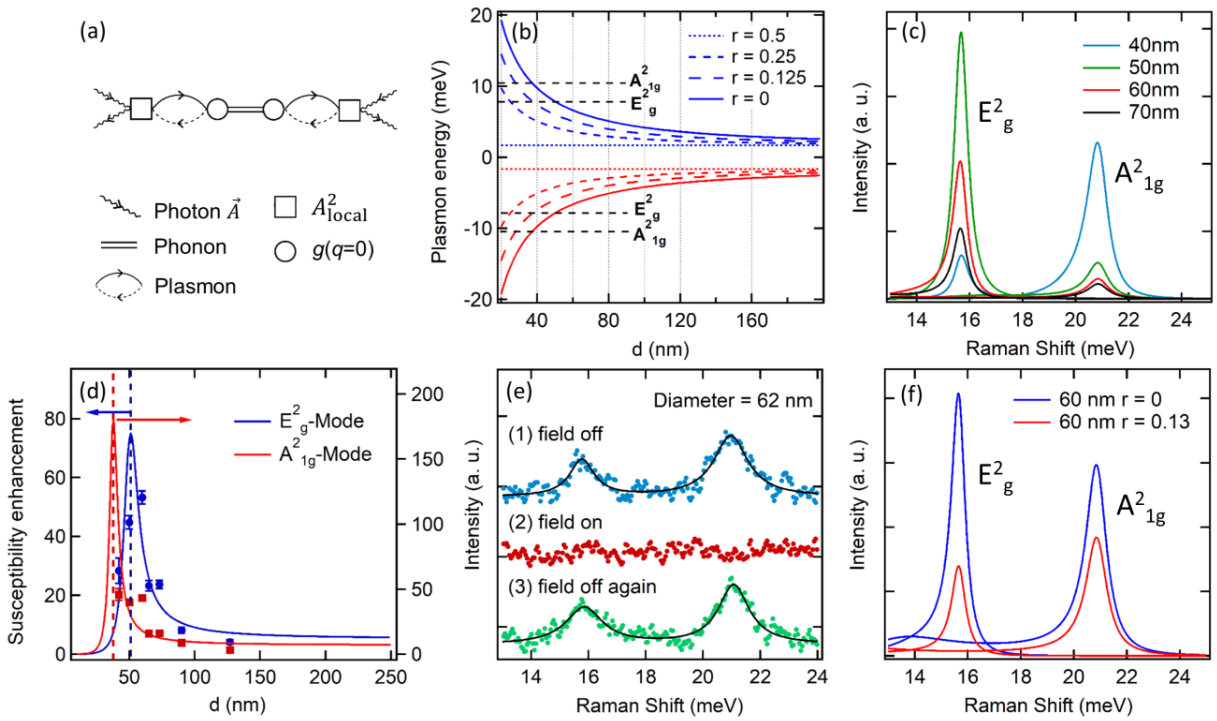

Figure 3. Simulation of the Raman data: (a) Feynman diagram showing the Raman process for phonons. (b) Dispersion $\varepsilon_{k,m,r}(R_0)$ for $m = 0$ (first sub band) of a cylindrical nanowire for finite momentum k = 0.0005 Å^{-1} as a function of wire diameter with $\alpha = 0.866$ and ratios r of the magnetic flux quantum ($r = 0$ to r = 0.5). Dashed straight lines mark the phonon energies. As the gap opens, the surface plasmons interact with the phonons and enhance the observed Raman phonon intensities. (c) Calculated non-resonant SERS of the 1D TI nanowires for different wire diameters. The E^2_g-mode at 15.6 meV goes into resonance for larger wire diameters as compared to the A^2_{1g}-mode at 20.86 meV. (d) Calculated (solid line) and experimentally observed (markers) susceptibility enhancement of the E^2_g- and A^2_{1g}-mode. The Raman susceptibilities were normalized to the susceptibilities at 411 nm. (e) Experimental Raman spectra of a 62 nm wire without, with, and again without magnetic field of 80 mT (see SI 4). (f) Simulated Raman spectra as a function of magnetic field.

In conclusion, we have shown the geometrical crossover from a 2D to 1D confined topologically protected SS below a critical nanowire diameter of about 100 nm. The 1D TI SS exhibits SERS that is strongly dependent on the diameter of the nanowires. We attribute these effects to novel spin-polarized plasmonic excitations within the SBP. We support this assignment by the observed SERS signal and the signal quenching induced by very small magnetic fluxes along the wire axis. The basic features of our experiments could be understood by modelling the coupling between spin-polarized 1D plasmons of the TI with the phonons. The 1D plasmons obey the expected dispersion relation and the only free parameters used in our model are α and τ representing the ratio between inter-spin to inter-orbital coupling strengths and the plasmon lifetime, respectively. Thus, we have provided clear evidence that spin-polarized plasmonic excitations of the SBP

dominate the electronic excitation spectrum and we have established a new route to study low-energy excitation spectrum of 1D TI nanowires by means of Raman scattering.

ASSOCIATED CONTENT

Supporting Information. PDF is available divided into the following sections: Bi_2Se_3 nanowire synthesis (SI 1); Sample characterization (SI 2); Raman measurements (SI 3); Magnetic field dependent Raman measurements (SI 4); Data analysis (SI 5); Line shape analysis (SI 6); Calculation (SI 7); Nanowires and magnetic-transport measurements (SI 8).

AUTHOR INFORMATION

Corresponding Author

* C.N.: cnweze@physnet.uni-hamburg.de, T.E.G.: tglier@physnet.uni-hamburg.de, M.R.: ruebhausen@physnet.uni-hamburg.de

Author Contributions

Design of the study: M.R., C.N., T.E.G.; Oven CVD: C.N. L.A. S.B.; Sample synthesis and fabrication: C.N.; Raman setup: M.R., T.E.G., L.W., F.B.; Raman measurements: T.E.G., C. N., L.W., S.S., M.R.; SEM/EDX: R.F., C.N., N.H., S.S.; TEM/EDX: N.K., C.N., L.K., L.A.; AFM: C.N., S.S., F.B.; Transport measurements and analysis: R.Z., I.G.D.-P., R.B., C.N., S.B.; Device fabrication: C.N., I.G.D.-P., R.Z., R.B.; Theory and simulation: M.R. and T.E.G.; Writing of the manuscript: M.R., T.E.G., C.N., N.H., with input from all co-authors. ‡These authors contributed equally.

Funding Sources

We acknowledge financial support via HGF/DESY and DFG RU 773/8-1 (M.R.) and KI 1263/17-1 (L.K.). C.N. is Funded by Tertiary Education Trust Fund (TETFund) Abuja, Nigeria, through Nnamdi Azikiwe University, Awka, Nigeria under Academic Staff Training and Development Programme.

ACKNOWLEDGMENT

The authors thank Dirk Manske (MPI Stuttgart), Andrivo Rusydi (NUS), and Lance Cooper (UIUC) for productive discussions. We acknowledge the Siemens PLM Software for using Solid Edge 2020.

ABBREVIATIONS

AFM, atomic force microscopy; EFTEM, energy filtered TEM; FFT, fast Fourier transformation; SBP, Spin Berry Phase; SEM, scanning electron microscopy; SERS, surface enhanced Raman

scattering; SS, surface states; TEM, transmission electron microscopy; HRTEM, high resolution TEM; TI, topological insulator.

REFERENCES

(1) Fu, L.; Kane, C. L.; Mele, E. J. Topological Insulators in Three Dimensions. *Phys. Rev. Lett.* **2007**, *98* (10), 106803. https://doi.org/10.1103/PhysRevLett.98.106803.

(2) Fu, L.; Kane, C. L. Topological Insulators with Inversion Symmetry. *Phys. Rev. B* **2007**, *76* (4), 045302. https://doi.org/10.1103/PhysRevB.76.045302.

(3) Qi, X.-L.; Zhang, S.-C. Topological Insulators and Superconductors. *Rev. Mod. Phys.* **2011**, *83* (4), 1057–1110. https://doi.org/10.1103/RevModPhys.83.1057.

(4) Eibl, O.; Nielsch, K.; Peranio, N.; Völklein, F. *Thermoelectric Bi2Te3 Nanomaterials*; Eibl, O., Nielsch, K., Peranio, N., Völklein, F., Eds.; Wiley-VCH Verlag GmbH & Co. KGaA: Weinheim, Germany, 2015. https://doi.org/10.1002/9783527672608.

(5) Dufouleur, J.; Veyrat, L.; Teichgraeber, A.; Neuhaus, S.; Nowka, C.; Hampel, S.; Cayssol, J.; Schumann, J.; Eichler, B.; Schmidt, O.; et al. Quasi-Ballistic Transport of Dirac Fermions in a Bi2Se3 Nanowire. *Phys. Rev. Lett.* **2012**, *110* (18), 186806. https://doi.org/10.1103/PhysRevLett.110.186806.

(6) Gooth, J.; Niemann, A. C.; Meng, T.; Grushin, A. G.; Landsteiner, K.; Gotsmann, B.; Menges, F.; Schmidt, M.; Shekhar, C.; Süß, V.; et al. Experimental Signatures of the Mixed Axial–Gravitational Anomaly in the Weyl Semimetal NbP. *Nature* **2017**, *547* (7663), 324–327. https://doi.org/10.1038/nature23005.

(7) Peng, H.; Lai, K.; Kong, D.; Meister, S.; Chen, Y.; Qi, X.-L.; Zhang, S.-C.; Shen, Z.-X.; Cui, Y. Aharonov–Bohm Interference in Topological Insulator Nanoribbons. *Nat. Mater.* **2010**, *9* (3), 225–229. https://doi.org/10.1038/nmat2609.

(8) Kong, D.; Randel, J. C.; Peng, H.; Cha, J. J.; Meister, S.; Lai, K.; Chen, Y.; Shen, Z.-X.; Manoharan, H. C.; Cui, Y. Topological Insulator Nanowires and Nanoribbons. *Nano Lett.* **2010**, *10* (1), 329–333. https://doi.org/10.1021/nl903663a.

(9) Hong, S. S.; Zhang, Y.; Cha, J. J.; Qi, X.-L.; Cui, Y. One-Dimensional Helical Transport in Topological Insulator Nanowire Interferometers. *Nano Lett.* **2014**, *14* (5), 2815–2821. https://doi.org/10.1021/nl500822g.

(10) Zhang, K.; Pan, H.; Wei, Z.; Zhang, M.; Song, F.; Wang, X.; Zhang, R. Synthesis and Magnetotransport Properties of Bi2Te3 Nanowires. *Chinese Phys. B* **2017**, *26* (9), 096101. https://doi.org/10.1088/1674-1056/26/9/096101.

(11) Bardarson, J. H.; Brouwer, P. W.; Moore, J. E. Aharonov-Bohm Oscillations in Disordered Topological Insulator Nanowires. *Phys. Rev. Lett.* **2010**. https://doi.org/10.1103/PhysRevLett.105.156803.

(12) Iorio, P.; Perroni, C. A.; Cataudella, V. Plasmons in Topological Insulator Cylindrical Nanowires. *Phys. Rev. B* **2017**, *95* (23), 235420. https://doi.org/10.1103/PhysRevB.95.235420.

(13) Imura, K.-I.; Takane, Y.; Tanaka, A. Spin Berry Phase in Anisotropic Topological Insulators. *Phys. Rev. B* **2011**, *84* (19), 195406. https://doi.org/10.1103/PhysRevB.84.195406.

(14) Iorio, P.; Perroni, C. A.; Cataudella, V. Quantum Interference Effects in Bi2Se3 Topological Insulator Nanowires with Variable Cross-Section Lengths. *Eur. Phys. J. B* **2016**, *89* (4), 97. https://doi.org/10.1140/epjb/e2016-70041-7.

(15) Shi, L.-K.; Lou, W.-K. Surface States of Bi2Se3 Nanowires in the Presence of Perpendicular Magnetic Fields. *Chinese Phys. Lett.* **2014**, *31* (6), 067304. https://doi.org/10.1088/0256-307X/31/6/067304.

(16) Zhang, H.; Liu, C.-X.; Qi, X.-L.; Dai, X.; Fang, Z.; Zhang, S.-C. Topological Insulators in Bi2Se3, Bi2Te3 and Sb2Te3 with a Single Dirac Cone on the Surface. *Nat. Phys.* **2009**, *5* (6), 438–442. https://doi.org/10.1038/nphys1270.

(17) Fei, Z.; Andreev, G. O.; Bao, W.; Zhang, L. M.; McLeod, A. S.; Wang, C.; Stewart, M. K.; Zhao, Z.; Dominguez, G.; Thiemens, M.; et al. Infrared Nanoscopy of Dirac Plasmons at the Graphene–SiO2 Interface. *Nano Lett.* **2011**, *11* (11), 4701–4705. https://doi.org/10.1021/nl202362d.

(18) Lai, Y.-P.; Lin, I.-T.; Wu, K.-H.; Liu, J.-M. Plasmonics in Topological Insulators. *Nanomater. Nanotechnol.* **2014**, *4* (1), 13. https://doi.org/10.5772/58558.

(19) Autore, M.; Engelkamp, H.; D'Apuzzo, F.; Gaspare, A. Di; Pietro, P. Di; Vecchio, I. Lo; Brahlek, M.; Koirala, N.; Oh, S.; Lupi, S. Observation of Magnetoplasmons in Bi2Se3 Topological Insulator. *ACS Photonics* **2015**, *2* (9), 1231–1235. https://doi.org/10.1021/acsphotonics.5b00036.

(20) Glinka, Y. D.; Babakiray, S.; Lederman, D. Plasmon-Enhanced Electron-Phonon Coupling in Dirac Surface States of the Thin-Film Topological Insulator Bi2Se3. *J. Appl. Phys.* **2015**, *118* (13), 135713. https://doi.org/10.1063/1.4932667.

(21) Shahil, K. M. F.; Hossain, M. Z.; Goyal, V.; Balandin, A. A. Micro-Raman Spectroscopy

of Mechanically Exfoliated Few-Quintuple Layers of Bi2Te3, Bi2Se3, and Sb2Te3 Materials. *J. Appl. Phys.* **2012**, *111* (5), 054305. https://doi.org/10.1063/1.3690913.

(22) Eddrief, M.; Atkinson, P.; Etgens, V.; Jusserand, B. Low-Temperature Raman Fingerprints for Few-Quintuple Layer Topological Insulator Bi2Se3 Films Epitaxied on GaAs. *Nanotechnology* **2014**, *25* (24), 245701. https://doi.org/10.1088/0957-4484/25/24/245701.

(23) Zhang, J.; Peng, Z.; Soni, A.; Zhao, Y.; Xiong, Y.; Peng, B.; Wang, J.; Dresselhaus, M. S.; Xiong, Q. Raman Spectroscopy of Few-Quintuple Layer Topological Insulator Bi2Se3 Nanoplatelets. *Nano Lett.* **2011**, *11* (6), 2407–2414. https://doi.org/10.1021/nl200773n.

(24) Lee, S. J.; Guan, Z.; Xu, H.; Moskovits, M. Surface-Enhanced Raman Spectroscopy and Nanogeometry: The Plasmonic Origin of SERS. *J. Phys. Chem. C* **2007**, *111* (49), 17985–17988. https://doi.org/10.1021/jp077422g.

(25) Santoro, G.; Yu, S.; Schwartzkopf, M.; Zhang, P.; Koyiloth Vayalil, S.; Risch, J. F. H.; Rübhausen, M. A.; Hernández, M.; Domingo, C.; Roth, S. V. Silver Substrates for Surface Enhanced Raman Scattering: Correlation between Nanostructure and Raman Scattering Enhancement. *Appl. Phys. Lett.* **2014**, *104* (24), 243107. https://doi.org/10.1063/1.4884423.

(26) Schulz, B.; Bäckström, J.; Budelmann, D.; Maeser, R.; Rübhausen, M.; Klein, M. V.; Schoeffel, E.; Mihill, A.; Yoon, S. Fully Reflective Deep Ultraviolet to near Infrared Spectrometer and Entrance Optics for Resonance Raman Spectroscopy. *Rev. Sci. Instrum.* **2005**, *76* (7), 073107. https://doi.org/10.1063/1.1946985.

(27) Yan, Y.; Liao, Z.-M.; Zhou, Y.-B.; Wu, H.-C.; Bie, Y.-Q.; Chen, J.-J.; Meng, J.; Wu, X.-S.; Yu, D.-P. Synthesis and Quantum Transport Properties of Bi2Se3 Topological Insulator Nanostructures. *Sci. Rep.* **2013**, *3* (1), 1264. https://doi.org/10.1038/srep01264.

(28) Buchenau, S.; Akinsinde, L. O.; Zocher, M.; Rukser, D.; Schürmann, U.; Kienle, L.; Grimm-Lebsanft, B.; Rübhausen, M. Scalable Polyol Synthesis for Few Quintuple Layer Thin and Ultra High Aspect Ratio Bi2Se3 Structures. *Solid State Commun.* **2018**, *281*, 49–52. https://doi.org/10.1016/j.ssc.2018.07.003.

(29) Buchenau, S.; Sergelius, P.; Wiegand, C.; Bäßler, S.; Zierold, R.; Shin, H. S.; Rübhausen, M.; Gooth, J.; Nielsch, K. Symmetry Breaking of the Surface Mediated Quantum Hall Effect in Bi2Se3 Nanoplates Using Fe3O4 Substrates. *2D Mater.* **2017**, *4* (1), 015044. https://doi.org/10.1088/2053-1583/aa525e.

(30) Bäßler, S.; Hamdou, B.; Sergelius, P.; Michel, A.-K.; Zierold, R.; Reith, H.; Gooth, J.; Nielsch, K. One-Dimensional Edge Transport on the Surface of Cylindrical Bi x Te 3−y Se y Nanowires in Transverse Magnetic Fields. *Appl. Phys. Lett.* **2015**, *107* (18), 181602. https://doi.org/10.1063/1.4935244.

(31) Hamdou, B.; Gooth, J.; Dorn, A.; Pippel, E.; Nielsch, K. Aharonov-Bohm Oscillations and Weak Antilocalization in Topological Insulator Sb 2 Te 3 Nanowires. *Appl. Phys. Lett.* **2013**, *102* (22), 223110. https://doi.org/10.1063/1.4809826.

(32) Richter, W.; Becker, C. R. A Raman and Far-Infrared Investigation of Phonons in the Rhombohedral V2–VI3 Compounds Bi2Te3, Bi2Se3, Sb2Te3 and Bi2(Te1−xSex)3 (0 <x < 1), (Bi1−ySby)2Te3 (0 <y < 1). *Phys. Status Solidi* **1977**, *84* (2), 619–628. https://doi.org/10.1002/pssb.2220840226.

(33) Bock, A.; Ostertun, S.; Das Sharma, R.; Rübhausen, M.; Subke, K.-O.; Rieck, C. T. Anomalous Self-Energy Effects of the B1g Phonon in Y1-x(Pr,Ca)XBa2Cu3O7 Films. *Phys. Rev. B* **1999**, *60* (5), 3532–3537. https://doi.org/10.1103/PhysRevB.60.3532.

(34) Chen, X. K.; Altendorf, E.; Irwin, J. C.; Liang, R.; Hardy, W. N. Oxygen-Concentration Dependence of the Raman Continua in YBa2Cu3Oy Single Crystals. *Phys. Rev. B* **1993**, *48* (14), 10530–10536. https://doi.org/10.1103/PhysRevB.48.10530.

(35) Friedl, B.; Thomsen, C.; Cardona, M. Determination of the Superconducting Gap in RBa2Cu3O7−δ. *Phys. Rev. Lett.* **1990**, *65* (7), 915–918. https://doi.org/10.1103/PhysRevLett.65.915.

(36) Cooper, S. L.; Klein, M. V. Light Scattering Studies of the Low Frequency Excitation Spectra of High Temperature Superconductors. *Comments Cond. Mat. Phys* **1990**, *15* (2), 99–124. https://doi.org/10.1007/978-3-662-04221-2_6.

(37) Bechstedt, F. *Many-Body Approach to Electronic Excitations - Concepts and Applications*; 2015. https://doi.org/10.1007/978-3-662-44593-8_19.

(38) Kawabata, A. Green Function Theory of Raman Scattering. *J. Phys. Soc. Japan* **1971**, *30* (1), 68–85. https://doi.org/10.1143/JPSJ.30.68.

(39) Mattuck, R. D. *A Guide to Feynman Diagrams in the Many-Body Problem*; 1967.

Chapter 5

5 Acknowledgments

"Die Geschichte der Griechischen Philisophie von Thales bis zu Platon ist großartig. Sie ist fast zu schön, um wahr zu sein. In jeder Generation finden wir eine neue Philosophie, eine neue Kosmologie von atemberaubender Originalität und Tiefe. Wie war das möglich? Es gibt natürlich keine Erklärung für Originalität und Tiefe. Aber man kann versuchen, vielleicht etwas Licht auf diese Entwicklung zu werfen. Was war das Geheimnis der Alten? Ich vermute, es war eine neuentstandene Tradition - die Tradition der kritischen Diskussion."

Karl R. Popper in *Karl Popper Lesebuch: Ausgewählte Texte zur Erkenntnistheorie, Philosophie der Naturwissenschaften, Metaphysik, Sozialphilosophie.*[225]

At this point I want to express my gratitude to all people who worked with me and who supported me during my thesis. I am surrounded by a team without whom this research would not have been possible. I am very grateful for the opportunity to be able to contribute to excellent research in a great location under best conditions. First of all, I would like to thank **Michael Rübhausen** for the supervision, support, guidance, and creative collaboration. The joint research taught me, step by step, how to become a scientist. I was allowed to do this in an environment, in which I recognized science as an inexhaustible source of new, fascinating, and illuminating moments. Michael, I am grateful for this opportunity. In this context, I also gratefully acknowledge the co-supervision of this thesis by **Stephan V. Roth**. Thank you, Stephan, for being a backbone and source of inspiration for joint projects with P03 at DESY. I thank both of you for introducing me to the international research community.

Many thanks to **Benjamin Grimm-Lebsanft** for your all-out assistance and guidance in programming and lab work. Thank you for your effort and for being always a contact person to me. I am grateful to **Christian Nweze** for very inspiring lab experiences and discussions about science and culture. Christian, I hope for a long term cooperation in the future. I would like to thank **Florian Biebl** for the diverse cooperation, and support and help in countless situations. Thanks to **Lewis Akinsinde**, who supported me from the scientific and technical side, and who is a source of good and positive vibes at any

time. I am thankful to **Melissa Teubner** for the warm neighboring in the office and her scientific input.

I am particularly grateful to **Sarah Scheitz** for fruitful joint projects and a very coherent collaboration. Sarah, I thank you for you support during all the beam times and I hope that we will keep up our good team work. I thank **Sören Buchenau** for a scientific partnership that began when we were learning the basics of nanosciences in the university lecture hall and which finally brought me to the research group. I am always very happy when our scientific projects overlap. Many thanks to **Stephanie Baer** for her support in administrative processes, but also for being a permanent, helpful, and always encouraging contact person.

Thank you to everyone else who has invested their time and energy in promoting collaborative scientific projects. In this context I thank **Dorothee Herrmann**, **Isa Moch**, **Mika Rerrer**, and **Patrick Klein**. Thanks to **Ferdinand Otto**, **Malwin Paufler**, **Mariam Hashemi**, **Lukas Grote**, and **Lukas Daams**, who laid the groundwork of the synthesis of conductive nano composites in the group. I also benefited by the outstanding work of **Marie Betker**, who obtained excellent results in stretching of flexible nanowire composites during her Master's project. The same applies to **Lea Westphal**, who made a significant contribution to the development of the micro-Raman instrument with her Bachelor's project and, apart from that, brings great enthusiasm, joy and creativity to the team. It is also very important to me to say thank you to **Malte van Heek** for his profound scientific inspiration and inventiveness, and for being a friend who supported me in every opportunity. I am very grateful for our deep connection.

Furthermore, I would like to thank **Matthias Schwartzkopf** for using the sputter chamber and Plasma equipment, many support during beam times, and general scientific input. I am grateful to the whole team of P03. I thank **Milena Lippmann**, **Wiebke Ohm**, **Marc Gensch**, **Andrei Chumakov**, and **Calvin J. Brett** for the productive cooperation.

Thank you **Andrivo Rusydi** for the opportunity to visit the Singapore Synchrotron Light Source in June 2019. It was an absolutely outstanding trip to a great research location, which unfortunately passed far too quickly. I thank **Pranab Kumar Das**, **Teguh Citra Asmara**, **Muhammad Avicenna Naradipa**, and **Jason Lim Chee Wai** for the nice time and scientific collaboration at the SSLS.

I sincerely thank **Soekhyun Yoon** and **Jayeong Kim** from Ewha Womans University (Seoul, Korea) for a highly interesting and inspiring international research collaboration, which extended this thesis by a chemical SERS study.

I appreciate the fruitful cooperation with **Frank Fischer** and **Maximilian Witte** from Beiersdorf AG, who widened the analysis of nanowire network morphology by their innovative FINE method.

I thank **Lorenz Kienle**, **Niklas Kohlmann**, and everyone involved from Christian-Albrechts-Universität Kiel for the collaboration resulting in excellent TEM studies on the topological insulator nanowires.

Many thanks to **Nils Huse** and **Robert Frömter** for the possibility to use the scanning electron microscope, the atomic force microscope, as well as for their scientific input in our work on topological insulators.

I thank **Toru Matsuyama**, **Boris Fiedler**, and **Birger Höhling** from Max-Planck Institute for the Structure and Dynamics of Matter for their support in electrical measurements and the fabrication of circuit boards.

Furthermore, I would like to acknowledge all help from the CFEL community, in particular from **Ralf Koehn**, **Gisbert Mantei**, and **Sakir Sagir**.

The support from my family was and is of particular importance to me. I thank my grandparents **Monika & Walter Glier**, my aunt and uncle **Antje & Mark Paßkowski**, and my cousins **Janik & Lotta Paßkowski** for always being a loving home to me. I also thank **Dieter, Tino, & Nantje Kügler** for their interest in my work. I thank my mother **Sabine Glier** for promoting my interests and standing behind me in every situation. The same applies to my father **Christian Glier**, whom I also thank for accompanying my studies and reading all papers with great enthusiasm.

Finally, I would like to apologize for the fact that I have certainly not been able to name everyone who made this research possible. I see science as a large community and I am grateful to be part of it.

The Latex template was provided by the Ostbayerische Technische Hochschule Regensburg. I acknowledge Siemens for using Solid Edge 2020, Maxon Computer GmbH for using the Cinema 4D student license, and Autodesk for a 3DS Max student license.

I appreciate the funding of the Universität Hamburg and the Helmholtz Society through DESY.

Chapter 6

6 Literature

[1] Feynman, R. P. There's plenty of room at the bottom. *Engineering and Science* **1960**, *23*, 22–36.

[2] Kossovsky, A. E. *The birth of science*; Springer, Cham, 2020.

[3] Habing, H. J. *The birth of modern astronomy*; Springer, Cham, 2018.

[4] Honerkamp, J. *Die Vorsokratiker und die moderne Physik*; Springer, Berlin, Heidelberg, 2020.

[5] Breidbach, O. *Geschichte der Naturwissenschaften I: Die Antike*; Springer Spektrum, Berlin, Heidelberg, 2015.

[6] Evans, L. Particle accelerators at CERN: From the early days to the LHC and beyond. *Technological Forecasting and Social Change* **2016**, *112*, 4–12.

[7] Whitesides, G. M. Nanoscience, nanotechnology, and chemistry. *Small* **2005**, *1*, 172–179.

[8] Durner, J. Clinical chemistry: challenges for analytical chemistry and the nanoscience from medicine. *Angewandte Chemie* **2010**, *49*, 1026–1051.

[9] Hoffmann, R. Small but strong lessons from chemistry for nanoscience. *Angewandte Chemie* **2013**, *52*, 93–103.

[10] Bhushan, B. In *Springer Handbook of Nanotechnology*; Bhushan, B., Ed.; Springer, Berlin, Heidelberg., 2004; Chapter Introduction to nanotechnology, pp 1–6.

[11] Morris, R. E.; Wheatley, P. S. Gas storage in nanoporous materials. *Angewandte Chemie* **2008**, *47*, 4966–4981.

[12] De, M.; Ghosh, P. S.; Rotello, V. M. Applications of nanoparticles in biology. *Advanced Materials* **2008**, *20*, 4225–4241.

[13] Bhaskaran, S.; Franz, J. M. Optimal design of gas pipeline networks. *Journal of the Operational Research Society* **1979**, *30*, 1047–1060.

[14] Glier, T. E. *et al.* Functional printing of conductive silver-nanowire photopolymer composites. *Scientific Reports* **2019**, *9*, 6465.

[15] Glier, T. E.; Betker, M.; Witte, M.; Matsuyama, T.; Westphal, L.; Grimm-Lebsanft, B.; Biebl, F.; Akinsinde, L. O.; Fischer, F.; Rübhausen, M. Electrical and network properties of flexible silver-nanowire composite electrodes under mechanical strain. *Nanoscale* **2020**, *20*, 23831–23837.

[16] Verma, P.; Gupta, L.; Abbi, S. C.; Jain, K. P. Confinement effects on the electronic and vibronic properties of $CdS_{0.65}Se_{0.35}$ nanoparticles grown by thermal annealing. *Journal of Applied Physics* **2000**, *88*, 4109–4116.

[17] Mohammad, S. N. Understanding quantum confinement in nanowires: basics, applications and possible laws. *Journal of Physics: Condesed Matter* **2014**, *26*, 423202.

[18] Iijima, S. Helical microtubules of graphitic carbon. *Nature* **1991**, *354*, 56–58.

[19] Sun, Y.; Gates, B.; Mayers, B.; Xia, Y. Crystalline silver nanowires by soft solution processing. *Nano Letters* **2002**, *2*, 165–168.

[20] Seisyan, R. P. Nanolithography in microelectronics: a review. *Technical Physics* **2011**, *81*, 1–14.

[21] Piraux, L. Magnetic nanowires. *Applied Sciences* **2020**, *10*, 1832.

[22] Nweze, C.; Glier, T. E.; Scheitz, S.; Westphal, L.; Biebl, F.; Buchenau, S.; Akinsinde, L. O.; Kohlmann, N.; Kienle, L.; González Díaz-Placio, I.; Frömter, R.; Zierold, R.; Blick, R.; Huse, N.; Rübhausen, M. Quantum confinement of the Spin Berry Phase on 1D topological surfaces of single Bi_2Se_3 nanowires. *Nano Letters*, under review.

[23] Lauhon, L. J.; Gudiksen, M. S.; Wang, D.; Lieber, C. M. Epitaxial core-shell and core-multishell nanowire heterostructures. *Nature* **2002**, *420*, 57–61.

[24] Kim, J.; Glier, T. E.; Grimm-Lebsanft, B.; Buchenau, S.; Teubner, M.; Biebl, F.; Kim, N.-J.; Kim, H.; Yi, G.-C.; Rübhausen, M.; Yoon, S. Quantum confinement induced excitonic mechanism in zinc-oxide-nanowalled microrod arrays for UV-Vis surface-enhanced Raman scattering. *The Journal of Physical Chemistry C* **2019**, *123*, 24957–24962.

[25] Ibach, H.; Lüth, H. *Festkörperphysik*; Springer, 2008; Chapter 3: Die Beugung an periodischen Strukturen, pp 51–69.

[26] Mattuck, R. D. *A guide to feynman diagrams in the many body problem*; Dover Publications, 1976.

[27] Rübhausen, M. A. *PhD-Thesis - Electronic correlations in cuprate superconductors - An inelastic light scattering study*; Universität Hamburg, 1998; Chapter Appendix C - Fundamentals, pp 107–140.

[28] Dirac, P. A. M. The quantum theory of the electron. *Proc. R. Soc. Lond. A* **1928**, *117*, 610–624.

[29] Dirac, P. A. M. The quantum theory of the electron. Part II. *Proc. R. Soc. Lond. A* **1928**, *118*, 351–361.

[30] Gross, R.; Marx, A. *Festkörperphysik*; De Gruyter, 2018; Chapter 8 Energiebänder, pp 315–367.

[31] Gross, R.; Marx, A. *Festkörperphysik*; De Gruyter, 2018; Chapter 10 Halbleiter, pp 483–571.

[32] Yu, P. Y.; Cardona, M. *Fundamentals of semiconductors*, 3rd ed.; Springer, Berlin, Heidelberg, 2010.

[33] Fradkin, E.; Dagotto, E. Physical realization of the parity anomaly in condensed matter physics. *Physical Review Letters* **1986**, *57*, 2967–2970.

[34] Hasan, M. Z.; Kane, C. L. Colloquium: Topologial insulators. *Reviews of Modern Physics* **2010**, *82*, 3045–3067.

[35] von Klitzing, K. The quantized Hall effect. *Reviews of Modern Physics* **1986**, *58*, 519.

[36] Gross, R.; Marx, A. *Festkörperphysik*; De Gruyter, 2018; Chapter 7 Das freie Elektronengas, pp 259–314.

[37] de Broglie, L. Waves and quanta. *Nature* **1923**, *112*, 540.

[38] Grundmann, M. *The physics of semiconductors*; Springer, Cham, 2016; Chapter Band Structure, pp 153–201.

[39] Slater, J. C.; Koster, G. F. Simplified LCAO method for the periodic potential problem. *Physical Review* **1954**, *94*, 1498.

[40] Reich, S.; Maultzsch, J.; Thomson, C.; Ordejon, P. Tight-binding description of graphene. *Physical Review B* **2002**, *66*, 035412.

[41] Janotti, A.; de Walle, C. G. V. Fundamentals of zinc oxide as a semiconductor. *Reports on Progress in Physics* **2009**, *72*, 126501.

[42] Mosquera, A. A.; Horwat, D.; Rashkovskiy, A.; Kovalev, A.; Miska, P.; Wainstein, D.; Albella, J. M.; Endrino, J. L. Exciton and core-level electron confinement effects in transparent ZnO thin films. *Scientific Reports* **2013**, *3*, 1714.

[43] Cayssol, J. Introduction to Dirac materials and topological insulators. *Comptes Rendus Physique* **2013**, *14*, 760–778.

[44] Zhang, Y.; Ran, Y.; Vishwanath, A. Topological insulators in three dimensions from spontaneous symmetry breaking. *Physical Review B* **2009**, *79*, 245331.

[45] Hsieh, D.; Xia, Y.; Wray, L.; Qian, D.; Pal, A.; Dil, J. H.; Osterwalder, J.; Meier, F.; Bihlmayer, G.; Kane, C. L.; Hor, Y. S.; Cava, R. J.; Hasan, M. Z. Observation of unconventional quantum spin textures in topological insulators. *Science* **2009**, *323*, 919–922.

[46] Kuroda, K.; Ye, M.; Kimura, A.; Eremeev, S. V.; Krasovskii, E. E.; Chulkov, E. V.; Ueda, Y.; Miyamoto, K.; Okuda, T.; Shimada, K.; Namatame, H.; Taniguchi, M. Experimetal realization of a three-dimensional topological insulator phase in ternary chalcogenide $TIBiSe_2$. *Physical Review Letters* **2010**, *105*, 146801.

[47] Berry, M. V. Quantal phase factors accompanying adabatic changes. *Proceedings of the Royal Society of London A A* **1984**, *392*, 45–57.

[48] Li, H.; Sheng, L.; Sheng, D. N.; Xing, D. Y. Chern number of thin films of the topological insulator Bi_2Se_3. *Physical Review B* **2010**, *82*, 165104.

[49] Gross, R.; Marx, A. *Festkörperphysik*; De Gruyter, 2018; Chapter 14 Topologische Quantenmaterie, pp 929–956.

[50] Yang, W.; Chang, K. Nonlinear Rashba model and spin relaxation in quantum wells. *Physical Review B* **2006**, *74*, 193314.

[51] Lou, W.-K.; Cheng, F.; Li, J. The persistent charge and spin currents in topological insulator Bi_2Se_3 nanowires. *Journal of Applied Physics* **2011**, *110*, 093714.

[52] Krishtopenko, S. S.; Yahniuk, I.; But, D. B.; Gavrilenko, V. I.; Knap, W.; Teppe, F. Pressure- and temperature-driven phase transitions in HgTe quantum wells. *Physical Review B* **2016**, *94*, 245402.

[53] Chege, S.; Ning'i, P.; Sifuna, J.; Amolo, G. O. Origin of band inversion in topological Bi_2Se_3. *AIP Advances* **2020**, *10*, 095018.

[54] Shen, S.-Q. *Topological insulators - Dirac equation in condensed matter*; Springer-Verlag Berlin Heidelberg, 2012.

[55] Osterhage, H.; Gooth, J.; Hamdou, B.; Gwozdz, P.; Zierold, R.; Nielsch, K. Thermoelectric properties of topological insulator Bi_2Te_3, Sb_2Te_3, and Bi_2Se_3 thin film quantum wells. *Applied Physics Letters* **2014**, *105*, 123117.

[56] Lu, H.-Z.; Shen, S.-Q. Weak localization of bulk channels in topological insulator thin films. *Physical Review B* **2011**, *84*, 125138.

[57] Münning, F.; Breunig, O.; Legg, H. F.; Roitsch, S.; Fan, D.; Rößler, M.; Risch, A.; Ando, Y. Quantum confinement of the Dirac surface states in topological-insulator nanowires. *Nature Communications* **2021**, *12*, 1038.

[58] Iorio, P.; Perroni, C. A.; Cataudella, V. Quantum interference effects in Bi_2Se_3 topological insulator nanowires with variable cross-section legths. *The European Physical Journal B* **2016**, *89*, 97.

[59] Iorio, P.; Perroni, C. A.; Cataudella, V. Plasmons in topological insulator cylindrical nanowires. *Physical Review B* **2017**, *95*, 235420.

[60] Imura, K.-I.; Takane, Y.; Tanaka, A. Spin Berry phase in anisotropic topological insulators. *Physical Review B* **2011**, *84*, 195406.

[61] Bardason, J. H.; Brouwer, P. W.; Moore, J. E. Aharonov-Bohn oscillations in disordered topological insulator nanowires. *Physical Review Letters* **2010**, *105*, 156803.

[62] Hong, S. S.; Zhang, Y.; Cha, J. J.; X, L. Q.; Cui, Y. One-dimensional helical transport in topological insulator nanowire interferometers. *Nano Letters* **2014**, *14*, 2815–2821.

[63] Ziegler, J.; Kozlovsky, R.; Gorini, C.; Liu, H.-H.; Weishäupl, S.; Maier, H.; Fischer, R.; Kozlov, D. A.; Kvon, Z. D.; Mikhailov, N.; Dvoretsky, S. A.; Richter, K.; Weiss, D. Probing spin helical surface states in topological HgTe nanowires. *Physical Review B* **2018**, *97*, 035157.

[64] Jauregui, L. A.; Pettes, M. T.; Pokhinson, L. P.; Shi, L.; Chen, Y. P. Magnetic field-induced helical mode and topological transitions in a topological insulator nanoribbon. *Nature Nanotechnology* **2016**, *11*, 345–351.

[65] Zhang, H.; Liu, C.-X.; Qi, X.-L.; Dai, X.; Fang, Z.; Zhang, S.-C. Topological insulators in Bi_2Se_3, Bi_2Te_3 and Sb_2Te_3 with a single Dirac cone on the surface. *Nature Physics* **2009**, *5*, 438–442.

[66] Zhang, J.; Peng, Z.; Soni, A.; Zhao, Y.; Xiong, Y.; Peng, B.; Wang, J.; Dresselhaus, M. S.; Xiong, Q. Raman spectroscopy of few-quintuple layer topological insulator Bi_2Se_3 nanoplatelets. *Nano Letters* **2011**, *11*, 2407–2414.

[67] Tedesco, E.; Giron, D.; Pfeffer, S. Crystal structure elucidation and morphology study of pharmaceuticals in development. *CrystEngComm* **2002**, *4*, 393–400.

[68] Schroer, C. G.; Agapov, I.; Brefeld, W.; Brinkmann, R.; Chae, Y.-C.; Chao, H.-C.; Eriksson, M.; Keil, J.; Gavalda, X. N.; Röhlsberger, R.; Seeck, O. H.; Sprung, M.; Tischer, M.; Wanzenberg, R.; Weckert, E. PETRA IV: the ultralow-emittance source project at DESY. *Journal of Synchrotron Radiation* **2018**, *25*, 1277–1290.

[69] Li, T.; Senesi, A. J.; Lee, B. Small angle X-ray scattering for nanoparticle research. *Chemical Reviews* **2016**, *116*, 11128–11180.

[70] Roth, S. V. A deep look into the spray coating process in real-time - the crucial role of X-Rays. *Journal of Physics: Condensed Matter* **2016**, *28*, 37pp.

[71] Hoffmann, A. *et al.* Catching an entatic state - A pair of copper complexes. *Angewandte Chemie* **2013**, *53*, 299–304.

[72] Pinczuk, A.; Burstein, E. In *Light scattering in solids I*; Cardona, M., Ed.; Springer-Verlag Berlin Heidelberg New York, 1983; Chapter 2 Fundamentals of inelastic light scattering in semiconductors and insulators, pp 23–78.

[73] Jha, S. S. Theory of light scattering from electronic excitations in solids. *Il Nuovo Cimento B* **1969**, *63*, 331–354.

[74] Ibach, H.; Lüth, H. *Festkörperphysik*; Springer, 2008; Chapter III: Raman Spektroskopie, pp 105–110.

[75] Martin, R. M.; Falicov, L. M. In *Light scattering in solids I*; Cardona, M., Ed.; Springer-Verlag Berlin Heidelberg New York, 1983; Chapter 3 Resonant raman scattering, pp 79–146.

[76] Kawabata, A. Green function theory of Raman scattering. *Journal of the Physical Society of Japan* **1971**, *30*, 68–85.

[77] Likharev, K. K. *Quantum mechanics - lecture notes*; IOP Publishing UK, 2019; Chapter 4.6 Quantum dynamics: three pictures, pp 4–33 – 4–45.

[78] Rübhausen, M. A. *PhD-Thesis - Electronic correlations in cuprate superconductors - An inelastic light scattering study*; Universität Hamburg, 1998; Chapter Appendix A - Fundamentals, pp 95–98.

[79] Baricz, A.; Masirevic, D. J.; Pogany, T. K. In *Series of Bessel and Kummer-type functions*; Morel, J.-M., Teissier, B., Eds.; Springer, 2017; Chapter 2 Neumann series, pp 27–86.

[80] Jorio, A.; Saitro, R.; Dresselhaus, G.; Dresselhaus, M. S. *Raman spectroscopy in graphene related systems*; WILEY-VCH Germany, 2011; Chapter Quantum description of Raman scattering, pp 103–120.

[81] Chen, X.; Wang, J.; Pan, R.; Roth, S.; Förster, S. Insights into growth kinetics of colloidal gold nanoparticles: In situ SAXS and UV-Vis evaluation. *The Journal of Physical Chemistry C* **2021**, *125*, 1087–1095.

[82] Liang, S.; Chen, W.; Yin, S.; Schaper, S. J.; Guo, R.; Drewes, J.; Carstens, N.; Strunskus, T.; Gensch, M.; Schwartzkopf, M.; Faupel, F.; Roth, S. V.; Cheng, Y.-J.; Müller-Buschbaum, P. Tailoring the optical properties of sputter-deposited gold nanostructures on nanostructured titanium dioxide templates based on in situ grazing-incidence small-angle X-ray scattering determined growth laws. *Applied Materials & Interfaces* **2021**, *13*, 14728–14740.

[83] de Casto, A. R. B.; Eremina, E.; Bostedt, C.; Hoener, M.; Thomas, H.; Möller, T. Numerical simulation of small angle scattering (SAXS) for large atomic clusters. *Journal of Electron Spectroscopy and Related Phenomena* **2009**, *166-167*, 21–27.

[84] Engel, M.; Stühn, B.; Schneider, J. J.; Cornelius, T.; Naumann, M. Small-angle X-ray scattering (SAXS) off parallel, cylindrical, well-defined nanopores: from random pore distribution to highly ordered samples. *Applied Physics A* **2009**, *97*, 99–108.

[85] Müller-Buschbaum, P. In *Applications of synchrotron light to scattering and diffraction in materials and life sciences. Lecture notes in physics*; Gomez, M., Nogales, A., Garcia-Gutierrez, M., Ezquerra, T., Eds.; Springer, Berlin, Heidelberg, 2009; Chapter A basic introduction to grazing incidence small-angle X-ray scattering, pp 61–89.

[86] Yoneda, Y. Anomalous surface reflection of X rays. *Physical Review* **1963**, *131*, 2010–2013.

[87] Lazzari, R. IsGISAXS: A program for grazing-incidence small-angle X-ray scattering analysis of supported islands. *Journal of Applied Crystallography* **2002**, *35*, 406–421.

[88] Lazzari, R.; Leroy, F.; Renaud, G. Grazing-incidence small-angle x-ray scattering from dense packing of islands on surfaces: Development of distorted wave Born

approximation and correlation between particle sizes and spacing. *Physical Review B* **2009**, *76*, 125411.

[89] Rauscher, M.; Paniago, R.; Metzger, H.; Kovats, Z.; Domke, J.; Peisl, J.; Pfannes, H.-D.; Schulze, J.; Eisele, I. Grazing incidence small angle X-ray scattering from free-standing nanostructures. *Journal of Applied Physics* **1999**, *86*, 6763.

[90] Schulz, B.; Bäckström, J.; Budelmann, D.; Maeser, R.; Rübhausen, M.; Klein, M. V.; Schoeffel, E.; Mihill, A.; Yoon, S. Fully reflective deep ultraviolet to near infrared spectrometer and entrance optics for resonance Raman spectroscopy. *Review of Scientific Instruments* **2005**, *76*, 073107.

[91] Misra, A.; Bist, H. D.; Navati, M. S.; Thareja, R. K.; Narayan, J. Thin film of aluminum oxide through pulsed laser deposition: a micro-Raman study. *Materials Science & Engineering B* **2001**,

[92] Dieckmann, N. *PhD-Thesis - Raman and micro-Raman analyses of $Y_xPr_{1-x}Ba_2Cu_3O_7$ single crystals, films, and devices*; Universität Hamburg, 1996.

[93] Westphal, L. *Bachelor Thesis - Mikro-Raman-Charakterisierung von nanostrukturierten Proben*; Universität Hamburg, 2020.

[94] Buffet, A.; Rothkirch, A.; Döhrmann, R.; Körstgens, V.; Kashem, M. M. A.; Perlich, J.; und M. Schwartzkopf, G. H.; Gehrke, R.; Müller-Buschbaum, P.; Roth, S. V. P03, the microfocus and nanofocus X-ray scattering (MiNaXS) beamline of the PETRA III storage ring: the microfocus endstation. *Journal of Synchrotron Radiation* **2012**, *19*, 647–653.

[95] Santoro, G.; Buffet, A.; Yu, R. D. S.; Körstgens, V.; Müller-Buschbaum, P.; Gedde, U.; Hedenqvist, M.; Roth, S. V. Use of intermediate focus for grazing incidence small and wide angle X-ray scattering experiments at the beamline P03 of PETRA III, DESY. *Review of Scientific Instruments* **2014**, *85*, 043901.

[96] Schwartzkopf, M.; Santoro, G.; Brett, C. J.; Rothkirch, A.; Polonskyi, O.; Hinz, A.; Metwalli, E.; Yao, Y.; Strunskus, T.; Faupel, F.; Müller-Buschbaum, P.; Roth, S. V. Real-time monitoring of morphology and optical properties during sputter deposition for tailoring metal-polymer interfaces. *Applied Materials and Interfaces* **2015**, *7*, 13547–13556.

[97] Akinsinde, L. O. *et al.* Surface characterization and resistance changes of silver-nanowire networks upon atmospheric plasma treatment. *Applied Surface Science* **2021**, *550*, 149362.

[98] With, S.; Trebbin, M.; Bartz, C. B. A.; Neuber, C.; Dulle, M.; Yu, S.; Roth, S. V.; Schmidt, H.-W.; Förster, S. Fast diffusion-limited lyotropic phase transitions studied in situ using continuous flow microfluidics/microfocus-SAXS. *Langmuir* **2014**, *30*, 12494–12502.

[99] Benecke, G.; Wagermaier, W.; Li, C.; Schwartzkopf, M.; Flucke, G.; Hoerth, R.; Zizak, I.; Burghammer, M.; Metwalli, E.; Müller-Buschbaum, P.; Trebbin, M.; Förster, S.; Paris, O.; Roth, S. V.; Fratzl, P. A customizable software for fast reduction and analysis of large X-ray scattering data sets: applications of the new DPDAK package to small-angle X-ray scattering and grazing-incidence small-angle X-ray scattering. *Journal of Applied Crystallography* **2014**, *47*, 1797–1803.

[100] Betker, M. *Master Thesis - Stretching of silver-nanowire-polymer-composites*; Universität Hamburg, 2020.

[101] van der Pauw, L. J. A method of measuring the resistivity and Hall coefficient on lamellae of arbitrary shape. *Philips Technical Review* **1958**, *20*, 220–224.

[102] Paul, D. R.; Robeson, L. M. Polymer nanotechnology: nanocomposites. *Polymer* **2008**, *49*, 3187–3204.

[103] Vivekchand, S. R. C.; Kam, K. C.; Gundiah, G.; Govindaraj, A.; Cheetham, A. K.; Rao, C. N. R. Electrical properties of inorganic nanowire-polymer composites. *Journal of Materials Chemistry* **2005**, *15*, 4922–4927.

[104] Balachander, N.; Seshadri, I.; Mehta, R. J.; Schadler, L. S.; Borca-Tasciuc, T.; Keblinski, P.; Ramanath, G. Nanowire-filled polymer composites with ultrahigh thermal conductivity. *Applied Physics Letters* **2013**, *102*, 093117.

[105] Moniruzzaman, M.; Winey, K. I. Polymer nanocomposites containing carbon nanotubes. *Macromolecules* **2006**, *39*, 5194–5205.

[106] Lu, S.; Sun, Y.; Ren, K.; Liu, K.; Wang, Z.; Qu, S. Recent development in ITO-free flexible polymer solar cells. *Polymers* **2018**, *10*, 1–30.

[107] Xu, Y.; Wei, X.; Wang, C.; Cao, J.; Chen, Y.; Ma, Z.; You, Y.; Wan, J.; Fang, X.; Chen, X. Silver nanowires modified with PEDOT:PSS and grahene for organic light-emitting diodes anode. *Scientific Reports* **2017**, *7*, 45392.

[108] Huynh, W. U.; Dittmer, J. J.; Alivisatos, A. P. Hybrid nanorod-polymer solar cells. *Science* **2002**, *295*, 2425–2427.

[109] Zhang, S.; Zhang, H.; Yao, G.; Liao, F.; Gao, M.; Huang, Z.; Li, K.; Lin, Y. Highly stretchable, sensitive, and flexible strain sensors based on silver nanoparticles/carbon nanotubes composites. *Journal of Alloys and Compounds* **2015**, *652*, 48–54.

[110] Xia, Y.; Yang, P.; Sun, Y.; Wu, Y.; Mayers, B.; Gates, B.; Yin, Y.; Kim, F.; Yan, H. One-dimensional nanostructures: synthesis, characterization, and applications. *Advanced Materials* **2003**, *15*, 353–389.

[111] Miller, M. S.; O'Kane, J. C.; Niec, A.; Carmichael, R. S.; Carmichael, T. B. Silver nanowire/optical adhesive coatings as transparent electrodes for flexible electronics. *Applied Materials and Interfaces* **2013**, *5*, 10165–10172.

[112] Li, J.; Tao, Y.; Chen, S.; Li, H.; Chen, P.; Wei, M.; Wang, H.; Li, K.; Mazzeo, M.; Duan, Y. A flexible plasma-treated silver-nanowire electrode for organic light-emitting devices. *Scientific Reports* **2017**, *7*, 16468.

[113] Zeng, X. Y.; Zhang, Q. K.; Yu, R. M.; Lu, C. Z. A new transparent conductor: silver nanowire film buried at the surface of a transparent polymer. *Advanced Materials* **2010**, *22*, 4484–4488.

[114] He, X.; Duan, F.; Liu, J.; Lan, Q.; Wu, J.; Yang, C.; Yang, W.; Zeng, Q.; Wang, H. Transparent electrode based on silver nanowires and polyimide for film heater and flexible solar cell. *Materials* **2017**, *10*, 1362.

[115] Sannicolo, T.; Lagrange, M.; Cabos, A.; Celle, C.; Simonato, J.-P.; Bellet, D. Metallic nanowire-based transparent electrodes for next generation flexible devices: a review. *Small* **2016**, *12*, 6052–6075.

[116] Yang, L.; Zhang, T.; Zhou, H.; Price, S. C.; Wiley, B. J.; You, W. Solution-processed flexible polymer solar cells with silver nanowire electrodes. *ACS Applied Materials & Interfaces* **2011**, *3*, 4075–4084.

[117] Yu, Z.; Zhang, Q.; Li, L.; Chen, Q.; Niu, X.; Liu, J.; Pei, Q. Highly flexible silver nanowire electrodes for shape-memory polymer light-emitting diodes. *Advanced Materials* **2011**, *23*, 664–668.

[118] Amjadi, M.; Pichitpajongkit, A.; Lee, S.; Ryu, S.; Park, I. Highly stretchable and sensitive strain sensor based on silver nanowire-elastomer nanocomposite. *ACS Nano* **2014**, *8*, 5154–5163.

[119] Xu, F.; Zhu, Y. Highly conductive and stretchable silver nanowire conductors. *Advanced Materials* **2012**, *24*, 5117–5122.

[120] Hofmann, M. 3D printing gets a boost and opportunities with polymer materials. *ACS Macro Letters* **2014**, *3*, 382–386.

[121] MacDonald, E.; Wicker, R. Multiprocess 3D printing for increasing component functionality. *Science* **2016**, *353*, aff2093.

[122] Liska, R.; Schuster, M.; Inführ, R.; Turecek, C.; Fritscher, C.; Seidl, B.; Schmidt, V.; Kuna, L.; Haase, H.; Varga, F.; Lichtenegger, H.; Stampfl, J. Photopolymers for rapid prototyping. *Journal of Coatings Technology and Research* **2007**, *4*, 505–510.

[123] Glier, T. E.; Betker, M.; Grimm-Lebsanft, B.; Scheitz, S.; Matsuyama, T.; Akinsinde, L. O.; Rübhausen, M. Conductance-strain behavior in silver-nanowire composites: network properties of a tunable strain sensor. *Nanotechnology* **2021**, *32*, 365701.

[124] Skrabalak, S. E.; Wiley, B. J.; Kim, M.; Formo, E. V.; Xia, Y. On the polyol synthesis of silver nanostructures: glycolaldehyde as a reducing agent. *Nano Letters* **2008**, *8*, 2077–2081.

[125] Xia, Y.; Xiong, Y.; Lim, B.; Skrabalak, S. E. Shape-controlled synthesis of metal nanocrystals: simple chemistry meets complex physics? *Angewandte Chemie* **2009**, *48*, 60–103.

[126] Zhang, S.; Jiang, Z.; Xie, Z.; Xu, X.; Huang, R.; Zheng, L. Growth of silver nanowires from solutions: a cyclic penta-twinned-crystal growth mechanism. *The Journal of Physical Chemistry B* **2005**, *109*, 9416–9421.

[127] Korte, K. E.; Skrabalak, S. E.; Xia, Y. Rapid synthesis of silver nanowires through a CuCl- or $CuCl_2$-mediated polyol process. *Journal of Materials Chemistry* **2008**, *18*, 437–441.

[128] Glier, T. E. Study on conductive silver nanowire composites for 3D printing. M.Sc. thesis, Universität Hamburg, 2018.

[129] Sun, Y.; Mayers, B.; Herricks, T.; Xia, Y. Polyol synthesis of uniform silver nanowires: a plausible growth mechanism and the supporting evidence. *Nano Letters* **2003**, *3*, 955–960.

[130] Nguyen, T.; Jirasattayaporn, K.; Kheawhom, S.; Shirahata, N.; Saw, T. Y. J.; Ghosh, B.; M., High aspect ratio and post-processing free silver nanowires as top electrodes for inverted-structured photodiodes. *ACS Omega* **2019**, *4*, 13303–13308.

[131] Balberg, I.; Binenbaum, N. Computer study of the percolation threshold in a two-dimensional anisotropic system of conducting sticks. *Physical Review B* **1983**, *28*, 3799–3812.

[132] Pike, G. E.; Seager, C. H. Percolation and conductivity: a computer study. I. *Physical Review B* **1974**, *10*, 1421–1434.

[133] Munson-McGee, S. H. Estimation of the critical concentration in an anisotropic percolation network. *Physical Review B* **1991**, *43*, 3331–3336.

[134] White, S. I.; Mutiso, R. M.; Vora, P. M.; Jahnke, D.; Hsu, S.; Kikkawa, J. M.; Li, J.; Fischer, J. E.; Winey, K. I. Electrical percolation behavior in silver nanowire-polystyrene composites: simulation and experiment. *Advanced Functional Materials* **2010**, *20*, 2709–2716.

[135] Nan, C.-W.; Shen, Y.; Ma, J. Physical properties of composites near percolation. *Annual Reviews* **2010**, *40*, 131–151.

[136] Yi, J. Y.; Choi, G. M. Percolation behavior of conductor-insulator composites with varying aspect ratio of conductive fiber. *Journal of Electroceramics* **1999**, *3*, 361–369.

[137] Madaria, A. R.; Kumar, A.; Ishikawa, F. N.; Zhou, C. Uniform, highly conductive, and patterned transparent films of a percolating silver nanowire network on rigid and flexible substrates using a dry transfer technique. *Nano Research* **2010**, *3*, 564–573.

[138] Kim, K. K.; Hong, S.; Cho, H. M.; Lee, J.; Suh, Y. D.; Ham, J.; Ko, S. H. Highly sensitive and stretchable multidimensional strain sensor with prestrained anisotropic metal nanowire percolation networks. *Nano Letters* **2015**, *15*, 5240–5247.

[139] Essam, J. W. Percolation theory. *Reports on Progress in Physics* **1980**, *43*, 833–912.

[140] Balberg, I.; Binenbaum, N.; Anderson, C. H. Critical behavior of the two-dimensional sticks system. *Physical Review Letters* **1983**, *51*, 1605–1608.

[141] Fischer, M. E.; Essam, J. W. Some cluster size and percolation problems. *Journal of Mathematical Physics* **1961**, *2*, 609–619.

[142] Sykes, M. F.; Essam, J. W. Exact critical percolation probabilities for site and bond problems in two dimensions. *Journal of Mathematical Physics* **1964**, *5*, 1117–1127.

[143] Ni, X.; Hui, C.; Su, N.; Jiang, W.; Liu, F. Monte Carlo simulations of electrical percolation in multicomponent thin films with nanofillers. *Nanotechnology* **2018**, *29*, 075401.

[144] Newman, M. E. J.; Ziff, R. M. Fast Monte Carlo algorithm for site or bond percolation. *Physical Review E* **2001**, *64*, 016706.

[145] Gawlinski, E. T.; Stanley, H. E. Continuum percolation in two dimensions: Monte Carlo tests of scaling and universality for non-interacting discs. *Journal of Physics A: Mathematical and General* **1981**, *14*, L291–L299.

[146] Rottereau, M.; Gimel, J. C.; Nicolai, T.; Durand, D. 3d Monte Carlo simulation of site-bond continuum percolation of spheres. *The European Physical Journal E* **2003**, *11*, 61–64.

[147] Yook, S.-H.; Choi, W.; Kim, Y. Conductivity of stick percolation clusters with anisotropic alignments. *Journal of the Korean Physical Society* **2012**, *61*, 1257–1262.

[148] Metropolis, N.; Rosenbluth, A. W.; Rosenbluth, M. N.; Teller, A. H. Equation of state calculations by fast computing machines. *The Journal of Chemical Physics* **1953**, *21*, 1087–1092.

[149] Rosenbluth, M. N.; Rosenbluth, A. W. Further results on Monte Carlo equations of state. *The Journal of Chemical Physics* **1954**, *22*, 881–884.

[150] Rosenbluth, M. N.; Rosenbluth, A. W. Monte Carlo calculation of the average extension of molecular chains. *The Journal of Chemical Physics* **1955**, *23*, 356–359.

[151] Metropolis, N. The beginning of the Monte Carlo method. *Los Alamos Science* **1987**, *Special Issue*, 125–130.

[152] Anderson, H. L. Metropolis, Monte Carlo, and the MANIAC. *Los Alamos Science* **1986**, *Fall*, 96–107.

[153] Rubinstein, R. Y.; Kroese, D. P. *Simulation and the Monte Carlo method*, 3rd ed.; Wiley-Interscience, 2016.

[154] Wu, F. Y. Theory of resistor networks: the two-point resistance. *Journal of Physics A: Mathematical and General* **2004**, *37*, 6653–6673.

[155] The NumPy community, numpy.linalg.eigh. 2021; `https://numpy.org/doc/stable/reference/generated/numpy.linalg.eigh.html`.

[156] Schmid, H.; Lendemann, K.; Petasch, H. U. K.; and, B. K. Low-pressure plasma cleaning: a process for precision cleaning applications. *Surface and Coatings Technology* **1997**, *97*, 176–181.

[157] Wu, C. C.; Wu, C. I.; Sturm, J. C.; Kahn, A. Surface modification of indium tin oxide by plasma treatment: an effective method to improve the efficiency, brightness, and reliability of organic light emitting devices. *Applied Physics Letters* **1997**, *70*, 1348–1350.

[158] Hegemann, D.; Brunner, H.; Oehr, C. Plasma treatment of polymers for surface and adhesion improvement. *Nuclear Instruments and Methods in Physics Reasearch Section B* **2003**, *208*, 281–286.

[159] Liston, E. M. Plasma treatment for improved bonding: a review. *The Journal of Adhesion* **1989**, *30*, 199–218.

[160] Tantec, The basics of plasma treatment - what is Plasma? 2020; `https://tantec.com/the-basics-of-plasma-treatment/`.

[161] Abourayana, H.; Dobbyn, P.; Dowling, D. Enhancing the mechanical performance of additive manufactured polymer components using atmospheric plasma pretreatments. *Plasma Processes and Polymers* **2018**, *15*, 1700141.

[162] Zhang, C.; Fang, K. Surface modification of polyester fabrics for inkjet printing with atmospheric-pressure air/Ar plasma. *Surface & Coatings Technology* **2009**, *203*, 2058–2063.

[163] Tendero, C.; Tixier, C.; Tristant, P.; Desmaison, J.; Leprince, P. Atmospheric pressure plasmas: a review. *Spectrochimica Acta Part B* **2006**, *61*, 2–30.

[164] Plasma Etch, Inc., Plasma Wand hand-held atmospheric plasma cleaner. 2020; `https://www.plasmaetch.com/atmospheric-plasma-wand-cleaner.php`.

[165] Witte, M.; Jaspers, S.; Wenck, H.; und F. Fischer, M. R. Noise reduction and quantification of fiber orientations in greyscale images. *Plos One* **2020**, *15*, e0227534.

[166] Witte, M.; Jaspers, S.; Wenck, H.; Rübhausen, M.; Fisher, F. General method for classification of fiber families in fiber-reinforced materials: application to in-vivo human skin images. *Scientific Reports* **2020**,

[167] Davim, J. P., Charitidis, C. A., Eds. *Nanocomposites - materials, manufacturing and engineering*; De Gruyter, 2013.

[168] Fischer, H. Polymer nanocomposites: from fundamental research to specific applications. *Materials Science and Engineering: C* **2003**, *23*, 763–772.

[169] Hanemann, T.; Szabó, D. V. Polymer-nanoparticle composites: from synthesis to modern applications. *Materials* **2010**, *3*, 3468–3517.

[170] Crosby, A. J.; Lee, J. Polymer nanocomposites: the "Nano" effect on mechanical properties. *Polymer Reviews* **2007**, *47*, 217–229.

[171] Minnai, C.; Vece, M. D.; Milani, P. Mechanical-optical-electro modulation by stretching a polymer-metal nanocomposite. *Nanotechnology* **2017**, *28*, 355702.

[172] Minnai, C.; Milani, P. Metal-polymer nanocomposite with stable plasmonic tuning under cyclic strain conditions. *Applied Physics Letters* **2015**, *107*, 073106.

[173] Lu, Z.; Wang, Y.; Ruan, X. The critical particle size for enhancing thermal conductivity in metal nanoparticle-polymer composites. *Journal of Applied Physics* **2018**, *123*, 074302.

[174] Campbell, T. A.; Ivanova, O. S. 3D printing of multifunctional nanocomposites. *Nanotoday* **2013**, *8*, 119–120.

[175] Wong, K. V.; Hernandez, A. A review of additive manufacturing. *International Scholarly Research Network* **2012**, *2012*, 1–10.

[176] Farahani, R. D.; Dubé, M. Printing polymer nanocomposites and composites in three dimensions. *Advanced Engineering Materials* **2017**, *20*, 1700539.

[177] Zhang, J.; Xiao, P. 3D printing of photopolymers. *Polymer Chemistry* **2018**, *9*, 1530–1540.

[178] Bagheri, A.; Jin, J. Photopolymerization in 3D printing. *Applied Polymer Materials* **2019**, *1*, 593–611.

[179] Ikemura, K.; Ichizawa, K.; Yoshida, M.; Ito, S.; Endo, T. UV-VIS spectra and photoinitiation behaviors of acylphosphine oxide and bisacylphosphine oxide derivatives in unfilled, light-cured dental resins. *Dental Materials Journal* **2008**, *27*, 765–774.

[180] Kaur, M.; Srivastava, A. K. Photopolymerization: a review. *Journal of Macromolecular Science, Part C* **2006**, *42*, 481–512.

[181] Hoyle, C. E.; Keel, M.; Kim, K.-J. Photopolymerization of 1,6-hexanediol diacrylate: The effect of functionalized amines. *Polymer* **1988**, *29*, 18–23.

[182] EQ-99X LDLS Compact, high-brightness, long-life, broadband laser-driven light source, Data sheet. Energetiq Technology, May 2021.

[183] Hooke, R. *Lectures de potentia reflitutiva or of spring: explaining the power of springing bodies*; 1678.

[184] Li, C.; Thistenson, E. T.; Chou, T.-W. Dominant role of tunneling resistance in the electrical conductivity of carbon nanotube-based composites. *Applied Physics Letters* **2007**, *91*, 223114.

[185] Balberg, I. Tunneling and nonuniversal conductivity in composite materials. *Physical Review Letters* **1987**, *59*, 1305–1308.

[186] Harwood, J. A. C.; Payne, A. R.; Whittaker, R. E. Stress-softening and reinforcement of rubber. *Journal of Macromolecular Science, Part B* **1971**, *5*, 473–486.

[187] Wu, J.; Zhang, J.; Rathmell, A. R.; Zhao, X.; Wiley, B. J. Reversible sliding in networks of nanowires. *Nano Letters* **2013**, *13*, 2381–2386.

[188] Nadgorny, M.; Ameli, A. Functional polymers and nanocomposites for 3D printing of smart structures and devices. *Applied Materials & Interfaces* **2018**, *10*, 17489–17507.

[189] Amjadi, M.; Kyung, K.-U.; Park, I.; Sitti, M. Stretchable, skin-mountable, and wearable strain sensors and their potential applications: a review. *Advanced Functional Materials* **2016**, *26*, 1678–1698.

[190] Pang, C.; Lee, G.-Y.; Kim, T.; Kim, S. M.; Kim, H. N.; Ahn, S.-H.; Suh, K.-Y. A flexible and highly sensitive strain-gauge sensor using reversible interlocking of nanofibres. *Nature Materials* **2012**, *11*, 795–801.

[191] Gong, S.; Schwalb, W.; Wang, Y.; Chen, Y.; Tang, Y.; Si, J.; Shirinzadeh, B.; Cheng, W. A wearable and highly sensitive pressure sensor with ultrathin gold nanowires. *Nature Communications* **2014**, *5*, 3132.

[192] Choi, S. *et al.* Highly conductive, stretchable and biocompatible Ag-Au core-sheath nanowire composite for wearable and implantable bioelectronics. *Nature Nanotechnology* **2018**, *13*, 1048–1056.

[193] Xu, H.; Lv, Y.; Qiu, D.; Zhou, Y.; Zeng, H.; Chu, Y. An ultra-stretchable, highly sensitive and biocompatible capacitive strain sensor from an ionic nanocomposite for on-skin monitoring. *Nanoscale* **2019**, *11*, 1570–1578.

[194] Lee, C.-J.; Park, K. H.; Han, C. J.; Oh, M. S.; You, B.; Kim, Y.-S.; Kim, J.-W. Crack-induced Ag nanowire networks for transparent, stretchable, and highly sensitive strain sensors. *Scientific Reports* **2017**, *7*, 7959.

[195] Xiao, X.; Yuan, L.; Zhong, J.; Ding, T.; Liu, Y.; Cai, Z.; Rong, Y.; Han, H.; Zhou, J.; Wang, Z. L. High-strain sensors based on ZnO nanowire/polystyrene hybridized flexible films. *Advanced Materials* **2011**, *23*, 5440–5444.

[196] Li, X.; Zhang, R.; Yu, W.; Wang, K.; Wei, J.; Wu, D.; Cao, A.; Li, Z.; Cheng, Y.; Zheng, Q.; Ruoff, R. S.; Zhu, H. Stretchable and highly sensitive graphene-on-polymer strain sensors. *Scientific Reports* **2012**, *2*, 870.

[197] Ji, L.; Chang, W.; Cui, M.; Nie, J. Photopolymerization kinetics and volume shrinkage of 1,6-hexanediol diacrylate at different temperatures. *Journal of Photochemistry and Photobiology A: Chemistry* **2013**, *252*, 216–221.

[198] Griffiths, D. J. *Elektrodynamik: eine Einführung*; Pearson Studium, 2018.

[199] Ackermann, T.; Neuhaus, R.; Roth, S. The effect of rod orientation on electrical anisotropy in silver nanowire networks for ultra-transparent electrodes. *Scientific Reports* **2016**, *6*, 34289.

[200] Shan, X.; Mao, P.; Li, H.; Geske, T.; Bahadur, D.; Xin, Y.; Ramakrishna, S.; Yu, Z. 3D-printed photoactive semiconducting nanowire-polymer composites for light sensors. *Applied Nano Materials* **2020**, *3*, 969–976.

[201] Chang, C.-Y.; Tsao, F.-C.; Pan, C.-J.; Chi, G.-C.; Wang, H.-T.; Chen, J.-J.; Ren, F.; Norton, D. P.; Pearton, S. J.; Chen, K.-H.; Chen, L.-C. Electroluminescence from ZnO nanowire/polymer composite p-n junction. *Applied Physics Letters* **2006**, *88*, 173503.

[202] Kim, A.; Won, Y.; Woo, K.; Kim, C.-H.; Moon, J. Highly transparent low resistance ZnO/Ag nanowire/ZnO composite electrode for thin film solar cells. *ACS Nano* **2013**, *7*, 1081–1091.

[203] Yang, Y.; Lin, Z.-H.; Hou, T.; Zhang, F.; Wang, Z. L. Nanowire-composite based flexible thermoelectric nanogenerators and self-powered temperature sensors. *Nano Research* **2012**, *5*, 888–895.

[204] Manapat, J. Z.; Chen, Q.; Ye, P.; Advincula, R. C. 3D printing of polymer nanocomposites via stereolithography. *Macromolecular Materials and Engineering* **2017**, *302*, 1600553.

[205] Sciancalepore, C.; Moroni, F.; Messori, M.; Bondioli, F. Acrylate-based silver nanocomposite by simultaneous polymerization-reduction approach via 3D stereolithography. *Composites Communications* **2017**, *6*, 11–16.

[206] Choi, J.-W.; Kim, H.-C.; Wicker, R. Multi-material stereolithography. *Journal of Materials Processing Technology* **2011**, *211*, 318–328.

[207] Singh, M.; Haverinen, H. M.; Dhagat, P.; Jabbour, G. E. Inkjet printing - process and its applications. *Advanced Materials* **2010**, *22*, 673–685.

[208] Mosier-Boss, P. A. Review of SERS substrates for chemical sensing. *Nanomaterials* **2017**, *7*, 142.

[209] Alvarez-Puebla, R. A.; Liz-Marzan, L. M. SERS detection of small inorganic molecules and ions. *Angewandte Chemie* **2012**, *51*, 11214–11223.

[210] Poscik, I.; Veres, M.; Füle, M.; Toth, S.; Koos, M. Specific statistical features of surface enhanced Raman scattering (SERS) spectra of graphite. *Journal of Non-Crystalline Solids* **2004**, *338-340*, 496–498.

[211] Zrimsek, A. B.; Wong, N. L.; Duyne, R. P. V. Single molecule surface-enhanced Raman spectroscopy: a critical analysis of the bianalyte versus isotopologue proof. *Journal of Physical Chemistry C* **2016**, *120*, 5133–5142.

[212] Etchegoin, P. G.; Ru, E. L. A perspective on single molecule SERS: current status and future challenges. *Physical Chemistry Chemical Physics* **2008**, *10*, 6079–6089.

[213] Kahraman, M.; Mullen, E. R.; Korkmaz, A.; Wachsmann-Hogiu, S. Fundamentals and applications of SERS-based bioanalytical sensing. *Nanophotonics* **2017**, *6*, 831–852.

[214] Fleischmann, M.; Hendra, P. J.; McQuillan, A. J. Raman spectra of pyridine adsorbed at a silver electrode. *Chemical Physics Letters* **1974**, *26*, 163–166.

[215] Otto, A.; Mrozek, I.; Grabhorn, H.; Akemann, W. Surface-enhanced Raman scattering. *Journal of Physics: Condensed Matter* **1992**, *4*, 1143–1212.

[216] Pilot, R.; Signorini, R.; Durante, C.; Orian, L.; Bhamidipati, M.; Fabris, L. A review on surface-enhanced Raman scattering. *Biosensors* **2019**, *9*, 57.

[217] Kim, N.-J.; Kim, J.; Park, J.-B.; Kim, H.; Yi, G.-C.; Yoon, S. Direct observation of quantum tunnelling charge transfers between molecules and semiconductors for SERS. *Nanoscale* **2019**, *11*, 45–49.

[218] Kim, J.; Jang, Y.; Kim, N.-J.; Kim, H.; Yi, G.-C.; Shin, Y.; Kim, M. H.; Yoon, S. Study of chemical enhancement mechanism in non-plasmonic surface enhanced Raman spectroscopy (SERS). *Frontiers in Chemistry* **2019**, *7*, 582.

[219] Zhang, L.; Bai, Y.; Shang, Z.; Zhang, Y.; Mo, Y. Experiental and theoretical studies of Raman spectroscopy on 4-mercaptopyridine aqueous solution and 4-mercaptopyridine/Ag complex systems. *Journal of Raman Spectroscopy* **2007**, *38*, 1106–1111.

[220] Buchenau, S.; Scheitz, S.; Sethi, A.; Slimak, J. E.; Glier, T. E.; Das, P. K.; Dankwort, T.; Akinsinde, L.; Kienle, L.; Rusydi, A.; Ulrich, C.; Cooper, S. L.; Rübhausen, M. Temperature and magnetic field dependent Raman study of electron-phonon interactions in thin films of Bi_2Se_3 and Bi_2Te_3 nanoflakes. *Physical Review B* **2020**, *101*, 245431.

[221] Cooper, S.; Klein, M. Light scattering studies of the low frequency excitation spectra of high temperature superconductors. *Comments Cond. Mat. Phys.* **1990**, *15*, 99–124.

[222] Santoro, G.; Yu, S.; Schwartzkopf, M.; Zhang, P.; Vayalil, S. K.; Risch, J. F. H.; Rübhausen, M.; Hernandez, M.; Domingo, C.; Roth, S. V. Silver substrates for surface enhanced Raman scattering: Correlation between nanostructure and Raman scattering enhancement. *Applied Physics Letters* **2014**, *104*, 243107.

[223] Buchenau, S.; Sergelius, P.; Wiegand, C.; Bäßler, S.; Zierold, R.; Shin, H. S.; Rübhausen, M.; Gooth, J.; Nielsch, K. Symmetry breaking of the surface mediated quantum Hall Effect in Bi_2Se_3 nanoplates using Fe_3O_4 substrates. *2D Materials* **2017**, *4*, 015044.

[224] Weinhold, M.; Chatterjee, S.; Klar, P. J. Modifying graphene's lattice dynamics by hot-electron injection from single gold nanoparticles. *Communications Physics* **2019**, *2*, 18.

[225] Popper, K. R. In *Karl Popper Lesebuch: Ausgewählte Texte zur Erkenntnistheorie, Philosophie der Naturwissenschaften, Metaphysik, Sozialphilosophie*, 2nd ed.; Miller, D., Ed.; Mohr Siebeck, 1997; Chapter Teil I Erkenntnistheorie, p 5.

Appendix A

A Further Methods

Atomic force microscopy (AFM) was conducted with a commercially available AFM Q-Scope 250 model with (40 × 40) µm^2 scan head, a lateral resolution of 0.6 nm, and a vertical resolution of 0.05 nm. During the measurements, the cantilever was in intermittent contact and scanned along the x-axis (horizontal scan mode).[22]

Optical transmission measurements (silver nanowires on glass) were carried out with an Ulbricht sphere of calibrated spectral characteristics (DKD, Gigahertz Optik) coupled to a QE65000 spectrometer (Ocean optics, USA) in a spectral range between 400 nm and 900 nm.[14]

The **photocurrent** of a composite coated solar cell was measured with a digital multimeter (Voltcraft, VC 850). The samples were illuminated with an Ulbricht sphere of calibrated spectral characteristics (DKD, Gigahertz Optik). An area with a diameter of approximately 5 mm was exposed with a power of about 20 mW cm^{-2}.[14]

For **resistivity measurements** in four-point geometry at static samples (no stretching) DPP 105-M/V-Al-S positioners (CascadeMicrotech, USA) were used together with a DC voltage/current source GS200 (Yokogawa, Japan) and a 34401A 6 1/2 Digit Multimeter (Keysight, USA).[14]

Scanning electron microscopy (SEM) measurements were conducted to determine the shape and size of silver nanowires and Bi_2Se_3 nanowires. The measurements were performed with a commercial field effect SEM (FESEM) equipment (Zeiss, Germany). Acceleration voltages of up to 15 kV were used. For high resolution, the in-lens detector and voltages of 1 kV to 8 kV were employed. Furthermore, the setup is equipped with an EDX system using a silicon drift detector (remX GmbH).[14, 15, 123, 22]

Profilometry measurements were performed with a Dektak XT equipment (Bruker, USA).[14]

A programmable HM8118 LCR bridge (Rohde & Schwarz, Germany) was used to determine the **capacitance** of our flexible capacitor at 1 kHz and at 100 kHz.[14]

B Appendix B
Tables

Tab. B.2, B.1, and B.3 list all parts utilized for the micro-Raman setup (see section 3.1.1). The parts were purchased from Thorlabs Inc. (Newton, New Jersey, USA), Newport (Irvine, California, USA), Edmund Optics (Barrington, USA), The Imaging Source (Charlotte, North Carolina, USA), Olympus (Tokio, Japan), Physik Instrumente (PI, Karlsruhe, Germany), and Nanotec (Feldkirchen, Germany).

Tab. B.4 contains the parts used for the stretching setup (see section 3.3). The parts were purchased from Conrad Electronics (Hirschau, Germany), Nanotec (Feldkirchen, Germany), and Thorlabs Inc. (Newton, New Jersey, USA).

The chemicals used for the silver nanowire synthesis (see section 4.1.2) are listed in Tab. B.5. Furthermore, Tab. B.6 contains information about the compounts used for the HDDA photoresin. Chemicals were purchased from Sigma Aldrich (St. Louis, Missouri, USA) and Carl Roth (Karlsruhe, Germany).

Tab. B.7 summarizes the measurement parameters of presented GISAXS measurements on silver nanowire samples on silicon substrates (silicon wafers from Si-Mat, <100>, p-type, doped with boron).[14, 128, 97]

Table B.1: Translation and piezo stages, and kinematic mounts used for micro-Raman.[93]

Name & Function	**Model**	**Company**
XYZ linear stage, dovetail, 14 mm XY, 5 mm Z	M-DS40-XYZ	Newport
25.0 mm translation stage with standard micrometer	PT1/M	Thorlabs
XY translating lens mount for ⌀1" optics	CXY1	Thorlabs
XYZ translation mount for ⌀1/2" optics	CXYZ05M	Thorlabs
SM1-threaded kinematic mount	KC1-T/M	Thorlabs
Right-angle kinematic mirror mount	KCB1C/M	Thorlabs
Right-angle kinematic elliptical mirror mount	KCB05E/M	Thorlabs
Gimbal mirror mount	KC45D	Thorlabs
Cage cube precision kinematic rotation platform	B4CRP/M	Thorlabs
Multi-axis piezo scanner	P-517	PI
Piezo stage controller	E-710.3CD	PI

Table B.2: Parts used for the micro-Raman construction based on the Thorlabs cage system.[93]

Name & Function	**Model**	**Company**
Aluminum breadboard, 200 mm × 200 mm	MB2020/M	Thorlabs
Optical rail	PRL-12	Newport
Optical rail carrier	M-PRC-3	Newport
Cage assembly rod	ER05	Thorlabs
Cage assembly rod	ER1.5	Thorlabs
Cage assembly rod	ER6	Thorlabs
Cage assembly rod	ER18	Thorlabs
Swivel coupler	C2A	Thorlabs
Cage cube	C4W	Thorlabs
Blank cover plate for cage cube	B1C/M	Thorlabs
Cage cube connector	C4W-CC	Thorlabs
SM1-threaded standard cage plates	CP33/M	Thorlabs
SM1 lens tube spacer, 1” long	SM1S10	Thorlabs
SM1 lens tube, 2”	SM1L20	Thorlabs
SM2 lens tube, 3”	SM2L30	Thorlabs
SM1-threaded adapter	AD11F	Thorlabs
SM2 coupler, external threads	SM2T2	Thorlabs
SM1 coupler, external threads	SM1T2	Thorlabs
Adapter; external SM1 and internal SM2	SM1A2	Thorlabs
Adapter: external SM1 and internal M26 × 0.706	SM1A27	Thorlabs
Adapter: external M26 × 0.706 and internal SM1	SM1A28	Thorlabs
Mitutoyo to C-mount extension tube	56-992	Edmund Optics
Stepper motor	ST4118M1804-B	Nanotec
Closed-loop stepper-motor controller	SMCI33-2	Nanotec

Table B.3: Optical components used for the micro-Raman setup.[93]

Name & Function	Model	Company
Cage iris diaphragm	CP20S	Thorlabs
SM1 lever-actuated zero aperture iris diaphragm	SM1D12SZ	Thorlabs
Mounted pinhole, 20 ± 2 µm pinhole diameter	P20D	Thorlabs
Protected silver mirror	PF10-03-P01	Thorlabs
1/2" broadband dielectric elliptical mirror	BBE05-E02	Thorlabs
Lens $f = 25$ mm, ⌀1/2", ARC: 400 - 1100 nm	AC127-025-AB	Thorlabs
Lens $f = 75$ mm, ⌀1/2", ARC: 400 - 1100 nm	AC127-075-AB	Thorlabs
Plano-convex lens, 2", $f = 60$ mm, AR Coating	LA1401-A	Thorlabs
Plano-convex lens, 1", $f = 25$ mm, AR Coating	LA1951-A	Thorlabs
Non-polarizing beamsplitter cube, 70:30 (R:T)	BS064	Thorlabs
Non-polarizing beamsplitter cube, 10:90 (R:T)	BS043	Thorlabs
N-BK7 ground glass diffuser	DG10-1500	Thorlabs
Quartz tungsten-halogen lamp	QTH10/M	Thorlabs
Collimated laser for adjustment (635 nm, 1.2 mW)	CPS635R	Thorlabs
50X Mitutoyo Plan Apo	46-146	Edmund Optics
50X Mitutoyo Plan Apo HR	58-237	Edmund Optics
MT-40 accessory tube lens	83-911	Edmund Optics
Focusing objective	IC50	Olympus
USB 3.1 color industrial camera	DFK37BUX264	The Imaging Source

Table B.4: Parts used for the stretching setup.[100]

Name & Function	Model	Company
25.0 mm translation stage	PT1/M	Thorlabs
Power supply	NTS-24V-5A	Nanotec
Stepper motor 0,9°NEMA 17	ST4209S1006-B	Nanotec
Closed-loop stepper-motor controller	SMCI33-2	Nanotec
Capacitor 4700 µF	Z-K4700/50	Nanotec
D-SUB 90° 9 pin female terminal	DSUB09F-10TB-2	Conrad Electronics

Table B.5: Chemicals for silver nanowire synthesis.[128, 14]

Name	Information	Company	Amount
Ethylene glycol (EG)	anhydrous, 99.8 % purity	Sigma Aldrich	11 mL, 0.20 mol
Silver nitrate ($AgNO_3$)	>99.9 % purity	Carl Roth	0.03 g, 0.18 mmol
Polyvinylpyrrolidone (PVP)	55000 MW	Sigma Aldrich	0.03 g, 0.55 µmol
	360000 MW	Carl Roth	0.06 g, 0.17 µmol
Copper(II) chloride dihydrate ($CuCl_2 \cdot 2\,H_2O$)	99.999 % purity	Sigma Aldrich	3 µL of solution (c = 0.0519 mol/L), 0.156 µmol

Table B.6: Chemical compounds of the HDDA-based resin.[128, 14]

Name	Function	Company	Amount
HDDA	monomer	Sigma-Aldrich	3 mL, $n = 0.013$ mol
BAPO	initiator	Sigma-Aldrich	0.33 g, $n = 0.789$ mmol
DPPHA	cross-linker	Sigma-Aldrich	5 mL, $n = 0.011$ mol

Table B.7: GISAXS measurement parameters (angle of incidence α_i, wavelength λ, and sample to detector distance (SDD)) for silver nanowire (Ag-NW) samples.[14, 97, 128]

Sample	α_i	λ	SDD
Ag-NWs on Si (Fig. 4.3(a) & Fig. 4.19(a))	0.527°	0.972 ± 0.002 Å	4990 ± 1 mm
Ag-NWs on Si *in situ* plasma treatment (Fig. 4.9(a)-(d))	0.425°	0.965 ± 0.002 Å	4380 ± 2 mm
HDDA photopolymer on Si (Fig. 4.19(b))	0.527°	0.972 ± 0.002 Å	3600 ± 1 mm
HDDA Ag-NW composite on Si (Fig. 4.19(c))	0.462°	0.972 ± 0.002 Å	4990 ± 1 mm

Appendix C

C Publication List

I contributed to the following publications as first or shared-first author: (I), (II), (III), (V), (VII), and (VIII). Corresponding authors are indicated by asterisks (*) at the author's names.

(I) Glier*, T. E.; Akinsinde, L. O.; Paufler, M.; Otto, F.; Hashemi, M.; Grote, L.; Daams, L.; Neuber, G.; Grimm-Lebsanft, B.; Biebl, F.; Rukser, D.; Lippmann, M.; Ohm, W.; Schwartzkopf, M.; Brett, C. J.; Matsuyama, T.; Roth*, S. V.; Rübhausen*, M. Functional printing of conductive silver-nanowire photopolymer composites. *Scientific Reports* **2019**, 9, 6465.

(II) Kim*, J.; Glier*, T. E.; Grimm-Lebsanft, B.; Buchenau, S.; Teubner, M.; Biebl, F.; Kim, N.-J.; Kim, H.; Yi, G.-C.; Rübhausen*, M.; Yoon*, S. Quantum confinement induced excitonic mechanism in zinc-oxide-nanowalled microrod arrays for UV-Vis surface-enhanced Raman spectroscopy. *Journal of Physical Chemistry C* **2019**, 123, 24957-24962.

(III) Glier, T. E.; Vakili, M.; Trebbin*, M. Microfluidic synthesis of thermo-responsive block copolymer nano-objects via RAFT polymerization, *Journal of Polymer Research* **2020**, 27, 333.

(IV) Buchenau*, S.; Scheitz, S.; Sethi, A.; Slimak, J. E.; Glier, T. E.; Das, P. K.; Dankwort, T.; Akinsinde, L.; Kienle, L.; Rusydi, A.; Ulrich, C.; Cooper, S. L.; Rübhausen, M. Temperature and magnetic field dependent Raman study of electron-phonon interactions in thin films of Bi_2Se_3 and Bi_2Te_3 nanoflakes. *Physical Review B* **2020**, 101, 245431.

(V) Glier*, T. E.; Betker, M.; Witte, M.; Matsuyama, T.; Westphal, L.; Grimm-Lebsanft, B.; Biebl, F.; Akinsinde, L. O.; Fischer, F.; Rübhausen*, M. Electrical and network properties of flexible silver-nanowire composite electrodes under mechanical stain. *Nanoscale* **2020**, 20, 23831-23837.

(VI) Akinsinde*, L. O.; Glier*, T. E.; Schwartzkopf*, M.; Betker, M.; Nissen, M.; Witte, M.; Scheitz, S.; Nweze, C.; Grimm-Lebsanft, B.; Gensch, M.; Chumakov, A.; Baev, I.; Schürmann, U.; Dankwort, T.; Fischer, F.; Martins, M.; Roth, S. V.; Kienle, L.; Rübhausen*, M. Surface characterization and resistance changes of silver-nanowire networks upon atmospheric plasma treatment. *Applied Surface Science* **2021**, 550, 1493262.

(VII) Glier*, T.E.; Betker*, M.; Grimm-Lebsanft, B.; Scheitz, S.; Matsuyama, T.; Akinsinde, L. O.; Rübhausen*, M. Conductance-strain behavior in silver-nanowire composites: network properties of a tunable strain sensor. *Nanotechnology* **2021**, 32, 365701.

(VIII) Nweze*, C.; Glier*, T. E.; Scheitz, S.; Westphal, L.; Biebl, F.; Buchenau, S.; Akinsinde, L. O.; Kohlmann, N.; Kienle, L.; González Díaz-Placio, I.; Frömter, R.; Zierold, R.; Blick, R.; Huse, N.; Rübhausen*, M. Quantum Confinement of the Spin-Berry phase on 1D topological surfaces of single Bi_2Se_3 nanowires. Submitted to *Nano Letters*.

Appendix D

D Eidesstattliche Erklärung

Hiermit versichere ich an Eides statt, die vorliegende Dissertationsschrift selbst verfasst und keine anderen als die angegebenen Hilfsmittel und Quellen benutzt zu haben.

Die eingereichte schriftliche Fassung entspricht der auf dem elektronischen Speichermedium.

Die Dissertation wurde in der vorgelegten oder einer ähnlichen Form nicht schon einmal in einem früheren Promotionsverfahren angenommen oder als ungenügend beurteilt.

Hamburg, den 21.07.2021